Thermal Stress Analysis of Unidirectional Fiber Reinforced Composites

A Thesis
Submitted to the College of Graduate Studies and Research
in Partial Fulfillment of the Requirements
for the Degree of Doctor of Philosophy
in the
Department of Mechanical Engineering
University of Saskatchewan
Saskatoon, Saskatchewan

By

Ali Abedian
Fall, 1998

Permission to Use

In presenting this thesis in partial fulfillment of the requirements for a Postgraduate degree from the University of Saskatchewan, I agree that the Libraries of this University may make it freely available for inspection. I further agree that permission for copying of this thesis in any manner, in whole or in part, for scholarly purposes may be granted by the professors who supervised my thesis work or, in their absence, by the Head of the Department or the Dean of the College in which my thesis work was done. It is understood that any copying or publication or use of this thesis or parts thereof for financial gain shall not be allowed without my written permission. It is also understood that due recognition shall be given to me and to the University of Saskatchewan in any scholarly use which may be made of any material in my thesis.

Requests for permission to copy or to make other use of material in this thesis in whole or part should be addressed to:

Head of the Department of Mechanical Engineering
University of Saskatchewan
Saskatoon, Saskatchewan S7N 5A9

Dedication

The sacrifices, encouragement, and support which the author received from his family cannot be compensated by dedication of this piece of work to them. However, the author would like to dedicate this thesis to his wife Atefeh and his daughter Mahdieh. The author's special thanks and appreciation also go to his parents Abbas and Sedigheh and his uncles and their wives Mohammad-Ali, Farideh, Mohammad-Hassan, and Mahbobeh.

Acknowledgements

May All Praise Be to **Allah (God)**

The author would like to express his sincere gratitude and a deep feeling of indebtedness to his supervisors, Dr. W. Szyszkowski and Dr. S. Yannacopoulos, for their invaluable guidance and advice throughout the course of this work. Their encouragement and positive criticism have been mainly responsible for the success of this project.

The author wishes to express his appreciation to Mr. I. J. MacPhedran of Engineering Computing Services in support of computer problems. Also, the technical assistance from Mr. P. W. Siminoff and Mr. H. J. Steinmetz are gratefully acknowledged. The author also wishes to thank Mr. Ike Ogocha for his editing assistance. The author's cordial thanks are due to the members of the supervisory committee; Dr. T. Rezansoff[1], Dr. L. G. Watson[2], Dr. A. T. Dolovich[3]. Also, the memories of Dr. H. T. Danyluk and the author's best friend Mr. M. K. Hoetzel, whose demise caused a great deal of pain and sadness to the author, are remembered.

The author acknowledges the financial support by the University of Saskatchewan Graduate Scholarship and the support provided in the form of scholarship by the Ministry of Culture and Higher Education and the Ministry of Reconstruction of the Islamic Republic of Iran. Also, financial assistance provided by Dr. W. Szyszkowski and Dr. S. Yannacopoulos in the form of a research assistantship from the Natural Science and Engineering Research Council (NSERC) of Canada is thankfully acknowledged.

---

[1] Prof., Dept. of Civil Engineering, Univ. of Saskatchewan.
[2] Prof., Dept. of Mechanical Engineering, Univ. of Saskatchewan.
[3] Prof., Dept. of Mechanical Engineering, Univ. of Saskatchewan.

Abstract

Composite materials are widely used in temperature fluctuating environments, which make these materials highly prone to cracking. The cracking phenomenon is a result of high thermal stresses that are generated by the mismatch in properties of the composite constituents, particularly the mismatch in the thermal expansion coefficient. The main objective of this study is to understand the micromechanics of such a phenomenon. The problem has been investigated using the finite element method (FEM).

The analyses were performed utilizing 3-D prism and axisymmetric models. Hexagonal fiber packing of unidirectional composites was considered. The dimensions of the models were assumed such that the models could provide sufficient information on the behavior near the free surface as well as the interior of fiber composites. Properties of the constituents were considered to be temperature dependent. The elasto-plastic and visco-elastic characteristics of the materials were also included.

The transient thermal analysis of the models showed that, for most practical applications, the temperature gradient in the composite constituents has minor effects on the stresses generated. Therefore, several stress analyses were performed assuming a uniformly changing temperature throughout the composite.

The elastic analysis of thermal stresses and deformations showed high radial and hoop stress concentrations occurring at the fiber end on the free surface. This is contrary to the shear-lag theorem, which assumes that these stress components are negligible. An overlapping hypothesis, based on the deformation of the fiber and matrix, is proposed to explain such high radial and hoop stresses.

Using regular FEM elements, it was concluded that the stresses are singular in nature. The stress singularity was numerically investigated and found to be of the type $r^{-\alpha}$ with α being dependent on the material properties but having a value close to 1/3.

The elasto-visco-plastic behavior of composites was also analyzed. Large plastic strains were localized at the fiber end even for a small temperature change. Creep effects that were significant at elevated temperatures brought about some stress relaxation during the manufacturing process.

Thermally induced stress concentration in composites can be controlled, to some extent, by changing the geometry of the free surface. The analysis of such effects indicated that reduction of the contact angle between the fiber and the matrix on the free surface reduced the high radial and hoop stress magnitudes. Also, the influence of covering the free surface of the composite with a thin layer of matrix-like material was studied. The magnitudes of the radial and hoop stress components were substantially reduced. The case when the cover and the composite are made in separate stages (two-stage covering), was also studied. Based on the analysis, effective and practical ways of applying the cover are recommended.

To verify the effects of the covering process, experiments were conducted on large-scale laboratory-made composite samples. The samples with the free surface covered with a thin layer of matrix-like material showed no trace of cracking or fiber/matrix debonding even after 1000 thermal cycles. On the other hand, in the samples without cover, exposed to identical thermal cycling, numerous matrix cracks and extensive fiber/matrix debonding were observed.

Table of Contents

List of Figures

List of Tables

Nomenclature

α	Order of singularity
σ	Stress
σ_{eq}	Equivalent von Mises Stress
σ_y	Yield Strength
σ_y^h	Yield Strength of a Strain Hardened Material
τ	Shear Stress
ε	Strain
ε_{eq}^{pl}	Equivalent Plastic Strain
ϕ	Matrix Contact Angle
θ	Fiber Contact Angle
ψ	Matrix Ramp Contact Angle
υ	Poisson's Ratio
χ	Plastic Work
γ	Translation Tensor of the Yield Surface
G	Shear Modulus
E	Elastic Modulus
ρ	Radial Distance from the Singular Point
k	Coefficient of Thermal Conductivity
C	Coefficient of Thermal Capacitance
T	Change in Temperature from the Stress Free Temperature
T_p	Processing Temperature
T_c	Cycling Temperature
T_r	Room Temperature

ΔT	Uniform Temperature change
U_r	Radial Displacement
U_θ	Circumferencial Displacement
U_z	Axial Displacement
r_m	Matrix Radius
r_f	Fiber Radius
V_f	Fiber Volume Fraction
CTE	Coefficient of Thermal Expansion
MMC	Metal Matrix Composites
IMC	Intermetallic Matrix Composites
FMI	Fiber Matrix Interface
MRC	Manufacturer's Recommended Cure

1. Introduction

1.1 Background

For some time, mankind has learned that some combination of materials gives properties superior to those of their constituents. This experience goes back in history to the time of the Prophet Moses or even earlier. For example, the people in Egypt used mud bricks reinforced with straw, Mongols made bows from cattle tendons, wood, and silk bonded together. Today, materials made by combining two or more different types of materials are called composite materials. Composites consist of the load carrying components (reinforcements), the binder (matrix) which transfers the applied loads to the reinforcements and binds them together, and the interface between these two to secure integrity and performance.

Composites can be divided into two groups: natural and artificially-made composites. Examples of natural composites are wood, bone, and banana peel. The artificially-made composites are divided into many sub-groups on the basis of the type of reinforcements (fiber, particle, whiskers) and matrices (polymer, ceramic, metal).

In general, composites can be superior to conventional materials in terms of the ratio of their strength and/or stiffness to weight. Also, a better thermal dimensional stability (lower thermal expansion), higher fatigue strength, better corrosion resistance, and better elevated temperature properties can be achieved by combining two or more distinctly different materials. One of the main problems in composites resulting from their nature is the internal thermal stress resulting from temperature changes. Usually, this is due to a mismatch in the coefficient of thermal expansion (CTE) of the composite constituents. These internal thermal stresses may cause interfacial debonding and matrix cracking leading to structural integrity degradation.

1.2 Problem Definition

Thermal stress distribution plays a major role in the performance of composite materials. This becomes crucial when either the coefficients of thermal expansion (CTE) of the composite constituents are far apart in magnitude or the processing/working temperature is high. The difference in CTE causes different expansion or contraction in composite constituents under even a seemingly uniform temperature change. For example, Figs. 1.1(a) and 1.1(b) show a cylindrical single fiber composite (with the CTE much lower for the fiber than the matrix) under heating and cooling, respectively. To preserve continuity, the constituents internally constrain one another generating thermal stress in the material. Under high temperature, even a small mismatch in CTE creates high thermal stresses. Additional thermal stresses may be created if the coefficients of thermal conductivity and thermal capacity of the constituents are different or the mechanical and thermal properties of the materials are functions of temperature. These phenomena will create thermal gradients inside the material, which eventually generate thermal stresses.

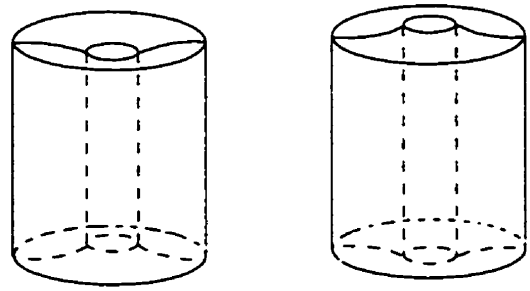

a) Heating b) Cooling

Fig. 1.1: Thermal deformation of a single fiber composite.

Typically, high thermal stresses are generated in metallic matrix composites by their high processing and service temperatures, while in polymeric matrix composites they are generated by significant differences in material properties of the constituents. In either case, these stresses would greatly degrade the composite performance. In particular, the exposed surfaces of composites show signs of fiber/matrix debonding and/or matrix cracking. These effects are observed to a lesser extent in the interior of the composites. A

free surface of a thermally cycled composite sample is shown in Fig. 1.2. Experiments have shown that cracking and debonding mostly occur as a result of the cooling phase of temperature cycles or upon cooling from the processing temperature.

Fig. 1.2: Free surface cracking of a thermally cycled composite (Hildebrandt, 1990).

The process of cracking usually starts at the interface on the free surface where the fiber has the largest distance to its neighboring fiber (see Fig. 1.3). Cracking then spreads into the area with the least distance to the adjacent fibers. Many researchers have studied this problem both theoretically and experimentally. Analytical solutions are extremely complex near the free surface of composites and this may be why more results have been published on calculating the thermal stresses deep inside the material rather than close to the free surface. Also, most of the finite element modeling studies provide information on the stress and deformation away from the composite free surface. In general, there is a lack of information regarding the free surface and the inter-relationship of the stress and deformation states at this region with those at the interior of composites. Moreover, in the finite element method (FEM), inadequate meshing, using improper type of elements in the

areas of high stress gradients, not considering proper model sizes, and utilizing many simplifying assumptions such as plane strain or stress states make the results insufficient for drawing reliable conclusions.

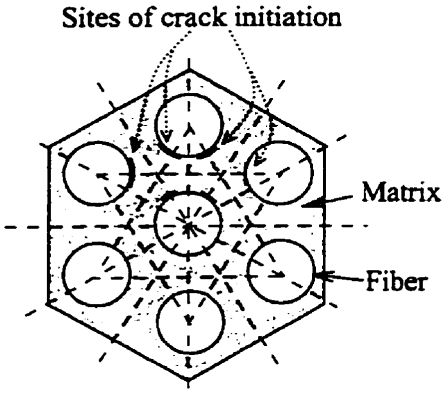

Fig. 1.3: Usual thermally induced cracking pattern around the fibers.

Many experimental as well as a few numerical studies have attempted to provide an insight into the reduction of the damaging effects of thermal stresses on the composite performance specifically at the fiber/matrix interface. For example, coating the fibers with a third material having properties intermediate to those of the fiber and the matrix was considered by Arnold et al. (1992). A stronger coating material relative to the matrix increases the capability of the composite in resisting the high stresses at the interface. Assisting diffusion of the matrix into the fiber is another way of strengthening composites against thermal stresses (Mall and Ermer, 1991). The matrix diffusion makes the interface stronger. This reduces the chance of fiber/matrix debonding under thermal load. Another method which has been tried, is that of utilizing different post-cure thermal treatments to relax thermal residual stresses. For instance, imposing temperature cycles with decaying maximum and minimum values has helped in some cases (Morris et al., 1989_a). However, no solution to the cracking phenomenon at the fiber/matrix interface on the exposed surfaces has been suggested yet.

1.3 Research Objectives

The present study is mainly focused on how to deal with the thermal stresses and how to strengthen composites in order to accommodate the unwanted thermal effects. In order to reduce the adverse effects of thermal stresses in composites, a comprehensive

study of the stress and deformation states is required. In general, it is important to know the behavior of composites during temperature changes and, more specifically, the nature of the stresses in various regions of the composites. Also, the influence of the stress fields (i.e. the stresses at the free surface and the interior of composites) on one another and, more importantly, the effects of physical deformations (which may be triggered by the temperature change) on the stresses should be fully understood. Therefore, to fulfill the prime objective of this research work, a careful modeling study was undertaken. To achieve this goal, it was necessary to study/model composites in an appropriate way. Thus, a comprehensive investigation of the available approaches/models was performed to identify their dominant limitations. It was required to develop an approach/model that does not have the limitations of the existing ones. The modeling results were checked with the available experimental results in terms of the nature of thermal stresses, formation of plastic strains, and deformation of the free surface and interior of composites during temperature changes. After achieving a good understanding of the stresses and displacements imposed due to a temperature change, methods of containing the undesired thermal effects were proposed and are discussed in detail.

1.4 Research Methodology

The equations governing the behavior of composites, along with all the boundary conditions and the continuity requirements, are presented in Appendix A. Analytical solutions to such a complex partial differential equation (PDE) set has been the subject of many studies which are reviewed in the next chapter. All of these investigations were conducted using many simplifying assumptions such as plane-stress, plane-strain, or generalized axisymmetric conditions. With these assumptions, the PDE can be reduced to the Lame-type of equation (see Appendix A). The Lame-equation is easier to solve, but the results are limited to the interior region of the composite for a very small value of the fiber volume fraction.

More sophisticated solutions have also been reported in the literature. For example, the variational technique has been employed for calculating stress components at the end

of a single broken fiber embedded in a matrix by Nairn (1992) and a 3-D solution of the reduced PDE for a single cylindrical fiber embedded in a matrix has been reported by Li and Folias (1991). One of Nairn's assumptions is that the axial displacements in the fiber and the matrix are the same at any location along the fiber length (Lame condition). The solution by Li and Folias was obtained assuming a large diameter for the fiber which makes it invalid for composites since they usually contain a large number of very thin fibers. Also, in addition to all of the simplifications, these solutions were obtained for a single fiber and the effects of the neighboring fibers on the stress and displacement states are yet to be taken into consideration. In addition, as will be discussed in Chapter 2, the solution by Li and Folias does not satisfy the boundary conditions at the end of the fiber on the free surface. To this date, the author is not aware of a complete solution of the PDE that satisfies all the boundary conditions and the continuity requirements.

An alternative to the analytical approach is the finite element method (FEM) which is broadly used in the engineering field. In this dissertation, the FEM is utilized to solve the PDE set. Here, ANSYS, a FEM commercial software package is used. All the possible nonlinearities such as structural nonlinearities (large strain, large deflection, stress stiffening) and material nonlinearities (plasticity, creep) are considered.

A high accuracy of the approximate FEM solution can be obtained if the material and geometry modeling are performed with sufficient care. The material should be modeled as closely as possible to its behavior under the loading condition. In particular, variation of the material parameters with temperature should be included. The geometry of the model has to be as representative of the problem as possible. For example, for unidirectional fiber composites, the 3-D FEM models should be considered to analyze the stress and displacements at the end of the fiber on the free surface and at the interior of the composite. Meshing of the model should be done in such a way that the size of the numerical problem does not compromise the accuracy of the analysis in terms of stress and displacements. In particular, dense meshing with higher order elements should be considered for the areas with high stress gradients. This requires some knowledge of the physics of the problem as well as other factors such as sharp corners, material

discontinuities, and geometric discontinuities that may affect the stress fields. Frequent verifications of the accuracy of the results should also be performed.

In this dissertation a micro-mechanistic approach to composites is applied using the FEM technique. Several important findings of the FEM analysis have been verified by experimental tests performed on composite specimens. Other results are verified by comparing them to the available experimental and analytical results obtained by other researchers.

2. Mechanics of Composite Materials; A Review

2.1 Introduction

Although composite materials have been used for a long time, the technology of modern composites has been essentially developed during the last three decades. The advances have been reported in a large number of publications and cover several areas of science and technology. In this chapter the most recent results relevant to the objectives of this dissertation are reviewed.

2.2 Basic Theories of Composite Materials

Composite materials are made from conventional materials by some special techniques. Conventional materials may be divided into three major groups; metals, ceramics, and polymers. In each category, the materials have some characteristic properties, which are distinct for that group. However, the materials in each group have weaknesses of their own that make them less desirable for some specific use. For example, metals are superior in terms of stiffness and hygroscopic sensitivity, but their weaknesses include high density and susceptibility to corrosion. Ceramics are ranked highest in terms of compressive strength, stiffness, creep resistance, and thermal stability, however they are brittle. The main advantages of polymers are low density and ductility, but they possess low stiffness, strength, creep resistance, thermal and dimensional stability, and erosion resistance. It would be desirable to combine various materials to make the best use of each group's characteristics for a particular application.

Inclusion of a solid material into another material creates a new system with new gross or macro material properties. For example, long fibers of one material may be incorporated into a second material referred to as matrix (Fig. 2.1). From a microscopic

point of view, considering the characteristic volumes J_1 or J_2, the individual materials may be isotropic. On a macroscopic scale the material system (volume I) is considered anisotropic because the properties vary with orientation.

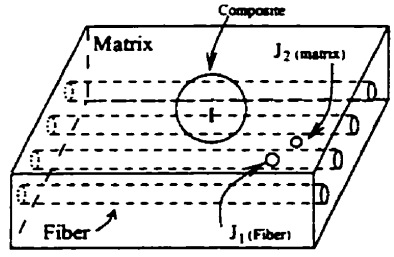

Fig. 2.1: Macroscopic (I) and microscopic (J_1 and J_2) observations of unidirectional composites.

Composites may contain continuous or discontinuous fibers. Fibers are also called the reinforcement since they usually carry most of the load. The matrix binds, separates, and transfers the load to the reinforcements. An additional phase, called the inter-phase, may exist between the reinforcements and the matrix resulting from a chemical reaction between the two components, or a purposely applied coating to enhance bonding.

Various types of reinforcements are used in composites depending on the kind of application. For low performance composites, short fibers or even particles are used to provide some stiffening but only local strengthening. In the case of high performance composites, long fibers are used to increase the stiffness and strength of the composite in the direction of the fibers.

A planar or curved layer of unidirectional or woven fibers in a matrix is called a lamina or ply. A unidirectional lamina is orthotropic in nature with three principal axes in the fiber direction (designated as 1), transverse to the fiber (2), and normal to the plane of fiber (3) (see Fig. 2.2).

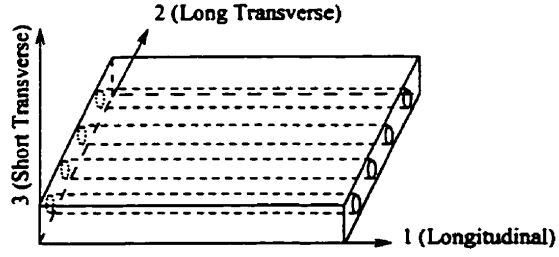

Fig. 2.2: Principal coordinate axes in unidirectional composites.

The level of consideration and the scale of analysis of a composite material depend upon a particular characteristic and behavior requirement of the composite under investigation. When local failures (such as buckling, breaking and failure of the fiber, matrix breaking, or debonding) are of concern, the analysis is performed at the fiber and matrix level and referred to as the micro-mechanics of composites (Fig. 2.3). This method of analysis is particularly important for the study of properties such as strength, fracture toughness, fatigue life, local plastic and viscoplastic deformations, and local stress concentrations. These properties cannot be inferred from averaged characteristics of the composite. The analyses in this dissertation are based on such a micro-mechanics approach and are performed at the fiber and matrix level.

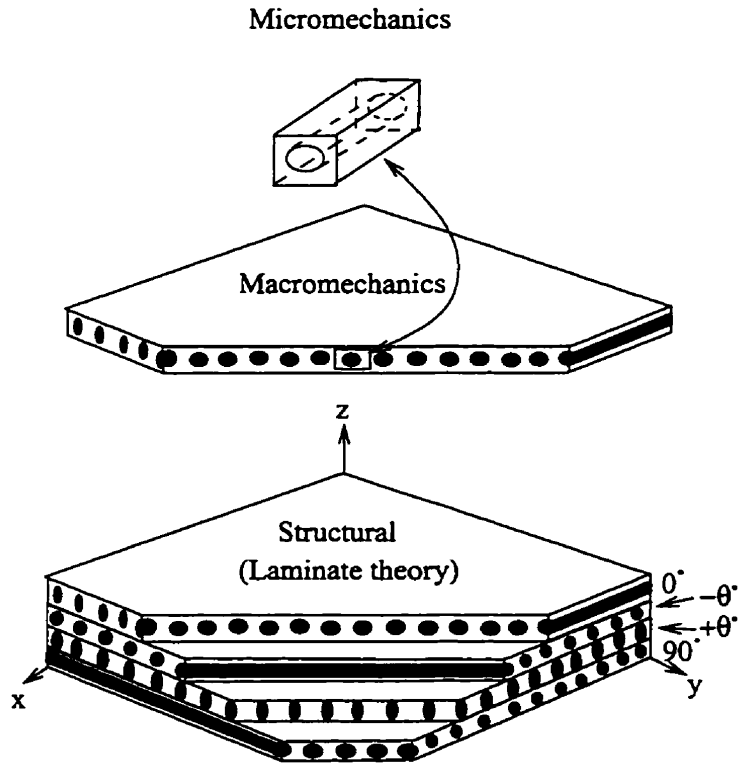

Fig. 2.3: Various levels of analysis of composite materials.

At the lamina level, composites can be considered as homogeneous anisotropic materials with average properties. In this approach, called macro-mechanics, the local failure mechanisms are not taken into account. Instead, failure criteria are expressed in terms of average stresses and overall lamina strength values. The overall behavior of a laminate is analyzed as a function of lamina properties and stacking sequence. This

approach is convenient for analysis of overall stiffness of composites. Details of the lamina theory are found in most textbooks on mechanics of composite materials, e.g., Daniel and Ishai (1994) and Chawla (1987).

In general, when compared to conventional materials, polymeric matrix composites provide a higher specific strength (ratio of material strength to density) in the direction of the high strength fibers. However, the transverse tensile strength of unidirectionally reinforced composites is substantially reduced due to local stress concentrations around fibers. The usually low fracture toughness of fibers is compensated by the matrix ductility and by higher energy dissipation at the fiber/matrix interface.

The anisotropic nature of composites adds to the complexity of the macro-mechanical analysis. The average material properties required for analysis of composite structures can be calculated from the properties and arrangement of their constituents. The experimental verification requires complex tests for determination of many material constants.

2.3 Mechanics of Composite Materials

Analysis of stress-strain relationships in composite materials is complicated because of the involvement of many parameters. For example, the type of reinforcement, reinforcement volume fraction, interface strength, and properties of the constituents influence the stress distribution in composites. The objective of the present research work is to study the behavior of unidirectional composites subject to temperature changes. The micro-mechanical approach is employed with the analyses conducted at the level of a fiber and the surrounding matrix. In order to include the free surface effects the composite is considered in a 3-D space. Several mathematical models of unidirectional composites are considered. First, the difficulties of obtaining any 3-D analytical solution to the problem involving a single fiber embedded in a matrix are addressed. Next, the application of FEM in analyzing the elastic stress state in composites and the occurrence of possible singular stress fields is discussed. Following this, the inelastic behavior of composites during manufacturing and at service temperatures is analyzed.

2.4 Micro-mechanical Analysis of Unidirectional Fiber Composites

The local stress and deformation fields on a microscopic level directly affect the performance of a composite structure. Prediction of the stress and deformation along the fiber length and surrounding matrix and at their interface can help in detecting areas that are susceptible to local damage. Normally, in the micro-mechanical approach, a single fiber embedded in matrix is the basic element for the analysis. The derivation of the governing equations for an arbitrary element in the fiber or the matrix are presented in Appendix A. These equations are solved for a unit cell the geometry of which varies depending on the type of fiber packing (Fig. 2.4) as discussed in Chapter 3.

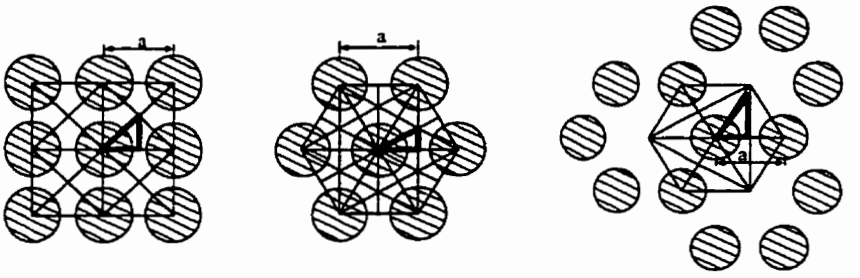

Rectangular pattern Hexagonal pattern Triangular pattern

Fig. 2.4: Different fiber packing in unidirectional composites.

An analytical solution of the problem is very complicated or almost impossible. So far, there have been many attempts to solve the equations by using many simplifications. Most of the theoretical micro-mechanical studies conducted in the field of composite materials assume plane strain or plane stress conditions. Any changes along the fiber direction are neglected. Some of the results obtained from these analyses are applicable to the interior of composites where the 2-D plane strain or plane stress conditions prevail. Some solutions originate from the mechanics of edge-bonded dissimilar materials and the analysis of inclusions in homogenous materials. Some of these results are presented in the following two sections.

2.4.1 Mechanics of Edge-Bonded Dissimilar Materials

The nature and distribution of stresses along the interface and at the contact corner of edge-bonded dissimilar materials (see Fig. 2.5) generated by a variety of load and

boundary conditions have been studied by many researchers. The stress distribution along the interface may contain singularities at the contact corner. A singular stress field of the type $r^{-\alpha}$ was identified in many publications, where r is the distance to the contact corner and α is a positive constant dependent on the material properties and the angle of each material at the contact corner (e. g. θ_1 and θ_2). For example, Bogy (1968) studied two dissimilar materials bonded along one of their straight edges with $\theta_1 = \theta_2 = 90°$. The study has been conducted under normal and shear traction. The orthogonal wedges were considered to be elastic. It was determined that the order of singularity (α) depends on the ratio of the shear moduli and the Poisson's ratios of the materials.

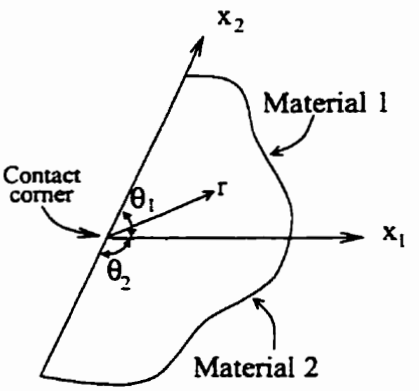

Fig. 2.5: General configuration of edge-bonded dissimilar materials.

Hein and Erdogan (1971) expanded Bogy's work to include a range of arbitrary angles for the wedges (provided $\theta_1 + \theta_2 = 180°$) and studied indenters bonded to a half plane (i.e. $\theta_2 = 180°$). Their results have shown that, depending on the wedge angle and the material type, the stress field at the contact corner of the materials could be either non-singular, or singular. For example, for $\theta_1 = 60°$ and $0.1 \le (E_1/E_2) \le 10$, the singular stress disappears provided that $\theta_1 + \theta_2 = 180°$. This is a very important result in the semiconductor industry. For example, a similar geometry occurs for the Si-SiO_2 or Si-Si_3N_4 semiconductors for which the ratio of E_1/E_2 is approximated either as 0.4 or 0.2. A similar study was conducted by Gdoutos and Theocaris (1975) where the Poisson's ratios of the materials were also considered as parameters. It was shown that the Poisson's ratio of the materials also influences the order of singularity.

The problem of a wedge with angle θ contacting with a half plane under surface traction was studied by Dundurs and Lee (1972). It was found that the order of the singular stress field depends on two of the properties (E and ν) of the wedge and the half plane and also the angle of the wedge. For $\theta = 180°$, for all types of material properties, a singularity of order $\alpha = ½$ (the crack type) was found.

Most recently, the thermal stress field at the contact corner of two edge-bonded materials has been analyzed by Ioka et al. (1995, 1996) using the boundary element method. They were able to convert the thermoelastic problem to an elastostatic problem. It was shown again that the stresses near the contact corner have the singular form of the type $r^{-\alpha}$. Independently, Chen and Nisitani (1993) also converted the thermal problem to an elastostatic problem.

Designers of lap joints are aware that tapering or varying the shape of the adherents can improve the strength of a connection. Chang and Muki (1974) were among the first researchers to launch a study to understand the mechanism of this improvement. However, their approach used over-simplified geometry near the contact corner of the joint. As a result, prediction of the stress field at this point was not sufficiently accurate. Their work was expanded by Westman (1975) who established a link between the loading condition and the stress singularity. A possibility of minimizing the singularity by selecting a particular value for the angle at the contact corner was discussed.

A shape optimization procedure was proposed by Muraka and Ueda (1989). They reduced the failure of the Cu/Al_2O_3 joint with $\theta_1 = \theta_2 = 90°$ by modifying the boundary of the side surface of the metal part 2 mm from the interface (A-B in Fig. 2.6). The concave shapes were found to be effective in reducing the failure probability for the mechanical and combined (mechanical-thermal) load. For thermal load, both concave and convex shapes reduced the failure.

Similarities of the mechanics of unidirectional composites on a microscale with the mechanics of edge-bonded dissimilar materials leads to the conclusion that the stress field at the fiber/matrix interface at the free surface may be singular with the order of singularity dependent on the material properties. As in the results discussed above, this singularity may disappear for certain material types and contact angles. These problems are discussed in Chapters 6 and 9, in detail.

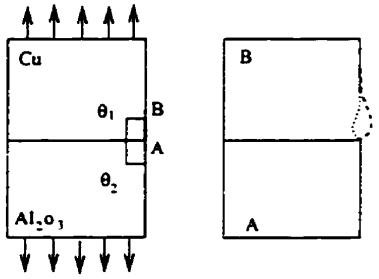

Fig. 2.6: Optimization of the angle at the contact corner of two edge-bonded dissimilar materials.

2.4.2 Disturbance in a Stress Field Due to Inclusions

The disturbance induced in a stress field by an inclusion has been the subject of many studies. The presence of a hole in a plate acts as a stress riser and generates a stress concentration at the circumference. Filling the hole with a rigid or elastic inclusion changes the stress regime by reducing the stress concentration induced by the hole, but it creates other stress concentrations. These stress concentrations practically vanish at a distance of about four diameters away from the inclusion. The governing equation and some of the solutions have been found to be applicable to 2-D studies of composite materials.

Separation of a smooth circular inclusion from the matrix was treated by Keer et al. (1973). The stress and the extent of separation depend on the level of adhesion at the interface. The problem was solved for the matrix under bi-axial orthogonal tensile traction with the traction being higher in one direction than the other. It was shown that for certain combinations of the applied traction, the inclusion might separate from the matrix along

some part of the interface. The angle of separation was related to the material properties of the matrix and the inclusion.

Kelly and Wilhoit (1962) studied an equal sized rigid cylindrical multi-inclusion problem. The work was extended to unequal size inclusions embedded in an elastic matrix under in-plane stresses by Goree (1967). The problem was reduced to a 2-D plane strain study. The solutions provide some information on the effects of the Poisson's ratio and the ratio of the radius of the inclusions and their spacing on the stress concentration between inclusions. In general, the maximum principal stress sharply increased with decreasing spacing of the inclusions and increasing Poisson's ratio.

The disturbance by multiple inclusions in a uniform stress and/or bending stress field was discussed by Yu and Sendeckyj (1974). The general solution for a circular elastic inclusion was used for successive approximation of a multiple circular inclusion problem. It was shown that the stress concentration decreased with increasing moduli of the inclusions and with increasing number of inclusions. For example, when the number of inclusions increased from two to three, the magnitude of the stress concentration decreased by 30%.

The stress distribution around a single fiber embedded in a matrix under a lateral force was presented by Tirosh et al. (1979) who studied the interaction of radial and circumferencial cracks with the stresses around the fiber. The solution presented by the authors indicates that, surprisingly, the maximum of the stress concentration occurs in the matrix at a short distance away from the interface. The location of the maximum stress was found to be dependent on the matrix Poisson's ratio. This phenomenon may explain the initiation of tangential cracks in the matrix close to the interface, which are frequently observed in composites.

2.5 Stress Distribution Along the Fiber Length

The stress transfer between a single fiber and the matrix is usually analyzed with the help of the shear-lag theory by considering the variation of the normal axial and

longitudinal shear stresses along the fiber length. The early elastic stress analysis, which included the effects of the fiber length, was proposed by Cox (1952), Rosen (1964), and Amirbayat and Hearle (1969). Kelly and Tyson (1963) considered elastic-plastic deformations with the assumption of a constant interfacial shear stress in regions where the interface had failed.

The load transfer mechanism is explained by assuming a cylindrical fiber embedded in a cylindrical matrix. It is also assumed that the fiber and the matrix are perfectly bonded together and that their Poisson's ratios are similar in magnitude to avoid any radial stress between them. Applying an axial load to the ends of the matrix cylinder, deforms the matrix as shown in Fig. 2.7. The deformation is very high near the fiber ends and diminishes along the fiber toward the mid-length. Transfer of the applied load from the matrix to the fiber occurs by means of the shear stress at the interface. The treatment of the stresses depends on the elastic or elasto-plastic response of the matrix material. The detailed discussion of the shear-lag theory is presented in Appendix B where it is divided into two cases, when the matrix is elastic and elasto-plastic.

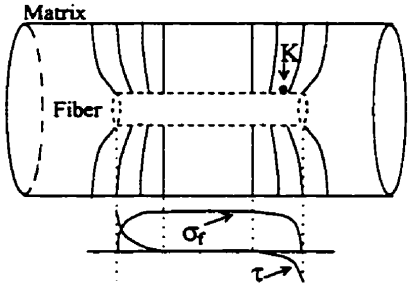

Fig. 2.7: Load transfer in fiber composites and axial and longitudinal shear stress distributions along the fiber length.

The high shear stress at the fiber end is referred to as the fiber end effects. Crack initiation at the fiber end has typically been related to these effects. In this dissertation, the end effects are discussed in detail in Chapter 5 using a 3-D approach.

The widely used shear-lag theory has several limitations. One of the problems is that the radial and hoop stress components are ignored by this one-dimensional analysis. These stress components are important for thermal loading (Abedian and Szyszkowski, 1997). In

particular, the radial stress becomes large because differential thermal contraction of the fiber and the matrix typically leads to a shrink fit or compressive radial stresses at the interface (Nairn, 1985). The shear-lag analysis produces a stress state that does not obey stress equilibrium (Whitney and Drzal, 1987). For a broken fiber embedded in a matrix, the shear-lag theory predicts that the maximum shear stress occurs at the fiber breaks, however the free surface boundary condition at the breaks requires zero shear stress at these locations. Even applying the post-failure stress analysis of Kelly and Tyson (1963) which is normally utilized to avoid some limitations of the shear-lag analysis does not provide satisfactory results at the broken end of the fiber.

There have been several FEM and analytical attempts to improve the shear-lag theory such as these by Carrara and McGarry (1968), Broutman and Agarwal (1974), Whitney and Drzal (1987), and Nairn (1992). Among them, Nairn's semi-3D variational technique provides an analytical solution that satisfies the boundary conditions (zero shear stress at the fiber break) and also provides some information on the nature of the radial stress distribution along the fiber length. This analysis begins with an admissible stress state that obeys equilibrium and traction boundary conditions precisely. An approximate stress state is then found by minimizing the complementary energy. The most important fact about these results is the concentration of the radial stress at the fiber break. One conclusion from this semi-3D analysis is that a more precise 3-D analysis of the stresses at the fiber end on the free surface of unidirectional composites is required.

The axisymmetric analysis of a cylindrical rigid rod partially embedded and axially loaded in an elastic half space was presented by Luk and Keer (1979). The numerical solution, despite the free surface boundary condition, gives a singular longitudinal shear stress component on the free surface of the half space. This inconsistency of the solution was attributed to the numerical scheme adopted.

The singularity in the neighborhood of the intersection of a cylindrical inclusion and a free surface was investigated by Folias (1989). The inclusion was assumed to be in the form of a homogeneous isotropic material embedded in an isotropic plate of arbitrary

thickness. Loading was in the form of a tensile lateral force in the plane of the plate. The results reveal some interesting facts about the singularity such as the dependence of the order of singularity on constituent properties such as shear modulus and Poisson's ratio. It was shown that the singularity exists when the elastic modulus of the inclusion is higher than that of the plate material. The solution suggests that the singularity is of the type $r^{-\alpha}$, where $\alpha = 2 - \beta$ and $1 < \beta < 2$. The order of the singularity increases with increasing ratio of the shear moduli of the inclusion and the plate. Penado and Folias (1989) presented the distribution of some of the stress components in the vicinity of the singular point. It was concluded that the maximum octahedral shear stress occurs at the interface.

More recently, Li and Folias (1991) have expanded the Penado and Folias study by considering the fiber to be transversely isotropic. The value of β for carbon and glass fibers (which typically have small diameters) in epoxy matrix was calculated to be equal to 1.693 and 1.737, respectively. It was suggested that the presence of a carbon fiber induces a slightly higher singular stress field than that of a glass fiber and consequently the carbon/epoxy composite is more prone to failure. One major drawback to the solution is that the axial and longitudinal shear stress components on the free surface, instead of being zero, are also singular.

2.6 FEM Analysis of the Stress Field in Composites

The finite element approach seems to be the only practical tool that is capable of satisfying the boundary conditions corresponding to the assumed fiber packing configuration. Different FEM models used, for example, by Bigelow et al. (1989) and Fletcher and Oakeshott (1994_a) for elastic, elasto-plastic, and creep analyses of unidirectional composites are discussed in the following sections. The use of singular and regular FEM elements in analyzing the singular stress fields are also discussed.

2.6.1 FEM Modeling

In order to reduce the cost of FEM calculations it is necessary to assume a regular pattern for the fiber distribution in the matrix. Among the different patterns shown in

Fig. 2.4, the rectangular and hexagonal patterns are widely used. A comprehensive comparison of the models of different fiber patterns is provided by Bigelow et al. (1989) and Fletcher and Oakeshott ($1994_{a,b}$).

Bigelow et al. used four micro-mechanical models to analyze metal matrix composites. These models are the vanishing fiber diameter model (VFD), the Aboudi model, the multi-cell model, and the discrete fiber-matrix model (DFM). Their unit-cell representations are schematically shown in Fig. 2.8.

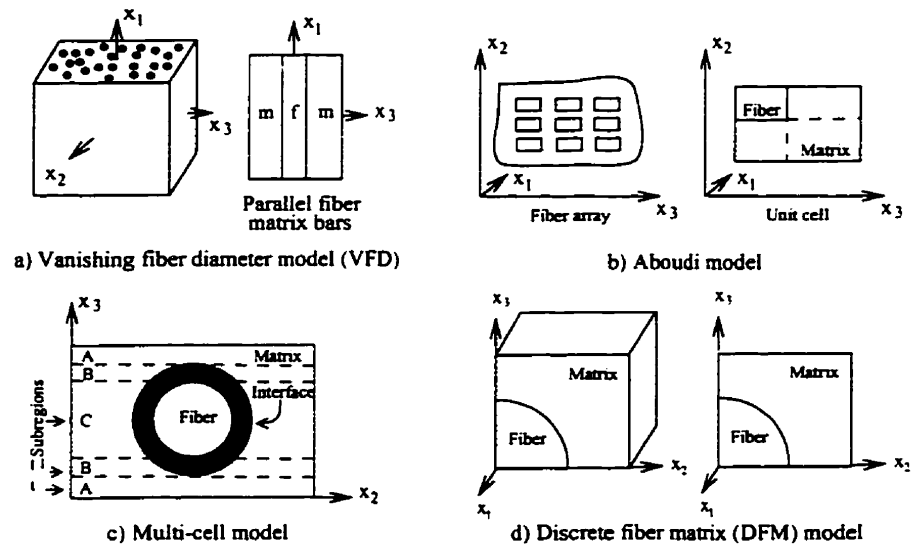

Fig. 2.8: Various micromechanical models.

For the VFD model, it is assumed that the fibers have a very small diameter. Although the fibers constitute an appreciable volume fraction of the composite, they do not influence the matrix deformation in the transverse and thickness directions, but only in the longitudinal direction.

The Aboudi model is based on the assumption that the continuous fibers extend in the x_1-direction and are arranged in a doubly periodic array in the transverse and thickness directions. With the multi-cell model, the periodic structure of unidirectional composite

ply is approximated by a square array unit cell model. The three sub-regions A, B, and C shown in Fig. 2.8(c) are defined to characterize the "through-the-thickness non-uniformity of the constituent stresses and material properties."

The discrete fiber-matrix model (DFM) together with a finite element analysis assumes that the fibers are dispersed in a uniform rectangular pattern in the matrix. This model was first used by Foye (1966).

The first three models were originally developed for predicting lamina or laminate properties or stress-strain behavior. The DFM model was designed primarily for the prediction of the constituent stresses. However, the DFM model can be used to calculate lamina properties. A comparison of the predicted lamina properties and constituent stresses by the models described so far indicated that the DFM model was the best model for calculating the constituent stresses. Also, this model provided lamina properties that were very close to those calculated by the other three models.

Fletcher and Oakeshott (1994_a) extended the above work by considering different fiber packing patterns shown in Fig. 2.4. The 2-D plane strain assumption was considered. It was shown that without a change in the other geometrical parameters the fiber packing does not affect the magnitude of the maximum principal stress. However, it affects the von Mises stresses. The stresses are reduced with increasing number of neighboring fibers. For example, the hexagonal fiber pattern provides a lower von Mises stress than either the rectangular or triangular patterns. However, the study does not provide a clear link between the change in the magnitude of the von Mises stresses with fiber volume fraction. The maximum of the von Mises stress was shown to occur at the interface along the line which connects the centers of two neighboring fibers. Unfortunately, no reason for all of the above results was offered. This phenomenon will be considered in this dissertation in Chapter 5.

The issue of random fiber distribution has been studied by several investigators. For example, Adams and Tsai (1969) investigated the effect of randomness in fiber

distribution on the transverse stiffness of unidirectional composites. Their random array analyses revealed the fact that the fibers in a composite conform more closely to the hexagonal array rather than the square array. The transverse stiffness predicted by the hexagonal array was more accurate in comparison with the experimental measurements on random arrays. Due to these reasons, the hexagonal regular fiber pattern is considered in this dissertation. The details of the FEM modeling will be discussed in Chapter 3.

The effects of randomness in fiber distribution on the predicted composite properties were analyzed by Davy and Guild (1988). Fletcher and Oakeshott (1994_b) studied the stress fields in the fiber composites considering the random fiber arrays described by the concept of a Voronoi cell (see Fig. 2.9). The Voronoi cell defines the region around a fiber where all points are at distances from the fiber less than or equal to the distance to any adjacent fiber. The study initially considers a "hypothetical" Voronoi cell model composed of unit cells that were used in modeling the regular fiber arrays (Fig. 2.4) by the same authors.

The model predicted that the maximum principal and von Mises stresses occur in the region with shortest inter-fiber distance. However, the locations of the stresses were shown to be in the matrix away from the interface where no traces of cracking were found experimentally. The magnitudes of the stresses were in excess of those calculated by means of the regular fiber arrays discussed earlier.

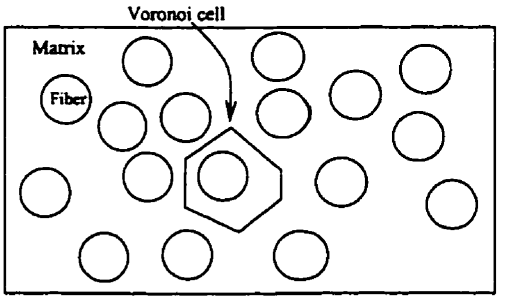

Fig. 2.9: Voronoi cell model (irregular fiber pattern).

2.6.2 Elastic Analysis of Unidirectional Composites

Many results on unidirectional composites were obtained assuming elastic properties for the constituents. The transverse stresses generated by the difference in Poisson's ratios of the constituents of unidirectional composites under an axial load were studied by Ostrowski et al. (1984). The interfacial pressure plotted along the fiber length indicated a concentration of the radial and hoop stresses at the fiber end. The results also showed that the stresses are reduced to some small values at a distance equal to about 5 fiber diameters away from the fiber end. It was also shown that the maximum radial stress occurred at the location with the shortest inter-fiber distance, while the maximum of the hoop stress occurred at the highest inter-fiber distance. The magnitude of the interfacial hoop stress was increased while that of the interfacial radial stress was reduced with increasing the fiber volume fraction. More explanation on the above results are provided in Chapter 5.

A 3-D thermo-elastic stress analysis of unidirectional composites was conducted by Haener and Ashbaugh (1967). Assuming a hexagonal pattern of fiber packing, it was shown that the nature of the interfacial radial stress at the fiber end on the free surface is different than the stress in the interior of the composite. The interfacial radial and hoop stress components on the free surface were found to be very high. The nature of the hoop stress on the free surface was shown to be similar to the interior of the composite. The axial stress seemed to satisfy the free surface boundary condition ($\sigma_{zz} = 0$), while the longitudinal shear stress was found to be increasing when moving along the interface toward the free surface. The study showed the stress concentrations at the fiber end but did not mention any stress singularity at this location.

Thermo-elastic stresses in unidirectional polymeric matrix composites were studied by Sottos et al. (1989) using hexagonal fiber packing. Using the Boundary Fitted Coordinate Technique (BFCS), the unit cell for the hexagonal fiber array was meshed with small rectangular elements. As stated by the authors, "this technique is essentially a transformation or mapping of the physical domain where the problem is defined into a simple computational domain where the problem is solved using traditional finite

difference technique". The interfacial stress components in the interior of the composite were calculated assuming perfect bonding at the interface and a decrease in temperature of 1°C. Upon cooling, it is expected that, due to the mismatch in coefficient of thermal expansion (CTE) of the constituents, the sign of the hoop stress is tensile for the matrix and compressive for the fiber. However, unexpectedly, it was shown that both of the stresses are compressive. Also, the axial stresses of the fiber and the matrix are expected to be of different signs, tensile in the matrix and compressive in the fiber, however they were both found to be compressive. The location of the maximum radial stress was predicted to be at the model corner in the matrix away from the interface. However, the study conducted by Abedian and Szyszkowski (1997), where a similar model was analyzed using FEM, showed the maximum radial stress to occur at the interface. A similar study by Szyszkowski and King (1995) on axisymmetric models also showed that the maximum radial stress occurs at the interface.

Sottos et al. also studied the effect of fiber volume fraction on the stress state. It was found that the radial, hoop, and axial stress components increase with decreasing fiber volume fraction (V_f). This is in contrary to the result obtained by Ostrowski et al. that was discussed earlier. The validity of these results will be examined in this dissertation in full detail (see Chapter 5). The effect of a weak interphase on the stresses was also analyzed by Sottos et al.. The results showed that a coating weaker than the matrix material (lower modulus, lower CTE) decreases the interfacial stresses which is in agreement with the results obtained by Tirosh et al. (1979).

The stress field in unidirectional composites subjected to thermo-mechanical loading was studied by Mikata and Taya (1985). The study focused on the effects of fiber coating and the composite was modeled by four concentric cylinders ("four-phase model"). The inner most cylinder was considered to represent the fiber and the outermost to be the bulk of the composite. The cylinder covering the fiber represented the coating and the cylinder surrounding the coating represented the matrix. The fiber and the bulk of the composite were considered to be transversely isotropic and the coating and the matrix were assumed to be isotropic. The properties of the outermost cylinder were obtained by using the rule of

mixture. A model for calculating the properties of the bulk composite using hexagonal fiber pattern, which was proposed by Soh (1994), was also used. As for the loading, axial and transversal mechanical loads as well as a temperature change were considered.

The stress distribution in the interior of the composite showed that the absolute value of the hoop stress in the coating is higher than that of the radial stress. This result is similar to the conclusion made by Sottos et al. (1989) who claimed that, in the interior of the composite, even in the absence of coating, the hoop stress is higher than the radial stress in the matrix. However, this is contrary to the results reported by Tirosh et al. (1979) who suggested that for a uniform temperature change the absolute value of the radial stress is always higher than that of the hoop stress.

Adams and Doner (1967) considered unidirectional composites with rectangular fiber packing subjected to uniform transverse stress and under uniform temperature change. The solution was obtained using the finite difference technique. The analyses showed that, under uniaxial transverse loading, the maximum principal stress occurs at the intersection of the line that connects the center of the two neighboring fibers with the interface. The study also showed that under uniform temperature change, the maximum radial stress occurs at the interface and increases with decreasing the fiber volume fraction. This is contrary to the results presented by Sottos et al.

The stress concentration around a broken fiber in a unidirectional polymeric composite was investigated by Nedele and Wisnom (1992). For a combined axial load and a temperature change, it was shown that the stress concentrations in the fibers adjacent to the broken fiber are less than that predicted by the shear lag theory.

Chandra and Xie (1993) extended the analytical solution proposed by Mikata and Taya (1985) for a single fiber embedded in a matrix to consider the effect of neighboring fibers on the stress distribution around a fixed fiber. Their results showed that the maximum absolute value of the radial stress occurred at the interface at locations with the

shortest interfiber distances. The stress value decreased with increasing number of fibers surrounding the central fiber.

Sherwood and Quimby (1995) using FEM analysis compared the stress-strain characteristic of perfectly bonded and also completely unbonded composites. The transverse properties of unidirectional composites were analyzed by De Kok et al. (1993). The numerical and experimental studies showed that under transverse uniaxial tensile mechanical loading, the interfacial bond strength did not affect the transverse tensile modulus of the composite.

2.6.3 Singular Stress Field and Regular FEM Elements

Since a singular stress field is expected at the fiber/matrix interface on the free surface, the question is, how singularity can be handled by the regular FEM elements and to what extent the results are accurate and reliable. There exist a vast amount of publications explaining the application of FEM in determining the singular stresses at the tip of a crack where the singularity is always of the type $r^{-\alpha}$ (Gallagher (1978), Yamada and Ezawa (1979), and Macherle and Fredriksson (1980)) with $\alpha = 0.5$. However, for problems dealing with the edge-bonded dissimilar materials, the order of singularity is unknown and lies in the range $0 < \alpha < 1$.

Many attempts have been made to develop special elements (variable power singularity elements) to deal with such problems (Tracey and Cook (1977), Akin (1976), Hughes and Akin (1980), and Stern (1979)). Several studies have been conducted to establish a way of analyzing such singular stress fields utilizing regular FEM elements (Staab (1983) and Schiermeier and Szabo (1989)). Such elements were used in the present work to study the stress field at the fiber/matrix interface on the free surface of fiber composites (see Chapter 6).

Staab investigated two known cases: the stress singularity at the tip of a crack in a homogeneous plate and the stress field at the tip of a crack perpendicular to the interface of

a perfectly bonded bi-material system. The stress was approximated by $\sigma = cr^{-\alpha}$ in the vicinity of the singularity where r is the radial distance from the singular point to the Gauss point of the closest element. Plotting the above equation on a log-log scale, the slope of the line (α) for the case of a crack in a homogeneous material was found to be very close to 0.5 which is exactly the same as calculated by analytical methods. It was shown that as the mesh becomes finer, the slope gets closer to 0.5.

Schiermeier and Szabo (1989) calculated the order of the singularity at the contact corner of edge-bonded dissimilar materials analytically and by means of FEM using conventional elements. The difference between the orders of singularity calculated by these two methods was found to be around 0.5%.

In this dissertation, a complete discussion of the order of singularity of the stress field at the fiber end for unidirectional composites is presented in Chapter 6.

2.7 Inelastic Analysis of Unidirectional Composites

Inelastic analysis of unidirectional composites requires a substantially greater numerical effort. It takes into account variation of thermo-mechanical properties of constituents with stress and temperature. There are a number of studies dealing with the generation of residual stresses during manufacturing and at service temperatures and the damage caused by these stresses. Most of the studies have focused on the interior of composites considering plane stress or plane strain assumptions. Only a few 3-D investigations have been performed and the fiber end effects were ignored.

2.7.1 Elasto-Plastic Analysis of Thermal Residual Stresses in Fiber Composites

The generation of thermal residual stresses in SiC/Ti-6Al-4V composite when cooling from a high manufacturing temperature was investigated by Nimmer et al. (1991). 3-D FEM elements were used to model the unit cell of the rectangle fiber array pattern. However, the boundary conditions assumed simulated the 2-D plane strain behavior of the composite. The von Mises yield condition was applied in conjunction with the kinematic

hardening rule. The maximum absolute values of the radial and equivalent stresses were shown to occur at the interface at the location with the least inter-fiber distance. The equivalent stress distribution showed that no plastic strain in the interior of the composite could occur.

Since there are different CTE values for Ti-6Al-4V in the literature, the authors repeated the study with the highest reported values of CTE. The results showed that with the new assumed property some plastic flow occurs in the matrix. However, the extent of the plastic strains and whether the plastic flow continues up to room temperature were not discussed. The results were found to correlate to some extent with the experimental results.

Similar thermal residual stresses resulting from the manufacturing process of the composite were reported by Ananth et al. (1993) who studied the Ti-6Al-4V and aluminum matrices reinforced with SCS-6 fibers. The von Mises yield criterion along with the associated flow rule were considered while strain hardening was ignored. The results showed that the Ti-6Al-4V matrix remains elastic during the entire manufacturing process, while the aluminum matrix showed a large amount of plastic strain.

Chandra et al. (1994) analyzed thermal residual stresses generated in SCS-6/Ti-24Al-11Nb and SCS-6/Ti-6Al-4V composites by means of FEM using a rectangular unit cell model. The effect of the stresses on the subsequent response of the composites to transverse loading was also examined. The von Mises yield criterion along with the associated flow rule and isotropic hardening were used. A comparison of the stresses obtained by incorporating different assumptions (plane strain, generalized plane strain, and 3-D model) was presented

The residual stresses in the Ti-6Al-4V matrix did not lead to any plastic deformation as in the previous studies. However, the stresses in the Ti-24Al-11Nb matrix indicated that a large part of the matrix yields plastically during the manufacturing process. The large plastic strains effectively influenced the stress distribution in the matrix. The results showed that the maximum of the hoop stress moves away from the interface due to the

relaxation and redistribution effects of the plastic flow of the matrix. The plastic strain was shown to be initiated at the interface at the locations with the smallest inter-fiber distances. A good agreement between the calculated and the measured plastic strains by means of Neutron Diffraction and X-ray Diffraction techniques (Wright et al., cited by the authors) was reported.

Generation of thermal residual stresses in SCS-6/Ti-24Al-11Nb composite during the manufacturing process was studied both experimentally and numerically by Rangaswamy et al. (1994). The residual stresses measured by means of X-ray diffraction were compared to those obtained using the FEM approach. The X-ray technique measures the stresses on the free surface. Layers of the material were removed by an electropolishing technique to find the stress distribution in the interior of composites. The measurements showed that the axial and hoop stresses are tensile in the matrix. The profile of the measured values showed that the stresses decrease as the fiber plane is approached. This result was found to be in contrast to the 2-D results obtained by other researches. This discrepancy was then attributed to microstructural features of the matrix examined by metallography of the electropolished surface. However, in a recently published study by Abedian et al. (1997), the nature of the stress distribution was attributed to the extensive plastic deformation of the matrix. More details about the nature of the stresses can be found in Chapter 7.

Rangaswamy and Jayaraman (1994) also modeled their X-ray tests using the FEM approach. Material removal was simulated by the element birth/death option that will be explained in Chapter 3. A perfect interface was assumed. The von Mises yield criterion with associated flow rule and isotropic hardening were assumed. The analysis showed a stress concentration at the fiber end on the free surface. The end effects diminished at a distance equal to about 3 fiber diameters from the fiber end. This effect was also explained by Abedian and Szyszkowski (1997).

Gdoutos et al. (1991) analyzed thermal stresses in SiC/6061-Al composite using concentric cylinder models. The deformation theory of plasticity was used in conjunction

with the von Mises yield criterion and the isotropic hardening rule. A good agreement between the theoretical prediction and experimental measurement of the longitudinal and transverse thermal residual strains of the composite was found.

The elasto-plastic analysis of thermal residual stresses in SCS-6/Ti-24Al-11Nb composite was also carried out by Coker et al. (1993). The finite difference method was used to analyze a representative volume element of the composite assuming generalized plane strain condition. The Prandtl-Reuss relations were considered. The results matched the FEM solution of the problem. Despite considering isotropic strain hardening and also considering the fact that the matrix under consideration undergoes very high plastic deformation, no evidence of the strain hardening effect was presented and the equivalent stress simply followed the yield strength value of the unreinforced matrix available in the literature. The effect of the residual stresses on the thermo-mechanical fatigue loading which is normally the loading condition for this type of composites was also investigated. Both the in-phase and out-of-phase conditions were considered. A good correlation between modeling and experimental results was found.

The effect of plastic flow of composite constituents on the stress state of fiber composites was studied by Hahn (1993) using a 3 concentric cylinder model to represent the fiber, coating, and matrix. The generalized plane strain condition was assumed. The study showed that the Tresca criterion is not sufficient for analysis of the plastic flow in the coating. The analytical solution for plastic flow of the coating in two planes was then developed using an approximate Prandtl-Reuss flow rule.

Residual stress development in polymeric matrix composites during the cure phase was investigated by White and Hahn (1992_a). A model was developed to predict the effects of chemical and thermal strains during curing. The model included visco-plastic material response, chemical and thermal shrinkage effects, and mechanical property development during curing. The model developed required several material properties as the input. The characterization and the experimental tests were reported in a companion paper (White and Hahn, 1992_b).

2.7.2 Temperature Cycling of Unidirectional Composites

A simplified analytical elastic analysis of unidirectional fiber composites under temperature cycling was performed by Misra (1993). The temperature dependent properties for both composite constituents were incorporated. Upon cooling, the radial, hoop, and axial stress components of the matrix were calculated. It was concluded that a more comprehensive study of the plasticity is required to understand the true nature of the stress components and the effective stress during the heating phase.

A numerical-experimental study of temperature cycling of metal matrix composites was conducted by Wetherhold and Westfall (1988). The one-dimensional FEM study was performed using beam elements. The stresses in the fiber and matrix and also the plastic strain of the matrix were calculated during a temperature cycle. The results of the study suggested that exposing the composite to an additional tensile load might decrease the matrix cyclic plastic strain and thus decrease the damage. The tensile load may prevent the compressive load from reversing the plastic strain. The experimental tests conducted on the fibers revealed no difference in the strength between the as fabricated and the thermally cycled fibers. The major drawback of this study is the one-dimensional analysis of the stresses and strains.

Morris et al. (1989_a) experimentally studied the effects of temperature cycling on the stress and deformation states of a polymeric matrix composite reinforced with graphite fibers. After a certain number of temperature cycles, the out-of-plane displacement of the matrix on the cross section of the composite, caused by heating the composite to a constant temperature level, was measured. The cut surface of the composite revealed many cracks at the fiber/matrix interface. Cracking was least around the fibers in densely packed clusters. Cracks were observed at the interface where the inter-fiber distance (the distance to the neighboring fiber) was the largest (see Fig. 1.3). Morris et al. (1989_b) and Biernacki (1996) also observed such a cracking pattern. In the Morris et al. (1989_a) study, the thermally cycled sample was sectioned and was heated again. It was observed that the fibers on the free surface expanded in the radial direction and the epoxy sank into a trough. The depth of

the trough was maximum at the center of the fiber triangle. The matrix deformation was opposite to what one would expect from the CTE mismatch of the fiber and matrix. This was attributed to thermal residual stresses. This study emphasized the history dependent behavior of the composite, but its major drawback was the lack of distinguishing between the characteristics of the free surface and the interior of the composite. Also, the analysis of thermal stresses presented is inadequate in explaining the real cause of the unexpected displacements in the matrix.

Thermal residual stresses in metal matrix composites reinforced with high or low modulus graphite fibers were studied by Cheong and Marcus (1987). The composites reinforced with PAN-based graphite fibers exhibited high residual stresses, while the stresses were found to be low in composites with pitch-based high modulus graphite fibers. The free surface deformation of the composites during a temperature cycle was monitored. The convex cross section of the pitch-based fibers and the low residual stresses in the composite were related to the low longitudinal shear strength of the fibers.

Comparing the Cheong and Marcus (1987) results with the results obtained by Morris et al. (1989_a) a difference between the free surface deformation of metal matrix and polymeric matrix composites reinforced with graphite fibers can be noticed. Upon heating, the fibers of the polymeric composite sank in a trough, while for the metal matrix composite the fibers protruded. This could be due to the different history-related behaviors of the matrices.

The response of magnesium matrix composites reinforced with different types of fibers (boron, silicon carbide, steel) to temperature cycling was investigated by Maksimovich et al. (1988). The fibers were made by vapor-gas deposition of boron and silicon carbide on tungsten wires. The composite samples were cycled between +150°C and -196°C either slowly or rapidly to induce thermal shock. Microscopy of the as-manufactured composite reinforced with boron fibers showed that 60% of the fibers contained cracks which were mostly initiated at the boron/tungsten interface. However, no cracks were initially detected in silicon-carbide/magnesium composite. The number of

cracked fibers in both of the composites increased by increasing the number of temperature cycles. Some cracks were observed in the matrix.

2.7.3 Creep Analysis of Unidirectional Composites

The behavior of aluminum reinforced carbon composites under temperature cycling and an axial tensile mechanical stress, including creep strain, was examined by Furness and Clyne (1991).

An elastic-viscoplastic micromechanical analysis of SiC/Ti-6Al-4V composite was performed by Durodola and Ruiz (1993) utilizing FEM and using a rectangular fiber pattern. It was shown that the cooling procedure affected the final residual stresses highly. The stresses calculated under creep conditions were found to be much lower than those calculated based on elastic and elasto-plastic assumptions. This was attributed to the relaxation effect of the creep phenomenon. The stresses calculated under the creep assumption were found to be in better agreement with the residual stresses in a thermally cycled sample measured by means of a neutron diffraction technique.

The effect of microstructural damage on flexural creep deformation of unidirectional composite materials was studied by Jeng and Yang (1993). The creep behavior of both unnotched and notched titanium matrix composites under constant load and at elevated temperatures was investigated. The unnotched composite sample exhibited a three-stage creep behavior, i.e. primary, secondary, and tertiary creep. The creep power-law was used to quantify the relationship between the creep strain rate and maximum applied stress at the quasi-steady state creep region. The initiation and accumulation of the damage was related to the creep behavior of the composite.

Cheng and Aravas (1997_a) using 3-D constitutive equations have investigated the creep behavior of unidirectional composites. The creep strain calculated using the proposed constitutive equation was verified by 2-D FEM results obtained utilizing a hexagonal fiber pattern. The creep model was found to produce satisfactory results in predicting the creep behavior of a unidirectional composite system.

The effects of the fiber damage on the creep behavior were also studied by the same authors (Cheng and Aravas, 1997_b). The main drawback of the study was that constant and uniform stresses in the fiber and matrix were assumed. In addition, it was assumed that the corresponding axial strain in the fibers and the matrix are equal to the macroscopic strain of the composite.

The momentary transverse creep behavior of thermoplastic polymer matrix composites has been studied by modifying a semi-empirical micromechanical model and also by means of the FEM approach by Wen et al. (1997). The visco-elastic transverse compliance of the composite was calculated by applying the correspondence principle to the semi-empirical equation for the elastic transverse modulus of the composite proposed by Tsai-Hahn. The fiber was assumed to remain elastic. Good agreement was found between the predicted values using the micromechanical model and the experimental measurements.

One-dimensional elasto-perfectly plastic and elasto-viscoplastic analyses of unidirectional composites subjected to varying temperatures were conducted by Daehn (1989). Both the fiber and the matrix were considered to deform plastically and undergo creep deformations obeying the power-law creep constitutive law. It was shown that the fiber volume fraction has a considerable influence on the amount of the resulting plastic strain. Two loading cases were considered namely a sinusoidal temperature cycle with or without an external force. The external load affected the strain rate greatly. At low applied stresses, the thermally cycled composite showed much higher deformation rates than expected under the rule of mixtures based on isothermal properties. This can be attributed to high thermally induced stresses. This study excluded the transverse stress components from the calculations.

The behavior of particle reinforced metal matrix composites under temperature cycling was investigated by Pickard and Derby (1991). The results of the study showed a large decrease in the exponent of the stress in the power law creep characteristic of the composite during cycling. Chen et al. (1990) used this weakening effect of temperature

cycling (when it is accompanied by a small external load) on particle and whisker reinforced metal matrix composites as a manufacturing procedure. Using this phenomenon, they could successfully shape the material into a dome-shape configuration without breaking the composite. This procedure generates large deformation in these types of composites.

2.7.4 Methods of Reduction of Thermal Stresses in Unidirectional Composites

The thermal residual stresses in unidirectional composites generated during manufacturing can be reduced by using high CTE fibers, fiber preheating, the compliant layer concept (which is defined later), appropriate curing and post-curing cycles, temperature cycling, and many other ways.

The compliant layer concept was used by Arnold et al. (1992) and it involves an interface material inserted between the fiber and the matrix to reduce residual stresses. A parametric study was conducted concerning the properties of the interface material. The elastic modulus, yield strength, plastic modulus, CTE, and the thickness of the layer were considered as parameters. In particular, the radial, hoop, and axial stresses in the fiber, matrix, and the interface layer were calculated as a function of the above parameters.

The effects of temperature rate and also annealing at constant temperature on the residual stresses of modified 9Cr-1Mo steel matrix reinforced with W fibers (MMC3 composite) were investigated by Yeh and Krempl (1993). Among different cooling histories tried, the stresses were found to be highest for the fastest cooling rates. However, the difference between the stresses from different cooling regimes was found to be negligible after about 30 days of storage time. Changing the cooling rate during processing was shown to have some effect on the stresses. Slow cooling rates from high temperatures followed by high cooling rates at lower temperatures were found to generate lower residual stresses. The study presented that, to reduce the room temperature residual stresses, an optimum cooling path for composites can be found.

White and Hahn (1993) studied reduction of thermal residual stresses in polymeric composites through optimization of the curing cycle. Three important parameters: time, temperature, and pressure were considered. The experimental measurements were compared to the calculated results obtained from an analytical model developed by the same authors (White and Hahn, 1992_a). The effects of curing temperature and time, cool-down rates, cool-down pressure, and post-curing procedures were investigated. Reduction in residual stresses with decreasing curing temperature was clearly evident where the curvature of the samples showed a high decrease relative to the curvature induced by the manufacturer's recommended cure (MRC). However, the degree of curing was found much lower than the MRC and as a result the undercurved samples led to a reduction of the mechanical properties. It was also concluded that curing at lower temperatures for longer time can reduce the residual stresses for thermosetting polymer systems compared to the MRC cycles.

In this dissertation, the effects of temperature cycling and different cooling rates on the residual stress level are presented in Chapters 7 and 8. The influence of the free surface geometry on the thermal stresses is considered in Chapter 9.

3. FEM Modeling and Procedures

3.1 Introduction

For a realistic computer simulation of a physical problem by the FEM an accurate modeling of the geometry, the material, and the loads involved is necessary. On the other hand, the FEM model must be numerically manageable and optimized in order to avoid excessive computer time and storage space requirements. In this chapter, the important aspects of balancing the accuracy with the numerical efficiency of the FEM analysis of unidirectional composites are discussed.

3.2 Material Modeling

Normally, in unidirectional composite materials, the fibers are made up of strong and rigid materials that carry most of the load and remain elastic during the normal service. On the other hand, most of the matrices that serve as a binder of the fibers are more ductile than the fibers, and may deform substantially. Due to the usually low yield strength of the matrices, the deformation may be inelastic. Also, since the processing temperature of the matrix is usually much lower than the melting temperature of the fibers, the creep processes are much more pronounced in the matrix.

In general, any heating or cooling affects the stresses and subsequent deformation of composites. Cooling the composite from the processing temperature in the manufacturing phase introduces complex residual thermal stresses that may affect the properties and performance of the composite. Any transient temperature field may be associated with significant temperature gradients throughout the fibers and the matrix that can cause additional large stresses and deformations.

In this study, it is assumed that the fibers are elastic. Elasto-plastic and creep properties are only considered for the matrix materials. The thermal properties related to heat transfer such as conductivity, convection, and capacitance coefficient are used in transient thermal stress problems. Radiation is not included. All the material data are assumed to be temperature-dependent.

3.2.1 Elastic Behavior

The fibers are assumed orthotropic with different mechanical properties and thermal expansion coefficients in the axial and transversal directions. The elastic behavior is, in general, characterized by the Young's modulus E(T) and the Poisson's ratio υ(T). The dependence of these properties on temperature makes the analysis nonlinear. Some iterative procedure is required to obtain solutions.

3.2.2 Elasto-Plastic Behavior

The elasto-plastic behavior of the matrix material will be modeled using the elastic modulus $E_e(T)$, the yield strength $\sigma_y(T)$, and the plastic modulus $E_p(T)$ as shown in Fig. 3.1(a). Such a model is referred to as the bilinear model. The elasto-plastic behavior of matrix materials is characterized by the yield surface defined for the whole temperature range. When the stress-strain characteristics of materials are temperature-dependent (Fig. 3.1(a)), the yield surface will change with temperature (Fig. 3.1(b)). For example, the yield surface will show an expansion with cooling of the material, i.e. material gets stronger at a lower temperature.

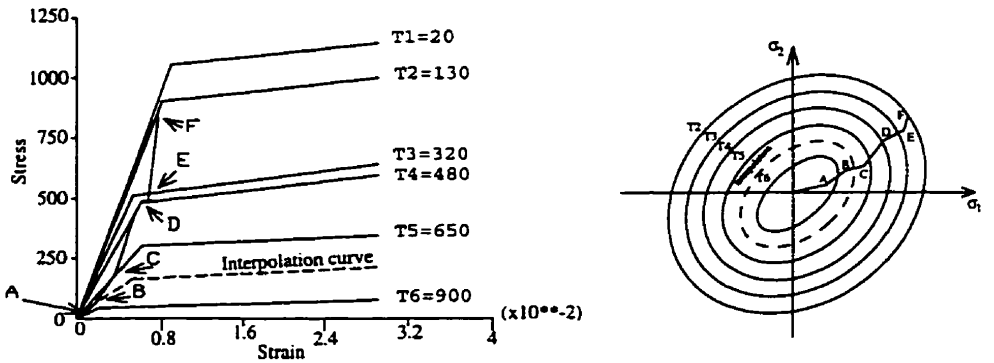

(a) (b)

Fig. 3. 1: Effect of temperature on the (a) the stress-strain characteristics (b) yield surface.

The strain-hardening characteristic of materials will also change the yield surface. That is, in subsequent loading and unloading cycles, the material will yield at different stress levels if any plastic flow occurs during previous loading. Two types of hypotheses, the isotropic (work) hardening and the kinematic hardening theorems, are normally used to calculate the effect of the strain hardening phenomenon in materials. The isotropic hardening causes the yield surface to expand uniformly. It assumes that the yield surface grows as shown in Fig. 3.1(b). Under kinematic hardening, it is assumed that the strain hardening pushes the yield surface or simply translates the yield surface axes. The mathematical aspects of these two theories are discussed below.

The 3-D constitutive relations representing the yield surface for the kinematic and/or for the isotropic hardening are assumed in the form

$$F(\sigma, \chi, \gamma) = 0 \tag{3.1}$$

$$\chi = \int \sigma^T d\varepsilon_{pl} \tag{3.2}$$

$$\gamma = \int C\, d\varepsilon_{pl} \tag{3.3}$$

where σ is the stress tensor (superscript T means transpose of the matrix), χ represents plastic work in the isotropic hardening rule, γ indicates translation tensor of the yield surface in the kinematic hardening rule, and ε_{pl} denotes the plastic strain tensor.

For isotropic hardening the yield surface is defined as

$$F = \frac{3}{2} S^T S - \hat{\sigma}_Y^2(T) = 0 \tag{3.4}$$

where S is the deviatoric stress tensor and

$$\hat{\sigma}_Y^2(T) = \sigma_Y^2(T) + 2\chi \hat{E}_p(T) \tag{3.5}$$

where

$$\hat{E}_p(T) = \frac{E_p(T)}{1 - \dfrac{E_p(T)}{E_e(T)}}. \tag{3.6}$$

Eq. (3.5) specifies the increase of the yield strength due to plastic deformation characterized by the parameter χ and due to temperature T.

The kinematic hardening rule is as follows

$$F = \frac{3}{2}(S-\gamma)^T(S-\gamma) - \sigma_Y^2(T) = 0 \tag{3.7}$$

where the coefficient C in the translation tensor γ is defined as

$$C = \frac{3}{2}\hat{E}_p(T) \tag{3.8}$$

Thus, the current yield surface is dependent on the temperature (since $\sigma_Y(T)$, $E_e(T)$ and $E_p(T)$ are functions of temperature) and the amount of plastic deformation accumulated.

In the present study, both of these theories are incorporated into the numerical code for calculating the plastic strains in unidirectional composites. The bilinear stress-strain option of the ANSYS (a FEM commercial software) is used to model the stress-strain relations at different temperatures. This option can accommodate bilinear curves for up to six different temperature levels. A linear interpolation is performed to get the stress-strain characteristics for temperatures between any two consecutive curves. The temperature-dependent properties add to the complication of the calculation of the elasto-plastic process. Note that the temperature change may have hardening or softening effects on the yield strength while the plastic strain always causes hardening (see Fig. 3.1). For example, for cooling, the first curve marked as T_6 represents the stress-strain characteristic of the composite as soon as it solidifies. When the matrix temperature is less than T_6 but higher than T_5, the stress-strain path travels to point B on the elastic section of the interpolated bilinear curve (see the dashed line in Fig. 3.1(a)). When the matrix temperature drops to T_5, the stress-strain path reaches point C that is still on the elastic section of the bilinear curve T_5. The elastic process continues until the stresses reach the yield strength level at T_4. Plastic deformation starts at point D and continues to E on the plastic section of the bilinear curve. The elasto-plastic process moves from one yield curve to another, from D to E, using hardening and the characteristics interpolated between temperatures T_4 and T_3 and then between T_3 and T_2. Depending on the changes in the material properties with temperature, plasticity may be either continued or terminated. When the increase in stress falls behind the increase in the yield strength, the stresses may end up again on the elastic part of the bilinear curve at point F. Then the process may remain elastic until room

temperature is reached. Thus, despite the stress level rising continuously, the process may switch back and forth between the elastic and the plastic domains.

Calculating the plastic strains with more accuracy is very important for determination of the residual stresses at service temperatures. The relaxation and redistribution of the stresses in subsequent temperature cycles are also highly dependent on the amount of plasticity. In general, high plastic deformations are associated with low residual stresses. Also, if the composite dimensional stability is of concern, a better estimation of the plastic strains is desirable. Moreover, overestimation of the plastic deformations gives a lower residual stress indication. This leaves some room for applying higher working (mechanical-thermal) loads than the composite load bearing capacity. Higher working loads may cause premature failure of composites.

3.2.3 Creep

Usually, creep becomes significant for a certain combination of temperature and stress. Typically, the creep effects should be included only if $T \geq 0.4T_m$, where T_m is the melting temperature of the material. In composites, creep is considered meaningful only in the matrix material.

In particular, during matrix solidification the creep phenomenon affects the residual stress state quite substantially. Also, under temperature cycling creep may be important. Understanding this phenomenon may help in controlling the level of thermal residual stresses in unidirectional composites by modifying different heating and cooling regimes or utilizing different maximum and minimum temperature levels for post-cure thermal cycles. In the present work, the ANSYS creep capability is utilized to calculate the creep strain imposed on the matrix by different rates of temperature change.

3.2.4 Transient Thermal Stresses

Thermal stresses in composites are generated mainly by the mismatch in mechanical and thermal properties of the fiber and the matrix, specifically the mismatch in CTE.

Another source of thermal stresses is temperature gradient. In general, temperature distribution depends on the difference in thermal properties of the constituents like thermal conductivity (k), thermal capacity (C), and density (ρ), especially for the transient process. For example, a material with high thermal conductivity experiences a high volume of heat transferred to the areas with low temperature in a short time. Hence, creating a high temperature gradient in the vicinity of the materials with lower k which would serve as a heat source. Also, a uniform temperature distribution throughout the material is achieved in a shorter time for high k.

The transient thermal behavior of the composite constituents and the effects of the thermal properties of the composites on the stresses are discussed in Chapters 4 and 9.

3.3 Geometry Modeling

It is usually assumed that the fibers are dispersed in the matrix in a regular pattern for a 3-D FEM modeling of composites. Considering the symmetric aspects of the fiber distribution in a composite leads to a representative volume or a unit cell. Regarding the symmetry surfaces of the unit cells, the corresponding prism model can be established for each pattern shown in Fig. 3.2. The whole composite can be rebuilt repeating each one of these unit cells. The fiber volume fraction (V_f) for each particular pattern in terms of the fiber radius (r) and the parameter (a) representing the distance between the fibers, is given as

$$V_f = \beta(r/a)^2. \tag{3.9}$$

For a given ratio of (r/a), the fiber volume fraction decreases from pattern A to pattern C. Values of the coefficient β can be easily calculated: $\beta = 2\pi/\sqrt{3}$ for pattern A, $\beta = \pi$ for pattern B, and $\beta = (4\pi)/(3\sqrt{3})$ for pattern C. Here, the unit cell of a regular hexagonal pattern of long and straight fibers of circular section is modeled by a 3-D prism as shown in Fig. 3.3. The details of the FEM meshing, types of elements, boundary conditions, and model dimensions will be discussed in the following subsections.

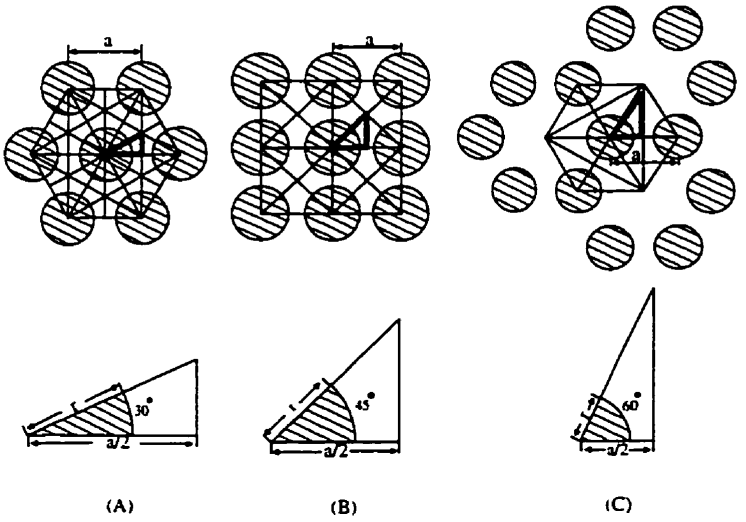

Fig. 3. 2: Various fiber packing arrangements in unidirectional composites.

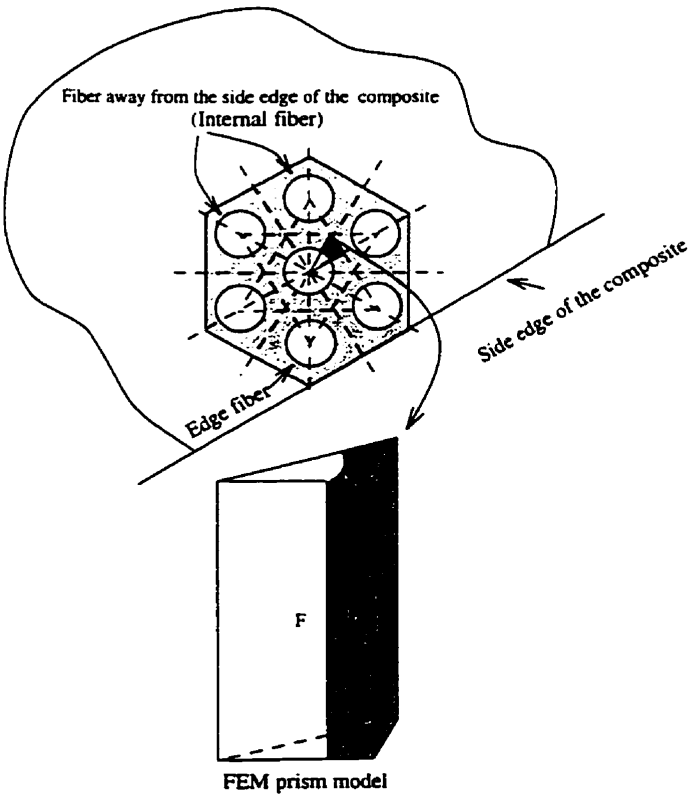

Fig. 3. 3: 3-D FEM prism model.

The stress and deformation patterns become independent of the location along the longitudinal axis away from the free surface. Therefore, 2-D plane strain or generalized plane strain analysis can be performed to model the interior of composites. Since no in-depth meshing is required in 2-D models, one can include more than one fiber in the model. Essentially, this type of modeling is used to analyze non-regular fiber distribution. The analysis of somewhat random fiber distribution by Fletcher and Oakeshott (1994_b) has shown that the maximum stresses are close to the stresses of a similar composite with regular fiber distribution of the hexagonal pattern. Also, a comprehensive study of the 2-D models presented by Fletcher and Oakeshott (1994_a) shows that the maximum principal and von-Mises stresses in composites are low for high values of β (i.e. the stresses in the hexagonal array of fibers (pattern A) are lower than in the other patterns). Note that in comparison to other models, each fiber in the hexagonal pattern is surrounded by the highest number of neighboring fibers. As suggested by Chandra and Xie (1993), this higher number of neighboring fibers increases the in-plane shear stress and reduces the radial stress that is of more interest here.

3.3.1 Details of the 3-D Model

As discussed earlier, fibers and matrices in composites have different thermomechanical properties. Due to material discontinuity, very high stresses may be generated at and near the interface. Such a situation should be reflected in a preliminary FEM mesh. Since the stress gradients are expected to be low in the central part of the fiber, larger and linear elements (8-noded isoparametric bricks) are used in this area as shown in Fig. 3.4. A dense mesh is applied in the vicinity of the interface in both the fiber and the matrix. Due to the large stress gradients expected at and near the interface, quadratic elements (20-noded isoparametric bricks) are employed. Again, 8-noded linear brick elements are used for the matrix in the areas away from the interface. The mesh density and the types of elements that were employed may be revised by performing an analysis of the stress discontinuity between the elements. A denser mesh with quadratic isoparametric elements may be used in the areas with a higher stress discontinuity.

For more accurate simulation of the behavior of the composite represented by the prism model, proper boundary conditions (B.C.) should be imposed. For a fiber sufficiently distant from the side-edge of the composite (typically two-three rows of fibers), several symmetry planes can be identified as shown in Fig. 3.3. These symmetry planes simulate the effects of the neighboring fibers on the fiber under consideration. Therefore, the corresponding B.C. should be imposed on all symmetry planes. The nodes on line OO' (shown in Fig. 3.4) are restrained in the X and Y directions while the nodes on the OO'B'B surface are restrained in the X-direction. The AA'B'B surface remains planar. The nodes on the OO'A'A surface are allowed to move in the OA-direction only. The surface AOB is assumed to remain planar during the cooling process to represent a plane of symmetry in the middle of the prism. The surface A'O'B' represents a free surface and the nodes on this surface (except the boundaries) are free to deform in any direction.

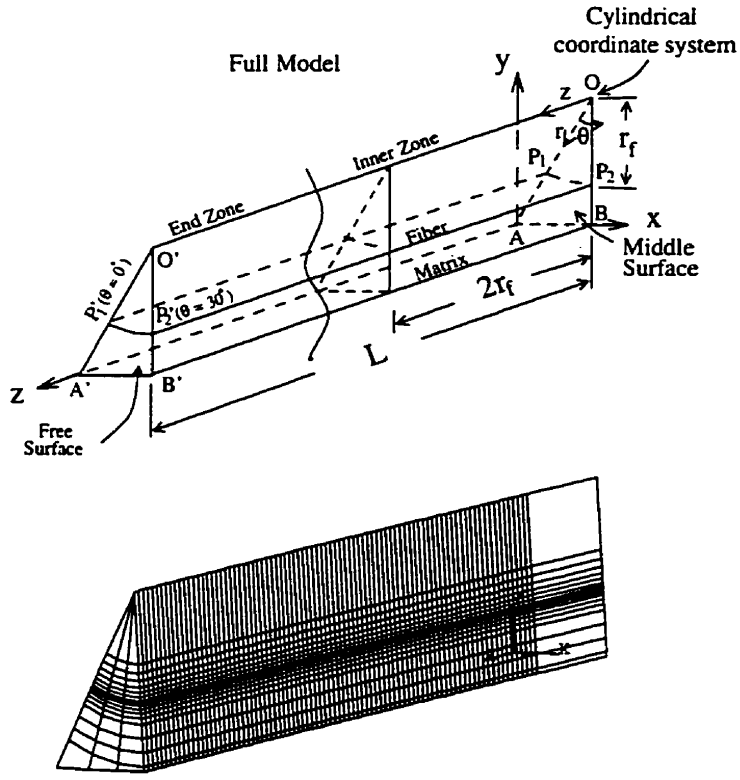

Fig. 3. 4: The 3-D prism model and FEM meshing.

Analysis of a fiber at the side-edge of the composite (edge-fiber) is much more complex than that of the internal fibers (see Fig. 3.3) due to lack of symmetry planes. An approximation of the stress/deformation state in such a fiber can be obtained by retaining all previous symmetry planes but leaving the surface AA'B'B free.

For a transient thermal analysis, the B.C. for the temperature and the heat flux must be imposed. When heating or cooling a composite, the edge-fibers have adiabatic B.C. (no heat flux) on all planes of symmetry. Also, the free surface O'A'B' is the only surface through which the heat to/from a medium is discharged/received through convection. Therefore, the convection B.C. should be applied on this face of the model. For the edge-fibers, the convection B.C. is also applied on the surface AA'B'B.

To perform a coupled thermal-stress analysis, the meshing of the thermal elements (for the thermal analysis) and the meshing of the structural elements (for the stress analysis) are identical. Normally, a less dense mesh is needed for the thermal analysis than for the stress analysis due to the lower mismatch between the thermal properties of the composite constituents.

3.3.2 Dimensions of the 3-D Model

The fiber diameter and the fiber volume fraction (the ratio of entire fiber volume to the total composite volume) define the dimensions of the 3-D model in the X-Y plane. In particular, the parameter 'a' in Eq. (3.9), which characterizes the width of the prism, is easy to find. However, the length of the model should be selected such that the model is as short as possible but is capable of representing both the vicinity of the free surface (the end zone) and the region distant from the free surface (the inner zone), even for very long fibers.

The length of the prism can be selected by observing the longitudinal interfacial shear stresses. These stresses decay substantially when moving away from the free surface and become negligible in the inner zone. Consequently, the axial strain component (in the z-direction) remains constant sufficiently away from the free surface and is practically independent of the fiber length. This state of generalized plane strain dominates in the rest of the composite. In order to represent both zones in the FEM analysis, the model must be long enough for the longitudinal shear stress to disappear. Therefore, several models with different lengths were considered in order to identify the ideal length for the model in terms of the accuracy of the stresses and computational effort. The longitudinal shear and

axial stresses at the distance of one fiber diameter from the plane of symmetry (the surface OAB in Fig. 3.4) for all the models were monitored. Typical dependence of these stresses on the model length is shown in Fig. 3.5. The shear stress decays to zero at a distance of about 2.5 fiber diameters from the free surface (see Fig. 3.5(a)). The results reported by Nairn (1985) and Ostrowski et al. (1984) suggested that the minimum length equal to five fiber diameters for decaying the longitudinal shear stress was required. The axial stress at the plane of symmetry for a sufficiently long model should converge to a Lame type solution. Analytically, this solution can be obtained by assuming a generalized plane strain state and solving Eq. (A.12) that is characteristic for the inner zone. Numerically, the inner zone solution can be determined by coupling the free surface nodes in the longitudinal direction. Fig. 3.5(b) shows how the calculated axial stresses for the model of a given length converge to the axial stresses obtained from the Lame solution. The graphs in Figs. 3.5(a) and (b) indicate that increasing the model length leads to a faster decrease in the shear stress than in the discrepancy between the calculated axial stress and the Lame stresses. Typically, when choosing a model about 3 fiber diameters long, the longitudinal shear stress practically vanishes (less than 0.05%) while the axial stress deviates from the Lame solution by less than 5%.

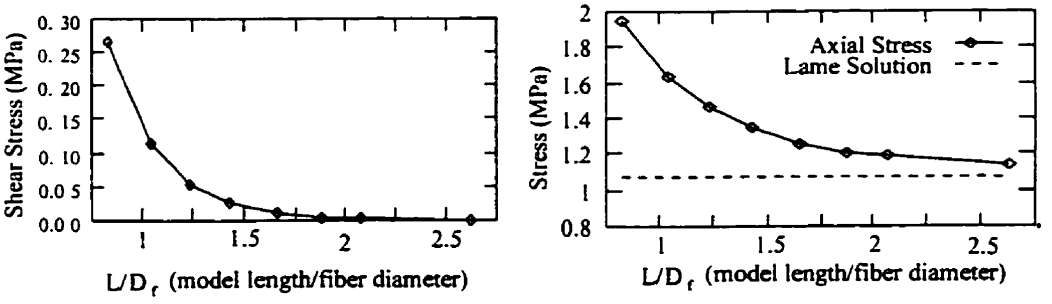

Fig. 3. 5: Normal axial and longitudinal shear stress components as a function of model length.

Here, in order to ensure that the numerical model is capable of simulating the fiber end and the stress state away from the fiber end, the length of the model is assumed to be equal to about five fiber diameters.

3.3.3 Sub-Modeling Procedure

A high number of elements should be used along the model length in order to provide a reasonable aspect ratio for the elements. Any further mesh refinement (the h-refinement) in the end zone might run out of computer resource limits. Therefore, in the present study, the h-refinement was performed by utilizing the sub-modeling capability of the ANSYS software, which allows a smaller portion of a previously analyzed model to be remeshed with smaller elements (see Fig. 3.6).

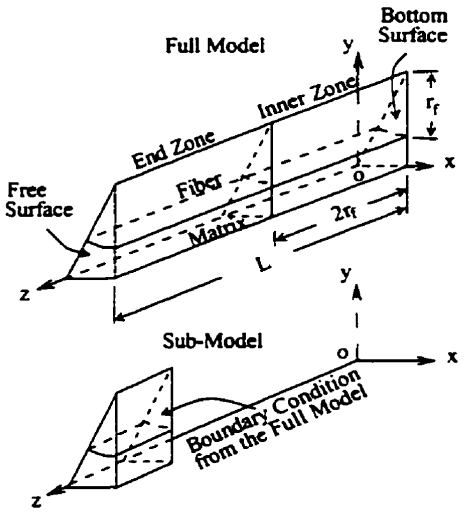

Fig. 3. 6: Sub-modeling procedure.

Repeating this procedure several times, element sizes equal to 1/62000 of the fiber radius were implemented to mesh the fiber/matrix interface at the free surface. This degree of h-refinement was required to study rapid stress variations in this area.

3.3.4 Element Birth and Death

To analyze the effects of any material adding/removing (machining some part of a material, casting or attaching new materials) the element birth and death capability of ANSYS is used. This option allows for adding or removing any number of elements during the solution phase of the calculations. For example, in stress analysis, the stiffness of the killed (or deactivated) elements is severely reduced or, in thermal analysis, the heat capacity of the elements is reduced and their thermal conductivity is highly increased.

More details about element birth and death procedure can be found in the ANSYS User's Manual (1996).

3.3.5 Axisymmetric Models

In the prism model, the highest stresses occur at the free surface in the narrow band near the fiber/matrix interface. These stresses vary only a little along the fiber circumference (see Chapter 5). This phenomenon is frequently used to reduce the calculation time by replacing the prism model by the corresponding axisymmetric model (Fig. 3.7). The stress/deformation states in the area of stress concentration for both models are very similar. The axisymmetric model allows for very dense meshing of the stress concentration zone.

The difference between the two types of models and their accuracy are discussed in the next chapters. The results of the thermal transient analysis of the two models are compared in Chapter 4, section 4.4 and the thermal stresses in both models will be discussed in Chapter 5.

Similar to the 3-D model presented in section 3.3.1, a very dense mesh is used at the fiber/matrix interface in the vicinity of the free surface of the axisymmetric model. Much coarser mesh is used in both the fiber and the matrix in the inner zone. The details of the axisymmetric model, with the boundary conditions and the mesh configuration, are shown in Fig. 3.8. For meshing the model, 8-noded axisymmetric quadratic isoparametric elements are used. Since the number of degrees of freedom for axisymmetric models is much less than for the 3-D model, this quadratic element is used for meshing the entire model. The free surface is represented by line DAM.

The model is selected to be sufficiently long so that the effects of the free surface on the other end of the model (line CBM) are negligible. The boundary conditions along CBM correspond to a generalized plane strain state characterization for the composite away from the free surface. The nodes on line MM are assumed to be coupled. Coupling the nodes along line MM in the radial direction results in the nodes being restrained

against the relative movement in this direction. This keeps the line straight at all times. The coupling assumption simulates the effects of an adjacent fiber on line MM. For edge-fibers, the nodes on line MM are not restrained by this boundary condition. For thermal analysis of internal fibers, an adiabatic boundary condition is assumed on all edges of the model except line DAM (shown in Fig. 3.8) that remains free with the convection coefficient applied on this line.

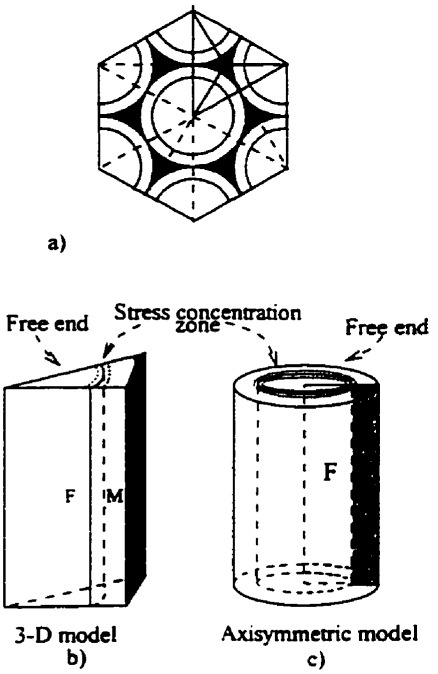

Fig. 3. 7: The 3-D prism and Axisymmetric models.

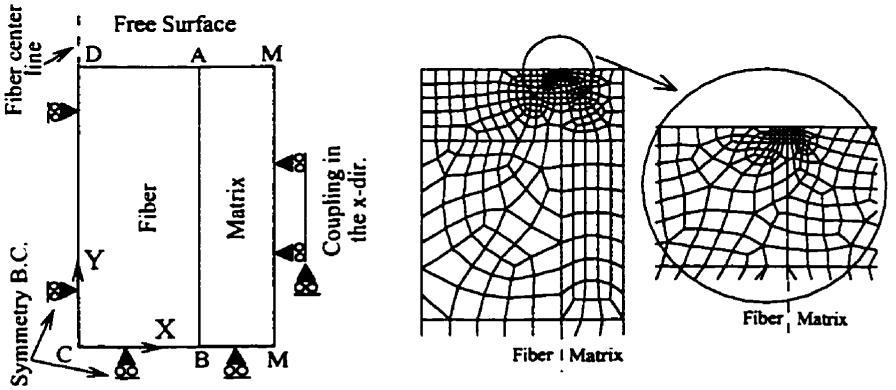

a) Axisymmetric model b) FEM mesh

Fig. 3. 8: Axisymmetric model and FEM meshing.

4. Thermal Transient Analysis

4.1 Introduction

Rapid changes in the temperature surrounding composites may cause sharp temperature gradients inside the material. To simulate such situations and to determine the corresponding thermal stresses a transient analysis is required. Such an analysis is especially important in determining the thermal stresses generated in composite materials during cooling from the processing temperature or the service temperatures. In this chapter, the thermal transient analyses of unidirectional composites by means of the prism and the axisymmetric models will be used to determine the temperature gradients that may occur during the cooling process.

For better understanding of the heat transfer mechanism in composites, the temperature distribution in a highly conductive fiber bonded to an almost insulating matrix will be discussed first. In order to investigate the effect of the model length on the results of the thermal analysis it is assumed that the model length is about 20 times of the fiber diameter. This length is six times longer than the model length required for the stress analysis discussed in Chapter 3. The analysis will be repeated for a model with the length required for the stress analysis.

A high mismatch in thermal capacity (C) of the fiber and the matrix, typically observed in the carbon fiber/polymeric matrix composites, will be assumed to investigate the effects of mismatch in thermal capacitance on the temperature distribution. The thermal behavior of metal matrix composites where the fiber and the matrix both are very good thermal conductors will also be considered. Polymeric matrix composites that have relatively higher thermal conductivity mismatch than metal matrix composites will also be discussed. Finally, the results of the 3-D model will be compared to those of the axisymmetric model.

4.2 Effects of the Mismatch in Thermal Properties of Composite Constituents

For transient processes, the thermal conductivity and thermal capacity of composite constituents play a key role in temperature distribution throughout composite materials. A combination of a high thermal conductivity fiber with a very low thermal conductivity matrix is used to analyze the mechanism of heat transfer along the fiber length. The length of the model is considered to be 20 times of the fiber diameter. It is assumed that the composite at uniform temperature of 900°C is placed in air of temperature 20°C. The thermal properties of the constituents are presented in Table 4.1. The 3-D prism model with the dimensions corresponding to the SCS-6 fibers is utilized. The diameters of the graphite and SCS-6 fibers are 7.62μm and 140μm, respectively, and the fiber volume fraction is set at 35%. The lateral dimension of the model is then determined by Eq. (3.9).

Table 4.1: Thermal properties of various composite components.

	Graphite*	Epoxy*	SCS-6*	Ti-6Al-4V**
k_l Kg.μm/(°K.s^3)	83.6×10^{6}	1.8×10^{5}	16×10^{6}	7×10^{6}
k_t Kg.μm/(°K.s^3)	8.36×10^{6}	1.8×10^{5}	16×10^{6}	7×10^{6}
C (μm/°Ks^3)	838.4×10^{12}	1048×10^{12}	1200×10^{12}	590×10^{12}
ρ (Kg/μm^3)	1.7475×10^{-15}	1.2759×10^{-15}	3.32×10^{-15}	4.4×10^{-15}

* Weeton et al. (1987) and ** Grayson (1983).

Cooling of such a model in air from processing temperature of 900°C takes a long time. The temperature distribution profile of the composite after 500 seconds of cooling in air is shown in Figs. 4.1(a) and (b). Due to the symmetrical geometry of the model, all the model sides are considered to be adiabatic except the free surface which discharges the heat to the air through convection. A uniform temperature is seen along the fiber length as the fiber has a very high conductivity. Due to the low matrix conductivity, the heat flow is slow in the matrix, so the layers of the matrix which are closer to the free surface lose more heat than the interior layers, Fig. 4.1(c).

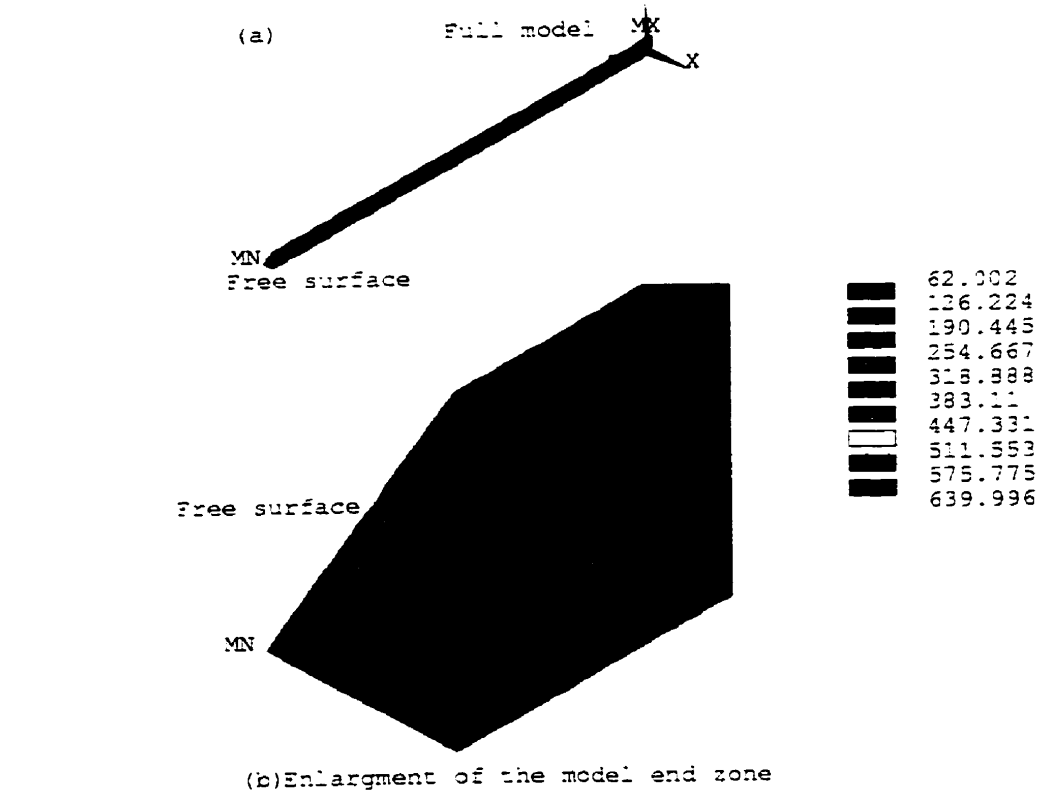

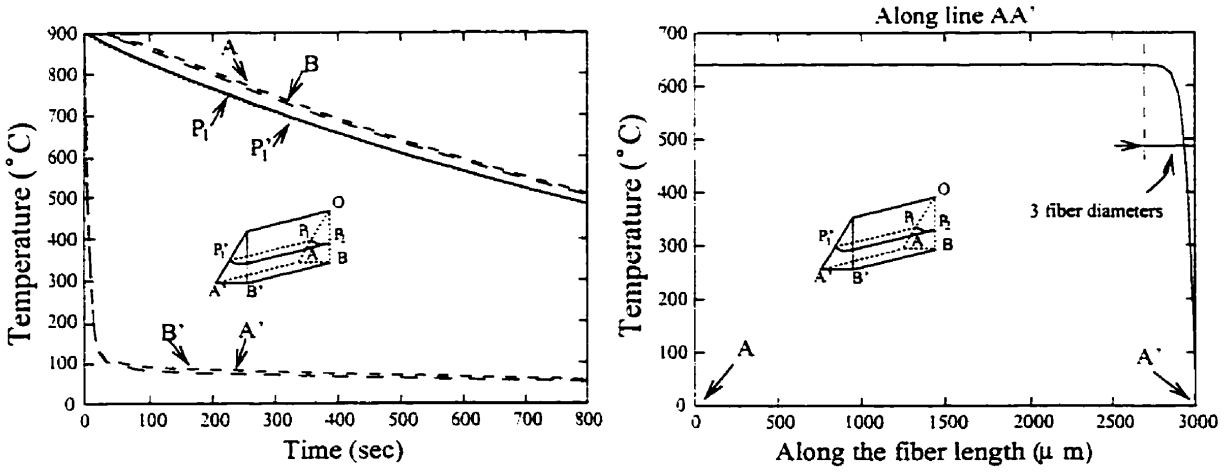

Fig. 4.1: (a)-(b) Temperature distribution after 500sec cooling in air, (c) temperature profiles in the interior and at the free surface with time, and (d) temperature gradient along the fiber length.

As the graphs show, the nodes on the free surface and away from the fiber (A' and B') are cooled very fast while the nodes on the interior surface (A, B, P_I) and the nodes on the free surface but close to the fiber (i.e. P'_I) are cooled rather slowly. The heat from the interior layers of the matrix does not travel fast enough to compensate for the heat lost by the free surface layers to the air, so a large temperature gradient occurs along the fiber length in the matrix (Fig. 4.1(d)). The temperature at the interior layers of the matrix is similar to the fiber temperature. This is due to the fact that the interior layers of the matrix serve as a heat source. These layers control the fiber temperature. The heat from the interior layers moves slowly to the fiber and rapidly discharges to the air. A small transverse temperature gradient is seen in the matrix near the interface in the interior layers due to the small radial dimension of the model compared to the axial dimension. The fiber that acts as a heat pipe also influences the temperature of the matrix layers close to the interface near the free surface. The temperature difference between points A and A' is higher than the difference in temperatures at B and B'. On surface OAB, the shorter distance of B to the fiber than A causes the temperature at B to drop faster. However, at the free surface, the higher distance of A' to the fiber than B' causes less fiber influence on A' than B'. Thus the minimum temperature in the matrix occurs away from the interface on the free surface (i.e. at A').

The cooling process is long, and steady state is reached when the temperature of the interior layers of the matrix drops to room temperature. The temperature gradient will be steeper and the cooling process will be longer for composites with matrices that have lower thermal conductivity and higher thermal capacity. The temperature around the fiber/matrix interface at the free surface is uniform (Fig. 4.1(b)). This is also due to the influence of the fiber temperature on the matrix at the interface. Therefore, this kind of thermal behavior may affect the matrix expansion and contraction along line AA'. This thermal behavior is more noticeable when the composite undergoes a thermal cycling load.

Two different temperature cycling schemes were considered. In the first scheme, the composite sample is moving back and forth between hot and cold reservoirs. In this way, the sample is heated and subsequently cooled in free convection. For the second scheme,

the sample is heated and cooled at constant temperature rates with prescribed temperatures applied to the nodes on the free surface (surface O'A'B'). In this scheme the heat is transferred through conduction only.

A plot of the temperature profiles with time under the first loading condition for points P'_1, A', and B' on the free surface and P_1, A, and B on the interior surface are shown in Fig. 4.2. The temperature profiles of points P_1, A, and B show a big time delay. Due to the insulating behavior of the matrix it takes a long time for the temperature of the interior layer to reach the heating/cooling temperature of the medium. Also, the fiber near the free surface at P'_1 shows the same time delay as the interior layer of the matrix. However, A' and B' on the free surface follow the medium temperature closely. They lose and gain heat very quickly because heat transfer between these points and the medium occurs at a higher rate than that with the rest of the model. This is due to the very low conductivity of the matrix.

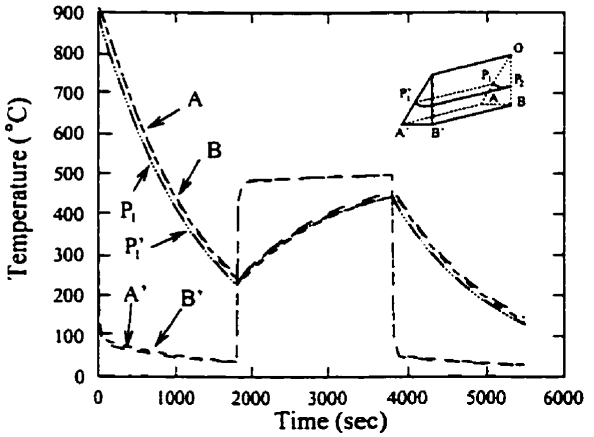

Fig. 4.2: Time-temperature profiles in the interior and at the free surface of the 3-D model thermally cycled assuming free convection.

For the second temperature cycling scheme, the free surface temperature is the same for the fiber and the matrix. The calculated temperature of the interior layer (Fig. 4.3) follows the free surface temperature with a small delay due to the low conductivity of the matrix. It is noted that the delay is not as significant as for the first scheme. That is because the free surface temperature of the fiber is fixed and in this case it is the fiber that supplies the heat to the interior layer and controls its temperature. The fiber supplies a large amount

of heat into the matrix. The difference between the matrix and the medium temperature is so small that it may be ignored.

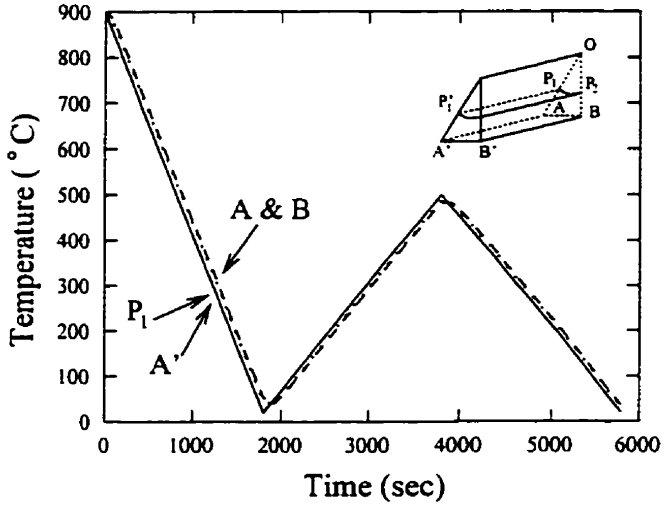

Fig. 4.3: Time-temperature profiles in the interior and at the free surface of the 3-D model thermally cycled assuming forced heating/cooling convection.

For the case of cooling the composite from the processing temperature, a plot of the temperature along the matrix edge (line AA', Fig. 4.1(d)) shows that the steepest temperature gradient appears along the length which is limited to about 3 to 5 fiber diameters from the free surface. This length is similar to the model length required for structural analysis as discussed in Chapter 3. To examine the possibility of improving the numerical efficiency, the thermal analysis was repeated for a model of 1/6th of the length of the original model (short model).

The temperature distribution during the cooling period for the short model shows that a temperature gradient indeed occurs along most of the length of the model, but the deepest descent is located closer to the free surface (see Fig. 4.4). Comparing the temperature gradient for the short model with that of the long model shown in Fig. 4.1(d) one can conclude that the temperature gradient depends on the model length only for a matrix with extremely low conductivity. Longer models are capable of storing more heat. Due to the low matrix conductivity assumed, the heat travels very slowly from one location to another causing a very high difference in the temperature along the length and producing much steeper temperature gradients. For short models, due to adiabatic

conditions assumed along the interior and the side boundaries and the low heat storage a lower temperature gradient is generated along the model length.

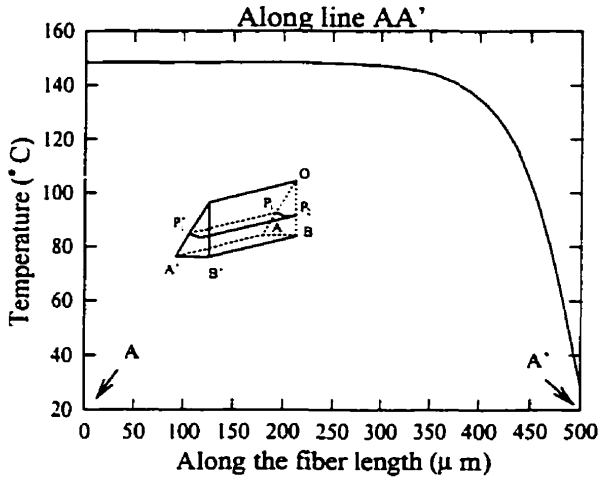

Fig. 4.4: Temperature gradient along the length of the short model.

To find the effects of thermal capacitance mismatch of the fiber and the matrix on the temperature gradient throughout composites, the analysis of the short model was repeated with the thermal capacitance for the fiber reduced by 10^6 times. Note that with reducing C for the fiber, the mismatch in C of the fiber and matrix is increased. Table 4.2 shows the temperature at points A', B', B, and A after 500 seconds for the previous analysis and for the current analysis with C for the fiber being 10^6 times smaller.

Table 4.2: Effect of mismatch in thermal capacitance on the temperature distribution.

Mismatch in C	A' (°C)	A (°C)	B' (°C)	B (°C)	A - A' (°C)	B - B' (°C)
High	22.77	66.76	22.99	62.57	43.99	39.58
Low	28.05	148.46	28.93	140.73	120.41	111.80

It seems that the temperature gradient along both lines AA' and BB' is reduced with increasing the mismatch in C of the composite constituents. The difference between the temperature at locations A and A' and B and B' (the columns marked with A-A' and B-B', respectively) are much lower for the case with higher mismatch in C. Fibers with high thermal capacitance store more heat than the fibers with low C. Therefore, it takes more time for the fiber to lose its heat to the cooling medium. However, when C for the fiber is

low, it discharges most of the heat it receives from the matrix to the surrounding medium. It appears that the thermal capacitance and thermal conductivity mismatches of composite constituents have opposite effects. The high mismatch in k increases the temperature gradient throughout the composite, while the increase in the mismatch of C decreases the temperature gradient.

4.3 Thermal Transient Analysis of Metallic and Polymeric Matrix Composites

Thermal analysis of a composite with its matrix having very low conductivity showed that a temperature gradient occurs along the length of both short and long models. The temperature gradient was reduced when the mismatch of the thermal capacitance of the composite constituents increased. In this section, the thermal behaviors of SCS-6/Ti-6Al-4V and graphite/epoxy composites are analyzed.

Due to the low mismatch in k and high mismatch in C of SCS-6 fibers with the Ti-6Al-4V matrix (Table 4.1), it seems that the temperature gradient throughout the composite is negligible. The composite is cooled from the processing temperature of 900°C in free convection. The time-temperature profiles of points P_1, A, B (on the interior surface) and P'_1, A', B' (on the free surface) presented in Fig. 4.5 indicate uniform temperature almost everywhere in the composite. It is noted that the difference between the minimum and the maximum temperatures is less than 1°C, which is negligible.

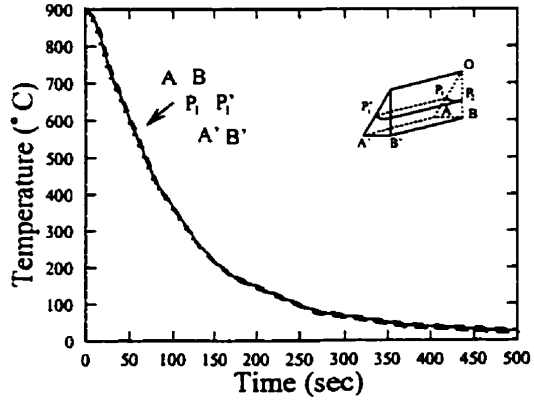

Fig. 4.5: Time-temperature profiles in the interior and at the free surface of the SCS-6/Ti-6Al-4V composite.

The minimum temperature occurs on the free surface at point A' (which has the maximum distance to the fiber) and the maximum temperature occurs at A on the interior surface.

Thermal analysis of polymeric matrix composite is presented here. For comparison with previous results, this composite is also cooled from 900°C. Since the graphite/epoxy composite has higher k and lower C mismatches than the metal matrix composite (Table 4.1), a higher temperature gradient is expected in the former than the latter. However, as Fig. 4.6 shows, the temperature values for the free surface and the interior layers of the composite are almost the same, i.e. the temperature gradient is negligible for this polymeric composite for the dimensions considered here. One reason for this unexpected result could be the low lateral dimension of the model due to the very small diameter of the graphite fiber (7.62 μm). This small fiber diameter accompanied by a 35% fiber volume fraction dictates a very small lateral size for the model (see Eq. (3.9)). This small lateral size makes the fiber thermal conductivity a dominant factor. As a result, the temperature of the composite is fully controlled by the fiber. Since the longitudinal thermal conductivity of the graphite fiber is almost 6 times higher than SCS-6 fiber and the diameter of graphite is small compared to that of the SCS-6 fiber (140 μm), the graphite/epoxy composite cools down faster than the SCS-6/Ti-6Al-4V composite (see Figs. 4.6 and 4.5).

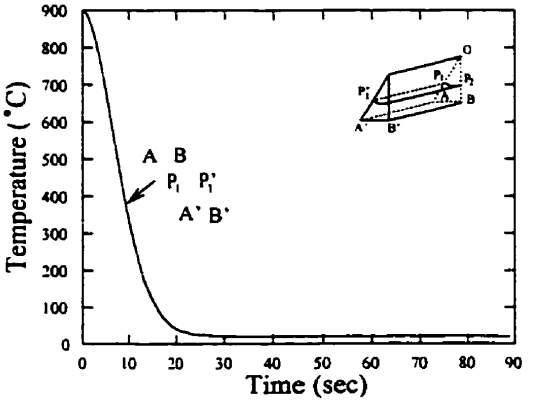

Fig. 4.6: Time-temperature profiles in the interior and at the free surface of the graphite/epoxy composite.

To see how the model length affects the temperature gradient in polymeric matrix composites, the analysis was repeated for a model with 6 times longer length. According to the time-temperature profiles of the aforementioned points both on the free surface and the

interior layer of the model (Fig. 4.7), the temperature gradient is again negligible. The only difference between the long and the short model is the longer time, which the long model needs to cool down to room temperature. This is due to the dependence of the stored heat in the composite on the model sizes.

From these analyses, it can be concluded that the temperature gradient for metallic and polymeric composites is almost negligible for the model length required for thermal-stress analysis. The temperature gradient is higher inside the composite that may change the stresses in the inner zone. However, such a change is not very significant. Therefore, in most of the elasto-plastic stress analyses, a uniform temperature can be considered for calculating the stresses for slow cooling rates. Only for visco-elastic analyses, in which the time directly affects the strain-stress relations, the rate of cooling/heating may influence creep deformation and final residual stress states.

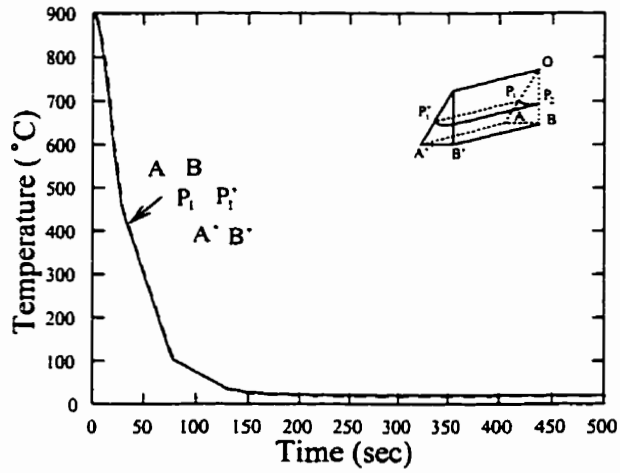

Fig. 4.7: Time-temperature profiles in the interior and at the free surface of the long graphite/epoxy composite model.

4.4 Thermal Transient Analysis of the Axisymmetric Model

As it was discussed in Chapter 3, the 3-D model may be replaced with an axisymmetric model but the accuracy of the analysis must be examined with the numerical effort. The axisymmetric model may be utilized when a very fine mesh is required and the computer resources are limited, or some simplifying assumptions do not affect significantly the accuracy but reduce the time and the cost of the calculations. Here, the

thermal transient analysis of the axisymmetric model is presented as the first test case and the results are compared to those of the 3-D model. In this section, the analysis of the composite with the very low conductivity matrix is repeated by using the axisymmetric model. The model is meshed with similar element sizes as those used in the 3-D model. Similar model dimensions and fiber volume fraction are also considered.

The contour plot of the temperature (Fig. 4.8) shows a similar distribution as for the 3-D model (Fig. 4.1(a)). The same reasoning, as discussed in section 4.2, is valid. The temperature profile along line MM' (Fig. 4.9) of the axisymmetric model lies between those of lines AA' and BB' of the 3-D model. The reason is that the axisymmetric model ignores the small matrix area confined between the hexagonal fiber cluster (see Fig. 3.7). Therefore, for V_f similar to the 3-D model, the distance of M' on the axisymmetric model to the fiber would be the average of the distances of A' and B' to the fiber for the 3-D model. Since the matrix behaves as an insulator, the distance of a location on the matrix to the fiber has a substantial effect on the temperature at that particular point. This temperature difference can affect the out of plane deformation of the matrix. This is one of those thermal details, which is ignored if the 3-D model is replaced with an axisymmetric model. Fortunately, this temperature difference is small for both metallic and polymeric matrix composites and its effect on the thermal gradient and the residual thermal stresses is negligible.

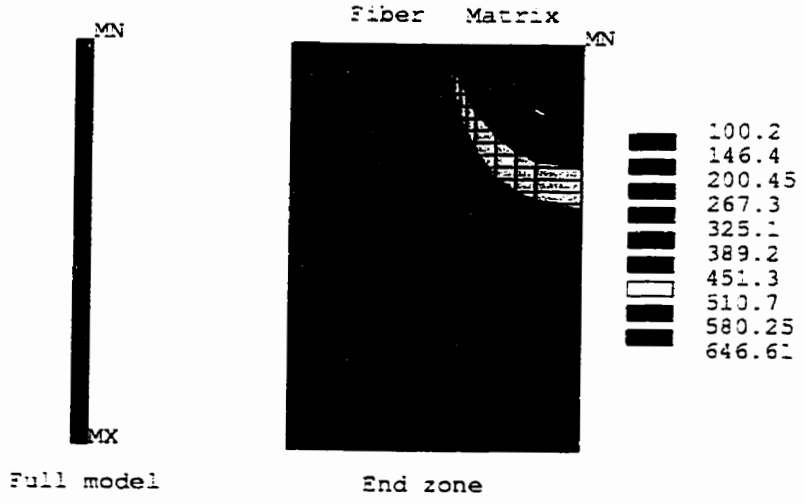

Fig. 4.8: Temperature distribution for the axisymmetric model.

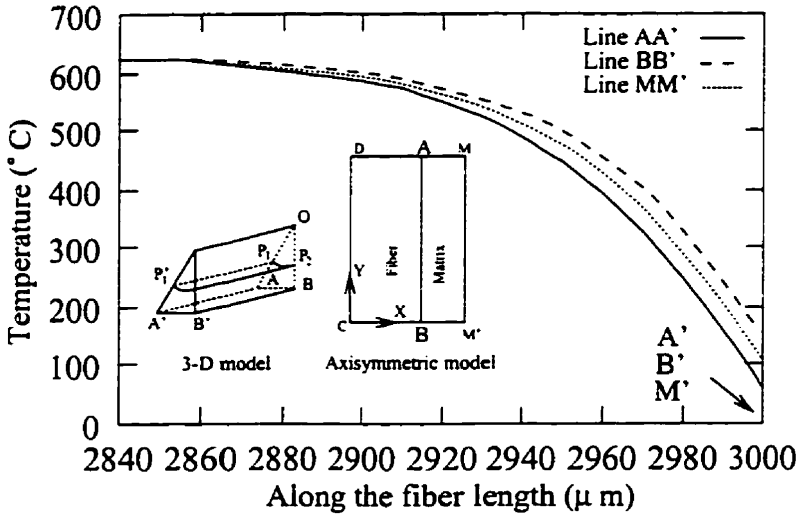

Fig. 4.9: Temperature profile along line MM'.

5. 3-D Elastic Analysis

5.1 Introduction

The thermal transient analysis presented in Chapter 4 showed that, due to the high thermal conductivity of the fibers that act as heat pipes, in the composite heated or cooled with sufficiently slow rate, the temperature gradients are small and the temperature is increasing or decreasing almost uniformly. Consequently, any thermal stress effects should be attributed to such a uniform temperature change and to the mismatch in the thermal expansion coefficient of the fiber and the matrix. In order to understand this phenomenon the elastic stress analysis under 1°C uniform temperature change is presented in this chapter. This unit temperature change is considered as a nominal thermal loading. Such a loading provides all the information about the thermal stress distribution due to the mismatch of the CTE without affecting any of the mechanical properties of the composite constituents. To estimate the stress magnitudes corresponding to a specified temperature increment (and if the variation of mechanical properties of both constituents within the temperature range considered is negligible and if the yield strength is not reached) one should multiply the values shown on the plots by this temperature increment. The results presented here were obtained for graphite (AS)/epoxy (IMHS) composite with 35% fiber volume fraction. The properties of the materials are listed in Table 5.1. Note that, in general, the fiber is assumed axisymmetrically orthotropic with subscripts l and t denoting the axial and transversal directions, respectively. The minor values of Poisson's ratios are denoted as ν_a and ν_d. Formally, in terms of the coordinate systems shown in Fig. 5.1 the following applies: $\nu_a = \nu_{zr}$ and $\nu_{tl} = \nu_{r\theta} = \nu_{rz}$. In this study, the models with a length of 4 fiber diameters were used for the 3-D analysis. The diameter of graphite fiber is set at 7.62 μm.

Table 5.1: Properties of the composite constituents used in the analysis Weeton et al. (1987).

	AS	IMLS	IMHS	Polyamide
E_l (GPa)	214	3.4	3.4	3.4
E_t (GPa)	13.7	3.4	3.4	3.4
ν_{tt}	0.2	0.41	0.35	0.35
ν_{tl}	0.25	0.41	0.35	0.35
$CTE_l (10^{-6})/°C$	-0.99	102.6	64.8	36
$CTE_t (10^{-6})/°C$	10.1	102.6	64.8	36

AS = Graphite fiber; IMLS = Intermediate modulus low strength epoxy; IMHS = Intermediate modulus High strength epoxy.

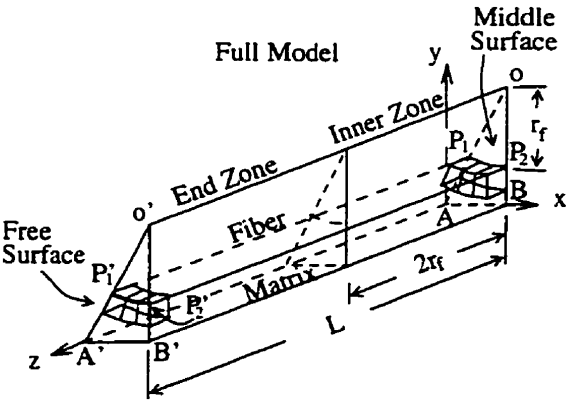

Fig. 5.1: Configuration of the 3-D prism model.

The analysis shows that the stress distribution near the free surface (the end zone) is substantially different from the stresses in the inner zone. The inner and the end zone divisions of the 3-D prism model were discussed in Chapter 3. The characteristic features of the stress distributions in both zones are presented separately. The effect of the fiber volume fraction V_f (8.3% to 66.6%) is also investigated. It will be shown that the stresses change with V_f. Composites with higher V_f have lower interfacial thermal stresses in the end zone compared to the composites with low V_f. However, in the inner zone, V_f will decrease some of the stress components while it increases the others. In addition, the composite dimensional stability i.e. the axial and transversal displacements are discussed. The results obtained by the axisymmetric model will be compared to the results obtained from the corresponding 3-D model.

5.2 Inner Zone

As explained in Chapter 3, the boundary conditions of the ABB'A' surface can determine whether the modeled fiber is away from the composite side edge or at the side edge. Such fibers are referred to as the internal-fiber and the edge-fiber, respectively. When the nodes on this surface are free (i.e. no restraining effect is applied on this surface by the neighboring fiber) the conditions for a fiber at the side edge of the composite prevails. It should also be mentioned that the main objective here is to determine the stress and deformation states of the internal fiber. Unless the edge fiber is mentioned, this chapter deals with the internal fiber.

The behavior of the inner zone is characteristic for the portion of the model where general plane strain state dominates. In this zone, the longitudinal interfacial shear stresses disappear and the stress components are independent of the location along the fiber. This solution is valid for an infinitely long fiber. In the prism model the stresses depend on the circumferential position around the fiber. The axial, radial, hoop, and equivalent von Mises stresses in the matrix on surface OAB at the interface as functions of angle θ are presented in Figs. 5.2(a-d). For comparison, similar stress components in the matrix for the edge-fiber are indicated with the broken lines. The stresses in the fiber along the interface are shown in Fig. 5.2(e).

Under a positive temperature change, the matrix expands more than the fiber due to its higher CTE value. In order to maintain continuity in the radial direction, a tensile radial stress must develop at the fiber/matrix interface (Fig. 5.2(b)). For continuity in the axial direction, the matrix has to be compressed (Fig. 5.2(a)) and the fiber must be stretched (Fig. 5.2(e)). For similar reasons, the hoop stresses are tensile in the fiber (Fig. 5.2(e)) and compressive in the matrix (Fig. 5.2(c)). A small in-plane shear stress also occurs at the interface.

Upon cooling, the sign of the stresses would be reversed. The matrix will experience high tensile hoop stress, which may cause the matrix to craze and crack around the fiber. However, the compressive radial stress will reinforce the fiber/matrix interfacial bond. As

discussed in Chapter 2, the interfacial stresses reported by Sottos et al. (1989) are not in full agreement with the results shown here. Much higher axial stress for the matrix relative to that of the fiber was reported. Also, the stress components in the fiber and matrix were of the same sign.

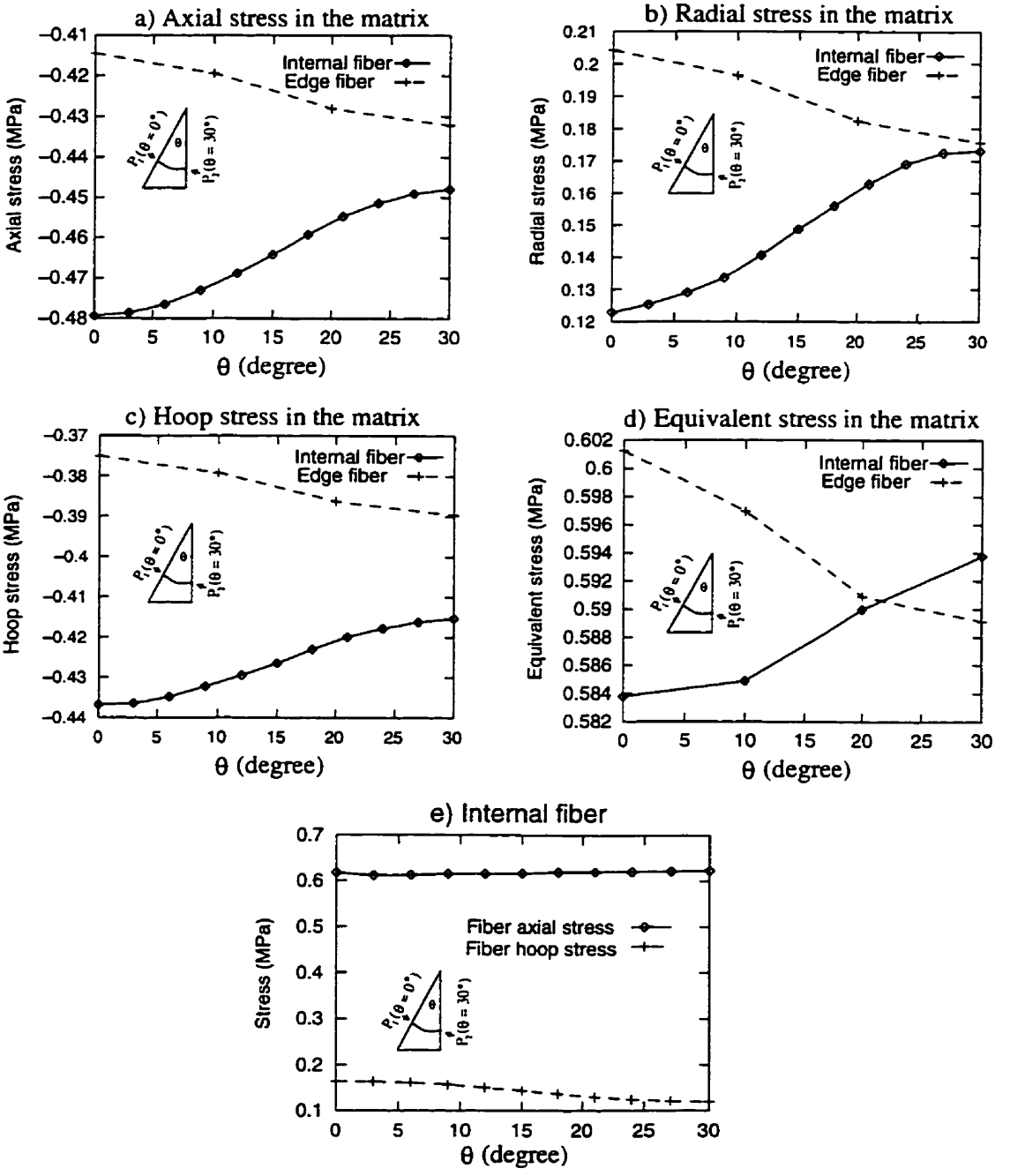

Fig. 5.2: The inner zone stress components in the fiber and matrix on surface OAB at the interface.

The other difference is related to the location of the maximum and minimum of radial stress. According to Sottos et al. (1989) and Szyszkowski and King (1995), a lower V_f results in higher interfacial stresses. Higher stresses in the areas with higher fiber distance to the neighboring fiber have been attributed to a lower local fiber volume fraction in these areas. The local fiber volume fraction is defined as the square of the ratio of fiber radius to the half distance between the center of two neighboring fibers ($(OP_1/OA)^2$ or $(OP_2/OB)^2$). Since, for the 3-D model $(OP_1/OA)^2 < (OP_2/OB)^2$, higher local stresses according to (Sottos et al., 1989) should be expected at P_1 ($\theta = 0°$). This effect has not been observed in this study. The graph for the radial stress (Fig. 5.2(b)) seems to have opposite curvature relative to the results presented by Sottos et al. (1989). The maximum radial stress was at $\theta = 0°$ in (Sottos et al., 1989), while in the present study it occurs at $\theta = 30°$. However, as the same figure shows, the radial stress distribution for the edge fiber is as predicted by Sottos et al. (1989) i.e. the maximum of the stress is at P_1 ($\theta = 0°$). The reason for this shift in the location of maximum stresses may be explained by the nature of the deformations under the temperature change for the edge fiber. Upon heating, for an internal fiber, the ABB'A' surface is required to remain planar and horizontal. However, if this boundary condition is removed for the edge fiber this surface deforms as shown in Fig. 5.3. The matrix expands more along line AP_1 than along line BP_2 and the whole surface 'rotates' counter-clockwise. In order to have the surface horizontal again for the internal fiber case, self-equilibrated extra radial stresses must be generated which are compressive along line AP_1 and tensile along BP_2. In the inner zone, this extra stress, raises the magnitude of the tensile radial stress at P_2 and lowers it at P_1. Thus, the results presented by Sottos et al. (1989) may have been produced by ignoring the symmetry boundary condition on the surface ABB'A'.

If the deformation mechanism outlined in Fig. 5.3 is applied to the interfacial elements in the inner zone along line P_1P_2 (the elements are shown in Fig. 5.1), the opposite nature of the stress components for the internal fiber and the edge fiber presented in Fig. 5.2 can be easily explained. The thermal radial and hoop stress components for the elements of the inner zone are presented in Fig. 5.4(a). Due to lower local V_f for P_1 (element 1) than P_2 (element 2), higher stresses occur for element 1. Therefore, for the

edge fiber, the deformation of element 1 will be higher than that of element 2 due to free movement of the nodes on ABB'A' surface as shown in Fig. 5.4(b). It is noted that, due to symmetry boundary conditions, face 1 of element 1 and face 3 of element 2 must remain straight. If surface ABB'A' is required to remain straight, the deformation of the elements must reach an equilibrium state. So, a compressive radial force on face 4 of element 1 and a tensile load on face 4 of element 2 are needed to bring the deformed elements to the equilibrium position. This extra compressive radial load on element 1 tends to expand the element in the circumferential direction, which is resisted by a compressive hoop stress. Meanwhile, the circumferential shrinkage of element 2 due to the tensile radial load on its face 2 is resisted by a tensile hoop stress (see Fig. 5.4(c)). As explained earlier, super-positioning of these extra radial and hoop stresses of Fig. 5.4(c) on the thermal stresses of Fig. 5.4(a) results in higher tensile radial stress at P_2 (θ = 30°) relative to P_1 (θ = 0°), whereas it is opposite for the hoop stress. The compressive hoop stress of element 1 in Fig. 5.4(c) increases the overall compressive hoop stress at P_1 (θ = 0°) and the tensile hoop stress of element 2 reduces the overall hoop stress at P_2 (θ = 30°), see Fig. 5.4(a-c).

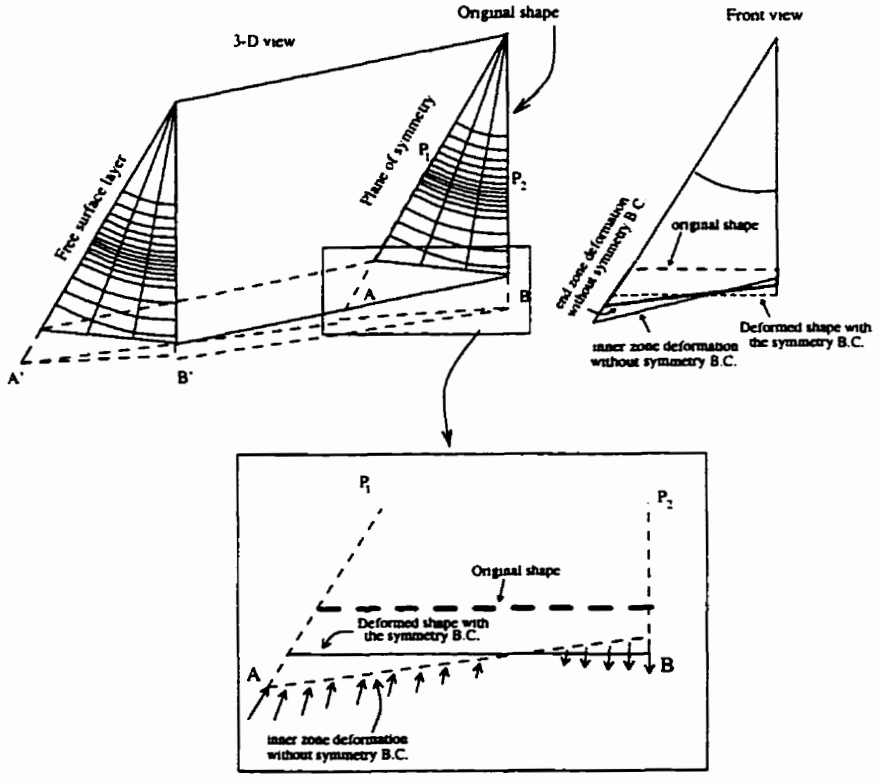

Fig. 5.3: Deformation pattern with the ABB'A' surface free.

These compressive extra radial and hoop stresses in Fig. 5.4(c) tend to impose an axial elongation on element 1 (if it is viewed in 3-D) which is resisted by a compressive axial stress, see Fig. 5.4(d). However, as the extra radial and hoop stress components are tensile for element 2, the resultant axial load have to be tensile to resist shrinkage. Adding these extra axial stresses to the thermal axial stress of the matrix at P_1 and P_2 which are compressive in nature, reduces the absolute value of the axial stress at P_2 ($\theta = 30°$), while the absolute value of the stress increases at P_1 ($\theta = 0°$), see Fig. 5.2(a).

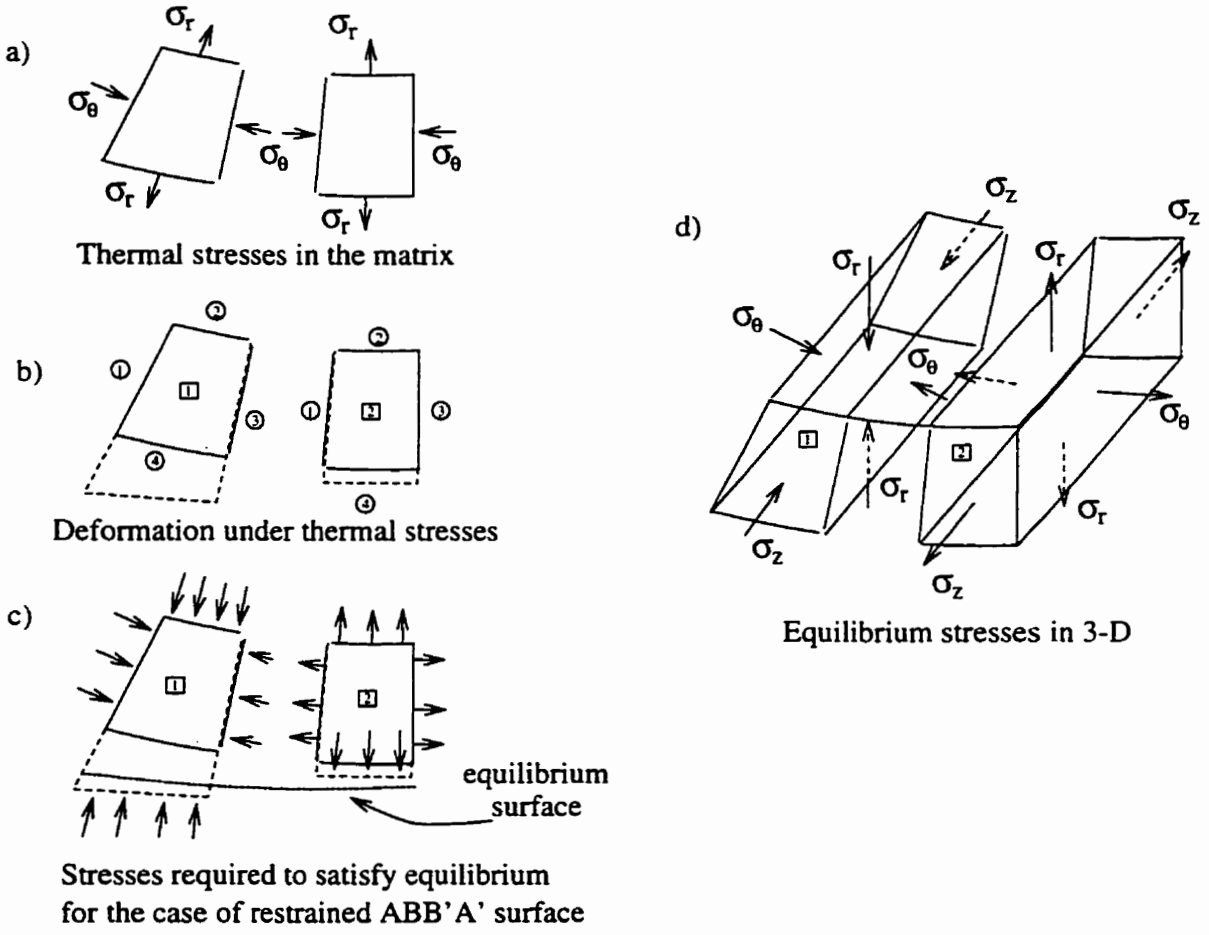

Fig. 5.4: Effects of the restrained ABB'A' surface on the stresses of the interfacial inner zone elements.

For the edge fiber, since the surface ABB'A' is free and due to lower local V_f at P_1 than at P_2, a higher radial stress occurs at P_1. This higher tensile radial stress is responsible for altering the rest of the stress components at this location.

The profile of the stress components discussed so far, directly affect the von Mises equivalent stress distribution for both types of the fibers as shown in Fig. 5.2(d). The main conclusion of this figure is that in the inner zone this stress is almost constant along the circumference. For the internal fiber, the stress is slightly higher at $\theta = 30°$ or where the fiber has the least distance to the neighboring fibers. However, for the edge fiber the stress is slightly higher at $\theta = 0°$ where the fiber has the largest distance to the neighboring fibers.

In order to understand the effects of fiber volume fraction on interfacial stresses, the above analyses were repeated for different V_f. Figs. 5.5(a-d) show the interfacial radial, hoop, axial, and equivalent stresses for the internal fiber where V_f varies from 8.3% to 66.6%. As the graphs show, the stresses are almost constant if $V_f \leq 33\%$.

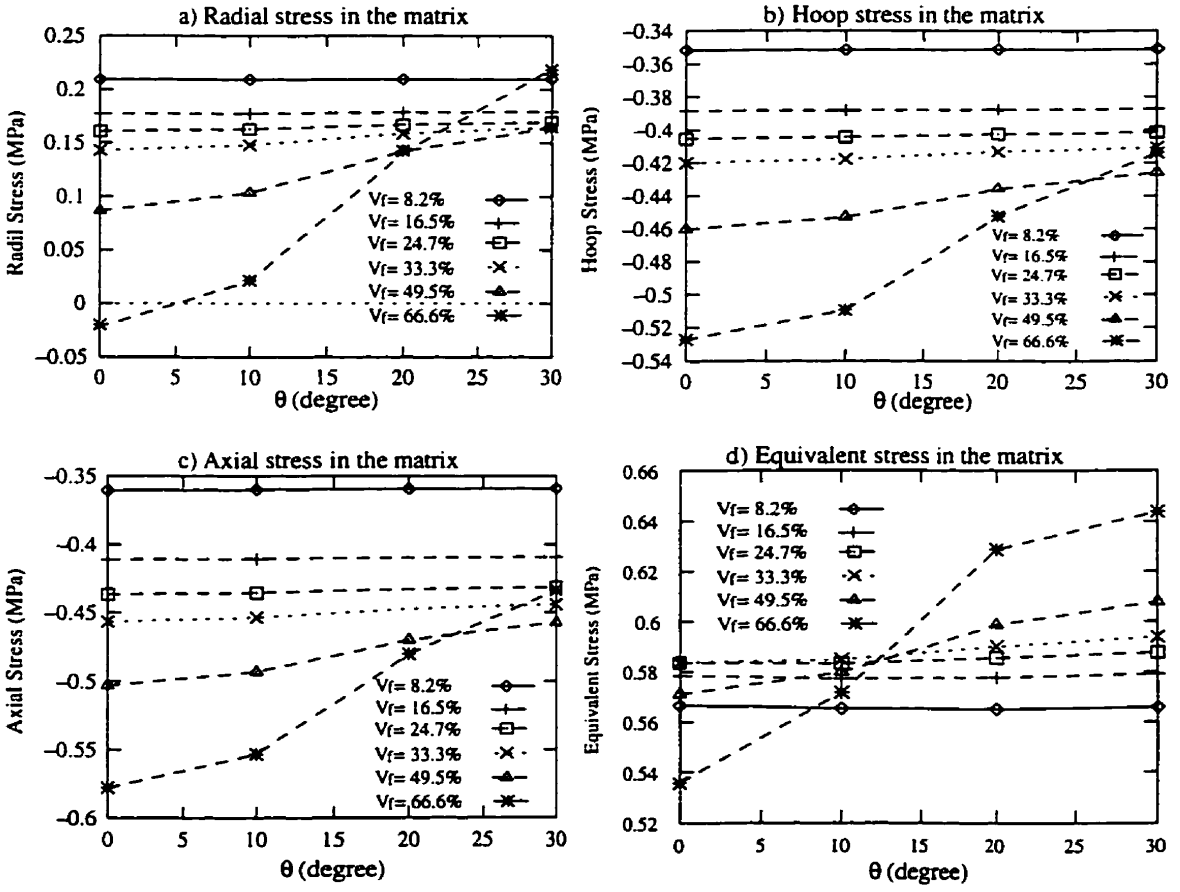

Fig. 5.5: Variation of the stress components of the matrix in the vicinity of the interface in the inner zone with V_f.

The average value of the stresses are plotted in Fig. 5.6 which are calculated from four stress values presented on each one of the stress curves (Figs. 5.5(a-c)). The average value of radial stress decreases with increasing V_f. However, the absolute average values of hoop and axial stresses increase with increasing V_f. For small V_f, the distance between the neighboring fibers is larger than the distance for a composite with high V_f. This allows for more radial deformation of the matrix at the interface. Therefore, considering free body thermal expansion of the fiber and matrix, a larger gap occurs between the fiber and matrix at the interface. To eliminate the large radial gap between the fiber and the matrix in order to satisfy the radial continuity, higher radial stresses are required. This effect is opposite for hoop and axial stresses. With decreasing V_f, the restraining axial and circumferential forces created by the fiber due to the CTE mismatch spread over a greater matrix area in both axial and hoop directions reducing the compressive axial and hoop stresses. Therefore, with increasing V_f higher absolute average interfacial axial and hoop stresses are detected in the matrix.

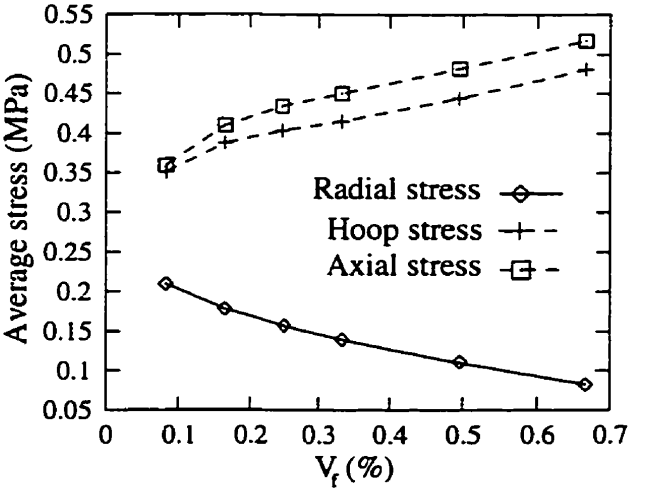

Fig. 5.6: The effect of volume fraction on the average value of the inner zone stress components in the matrix in the vicinity of the interface.

For the edge fiber, the effects of V_f on the average values of the stresses are basically the same as the effects shown for the internal fiber. However, the locations of the maximum and minimum of the stresses for different V_f are opposite of thoes discussed for the internal fiber.

A contour plot of the radial and hoop stresses in the inner zone is shown in Fig. 5.7. The characteristic elliptical pattern of the radial stress distribution was reported by Sottos et al. (1989) and also in the experimental photo-elastic study conducted by Marloff and Daniel (1969). A very similar state of the stress in the inner zone for a rectangular array of fibers was presented by Koufopoulos and Theocaris (1969) in the experimental study using photo-elastic models. This similarity indicates that the authors measured mainly the stresses in the inner zone. The stresses in the end zone (which are usually much higher and have opposite sign, but act in a relatively thin layer) did not seem to have contributed to the recorded photo-elastic effect. This might have been possible if the thickness of the photo-elastic model had been several times greater than the thickness of the end zone.

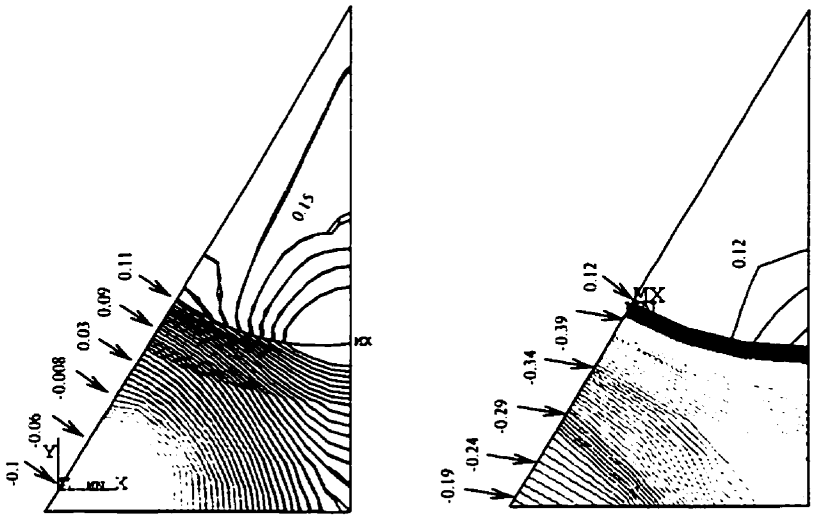

Radial stress (MPa) Hoop stress (MPa)

Fig. 5.7: The radial and hoop stress distributions in the inner zone of the 3-D prism model.

5.3 End Zone

The variations of stress components with the longitudinal distance from the free surface are presented in Fig. 5.8. The state of stress is different in the end zone than the inner zone. The graphs indicate high concentrations of radial and hoop stress components at the fiber/matrix interface near the free surface. They also show that both the radial and hoop stresses are compressive in the end zone. The axial and the longitudinal shear components are shown to decay to zero at the free surface. The stress distributions are

found to be in agreement with the work presented by Nairn (1992). How these stress concentrations are generated and why the sign of the radial stress is opposite to the inner zone stress have not been explained yet. This may be best explained by the difference in thermal expansion of the composite constituents. Considering free expansion of the composite constituents in the axial direction, the matrix expands more than the fiber due to the temperature increase and axial loads are needed to reattach them in order to satisfy the axial continuity requirements, Fig. 5.9(a). The modulus of elasticity of the matrix is much lower than that of the fiber and under the influence of the axial load should deform down and inward overlapping the fiber end. Away from the fiber end, the matrix expands more than the fiber in the radial direction, creating a gap between the two. To eliminate the overlap and the radial gap, a high compressive radial load is required at the fiber end and a tensile radial load at some distance from the end, Fig. 5.9(b).

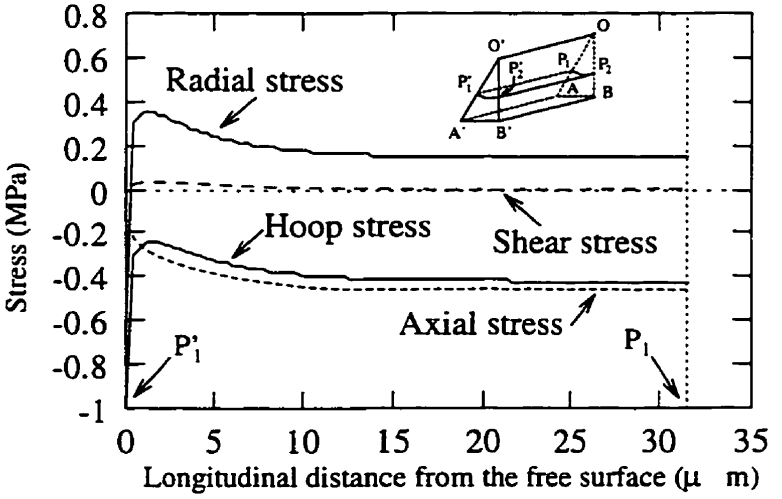

Fig. 5.8: Variation of the stress components in the matrix along the fiber length due to a 1°C temperature increase.

It is important to note that, upon cooling, the radial stress at the fiber end would be tensile and several times greater than the shear stress. The tensile radial stress pulls the fiber and the matrix apart and may contribute to debonding of the composite to a greater extent than the interfacial shear stress. The above explanation of the deformations under the thermal load is referred to as the overlapping hypothesis.

When considering the free expansion in the axial direction, only tensile hoop stress at the fiber end is expected when eliminating the overlapping. However, the stress contours show a high compressive hoop stress in this area. This could be explained by considering the deformation of a hollow cylinder under axial compressive thermal load on its inner wall. The inner rim does not deform in the circumferential direction as easily as in the radial direction due to the stronger structural support available to the material in this direction. This smaller deformation or higher strength in this direction results in a very high compressive hoop stress when the overlapping occurs. It is obvious that when the matrix overlaps the fiber end, it contracts circumferentially as well. This compressive stress is high enough so that the tensile hoop stress resulted from partial elimination of the overlapping does not affect the sign of the overall stress.

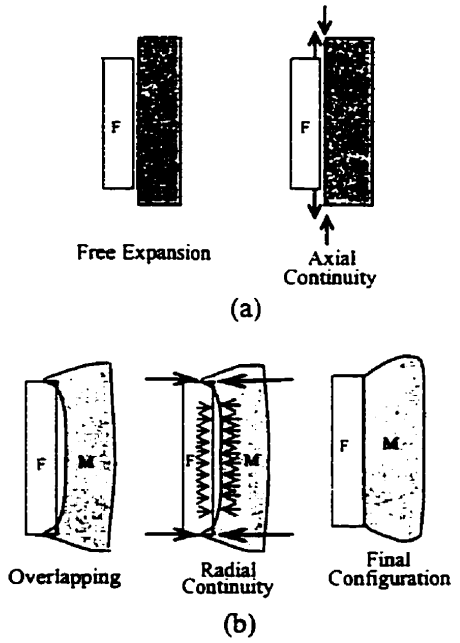

Fig. 5.9: Free body thermal expansion of the fiber and matrix (overlapping hypothesis).

To check upon the relationship of the stress concentrations and the element size, the FEM mesh was refined in the area where the maximum absolute values of the stresses occur. Using the sub-modeling technique, elements with minimum size of 1/62000 of the fiber radius were used in this area. Since the stress concentrations occur on the free surface, the radial and hoop stress distributions along lines O'A' and O'B' are presented in Fig. 5.10.

The plots show that the stresses are very low along the model edges except at the fiber/matrix interface which are almost eight times larger than those shown in Fig. 5.8. It is shown that the stresses are very sensitive to mesh sizing. Since the stress concentrations are changing rapidly with the mesh refinement, the stresses might have a singular nature and require more attention. The nature of these stress fields will be investigated in more detail in Chapter 6.

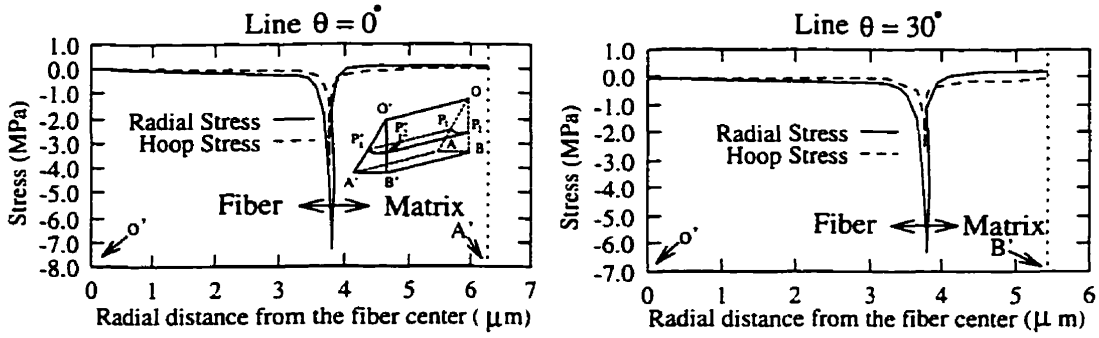

Fig. 5.10: The radial and hoop stress concentrations at the interface on the free surface at θ = 0° and at θ = 30° for a temperature increase of 1°C.

Note some differences in the stress magnitudes at those circumfrential positions around the fiber. This is due to the difference in 'local fiber volume fractions' at θ = 0° and at θ = 30° which was discussed earlier. Since the stresses are higher at θ = 0° this could be the reason for crack initiation at these locations on the free surface of composites. This kind of cracking was observed experimentally by Morris et al. ($1989_{a,b}$) and Biernacki et al. (1998). Such a phenomenon was attributed to the longitudinal interfacial shear stress in the literature by means of the shear lag theories. These one-dimensional theories, which were discussed in Appendix B, mainly ignore the radial and hoop stress components. However, the present study emphasizes the importance of these stress components in causing cracking and debonding at the fiber end. Referring to Fig. 5.9, it is important to note that, upon cooling, the radial and hoop stresses would be tensile and several times bigger than the shear stress. Therefore, the tensile radial and hoop stress components would be the most damaging factors to composite integrity. The tensile radial stresses pull the fiber and matrix apart and may substantially contribute to debonding of the composite, much more than the shear stress, while the high tensile hoop stress causes the matrix to

craze and radially crack on the free surface. The importance of radial and hoop stress components were also emphasized by Nairn (1992).

The effect of fiber volume fraction on the end zone stresses is shown in Fig. 5.11. The radial and hoop stresses are higher and more uniform for lower V_f.

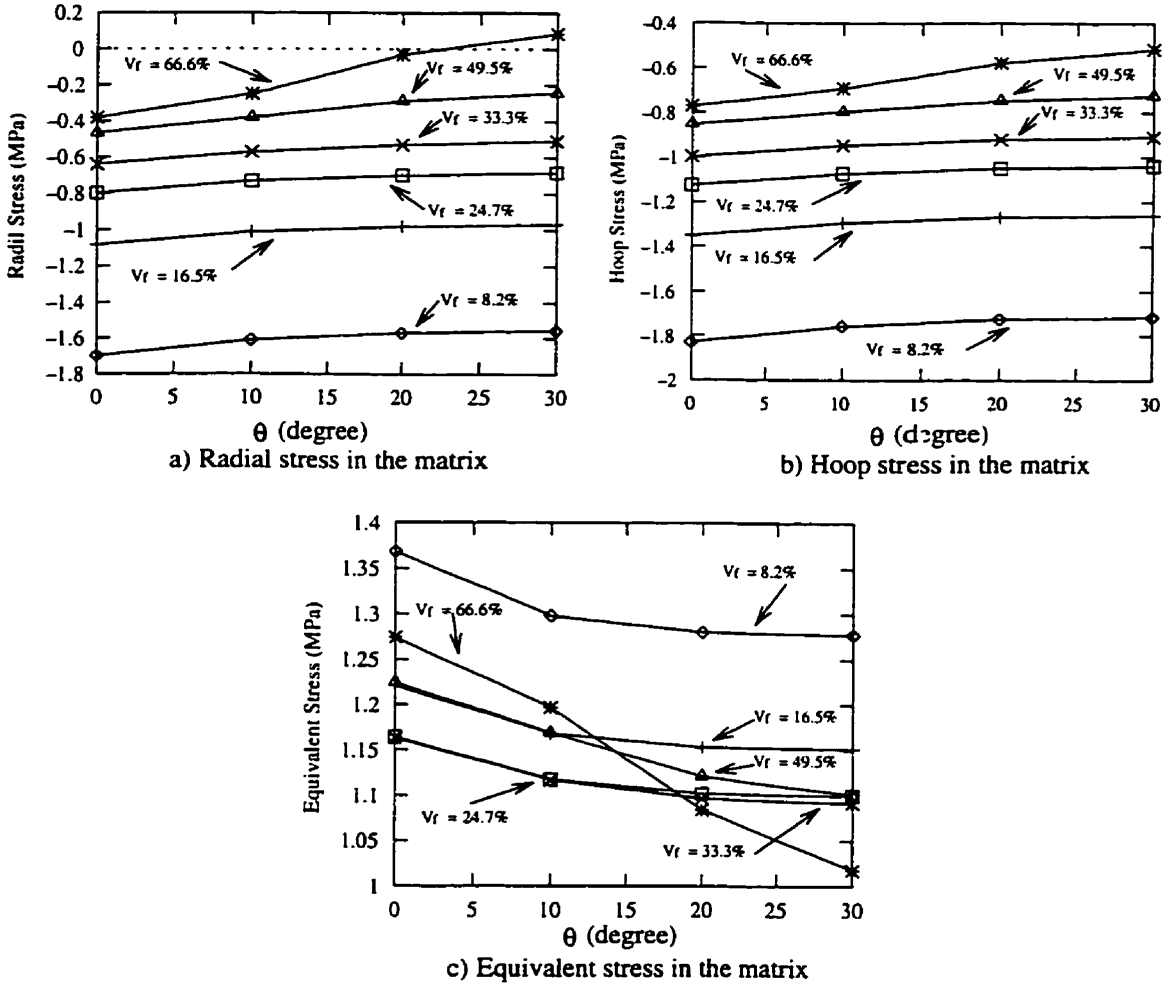

Fig. 5.11: Variation of the stress components in the matrix at the interface in the end zone with V_f.

Opposite to the inner zone, the maximum absolute value of the stresses occurs at P'_1 ($\theta = 0°$), the location with the higher inter-fiber distance. As Fig. 5.12 shows, the absolute average values of the radial and hoop stress components decrease with increasing V_f. As for the inner zone, the reduction of radial stress with the increase in V_f can be attributed to the effects of the neighboring fibers. The higher V_f means less matrix between the neighboring fibers. Therefore, the effects of the neighboring fiber on surface

ABB'A' which tries to keep this surface straight and planar is higher and this effect may account for the lower overlapping observed. Reduction of the fiber/matrix overlapping results in lower absolute values of radial and hoop stresses in the end zone.

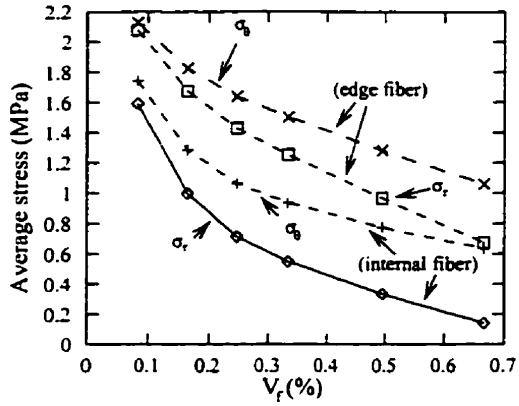

Fig. 5.12: Comparison of the average radial and hoop stress components in the matrix in the vicinity of interface in the end zone for the internal and edge fibers.

As for the inner zone (Fig. 5.2), the radial and hoop stress components in the end zone of the edge fiber are also different than those of the internal fiber. This difference appears to be only in the magnitude of the stresses here. The graphs of σ_r and σ_θ in Fig. 5.13 and also the absolute average value of the stresses presented in Fig. 5.12 indicate that the values of the stresses in the end zone for the edge-fiber are higher than that of the internal-fiber. This could be due to the higher overlapping of the fiber end by the matrix for the edge fiber relative to that of the internal fiber due to the free boundary condition of the ABB'A' surface. The difference between the deformation patterns of the two cases will be discussed in Chapter 9. For both types of fibers, the maximum absolute values of the stress components occur at P'_1 ($\theta = 0°$) due to the lower local fiber volume fraction.

The deformation pattern at the end zone of the edge fiber shows some differences with the inner zone deformations. The deformation is smaller in the end zone than the inner zone, see Fig. 5.3. This could be explained by considering the stress state of the interfacial elements in the end zone shown in Fig. 5.14. Both radial and hoop stress components in the end zone are compressive, hence, the deformation of the elements will be totally different than that for the elements in the inner zone. Also, the end zone stresses may not be influenced by the ABB'A' surface deformations as much as the inner zone stresses.

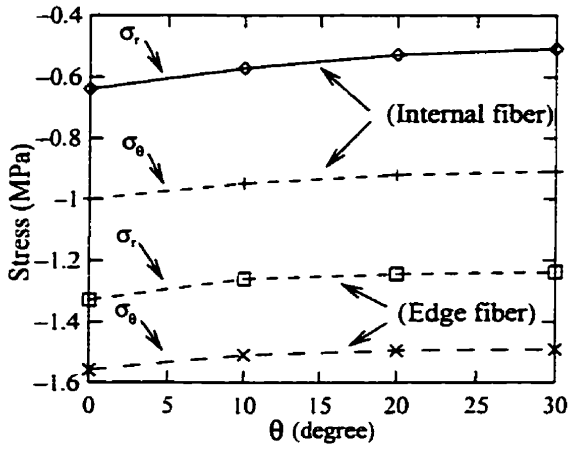

Fig. 5.13: Comparison of the radial and hoop stress components in the matrix in the vicinity of interface in the end zone for the internal and edge fibers.

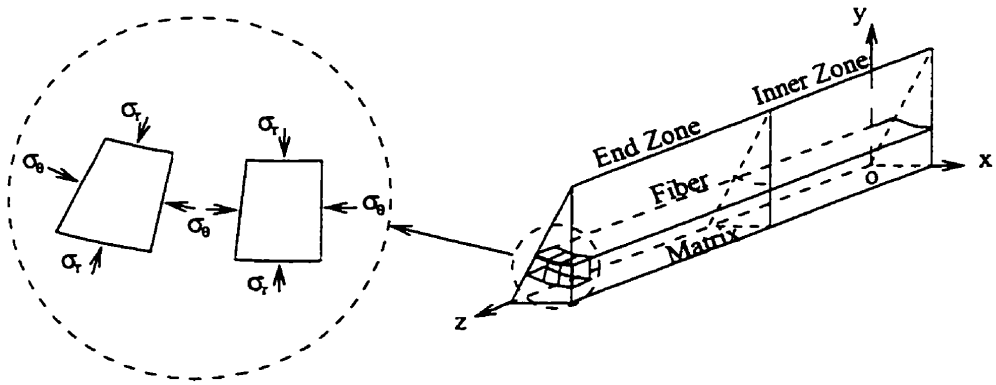

Thermal stresses at the end zone

Fig. 5.14: Thermal stress components in the matrix at the fiber end.

5.4 Temperature Induced Deformation of Unidirectional Fiber Composites

The geometrical stability of composites under a temperature change is of great concern since many are used in advanced engineering applications. Normally, due to higher CTE of the matrix than that of the fiber, the excessive expansion or contraction of the matrix may cause some problem when setting the tolerances in designing with

composites. In this section, mainly the elastic displacements of unidirectional composites due to temperature change are discussed.

A 3-D contour plot of axial displacements under 1°C temperature increase is presented in Fig. 5.15. Very high displacement occurs near the free surface with its maximum occurring at A' where the matrix has the maximum radial distance to the fiber. It has been experimentally observed that the maximum bulge out (or deep trough in case of cooling) occurs in the matrix in this area (Morris et al., 1989_a). In the end zone, for any location in the matrix, the radial distance to the fiber plays a major role in the amount of axial displacement which that location receives. However, in the inner zone, since the state of plane strain dominates, the axial displacement of the nodes in the matrix is the same and independent of their distance to the fiber.

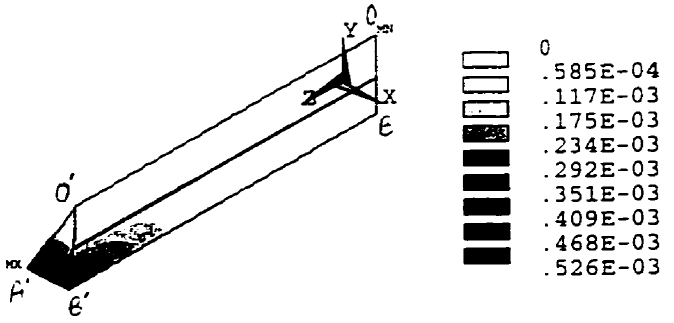

Fig. 5.15: Distribution of thermal axial displacement under 1°C temperature change.

Fig. 5.16(a) shows graphs of axial displacements along lines AA' and BB' which have different radial distances to the fiber. In the inner zone, the displacements are similar. In the vicinity of the free surface, however, the higher axial displacement along line AA' is due to the above fact that the nodes on this line have higher radial distance to the fiber. The higher distance affects the degree of axial restriction that the fiber imposes on the matrix due to its much lower CTE. Therefore, these nodes are much freer to move than the nodes on line BB'.

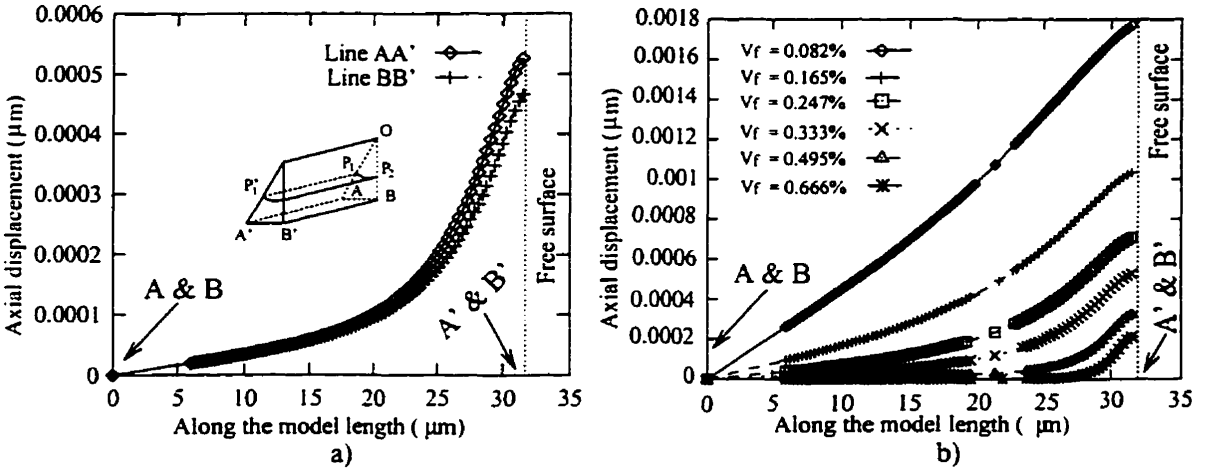

Fig. 5.16: Axial displacement in the matrix along lines AA' and BB' for various V_f.

To highlight the effect of this factor on the matrix displacements, the displacements of the nodes on line AA' for the range of V_f from 8.3% to 66.6% are shown in Fig. 5.16(b). For higher V_f, the nodes on surface ABB'A' will be closer to the fiber and as a result they will be influenced by the fiber in a higher extent. Thus, lower axial displacements occur for higher V_f. For the nodes in the matrix which are closer to the fiber, the compressive axial stress imposed by the fiber due to the CTE mismatch is higher. This is clearly shown for the nodes on lines AA' and BB' in Fig. 5.17(a). A higher compressive axial load on line BB' results in lower axial thermal expansion along this line. This is more pronounced in Fig. 5.17(b) which presents the axial stresses along line AA' for various V_f.

Comparing the graphs in Fig. 5.16(a) and the displacements for the edge fiber (see Fig. 5.18) indicates higher displacements along line AA' and BB' for the edge fiber. The higher displacements could be the result of the absence of the neighboring fiber effects for the case of an edge fiber. The lack of the restraining by the neighboring fiber permits for higher axial displacements along both lines AA' and BB'.

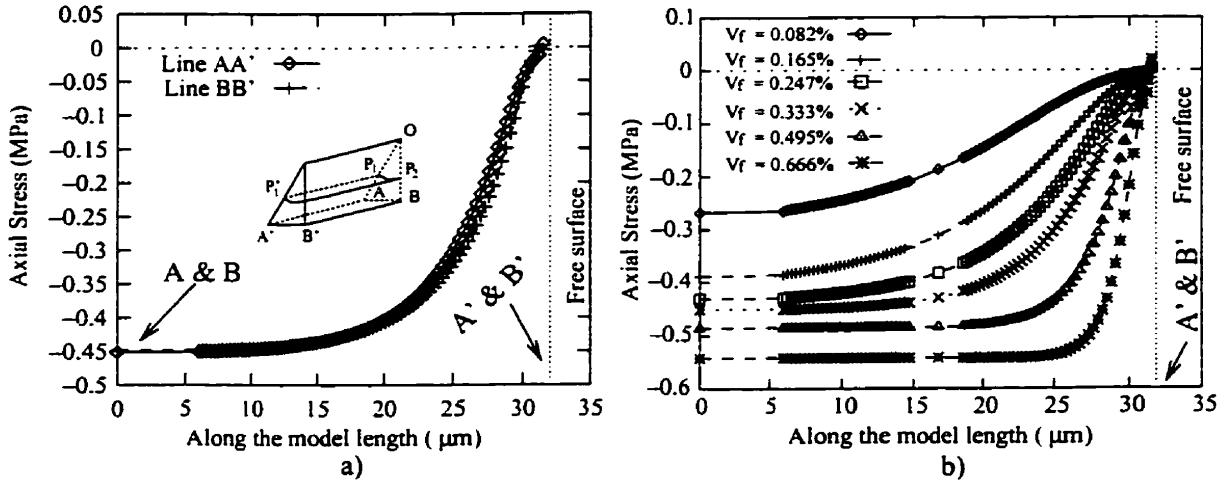

Fig. 5.17: (a) Thermal axial stress in the matrix along lines AA' and BB' and (b) thermal axial stress along line AA' for various V_f.

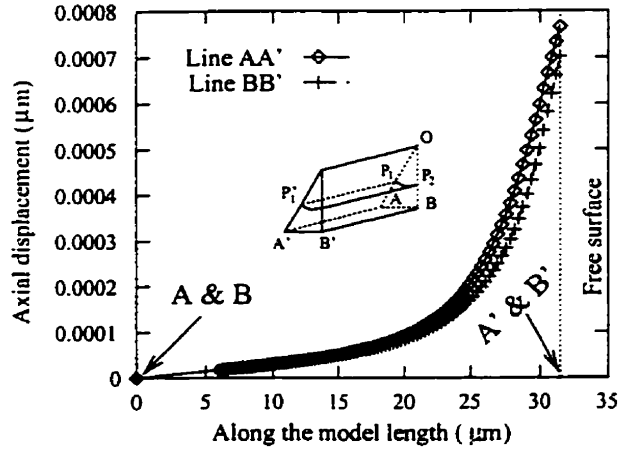

Fig. 5.18: Thermal axial displacement in the matrix along lines AA' and BB' for the edge-fiber.

Comparing the axial stress values along lines AA' and BB' in Fig. 5.17(a) with those of the edge fiber shown in Fig. 5.19 shows a high difference between the stress values along these lines. This supports the nature of the axial stress in the inner zone of the internal fiber due to the presence of the neighboring fiber (see Fig. 5.4(d)). This difference between the stress values is discussed here. In the inner zone, for the internal fiber (i.e. surface ABB'A' is restrained), Fig. 5.4(d) indicates that a compressive axial stress along line AA' and a tensile axial stress along line BB' must be added to the axial stresses purely generated by the mismatch in CTE of the fiber and the matrix (which are compressive in the matrix). However, if this boundary condition is removed (i.e. edge fiber), a big

difference between the axial stress for lines AA' and BB' is expected (see Fig. 5.19). Adding the compressive axial stress of Fig. 5.4(d) to the compressive axial stress of line AA' in Fig. 5.19 will result in a higher compressive axial stress for this line as shown in Fig. 5.17(a). In contrast, adding the tensile axial stress for line BB' (Fig. 5.4(d)) to the compressive axial stress for this line in Fig 5.19 reduces the overall value of the stress for line BB' (see Fig. 5.17(a)).

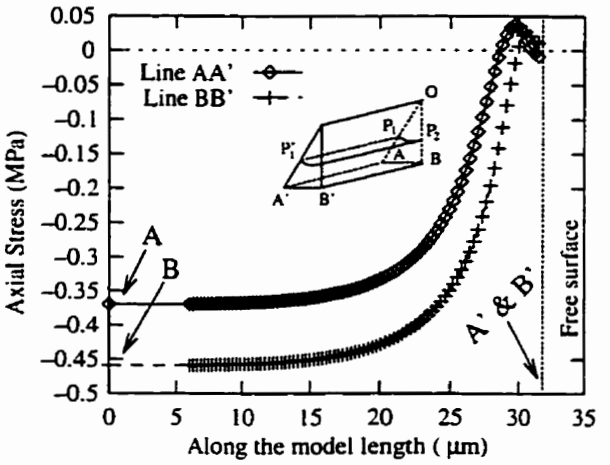

Fig. 5.19: Thermal axial stress in the matrix along lines AA' and BB' for the edge-fiber.

5.4.1 Lateral Displacements

The radial displacements of the nodes in the matrix are directly related to their distance to the interface as well. The displacement of a node increases uniformly by increasing the node distance to the interface. This is due to the fact that the restraining effect of the interface decreases when moving radially away from it. Note the circular pattern of the displacement shown in Fig. 5.20. Since, the surface AAB'A' should remain horizontal and planar, the radial displacement along the fiber length must be constant. Also, due to the same reason, the nodes on line AA' have higher radial displacements than the nodes on line BB'.

The maximum radial displacement (Fig. 5.20) is higher than the axial displacement presented in Fig. 5.15. These effects depend mainly on the CTE mismatch in axial and radial directions (which is actually higher in the axial direction for the graphite/epoxy

composite) but also may be dependent on the other physical deformations like overlapping or the imposed boundary conditions on the model. For example, for the edge fiber that does not have the restraining effects on its ABB'A' surface, the maximum of the axial displacement is higher than that of the radial displacement (see Fig. 5.21). It is also noted that for this model under the above circumstances, the radial displacement (Fig. 5.21(a)) is not constant along the fiber length and the maximum occurs in the inner zone due to the reasons discussed earlier (see Fig. 5.3).

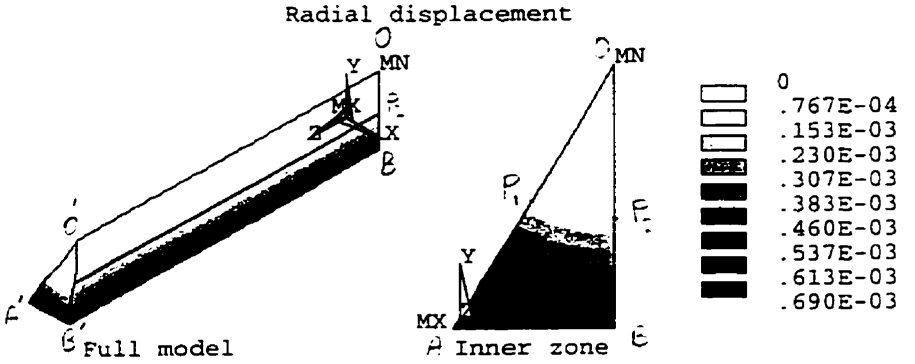

Fig. 5.20: Distribution of thermal radial displacement under (1°C) temperature change.

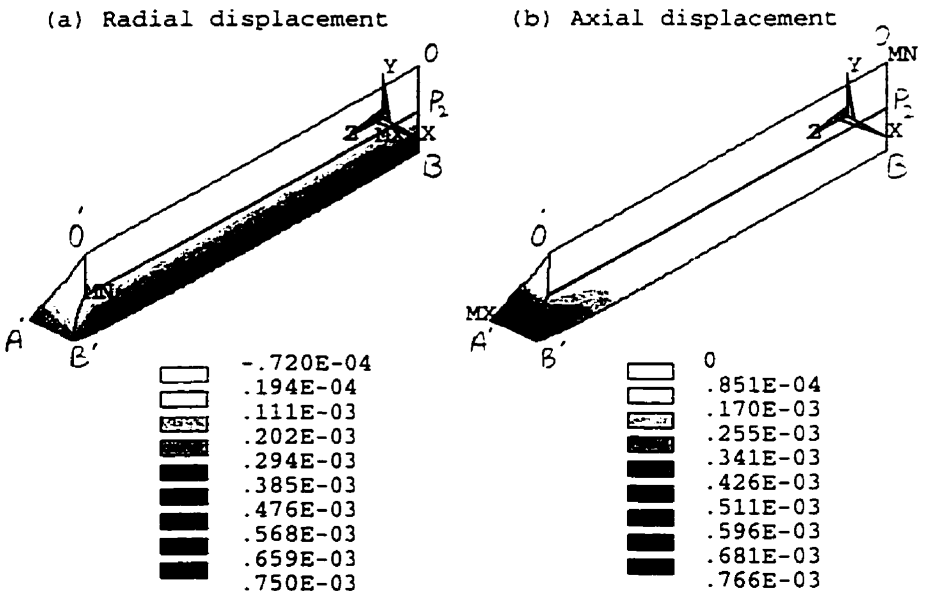

Fig. 5.21: Distribution of thermal radial and axial displacements for the edge-fiber.

A contour plot of circumferential deformation is presented in Fig. 5.22. Since OAA'O' and OBB'O' are symmetry surfaces, the nodes on these surfaces are restrained in the circumferential direction. Also, the nodes in the matrix which are closer to the fiber are effectively restrained to move circumferentially under the fiber influence. Therefore, only a small portion of the matrix close to ABB'A' surface can circumferentially expand under the temperature change. The expansion of the elements in this area compresses the adjacent elements to the OAA'O' and OBB'O' surfaces causing circumferential contraction on these surfaces. The value of the circumferential expansion is not constant along the fiber length. It is higher in the end zone than in the inner zone. This is due to the higher compressive self-equilibrated radial load in the inner zone which is generated by the imposed boundary condition on surface ABB'A'. As explained before (see Figs. 5.4) the higher compressive radial stress generates higher compressive circumferential stress in the inner zone, preventing circumferential expansion. However, the effects of these compressive forces are minimum in the end zone allowing for higher circumferential expansion in this location.

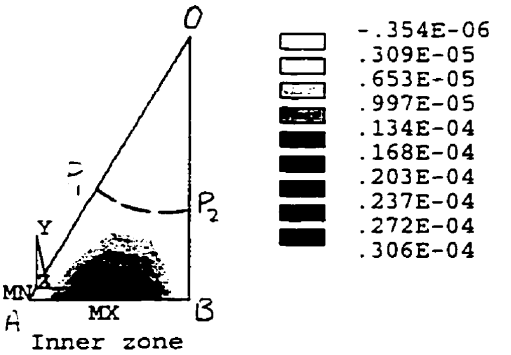

Fig. 5.22: Distribution of thermal circumferential displacement in the inner zone.

5.5 Axisymmetric Analysis of Thermal Stresses in Fiber Composites

As explained before, an axisymmetric FEM model can be selected for its numerical efficiency and a relative accuracy in comparison with the 3-D prism model. The axisymmetric model that is shown in Fig. 3.8, was exposed to 1°C temperature change.

The inner zone stresses at the interface for the 3-D and axisymmetric models are presented in Table 5. 2. The radial, hoop, and axial stresses at locations P_1 and P_2 and the average value of the stresses along the circumference of the fiber for the 3-D model are compared to the corresponding inner zone stresses at the interface of the axisymmetric model.

Table 5.2: Comparison of thermal stresses in the inner zone calculated by the 3-D and the corresponding axisymmetric models.

		Radial Stress (MPa)	Hoop Stress (MPa)	Axial Stress (MPa)
Axisymmetric Model	Location B	0.155	-0.426	-0.461
3-D Model	Location P_1	0.123	-0.437	-0.479
	Location P_2	0.173	-0.416	-0.448
	Average value	0.150	-0.421	-0.452

The inner zone stresses of the axisymmetric model presented in Table 5.2 are very close to the average value of the stresses calculated by the 3-D prism model.

The end zone stresses calculated by the axisymmetric model are also comparable with the results obtained by the 3-D model. The maximum radial and hoop stress components at the interface on the free surface (i.e. at locations P'_1 and P'_2 for the 3-D model and at location A for the axisymmetric model) are presented in Table 5.3. From similarities of the results of the two models it is concluded that, the axisymmetric model, which substantially reduces the computational time and the effort required for the mesh refinement, can also be used for stress analysis of fiber composites.

Table 5.3: Comparison of thermal stresses in the end zone calculated by the 3-D and the corresponding axisymmetric models.

		Radial Stress (MPa)	Hoop Stress (MPa)
Axisymmetric Model	Location A	-6.9	-3.5
3-D Model	Location P'_1	-7.4	-4.05
	Location P'_2	-6.2	-2.5

6. Stress Singularity

6.1 Introduction

The numerical elastic thermal stress analysis of unidirectional composites presented in Chapter 5 revealed high radial and hoop stress concentrations at the fiber end (Fig. 5.8). The stress concentrations were then shown to increase by refining the FEM mesh in this area (Fig. 5.10). Here, the relation of these stresses to the mesh size is studied more closely. The singular nature of the stresses is proven and analyzed.

As explained in Chapter 2, the singular stress field at the end of a single fiber has been and continues to be the subject of many analytical studies. This issue is still unresolved due to very complicated equations governing the behavior of composites.

In this part of the dissertation, the problem is attacked numerically. It is shown that how the regular FEM elements can be used to determine the order of singularity, which is a measure of the severity of the stress field. The dependence of the singularity on the material properties is presented. Some practical methods of reducing the severity of the singular stress field are discussed.

6.2 Stress Singularity

The analysis of the singularity is conducted here by the application of regular FEM elements. Since the order of singularity is unknown the existing singular element (of order 0.5 or 1) cannot be used. A closer look is taken at the stresses in the vicinity of the expected singular point for various sizes of the mesh. Thus, the method used in this study relies on the h-refinement where h refers to the size of an element.

6.2.1 Singularity vs. Element Size Relationship

It is important to mention that the original model had 4334 linear and quadratic brick elements which was practically the limit of the computer resources available. Therefore, the sub-modeling approach, discussed in Chapter 3, was used to refine the FEM mesh of the 3-D model. This way, only a portion of the model close to the singularity is remeshed with finer elements (see Fig. 3.6). The parameter h represents the size in the axial and radial direction of the element adjacent to point P'_2 (see Fig. 6.1).

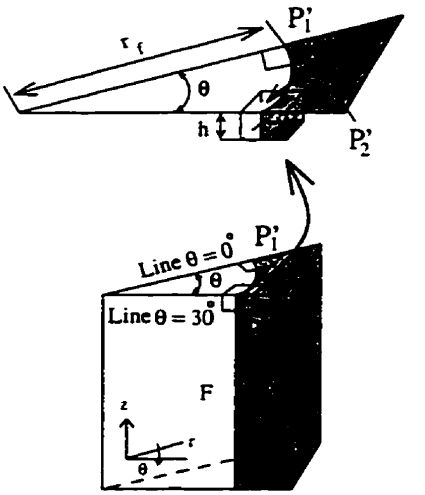

Fig. 6.1: The size of elements at the end of fiber for the 3-D prism model.

The radial and hoop stress components in the matrix at point P'_2 versus element size are shown in Fig. 6.2.

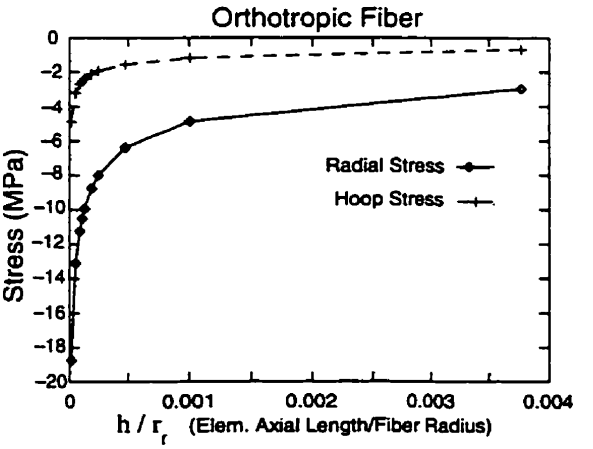

Fig. 6.2: The effect of element size on the radial and hoop stress components at the fiber end on the free surface.

It is clear that the absolute values of the stresses increase with decreasing the element size which is normalized by the fiber radius. For non-singular elements, this confirms the presence of the stress singularity at point P'_2.

The same relationship between the element size and the stress values can be approximated by a straight line if the log-log scale is used as in Fig. 6.3. In general, with the origin of the coordinate system at point P'_2 (see Fig. 6.4), the straight-line approximation on the log-log plots can be explained if the stresses in the vicinity of point P'_2 are approximated by the following relationship

$$\sigma \cong c\rho^{-\alpha} + \sum_n b_n \rho^n \tag{6.1}$$

where σ is the stress component, ρ is the distance from point P'_2, and c, b_n, α, and n are constants. As the singular point is approached ($\rho \rightarrow 0$), the singular term (the first term on the right hand side) dominates the stress value, while the second regular term comes into effect sufficiently away from P'_2.

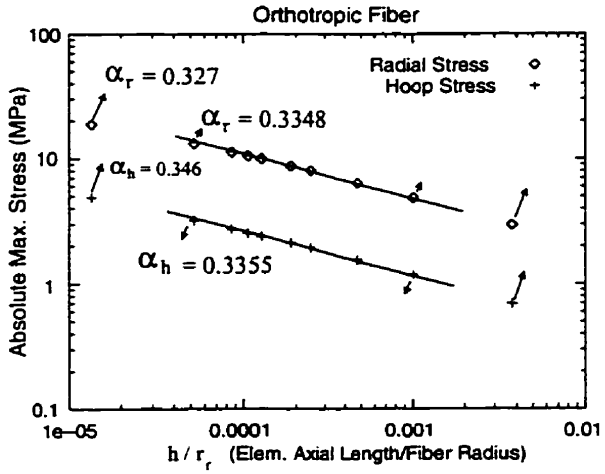

Fig. 6.3: The effect of element size on the radial and hoop stress components on a log-log scale.

In the FEM analysis, the element stresses calculated at the Gauss points are considered the most accurate. Next, these stresses are extrapolated to the nodal stresses. For isoparametric linear elements, the stresses in the plane r-Z are assumed in the form

$$\sigma(\xi,\eta) = a_1 + a_2\xi + a_3\eta + a_4\xi\eta \tag{6.2}$$

where, ξ and η are normalized coordinates and $a_1,\ldots, a_4$ are constants determined using the previously calculated values of the stress components at the four Gauss points. According to Eq. (6.2), the stresses along each face of the element ($\xi = \pm 1$ or $\eta = \pm 1$) are linear functions of the ξ or η coordinate. Since in the vicinity of P'_2, the visible side of elements (on the r-Z plane) is always rectangular, the coordinates ξ and η are proportional to the real coordinates r and Z. Thus, for a constant ξ (or r) the stress distribution in terms of η (or Z) is linear as shown in Fig. 6.5(a). The stresses at the Gauss point are assumed to be close to those represented by Eq. (6.1). In the most immediate element to the singular point, the regular term in Eq. (6.1) can be neglected and the stress (referred to as the true stress in Fig. 6.5) approximated by the singular term only. Therefore, the stress calculated at Z = 0 (the singular point) is really the true stress at some distance (ρ_{h1}) from the singular point. With decreasing element size (for example for $h_2 = h_1/2$), the Gauss points move closer to the singular point and the stress calculated at Z = 0 increases since the new distance ρ_{h2} decreases, see Fig. 6.5(b). Therefore, using an element with size h may be considered similar to calculating the singular stress field at some distance ρ_h. It can easily be shown (Szyszkowski and King, 1995) that ρ_h is proportional to h, that is

$$\rho_h = c_1 h \tag{6.3}$$

where the value of c_1 depends on the type of element used.

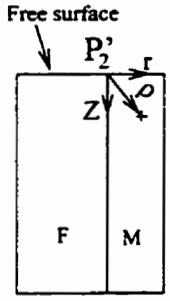

Fig. 6.4: Polar coordinate system located at the singular point.

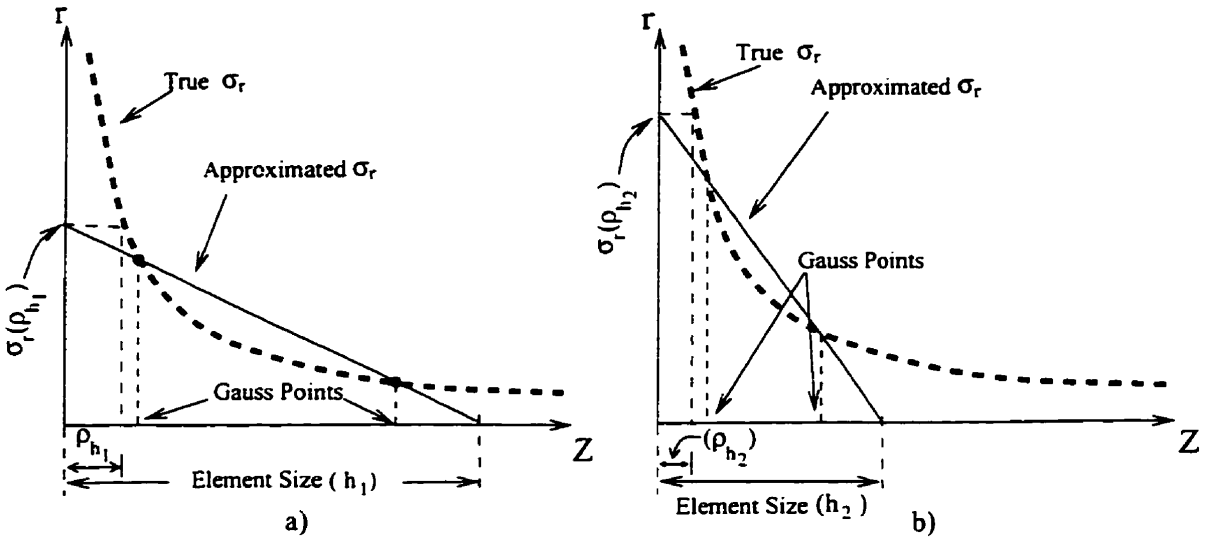

Fig. 6.5: FEM approximation of the radial stress in the vicinity of the free surface.

6.2.2 Order of Singularity

Using only the singular term in Eq. (6.1), this equation can be written in logarithmic form as

$$\log\sigma = -\alpha\log\rho_h + \log c \tag{6.4a}$$

or

$$\log\sigma = -\alpha\log h + \log c_2 \tag{6.4b}$$

where $c_2 = cc_1$. Clearly, on a log-log scale, Eq. (6.4b) represents a straight line with slope α. The FEM calculations presented in Fig. 6.3 can be approximated very closely by straight lines. Thus, Eq. (6.1) applies to this case. Consequently, the slopes of the lines in Fig. 6.3 could be interpreted as the orders of singularity for the radial and hoop stress components, respectively. The least square approximation procedure was applied to evaluate α using all ten different element sizes indicated in Fig. 6.3. It was found that $\alpha_r = 0.327$ for the radial stress and $\alpha_h = 0.346$ for the hoop stress. However, if the first point (for $h/r_f = 1/62000$) and the last point (for $h/r_f = 1/260$) are excluded, then the remaining eight points coincide much closer with the new lines characterized by $\alpha_r = 0.3348$ and $\alpha_h = 0.3355$, respectively. Therefore, the order of radial and hoop stress singularities

calculated by excluding the data for the nearest and the farthest points to the singular point are considered to be more accurate. A similar observation was made by Staab (1983) where a singularity around a crack tip was analyzed. In that study, it was concluded that exclusion of the nearest and farthest points from the crack tip improves the accuracy of the calculations of the order of singularity (the order for the crack in (Staab, 1983) was to be 0.5). The first point, which is nearest to the singularity, could be affected by the excessive calculations required and possible numerical round up errors. The last point may be influenced by the non-singular term of the stress in Eq. (6.1).

Similar values of the order of singularities were found using axisymmetric models. For axisymmetric models square elements were used in the vicinity of the singularity in both the fiber and the matrix (see Fig. 6.6). In this way the singular point is approached equally from the two directions r and Z. Again, excluding the first point and the last point in Fig. 6.7, the following values for α were obtained: $\alpha_r = 0.3339$ and $\alpha_h = 0.3350$.

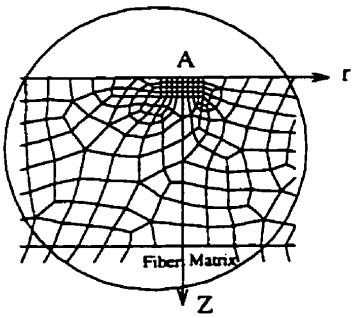

Fig. 6.6: FEM mesh of the axisymmetric model.

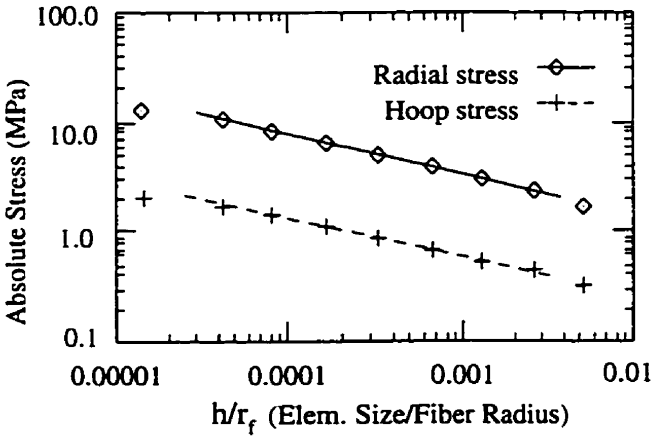

Fig. 6.7: The effect of element size on the radial and hoop stress components calculated using axisymmetric modeling.

6.2.3 Effects of Materials on the Order of Singularity

As discussed in Chapter 2, the singular stress field for two edge-bonded dissimilar materials is dependent on the properties of the materials and the materials angles at the contact corner. Here, the effects of the fiber and the matrix properties on the order of singularity are studied. A detailed discussion of the effects of the free surface geometry of composites on the singular stress field will be presented in Chapter 9.

Since the results obtained with the help of the prism and axisymmetric models are very close, in order to reduce the numerical effort, only the axisymmetric model was used to study the effects of the material properties on the order of singularity.

6.2.4 Effects of Composite Constituent Properties on the Order of Singularity

It is expected, (Li and Folias, 1991), that the physical properties of the fiber and the matrix should affect the order of singularity in unidirectional composites in a similar manner as with edge-bonded dissimilar materials (Hein and Erdogan (1971), Gdoutos and Theocaris (1975), and Dondurs and Lee (1972)). For example, assuming the fiber in Table 5.1 to be isotropic with;

$$E_l^f = E_t^f = 214 \text{ (GPa)};\ \upsilon_{lt}^f = \upsilon_{tl}^f = 0.2;\ CTE_l = CTE_t = -0.99\times10^{-6}/°C \qquad (6.5)$$

the results shown in Fig. 6.8 were obtained. Excluding the first and last points on the plot, the orders of singularity for the radial and hoop stresses are $\alpha_r = 0.363$ and $\alpha_h = 0.271$, respectively. In comparison with the results for the orthotropic fibers (Figs. 6.3 and 6.7), the singularity order increased for the radial stress but decreased for the hoop stress. In this case, the order of singularity for the radial stress is about 34% larger than the order of singularity for the hoop stress. Similar results have been obtained by Szyszkowski and King (1995) where isotropic fibers were analyzed. It should be noted that in fracture mechanics or in the analytical solution presented in (Li and Folias, 1991), identical orders of singularity were considered for all the stress components. Clearly, the order of singularity depends on the material properties and is different for different stress components. To investigate this dependence the calculations were repeated for a wide range of some material parameters.

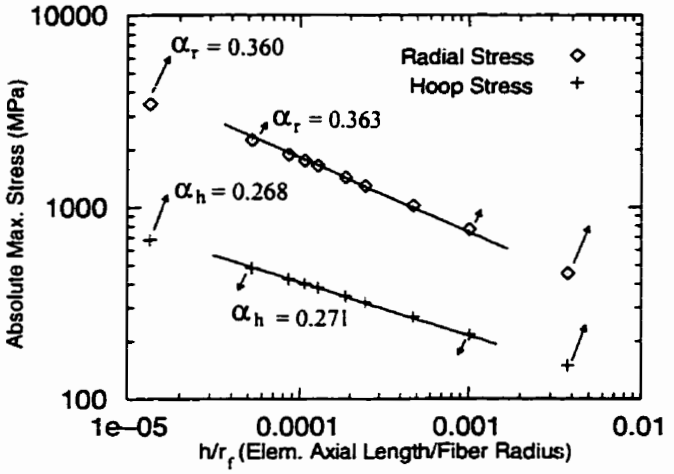

Fig. 6.8: The effect of element size on the stress components for a composite with isotropic fibers.

First, the calculations were performed for the IMLS epoxy matrix and the fibers defined by Eq. (6.5). The transverse modulus E_t^f, however, was varied from 13.7 GPa to 418 GPa. Fig. 6.9 shows the results obtained. The values of E_t^f on the horizontal axis were normalized by the longitudinal modulus E_l^f = 214 GPa. As can be seen, E_t^f has opposite effects on the order of singularity for radial and hoop stresses. By increasing E_t^f, the order of singularity for the radial stress increases, while it decreases for the hoop stress. When E_t^f decreases, the orders for both stress components become closer to one another. Note that, according to Table 5.1, since the matrix modulus (E^m) is smaller than E_t^f, increasing E_t^f will result in increasing the mismatch in E_t of the composite constituents.

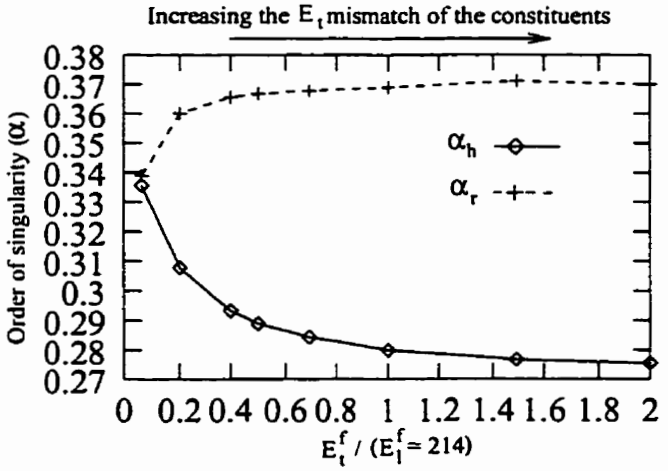

Fig. 6.9: The effect of the transverse modulus of the fiber on the order of singularity.

The effects of Poisson's ratio on the order of singularity are indicated in Fig. 6.10. These results were obtained assuming the properties given by Eq. (6.5), but changing υ_{tl}^f of the fiber gradually from 0.14 to 0.3. As can be seen, the order of singularity for the radial stress remains unaffected, but it increases with υ_{tl}^f for the hoop stress. The values of υ_{tl}^f on this plot are normalized by $\upsilon_{tt}^f = 0.2$.

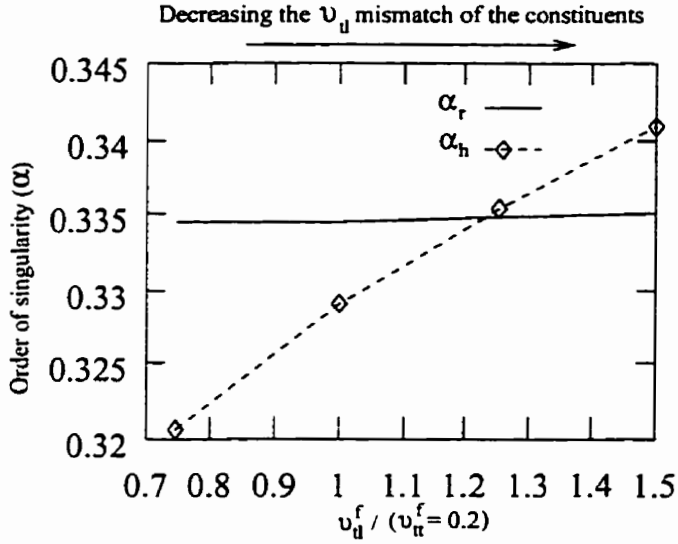

Fig. 6.10: The effect of the transverse Poisson's ratio of the fiber on the order of singularity.

The effect of CTE_t^f was examined assuming the properties in Eq. (6.5) and varying this parameter from $0.2\,CTE_t^f$ to $6\,CTE_t^f$ (where CTE_t^f = -0.99×10^{-6}/°C). The results are shown in Fig. 6.11. The graphs indicate that, the orders of singularity are insensitive to the changes in CTE_t^f.

Considering the results in Figs. 6.9 to 6.11, the lower α_h for the isotropic fiber than for the orthotropic fiber (compare Figs. 6.8 and 6.7) seems to be mostly due to the change in mismatch of the transversal modulus (E_t^f) for the constituents. Among the effects of three transversal properties discussed so far, it is only the E_t^f mismatch which effectively decreases α_h. The change in E_t^f may also be the main factor in increasing α_r for the

isotropic fiber compared to that of the orthotropic fiber since α_r is insensitive to the changes in both ν_a and CTE_t (see Figs. 6.10 and 6.11).

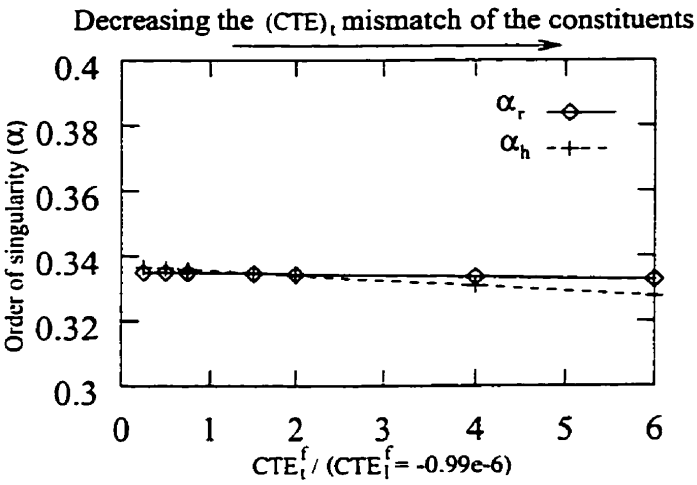

Fig. 6.11: The effect of the transverse CTE of the fiber on the order of singularity.

A similar study was also conducted to determine the effect of the longitudinal properties of the fiber such as E_l^f, υ_{la}^f, and CTE_l^f. The results are shown in Fig. 6.12. The nominal values used in the normalization were taken from Eq. (6.5). As can be seen, α_h is sensitive to the variation of E_l^f and υ_{la}^f. As for the variation of CTE_t^f both α_h and α_r remain unaffected.

The influence of the matrix properties on the orders of singularity was also analyzed. According to Table 5.1, the variation in longitudinal or transversal properties of the fiber changes the longitudinal or transversal mismatches in the constituents properties solely. However, for isotropic matrices, any change in the matrix properties, affects both the longitudinal and the transversal mismatch in properties of the composite constituents simultaneously. The effects of the matrix properties on the orders of singularity are presented in Fig. 6.13. The nominal values of the parameters for the IMLS matrix were taken from Table 5.1. As can be seen, α_r and α_h increases as E_m decreases or ν_m increases. Variation of the CTE_m seems to have negligible effects.

In addition to the above, the AS graphite fibers were matched with three types of matrices specified in Table 5.1. Note that these matrices have different CTE's. Fig. 6.14 shows the log-log plot of the stresses vs. mesh size for these matrices. The parallel lines obtained indicate that CTE_m does not affect the singularity, which is consistent with the results shown in Fig. 6.13.

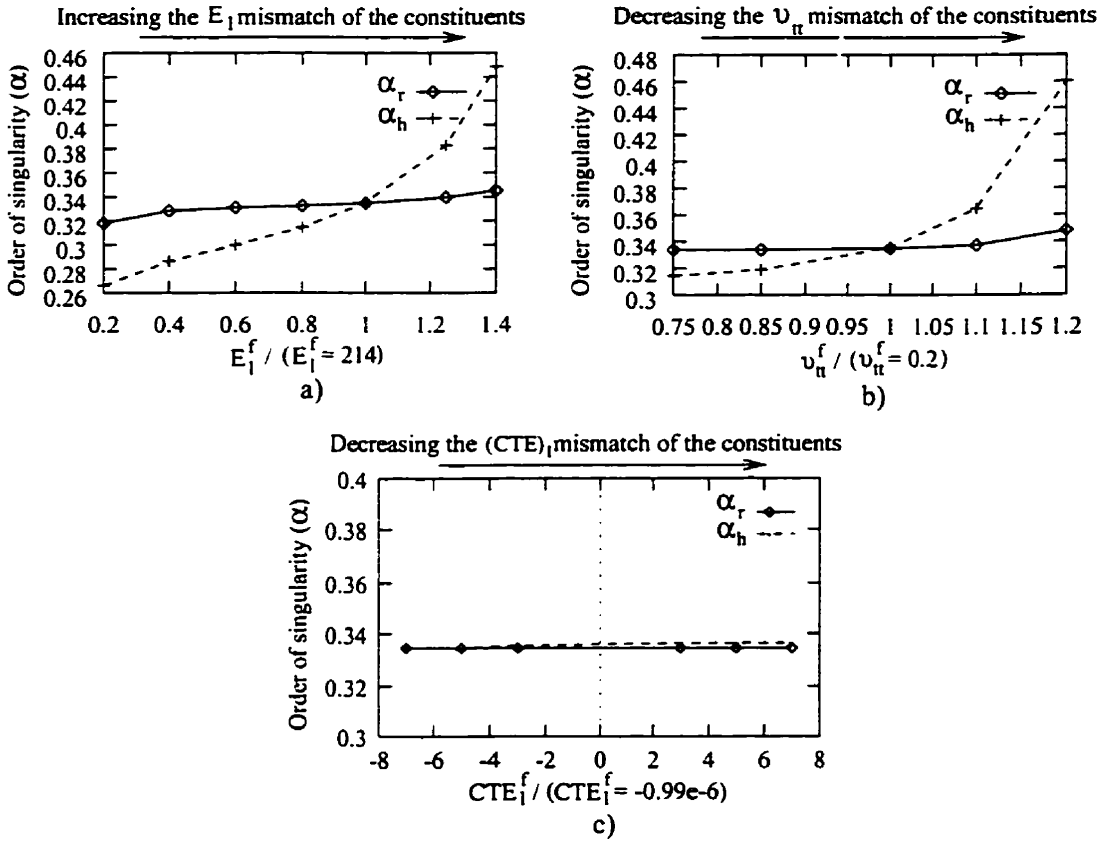

Fig. 6.12: The effect of the variation in longitudinal properties of the fiber on the order of singularity.

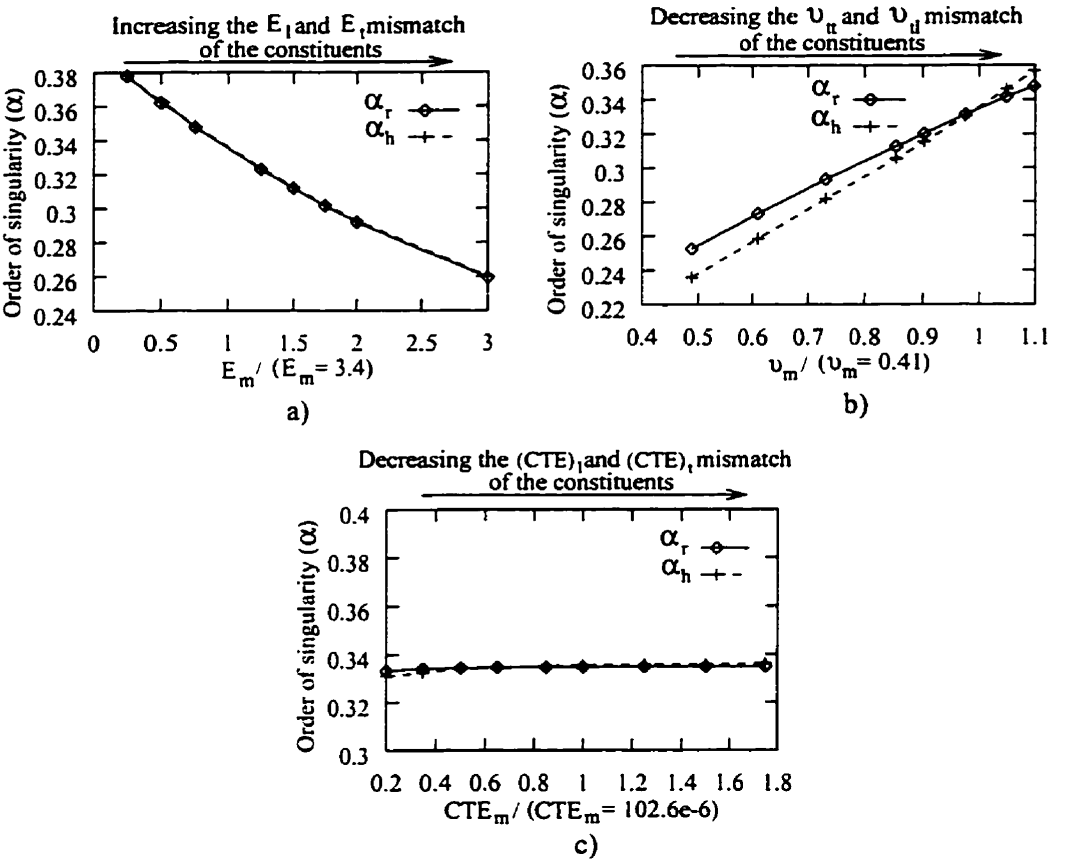

Fig. 6.13: The effect of the variation in properties of the matrix on the order of singularity.

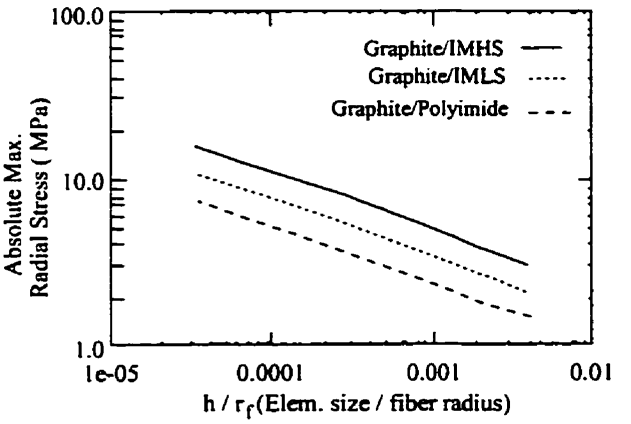

Fig. 6.14: The order of singularity for radial stress for composites with different matrix materials (the matrices are different only in their CTEs).

In general, reducing the mismatch in mechanical properties (E and υ) of the constituents may be helpful in containing the singularity. It is worthy to note that, although the thermal stresses are generated by the mismatch in CTE of the constituents, apparently this material property does not influence the order of singularity. In conclusion, since the order of singularity is found to be around 1/3, to interpret and to analytically relate this finding to the fracture mechanics is very challenging. It is considered to be beyond the scope of this project.

7. Elasto-Plastic Analysis of Unidirectional Fiber Composites

7.1 Introduction

The stress fields in unidirectional fiber composites discussed in Chapters 5 and 6 were obtained under the assumption of elastic fiber and matrix behavior. In this chapter, plastic deformations are included in the analysis of the stress and deformation states developed in the composite when it is cooled from the processing temperature (T_p) and during the service temperature (cycling temperature (T_c)). The creep effects will be considered in the next chapter.

Two composites, SCS-6/Ti-6Al-4V and SCS-6/Ti-24Al-11Nb, known for the high and low yield strength of their matrices, respectively, are used for the numerical analysis. The results provide a qualitative perspective on the effects of plastic strain on the stress and deformation states in such composites. The silicon carbide fiber (SCS-6) remains elastic and its properties with temperature are almost constant. The properties of the two matrices (Ti-6Al-4V and Ti-24Al-11Nb), which will be referred to as MMC (metal matrix composite) and IMC (inter-metallic matrix composite), are presented in Tables 7.1 and 7.2, respectively. The properties of the matrices are highly temperature dependent. At around T=370°C the yield strength of the MMC matrix remains constant for a small temperature range (see Table 7.1). The Prandtl-Reuss associated flow rule with the von Mises equivalent stress as the yield criterion are employed. Also, the isotropic hardening rule is adopted into the model. For comparison, the kinematic hardening analysis of the MMC is also performed. The material properties presented in the aforementioned tables are used with bilinear stress-strain characteristics defined for several specific temperature levels. The stress-strain characteristics are linearly interpolated between these levels.

Table 7.1: Properties of the Ti-6Al-4V (MMC) matrix at different temperatures (Nimmer et al., 1991).

Ti-6Al-4V (MMC)					
Temperature °C	E_e (GPa)	υ	σ_y (MPa)	E_p (GPa)	CTE×10^{-6}/°C (secant)
21	113.7	0.3	900	4.6	9.44
149	107.5	0.3	730	4.7	9.62
315	97.9	0.3	517	5.4	9.78
482	81.3	0.3	482	4.8	9.83
649	49.6	0.3	303	1.7	9.72
900	20.7	0.3	35	1.2	9.81

Table 7.2: Properties of the Ti-24Al-11Nb (IMC) matrix at different temperatures (Chandra et al., 1994).

Ti-24Al-11Nb (IMC)					
Temperature °C	E_e (GPa)	υ	σ_y (MPa)	E_p (GPa)	CTE×10^{-6}/°C (secant)
21	111	0.22	385	23	9
149	103.5	0.22	385	3	9.31
315	90	0.22	385	2.6	9.78
420	75.3	0.22	385	2.3	10.32
649	68	0.22	260	0.7	10.65
825	43	0.22	170	0.1	11.1

The SCS-6 fiber properties are $\nu = 0.33$, $E = 413.7$ GPa, CTE (secant) = 4.86e-06/°C.

For simulating the geometry, both the 3-D prism and the axisymmetric models are utilized. For clarity, the intersection of the fiber/matrix interface with the free surface will still be referred to as the singular point. This is in spite of the fact that the stresses are limited to within the yield surface in inelastic analysis. To determine the effects of the elasto-plastic behavior of the matrix on the stress and strain states, a series of mesh refinements in this region (close to the singular point) is implemented only for the axisymmetric model. The results of the two models are compared and it is shown that the results of the 3-D model are valid despite its coarser mesh near the singular point.

7.2 Residual Stresses in Unidirectional SCS-6/Ti-6Al-4V Composite

The MMC composite solidifies at about 900°C. Then the composite is cooled to room temperature (Fig. 7.1). The rate of cooling is assumed to be slow enough to neglect the temperature gradient effects. As explained in Chapter 5, thermal stresses are essentially induced by the mismatch in thermal expansion coefficients of the composite constituents. It is assumed that the fiber remains elastic during the whole process, and only the stress distribution in the matrix is presented.

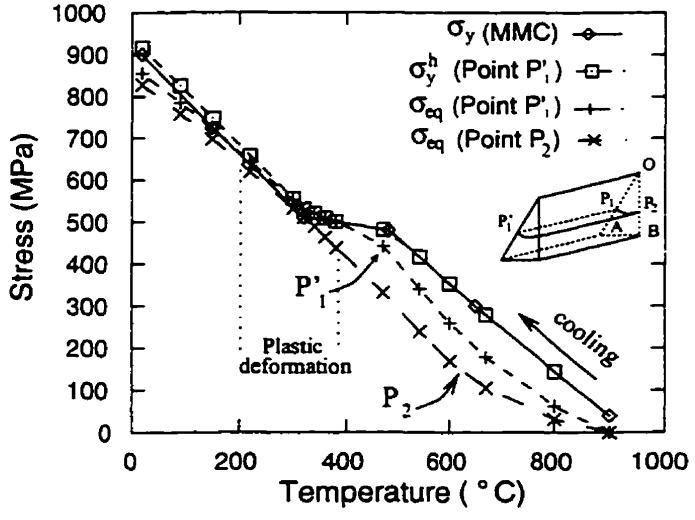

Fig. 7.1: Stress history for Ti-6Al-4V matrix in the end zone (P'_1) and the inner zone (P_2).

The equivalent stress, $\sigma_{eq} = \left(\frac{3}{2} S^T S\right)^{\frac{1}{2}}$, refers to the von Mises stress. In the end zone, the maximum stress occurs at location P'_1. However, in the inner zone, the maximum σ_{eq} appears at P_2. The stresses are much higher in the end zone and it is expected that plasticity will be first initiated in this zone.

Fig. 7.1 shows how the original yield strength of the matrix (σ_y) and the yield strength of the strain hardened matrix (σ_y^h) at P'_1 and P_2 vary with temperature, from $T_p = 900°C$ to $T_r = 20°C$.

When cooling from 900°C to 360°C, the process remains elastic because $\sigma_{eq} < \sigma_y$. The thermal stresses are high enough to cause yielding only in the temperature range of 360-320°C as indicated by the overlapping of the curves σ_{eq} and σ_y^h. In the temperature range between 320°C and 20°C, the increment in σ_{eq} falls behind the increment of the yield strength and plasticity is terminated. This was explained in Chapter 3. The process remains elastic until room temperature is reached. Contour plots of the radial, hoop, and equivalent stresses at 370°C are shown in Figs. 7.2(a) to 7.2(c), respectively.

Fig. 7.3 displays a distribution of the equivalent plastic strain, $\varepsilon_{eq}^{pl} = \left(\frac{3}{2} \varepsilon_{pl}^T \varepsilon_{pl}\right)^{\frac{1}{2}}$, in the matrix at various temperatures. Since plasticity occurs in a narrow temperature range, the magnitude of the plastic strain is small. The plastic region that starts at 360°C in the end zone (Fig. 7.3(a)) spreads into the inner zone at about T=320°C. Fig. 7.3(b) shows the equivalent plastic strain on the surface OAB (the inner zone) at 320°C. As can be seen, the plastic deformation is present only in a narrow layer at the interface. However, unlike in the end zone, the plastic strain in the inner zone appears first at location P_2 where the fiber has the least distance to the neighboring fibers. Fig. 7.4 shows that in the inner zone the minimum compressive value of radial stress also occurs at location P_2, contributing the most to the calculated σ_{eq} in the region.

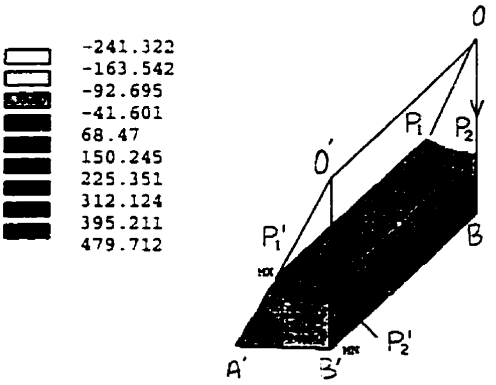

Radial stress (MPa)

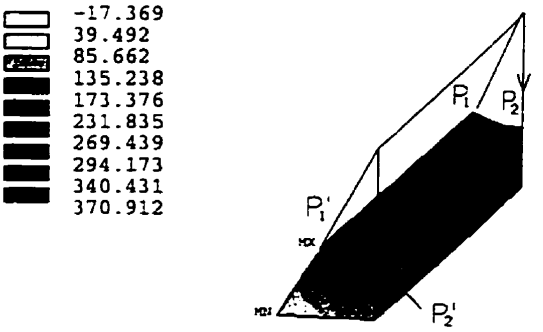

Hoop stress (MPa)

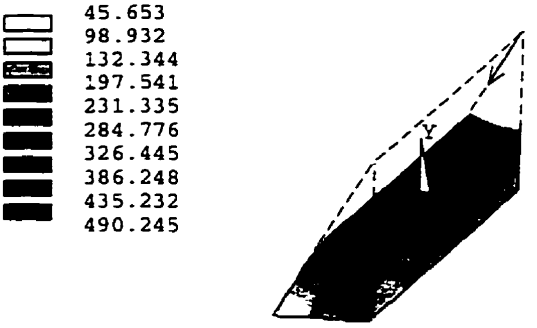

Equivalent stress (MPa)

Fig. 7.2: Distribution of stress components in the matrix at T = 370°C.

The reason why the minimum radial stress occurs at P_2 was described in Chapter 5. However, the problem was explained for heating. In cooling, the deformations would be opposite since the sign of the thermal stresses are reversed. The hoop stresses, (see Fig. 7.4(b)) are almost the same along the interface, although the maximum still occurs at location P_1. The axial stresses are relatively uniform due to the absence of shear stress (σ_{rz}) in this zone. Therefore, in the inner zone, the only factor, which may cause plastic deformation to start at location P_2 (instead of P_1), is the relocation of the maximum absolute value of the interfacial radial stress from P_1 to P_2.

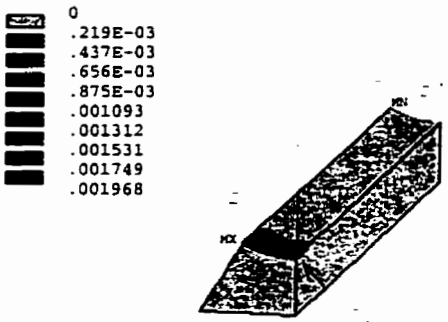

a) Start of plastic strain in the end zone at T=360° C. (The whole model)

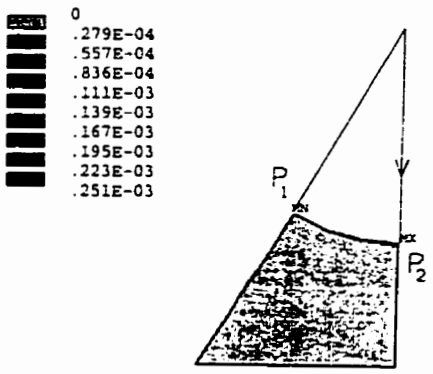

b) Start of plastic strain in the inner zone at T=320° C.

Fig. 7.3: Equivalent plastic strain in Ti-6Al-4V matrix.

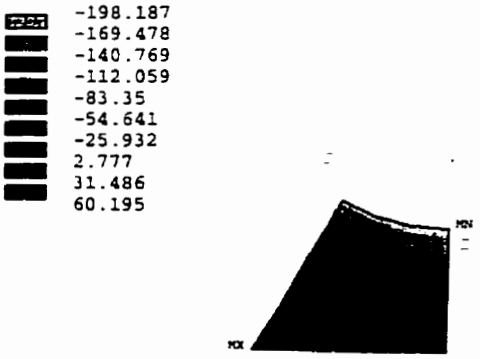

Radial stress (MPa)

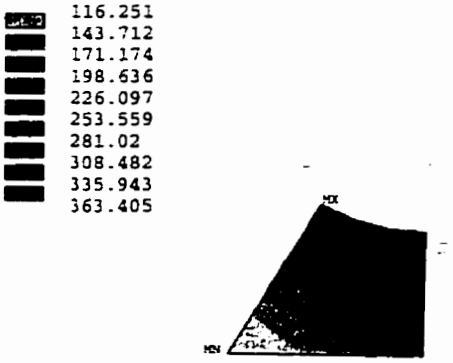

Hoop stress (MPa)

Fig. 7.4: Stress distribution in the inner zone for Ti-6Al-4V matrix at T = 320°C.

As Fig. 7.3(b) shows, only a limited amount of plastic deformation occurs in the inner zone. According to Fig. 7.1, plasticity occurs only in a small temperature range. This range is very narrow. Therefore, ε_{eq}^{pl} in the inner zone at 320°C (see Fig. 7.3(b)) and at room temperature (see Fig. 7.5(c)), are very similar. This suggests that when the temperature drops below 320°C no further plastic strain is generated. This is due to the nature of the material bilinear stress-strain curves as explained earlier. Comparing the stress distributions at room temperature (see Figs. 7.5(a) and (b)) with the stresses at 320°C (Fig. 7.4), it can be observed that, due to limited amount of plastic deformation, the location of the maximum absolute values of the stress components in the inner zone

remains unchanged. This is also true for the stresses in the end zone. This indicates that relaxation effect, which is inherent in plastic flow, is negligible due to the small plastic strains. From the stress distribution perspective, due to the small plastic deformation, the residual stresses in the matrix remain high and increase toward the interface. This could be very damaging to the composite, particularly to the fiber/matrix interface. This limited amount of plastic deformation has been observed experimentally by Kupperman et al. (1992) using the neutron diffraction technique and, also, determined numerically by Nimmer et al. (1991) and Rangaswamy and Jayaraman (1994). It should be mentioned that the CTE values used in these studies for the matrix were different than the ones used here. Various properties for the MMC matrix are reported in the literature. For example, the CTE values for the MMC matrix reported by Nimmer et al. (1991) are much higher than the values used in the present study. Clearly, higher mismatch in CTE of the fiber and matrix generates much higher thermal stresses. The 2-D inelastic analyses (Chandra et al. (1994) and Nimmer et al. (1991)) for rectangular fiber pattern of SCS-6/Ti-6Al-4V, with material properties similar to those used in the present study, have not indicated any plastic deformation in the interior of the composite.

The whole cooling process of the MMC composite was reanalyzed using the kinematic hardening rule. Very similar results were obtained. Specifically, the plastic process started at similar temperatures in both the end and inner zones and the amount of plastic deformation was found to be very close in both zones.

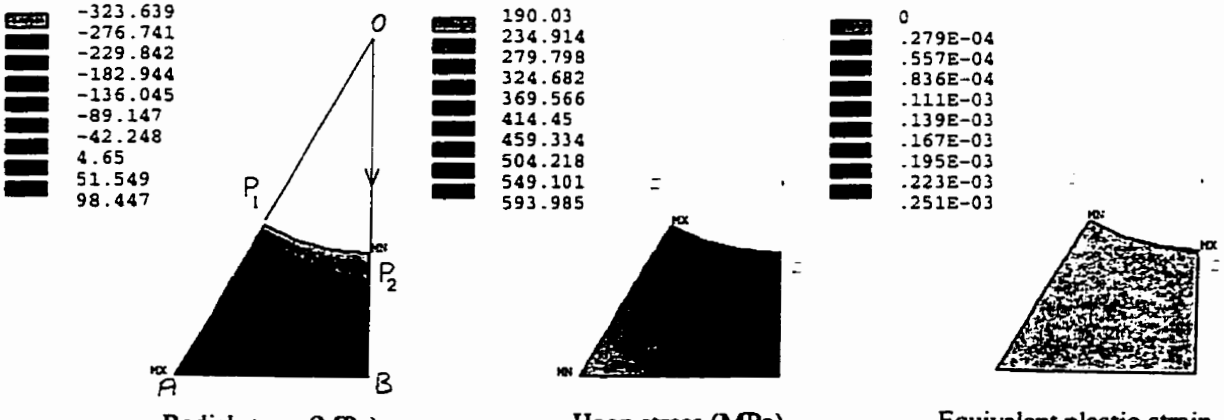

Radial stress (MPa) Hoop stress (MPa) Equivalent plastic strain

Fig. 7.5: Stress and plastic strain distribution in the inner zone for Ti-6Al-4V matrix at room temperature.

7.3 Response of SCS-6/Ti-6Al-4V Composite (MMC) to Temperature Cycling

Cooling the SCS-6/Ti-6Al-4V composite from the processing temperature (T_p) generates very high residual stresses at room temperature as shown in Fig. 7.5. It is of importance to determine the effects of these high residual stresses during temperature cycling. In this section, consideration is given to a composite that has already been cooled to room temperature and is subsequently thermally cycled using three different temperature patterns. The patterns (see Fig. 7.6), differ in their maximum temperatures only. The behavior of the matrix during the temperature cycles mentioned appears to be similar (the reason will be explained later). Therefore, only the results of the cycle with a maximum temperature of 900°C are discussed in detail.

As Fig. 7.1 shows, upon cooling the MMC composite from T_p to room temperature, a limited amount of plastic deformation occurs in both the inner and end zones but only within a narrow temperature range. Therefore, the behavior of the matrix can be divided into three stages: elastic (900°C to 360°C), elasto-plastic (360°C to 320°C), and elastic again (320°C to 20°C). Such a behavior can affect the stress state during subsequent temperature cycles. For example, Fig. 7.7 which shows σ_y, σ_y^h, and σ_{eq} at P'_1 for both cooling from T_p and during temperature cycling, reveals two distinct characteristics during the heating phase of the cycle.

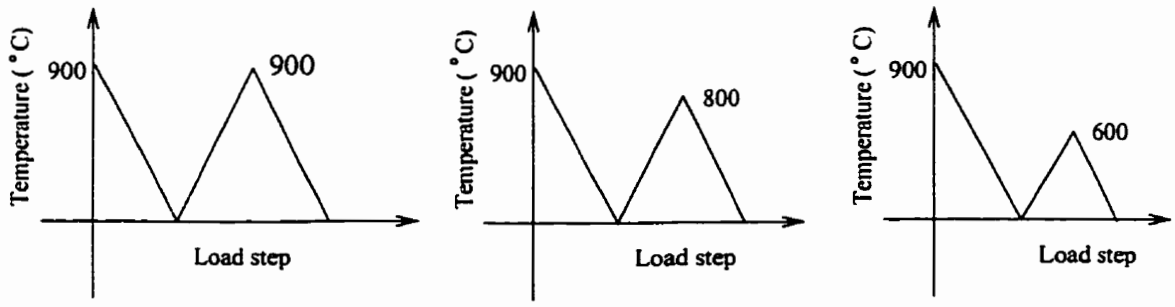

Fig. 7.6: Various temperature cycling patterns used in the analysis.

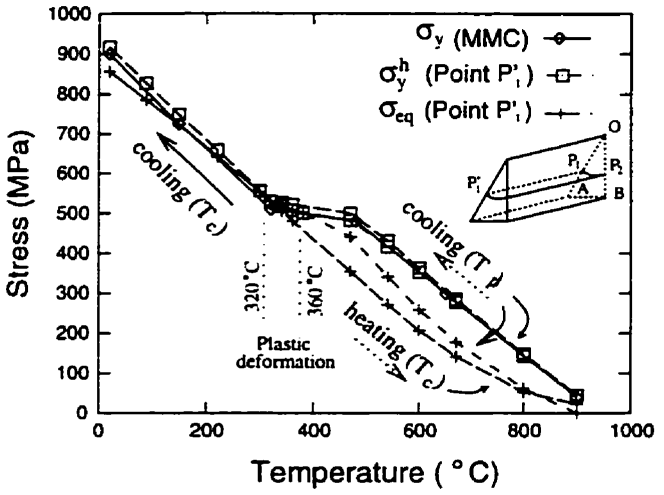

Fig. 7.7: Stress history for Ti-6Al-4V matrix in the end zone (P'_1) during temperature cycling.

In the heating range 20°C-320°C, σ_{eq} follows the same path as that of the cooling stage from T_p (see Fig. 7.7). This is due to the elastic behavior of the matrix in this temperature range during cooling from T_p. For temperatures above T = 320°C to about T = 900°C the value of σ_{eq} is lower for heating than for cooling. This is attributed to plastic deformation of the matrix generated during cooling from 360°C to 320°C. The effects of the plastic strain appear as a relaxation phenomenon when heating to above 320°C. However, σ_{eq} for T = 900°C in the heating phase is a small positive while it was zero for cooling from T_p. The reason could be explained by examining the history curves of the radial and hoop stress components at this location (point P'_1) as shown in Fig. 7.8. It is seen that both stress components have some negative values at T_c = 900°C. As explained in Chapter 5, the radial and hoop stress components at the end zone will be compressive during heating. In addition the relaxation effect due to the plastic history of the material will reduce the stresses even further. This change in stress components affects σ_{eq}.

The state of stress components and the variation of σ_{eq} with temperature in the inner zone for the temperature cycle are illustrated in Fig. 7.9. Since the plastic strain in the inner zone is very small, the relaxation effect, which results from plastic deformation, is almost negligible. Therefore, the difference between the stresses for the cooling phase (from T_p) and the heating phase of the temperature cycle is very small. The history of ε_{eq}^{pl}

versus temperature during cooling from T_p and the whole temperature cycle is shown in Fig. 7.10. Since there is no new plastic deformation during the temperature cycle (see Fig. 7.10), the process remains elastic and the stresses for both zones follow the same path during the heating and cooling phases of the cycle.

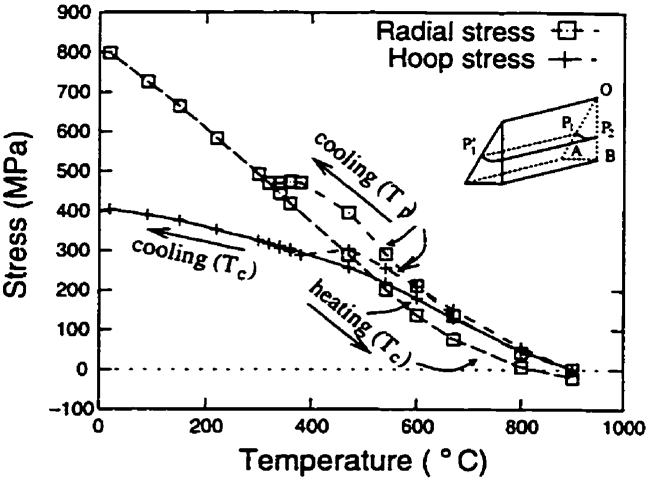

Fig. 7.8: Radial and hoop stress components in the end zone at (P'_1) during temperature cycling.

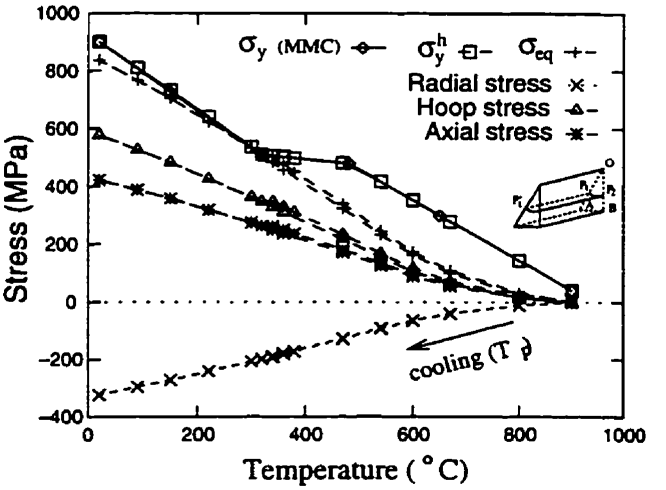

Fig. 7.9: Radial and hoop stress components in the inner zone at (P_2) during temperature cycling.

One important conclusion is that the magnitude of the residual stresses or the stresses at room temperature for both zones seem to be unaffected by temperature cycling. Consequently, no additional residual stresses are built up at service temperatures for this

composite. The undesirable effect is that it may not be possible to reduce the unwanted residual stresses by subsequent thermal treatments after the processing operations.

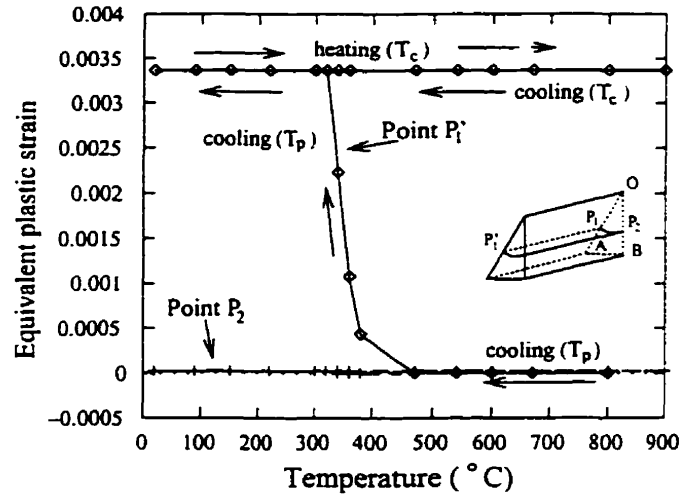

Fig. 7.10: Equivalent plastic strain in the end zone (P'_1) and the inner zone (P_2) during temperature cycling.

Next, dimensional changes in the composite during processing and temperature cycling are analyzed. A plot of the axial displacement at locations A' and B' on the free surface against temperature is shown in Fig. 7.11. Due to the elastic behavior of the matrix during the temperature cycle, the maximum and minimum axial displacements on the free surface that happen to occur at these locations (explained in Chapter 5) remain unchanged after one temperature cycle. The axial stress, which resists the thermal axial contraction of the matrix due to the presence of the fiber, remains constant. If the residual stresses increase after the temperature cycle, the absolute value of the displacements will decrease because the axial force is acting as a preventative force to thermal displacements. The small contraction of the matrix at the maximum temperature of the cycle (T_c = 900°C) can be explained by the existence of a small compressive axial stress. The thermal axial stress generated during cooling from T_p is relaxed by the limited amount of plastic strains. Upon heating, the matrix comes under a small compressive axial stress at T_c = 900°C. This compressive stress does not let the matrix contraction generated during cooling to relax completely.

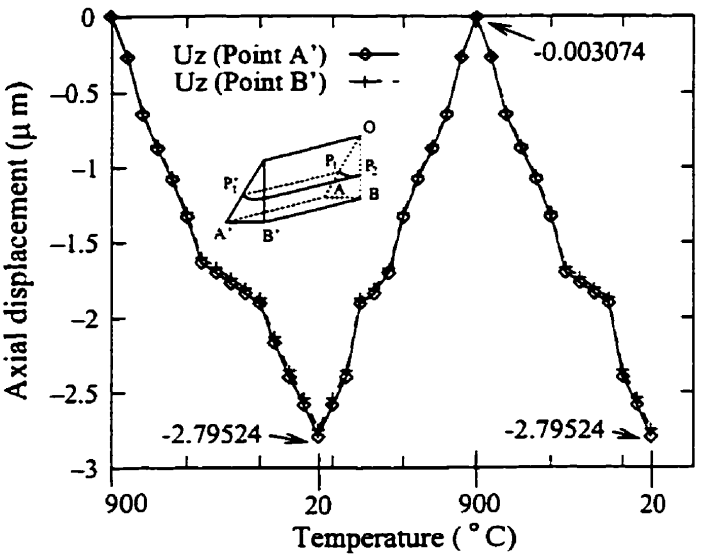

Fig. 7.11: The axial displacements of the matrix at locations A' and B' on the free surface during temperature cycling.

The last but important note about temperature cycling is the effect of strain hardening on the yield strength of the matrix. As Fig. 7.7 shows, the matrix gets hardened due to plastic deformation during cooling from the processing temperature. This process is explained here in more detail. For cooling from the processing temperature and the subsequent temperature cycle, σ_y and σ_y^h at location P'_1 are presented in Fig. 7.12. For cooling from T_p, as expected, σ_y^h of the material coincides with the σ_y in the temperature range 900°C-360°C, since there is no plastic deformation during this period. For temperatures lower than 360°C the small amount of plastic deformation strengthens the matrix. Therefore, the plastic work (χ) obtained by the earlier plastic strain will add to the strength of the material σ_y as explained in Chapter 3.

During the heating phase of the temperature cycle, in the temperature range 20°C-320°C, the values of the yield strength σ_y^h do not change in comparison to the values for the same temperature range during cooling from T_p. This is because the material has already been strengthened for temperature levels in this range. For the rest of the cycle i.e. in the temperature range 320°C-900°C the yield strength of the material again shows some increase. This is due to the fact that the plastic work (χ) increases the σ_y of the material for

temperatures higher than 320°C. Note that in spite of no more plastic deformation during the temperature cycle, the yield strength increases because of the plastic strain history. The plastic strain history at T=360°C of the heating phase is higher than for the same temperature during cooling from T_p. This difference affects the yield strength that is calculated by Eq. (3.5). Although the increase in the yield strength continues up to T=900°C of the heating phase, the yield strength for the cooling phase of the temperature cycle is the same as that for the heating phase due to the elastic behavior of the matrix.

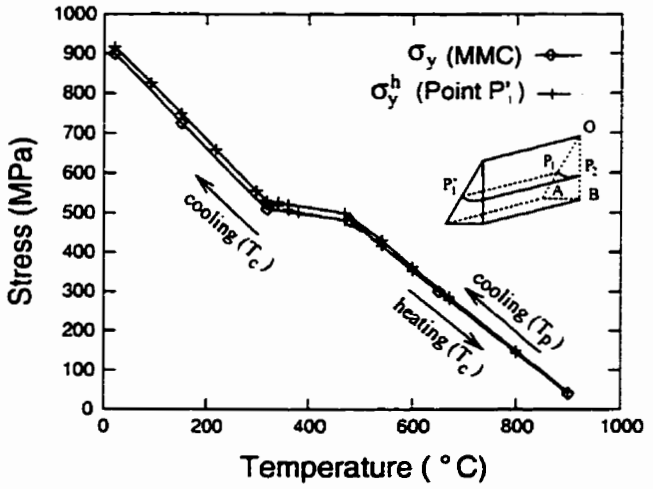

Fig. 7.12: Effect of temperature cycling on the strength of the matrix.

7.4 Residual Stresses in SCS-6/Ti-24Al-11Nb Composite (IMC)

The IMC matrix has lower yield strength than the MMC matrix. Therefore, upon cooling from the processing temperature, the IMC matrix deforms plastically much more than the MMC matrix as discussed earlier.

A history of σ_{eq}, σ_y, and σ_y^h for the matrix at location P'_1 (located in the end zone) during cooling from T_p is shown in Fig. 7.13(a). The matrix starts yielding in the end zone at about 500°C where σ_{eq} and σ_y overlap. Unlike in the previous case, yielding continues for a long temperature range before the process becomes elastic around T=200°C. Here, σ_{eq} falls again behind σ_y^h and this situation continues down to room temperature.

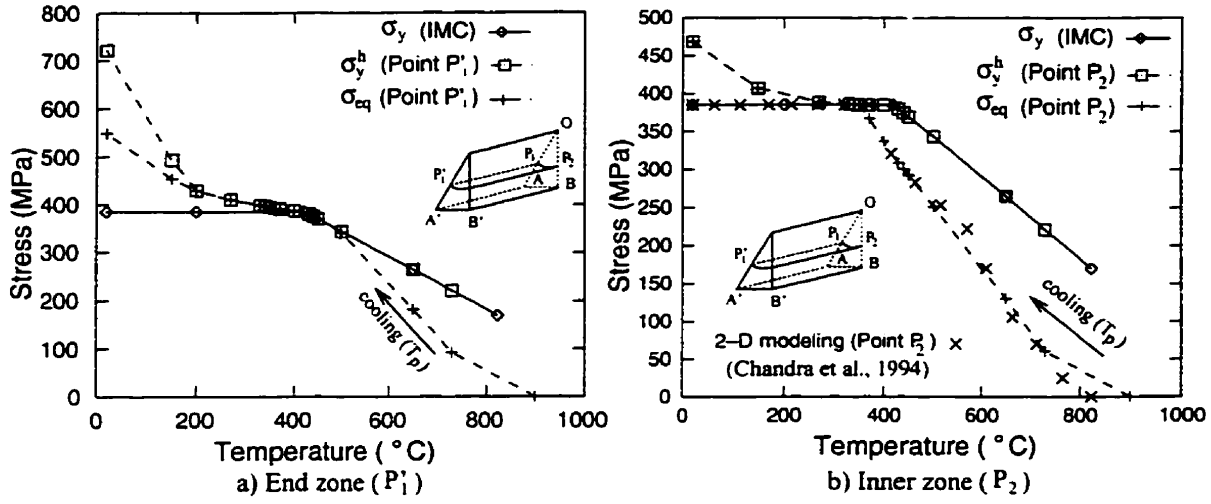

Fig. 7.13: Stress history for Ti-6Al-4V matrix during cooling from T_p.

A 3-D contour plot of ε_{eq}^{pl} in the matrix at room temperature is shown in Fig. 7.14. The plastic zone at this temperature is much wider than that in the MMC matrix, indicating that a significant portion of the matrix has already deformed permanently. Also, the magnitude of plastic strain which this matrix experiences is very high compared to that of the MMC matrix.

The increase in the amount of plastic deformation results from reduction in the yield strength and this can be attributed to the high aluminum content of the IMC matrix. Due to this large deformation and the stress-strain characteristic curve of the material at room temperature, σ_y^h at point P'_1 (which, for isotropic hardening is calculated from Eq. (3.5)) shows a sudden large increase. Therefore, due to high strain hardening, the material does not yield any more before room temperature is reached. This causes the thermal residual stresses to increase.

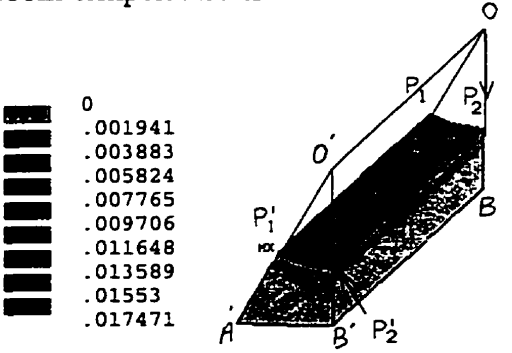

Fig. 7.14: Equivalent plastic strain in Ti-24Al-11Nb matrix at room temperature.

As Fig. 7.14 shows, the plastic strain is also high in the inner zone. Using 2-D models of rectangular fiber array, similar large plastic deformations have been reported by Chandra et al. (1994) and Coker et al. (1993). Comparing σ_{eq} obtained by the 3-D prism model and that by the 2-D plane strain model, Chandra et al. (1994), for the inner zone, indicates that the 3-D model predicts yielding to start at 340°C. However, according to Chandra et al. (1994), yielding starts at 370°C. The results obtained by Chandra et al. (1994), are shown in Fig. 7.13(b).

The strain hardening effect is more pronounced in IMC than MMC because of the high plastic deformation of the IMC matrix (compare Figs. 7.7 and 7.13). This is more noticeable for the end zone than for the inner zone due to higher plastic deformation in the end zone.

Very high plastic deformation can significantly redistribute and relax the stresses. For the matrix, the large plastic deformation changes greatly the stress distribution and also the stress values as indicated in Fig. 7.15. In this figure the radial, hoop, and axial stress components in the inner zone for a temperature before the onset of plastic deformation, T = 450°C, and at room temperature, T = 20°C, are presented. Due to stress redistribution, the maximum compressive radial stress, which is initially located on line P_2B at point P_2, is transferred at room temperature to point P_1 along line P_1A. The maximum hoop stress, which first occurred at point P_1 (before yielding starts), moves to a point inside the matrix area close to the interface on line P_2B. Similar changes in location of the maximum and minimum stresses have been reported by Ananth et al. (1993) for Al/SCS-6 composite. These changes were attributed to stress redistribution due to matrix plastic deformation. The plastic deformation changes the profile of the axial stress in the matrix in the inner zone from relatively uniform before yielding to a pattern with a stress reduction when moving towards the fiber/matrix interface. Similar axial and hoop stress profiles have been experimentally determined at room temperature by Rangaswamy et al. (1994) utilizing X-ray diffraction for the IMC composite. Comparable results have also been obtained by Rangaswamy and Jayaraman (1994) and James (1991).

Note that the 2-D analysis of the MMC composite by Chandra et al. (1994) and Nimmer et al. (1991) did not show any plastic deformation. Therefore, one can conclude that for this composite the 3-D analysis (which predicts plastic deformations) must have yielded higher stresses exceeding the yield strength. However, for the IMC composite the effects seem to be reversed. The results of the 2-D analysis taken from Chandra et al. (1994) are presented in Fig. 7.13(b). According to these data, plastic deformation starts at 370°C that is earlier than what is observed for the present 3-D model (at about 340°C). This shows that at 370°C the stresses calculated by the 3-D model are lower than those determined by the 2-D model. These discrepancies can be explained by the difference in plastic deformation of the two matrices and the relaxation and redistribution effects of this phenomenon on the stresses. The large plastic deformation in the end zone relaxes the stresses in the inner zone. Therefore, in the case of IMC, lower stresses occur in this zone. However, comparing the plastic strains of the two matrices, the relaxation phenomenon is negligible in the MMC matrix, thus allowing for more stress build-up in the inner zone. This shows another advantage of the 3-D model that is capable of accounting for stress relaxation and redistribution taking place in the direction of the fiber.

7.5 SCS-6/Ti-24Al-11Nb Composite in Service Temperatures

The effects of low matrix strength or high plastic strain on the behavior of unidirectional composites under temperature cycling are explained here using the IMC matrix. The composite is thermally cycled between room temperature and T_{max} = 900°C (see Fig. 7.6) after being cooled from T_p which was discussed in the previous section.

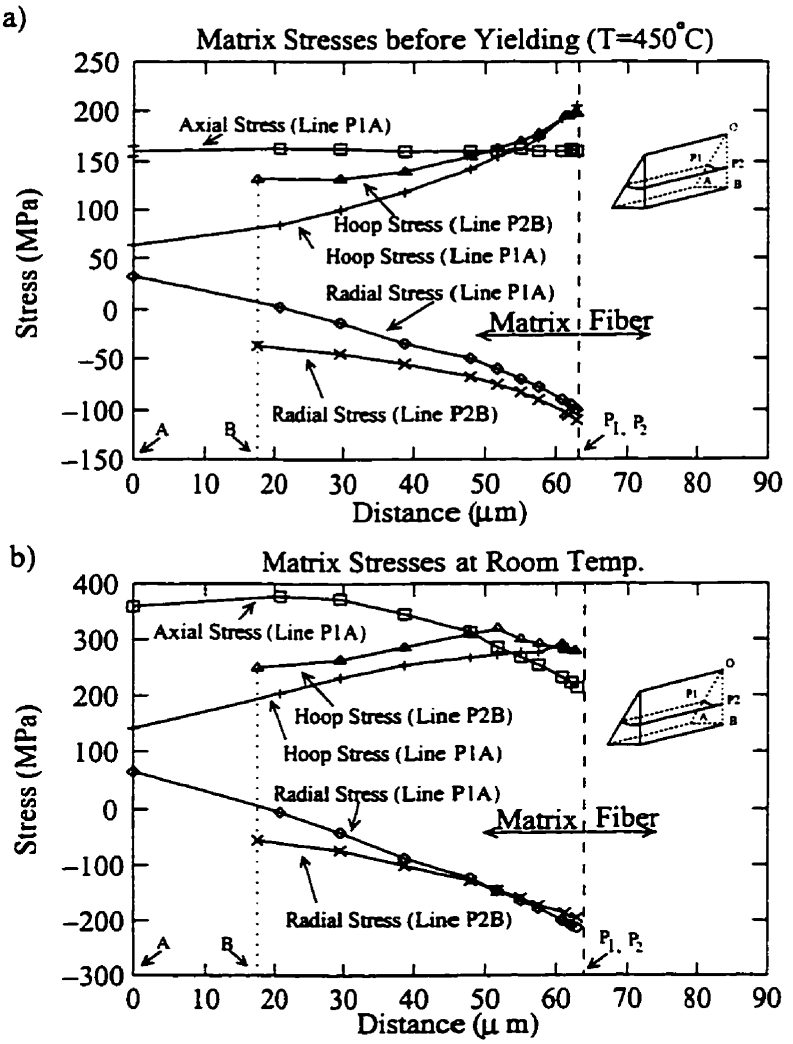

Fig. 7.15: Profile of stress components in the inner zone at T = 450°C and at room temperature for Ti-24Al-11Nb matrix.

Figs. 7.16(a) and (b) show σ_{eq}, σ_y, and σ_y^h for the cooling stage from T_p to room temperature and during the temperature cycle in the end zone (point P'_1) and the inner zone (point P_2), respectively. Due to high plastic deformation of the matrix in the cooling stage, the stresses are highly reduced in the next temperature cycle. The difference between σ_{eq} during the heating phase of the cycle and cooling from T_p is higher compared to that of the MMC matrix. This is due to high plastic deformation which causes high stress relaxation (see Figs. 7.16(a) and Fig. 7.7). During the temperature cycle, despite higher plastic strain in the end zone, σ_{eq} in the inner zone relaxes more than in the end zone. One reason could be the continuous increase in plastic strains in the inner zone up to room temperature

(when cooling from T_p). However, during the same period, the plastic deformation stops at about T = 200°C in the end zone. This elastic range affects the stresses during the temperature cycle. It prevents the stresses from relaxing upon heating. The variation of stress components with temperature for the inner zone is presented in Fig. 7.17. Note the high absolute value of the stress components at T = 900°C. These stresses cause the value of σ_{eq} in the inner zone (which is reduced during the heating phase up to T = 600°C) to increase (see Fig. 7.16(b)).

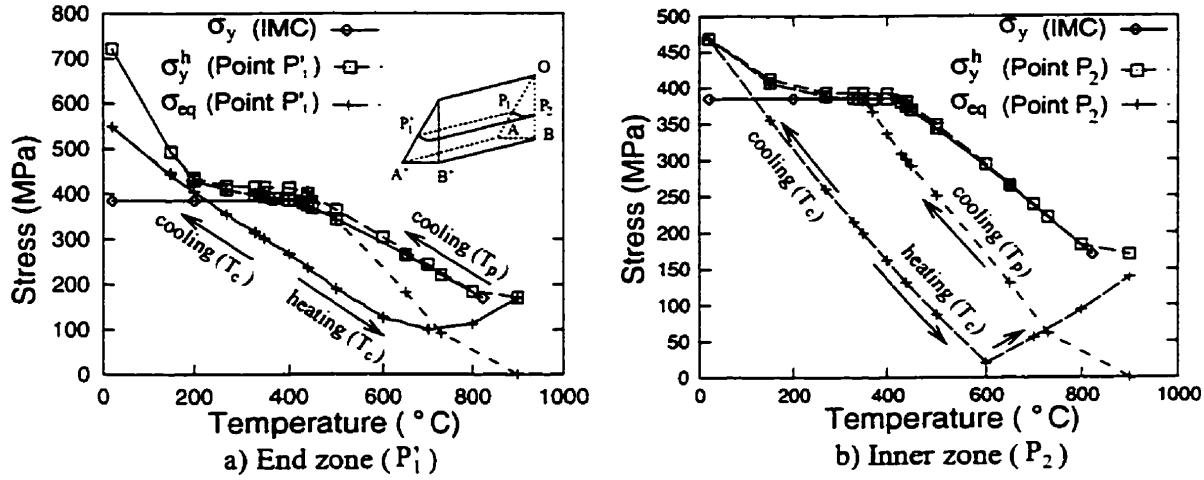

Fig. 7.16: Stress history for Ti-6Al-4V matrix during temperature cycling.

The variation of ε_{eq}^{pl} at locations P'_1 and P_2 for the cooling phase and the temperature cycle are shown in Fig. 7.18(a). The graphs show that all the plastic strain occurs when cooling from T_p and no more plastic deformation is generated during the temperature cycle. This indicates that the matrix behaves elastically for the whole temperature cycle. Therefore, as shown in Fig. 7.16, σ_{eq} for the cooling phase of the temperature cycle coincides with σ_{eq} of the heating phase. Comparing σ_{eq} and σ_y^h curves in Fig. 7.16, one can conclude that during the heating phase in both the inner and end zones, the strain hardening of the matrix is substantial at room temperature and negligible at T = 900°C despite the constant plastic strain. This phenomenon may be explained with the temperature-dependent properties of the matrix. The strain hardening effect depends on both the plastic strain history and the plastic modulus of the material at different temperatures ($E_p(T)$). Since $E_p(T)$ of the material is lower at T = 900°C compared to its

room temperature value, it reduces the strengthening effect of the plastic strain. Note that the plastic strain is constant during the temperature cycle.

As with the MMC matrix, it should also be mentioned that despite the high plastic deformation, the residual stresses at room temperature in both the inner and end zones remain unchanged after one temperature cycle (Figs. 7.16(a) and (b)). In the inner zone, due to the very small difference between σ_{eq} and σ_y^h at room temperature, any further mechanical load can easily cause the matrix to deform plastically.

The dimensional stability of the composite is also affected by the high plastic strain. Since the CTE values of the two matrices (MMC and IMC) are close (see Tables 7.1 and 7.2), the difference in their axial displacements could be a direct result of the difference in the amount of their plastic deformations. Comparing the maximum plastic strains of the two composites at location P'_1 (see Figs. 7.10 and 7.18(a)) shows that the strain in IMC is almost four times higher than the plastic strain for the MMC matrix. This difference between the plastic strains of the two composites is very noticeable in the inner zone (at point P_2). The plastic strain in the inner zone of IMC is close to the end zone value of the MMC. The tensile plastic strain affects the displacements of the composite. The axial displacements at locations A' and B' for the cooling stage and during the temperature cycle are shown in Fig. 7.18(b). The tensile plastic strain reduces the thermal contraction of the matrix. For example, at T = 900°C of the temperature cycle, the axial displacement of the matrix (which is supposed to be zero) is tensile due to the tensile plastic strain (see Fig. 7.18(b)). Comparing the displacements at T = 900°C for both types of matrices (Figs. 7.11 and 7.18(b)) shows that the displacement for MMC has a small negative value. This is because of the negligible plastic strain and the compressive axial load that was discussed earlier in section 7.3.

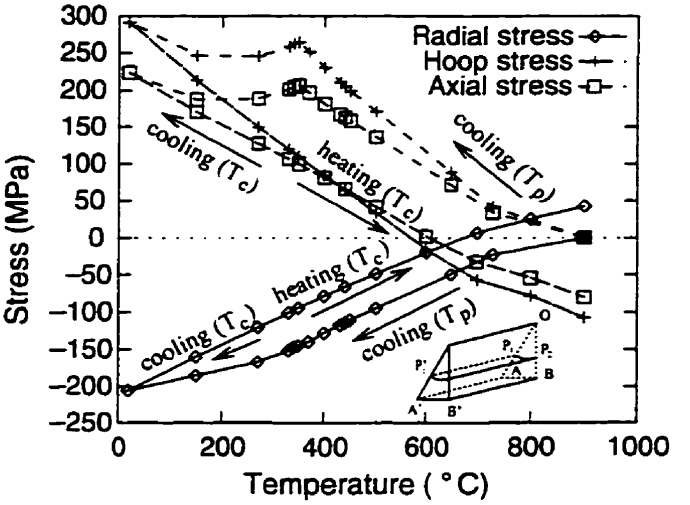

Fig. 7.17: Variation of stress components in the inner zone (P_2) during temperature cycling.

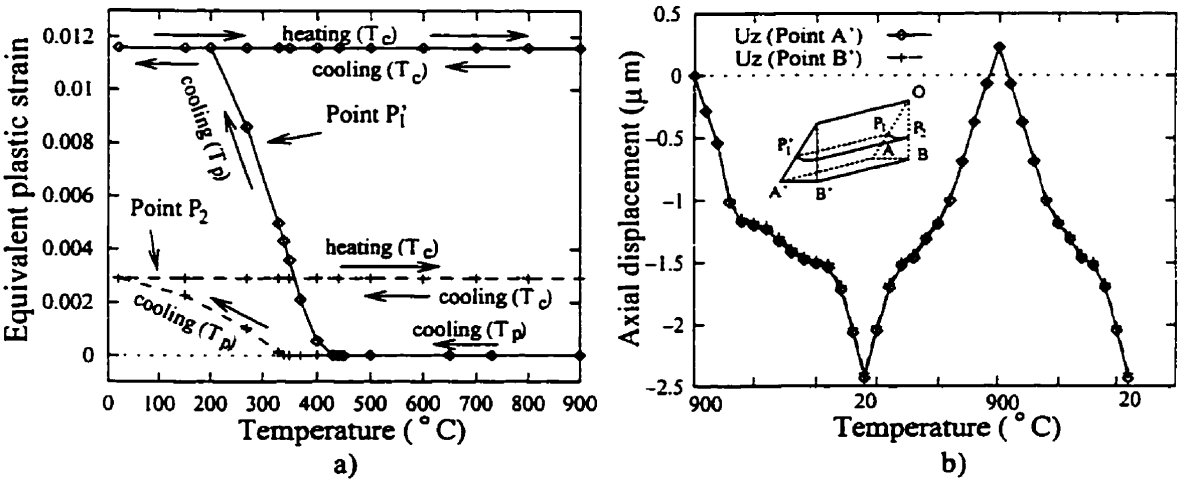

Fig. 7.18: (a) Equivalent plastic strain at locations P'_1 and P_2 and (b) axial displacement in the matrix at locations A' and B' on the free surface during temperature cycling.

7.6 Inelastic Analysis of SCS-6/Ti-6Al-4V Composite with Axisymmetric Models

The 3-D prism model has a relatively coarse mesh in the vicinity of the singular point. Therefore, the results obtained do not provide very precise information on the stress and displacement in the area very close to this point. It is possible to refine the mesh in this area, but the sub-modeling approach used in the elastic analysis is not valid here. Cutting the model at some distance away from the singularity 'freezes' the cut-off portion of the model in the subsequent formulation of the problem. Therefore, the sub-modeling mesh refinement does not provide any information on how the inter-relationship between the end zone and the inner zone stress and deformation states are influenced by plastic deformation. Therefore, it is important to verify the results of the 3-D model by comparing them with the axisymmetric model.

In this section, the elasto-plastic analysis of SCS-6/Ti-6Al-4V composite is repeated with axisymmetric models that allow the use of very small elements in the vicinity of the singular point. The details of the mesh configuration in the vicinity of the singular point are similar to the mesh presented in Fig. 3.8. The smallest element size is about 0.0002μm.

In the elastic analysis, the value of the stresses increases continuously to infinity with decreasing element size. This is due to the singular nature of the stress field at the fiber/matrix interface in the vicinity of the free surface. As explained earlier, the stresses are limited to within the yield surface (σ_y) in the inelastic analysis. As soon as the temperature is changed, very high stresses appear at the singular point and are accompanied by a large amount of plastic deformation. Consequently, the yield strength increases due to strain hardening effects.

Fig. 7.19(a) shows the variations in σ_{eq}, σ_y, and σ_y^h of the matrix with temperature in the inner and end zone locations. The corresponding equivalent plastic stains are shown in Fig. 7.19(b). Point A is located at the singularity, point J is 0.01μm away from the free surface at the interface and, finally, point B is in the inner zone. As soon as the composite begins to cool down, σ_{eq} reaches σ_y at point A and the matrix plastically yields. Note that

due to the coarser mesh of the 3-D model, the plastic deformation was shown to start at a much lower temperature while, in the present case, it occurs immediately in a very small zone around the singular point.

Since the elasto-plastic model used here does not have any limitations on the amount of plastic strain and the associated hardening effects, the plastic deformation at location A continues to increase up to about $\varepsilon_{eq}^{pl} = 0.8$ at room temperature (see Fig 7.19(b)). The strengthening effect of the plastic strain at this location is significant. The yield strength increases up to almost 5000MPa (from about 900MPa for the unstrained material). Such an increase in yield strength is extremely localized. For point J, which is located at the distance of 0.01μm from point A (fiber diameter 140μm), σ_y^h is only about 1200MPa. As expected, at location J and in the inner zone (point B), the stress and plastic strain are relatively close to the results of the prism model (see Figs. 7.1 and 7.10).

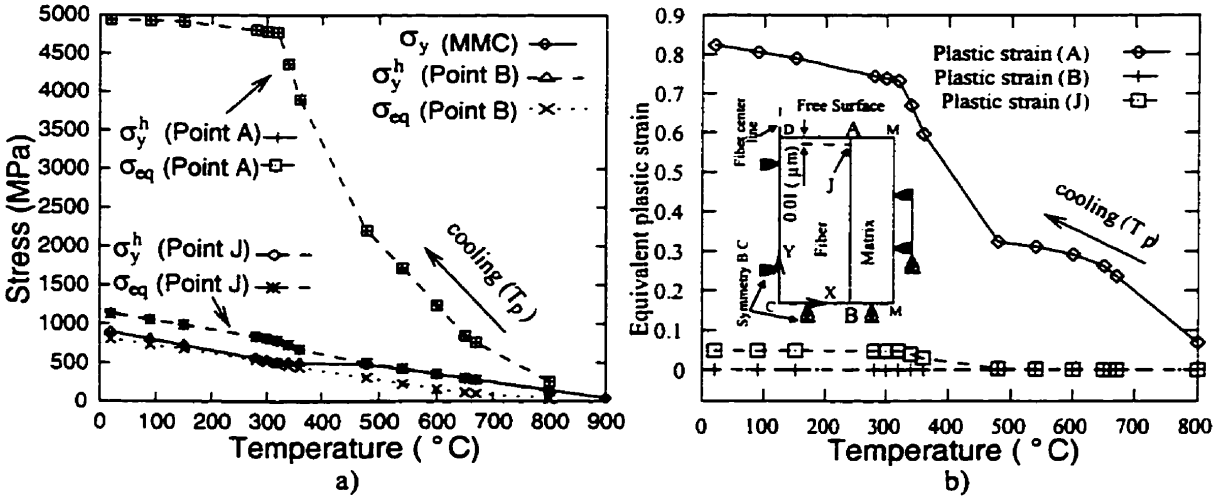

Fig. 7.19: Equivalent stress and equivalent plastic strain build-up at locations A, B, and J upon cooling from the processing temperature (T_p).

The distribution of the interfacial plastic strain along the longitudinal axis is shown in Fig. 7.20(a). The details of plastic strain in the vicinity of point A are shown in Fig. 7.20(b). The very high plastic deformation at A is reduced to about 0.05 at a distance less than 0.01μm away from the singularity (point J). It appears that the very high plastic

deformation is limited to a very small neighborhood of the singular field. As a result, the increase in the yield strength, which is strain dependent, is also a localized phenomenon.

Comparing these results with those of the 3-D model discussed at the beginning of this chapter in section 7.2, the following observations can be made. The results obtained from the 3-D model are good for a very small distance away from the singularity. Comparing the stress curve at point J (which is 0.01μm away from the singularity) in Fig. 7.19(a) with the stress curve for point P'_1 in Fig. 7.1 shows that the stresses are close in magnitude. A small difference between the stresses is due to the location of point J that is closer to the free surface compared to the location at which the results of the 3-D model were calculated. The stress curves for the inner zone are also very similar. It seems that the very high stress and large plastic strain at the singular area do not affect the stress and deformation states outside this area. Therefore, with the exception of the singular area, the 3-D model, which has a relatively coarser mesh than the axisymmetric model, provides reasonably accurate results.

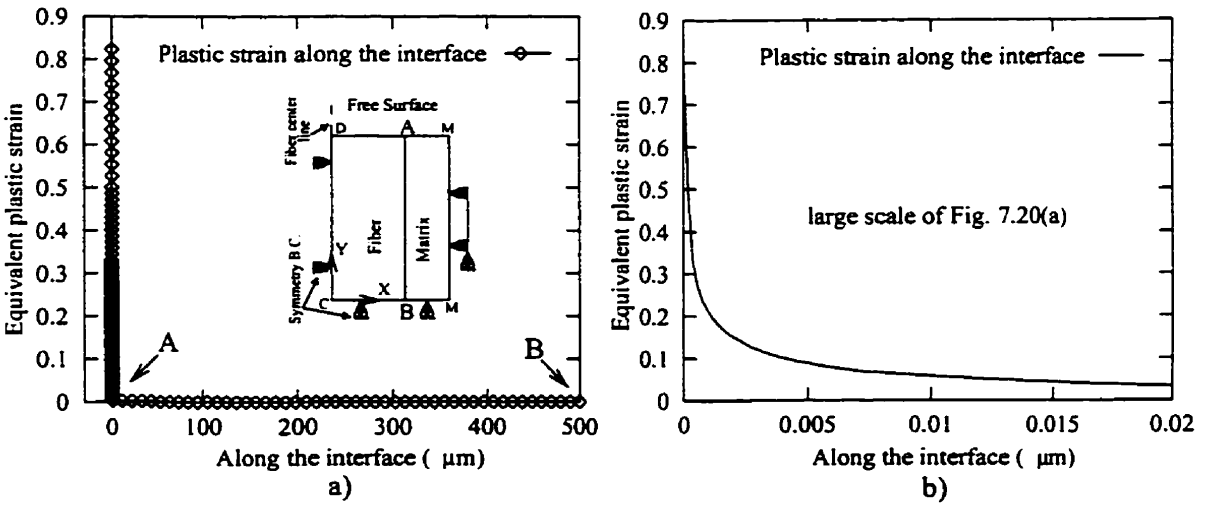

Fig. 7.20: Plastic strain distribution along the interface at room temperature.

The elasto-plastic analysis presented gives very high stress and strain values at location A due to the strain hardening model used. Most probably, these stresses would be unacceptable causing the matrix to crack or the fiber/matrix interface to debond. The cracking phenomenon would change the stress and strain states by relaxing some of the stresses and releasing the strain energy, (King, 1994). The stress relaxation disappeared

very rapidly with the distance from the singular point. Therefore, the results of the analysis assuming a perfect interface are acceptable at some distance from the singularity.

The temperature cycling of the 3-D prism model with a relatively coarse mesh in the vicinity of the singularity showed that no further plastic deformation occurs in the composite during the cycle. It was also found that the residual stresses are substantially reduced during the heating phase of the next temperature cycle. But after completion of the cycle, no change in the residual stress state was observed. To see how these results are affected by the meshing pattern, the temperature cycle with T_{max} = 600°C as shown in Fig. 7.6 is applied to the axisymmetric model with very fine elements.

A plot of σ_{eq} and σ_y^h for point A during the temperature cycle is shown in Fig. 7.21(a). As soon as the heating phase of the temperature cycle begins (from (2) to (3)), the residual stresses start to relieve resulting in lower equivalent stresses. However, the yield strength of the material is now higher as compared to the strength at the same temperatures in the cooling phase from T_p (from (1) to (2)). Also, there is some increase in σ_y^h during the cooling phase of the cycle (from (3) to (2)) compared to its values in the heating phase. This is due to a small plastic deformation that occurs at T = 600°C during the heating phase of the cycle at location A (see overlapping of σ_{eq} and σ_y^h in Fig. 7.21(a)).

The σ_{eq} in the heating phase of the cycle up to T = 360°C is lower than those in the same temperature range during cooling from T_p. This is due to the relaxation caused by previous plastic deformations. Above this temperature level up to 600°C, the stresses for the heating phase (from (2) to (3)) are higher than for the cooling phase (from (1) to (2)). This is in contrast to the results of the 3-D model, where σ_{eq} was lower throughout the heating phase of the cycle compared to σ_{eq} for the corresponding temperature levels during cooling from T_p (see Fig. 7.7). This discrepancy may be explained by the difference in the temperature level at which the plastic strain starts in the two models during cooling from T_p (from (1) to (2)). As Fig. 7.21(a) shows for the axisymmetric model, plasticity starts right away with cooling whereas it starts at lower temperatures for the 3-D model. The

immediate plastic flow of the matrix for the axisymmetric model limits the stress components in the material. The plastic strain appears before the stress components reach their expected levels. However, in the heating phase (from (2) to (3)), the stresses in the temperature range 360°C-600°C increase to higher levels. This is because the material gains strength at location A due to the high plastic deformation. These values are much higher than the stresses obtained during cooling from the processing temperature.

Fig. 7.21(b), which represents the stress components during the temperature cycle at location A, supports the above hypothesis. As the graphs show, the stress components are much higher for the heating phase of the cycle compared to the cooling phase from T_p for the temperature range of 360°C-600°C. Due to the small plastic strain that occurs at T = 600°C of the temperature cycle (see Fig. 7.21(a)), σ_{eq} decreases in the cooling phase of the cycle to room temperature because of the relaxation effect of the new plastic deformation. However, the residual stresses after one temperature cycle are not much lower than the stresses right after cooling the composite from T_p.

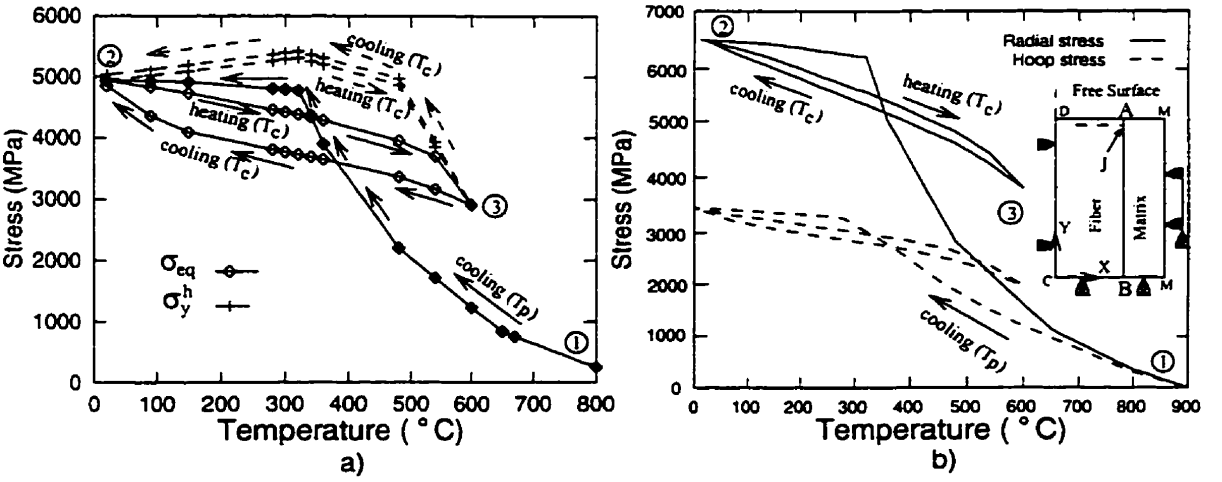

Fig. 7.21: Stress components at location A during temperature cycling.

The effect of temperature cycling is minimized at some small distance from the singularity (i.e. at point J) and in the interior of the composite (i.e. at point B). Thus, the plastic strains which occur at location A during the cycling do not change the residual stresses at locations J and B.

8. Effects of Creep on the Stress and Displacement States in Unidirectional Composites

8.1 Introduction

The creep phenomenon can effectively alter the stress and displacement states as previously discussed in Chapter 7. The creep effects are different for different materials. For example, the Ti-24Al-11Nb matrix (IMC) is considered to be insensitive to creep (Nimmer (1990) and Kroupa (1991)). Therefore, the effects of creep behavior in the Ti-6Al-4V matrix (MMC) are analyzed only.

Different cooling rates as well as temperature cycling are considered. Creep under residual stresses for a long period of time is also discussed. All the above analyses are performed utilizing the 3-D prism model.

8.2 Stress State Under Cooling Rate of 200°C/hr

The creep characteristic of the Ti-6Al-4V matrix is assumed to take the following form (Nimmer et al. (1991) and Ananth et al. (1993))

$$\varepsilon_c = a_0 \left(\sigma^{a_1}\right)\left(t^{a_2}\right)\exp\left[\frac{-a_3}{T+273}\right] \tag{8.1}$$

where σ is the equivalent von Mises stress in MPa, ε_c is the equivalent creep strain, T is the temperature in °K, and t is the elapsed time in hours. The constants a_0 to a_3 have the following values: $a_0 = 3.6\times10^{9}$ $(\text{MPa})^{-3.403}(\text{hr})^{-0.9251}$, $a_1 = 3.403$, $a_2 = 0.9251$, and $a_3 = 3.6\times10^{4}$ (°C).

An incremental formulation suitable for the FEM has the form

$$d\varepsilon_c = a_0 a_2 \left(\sigma^{a_1}\right)\left(t^{a_2-1}\right)\exp\left[\frac{-a_3}{T+273}\right]dt\,. \tag{8.2}$$

Eq. (8.2) represents the time-hardening creep hypothesis. It is used in the FEM together with an appropriate time integration scheme to obtain the stress-strain-time-temperature characteristics.

The creep phenomenon of MMC is very temperature dependent. Therefore, a high creep strain should be expected at high temperature levels. Consequently, it is required to take very small time steps for numerical convergence. This prolongs the computational time required for the transient analysis considerably. The time-ambient temperature profile of the cooling process is shown in Fig. 8.1 with the cooling steps indicated. At these cooling steps the stress-strain state is analyzed in detail. The 3-D prism model is used. It is assumed that the composite is cooled linearly and the temperature is similar on both the fiber and matrix and is uniformly distributed in the composite.

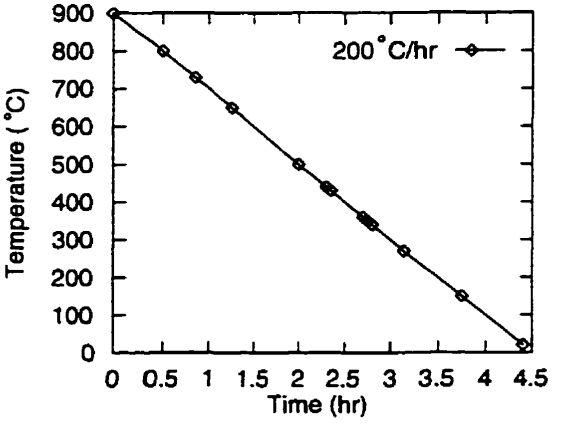

Fig. 8.1: Profile of the slow cooling process (200°C/hr).

The creep strain in both the end and inner zones are shown in Fig. 8.2. As the contour plots show, the creep strains occur in the first cooling step at T=800°C. The matrix develops a very high creep strain in both zones. The main factor, which contributes to the high creep strain, is high temperature. The creep strain is even observed in the inner zone where stresses are relatively small at this temperature. The creep strain for the inner zone and the end zone as a function of temperature for the complete cooling period is shown in Fig. 8.3. The figure also presents the absence of plastic strain in the end zone for location P'_1 over the entire cooling range. This will be

discussed later. Due to the higher stresses at the end zone, higher creep strains occur in this zone than in the inner zone. The material continues to creep strongly to about T = 500°C. Almost 40% of the total creep in the end zone and slightly over 32% of the total creep for the inner zone occur in the first 100°C of cooling. Below T=500°C, the material creeping slows down significantly. In comparison to the elasto-plastic analysis, the permanent strains (which include the plastic and creep strains) show a very high increase as illustrated in Figs. 7.10 and 8.3.

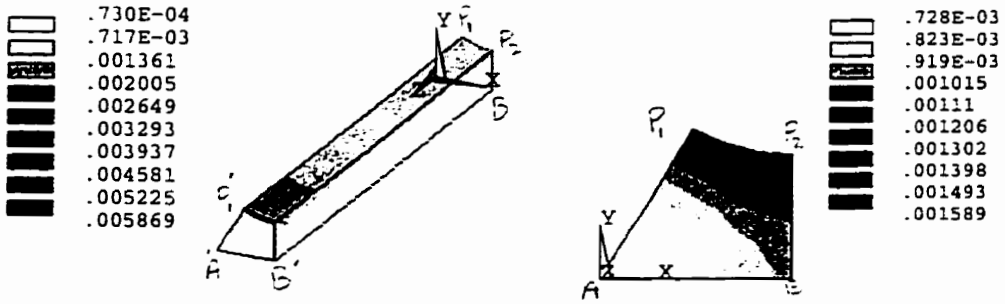

End zone Inner zone

Fig. 8.2: Creep strain distribution at T=800°C.

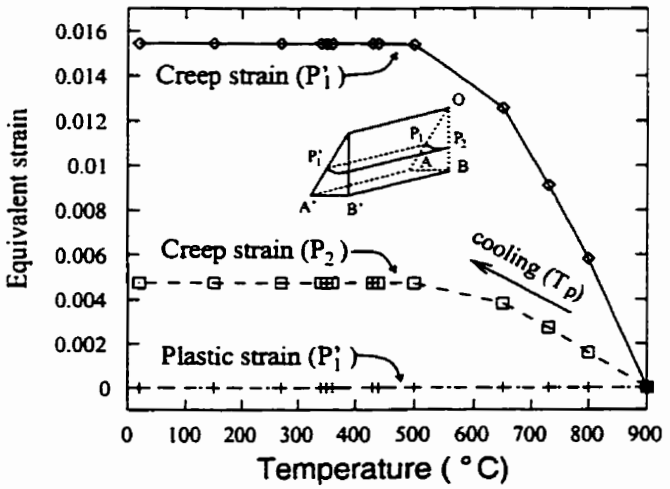

Fig. 8.3: Creep strain in the end zone (P'_1) and in the inner zone (P_2) during cooling from processing temperature (T_p).

The creep strains affect stress distribution in both the inner and end zones. The plot of stress components against temperature for the locations P'_1 in the end zone and P_2 in the inner zone are shown in Figs. 8.4(a) and (b), respectively. In comparison to the stresses for the same locations in the absence of creep (see Chapter 7, Figs. 7.8 and 7.9), the stresses show a large drop. The high relaxation due to creep deformation of the matrix will effectively alter the equivalent stresses at both the inner and end zones. The von Mises equivalent stress (σ_{eq}) for the locations P_2 and P'_1 are plotted in Fig. 8.5. In comparison to the equivalent stresses for the same locations depicted in Fig. 7.1, very high changes are observed. With creep deformation, σ_{eq} falls well under the yield strength of the matrix (σ_y) in both zones. Therefore, no plastic deformation would occur even in the end zone. The plastic strain for point P'_1 during the cooling process is plotted in Fig. 8.3. Note that the plastic deformation is zero due to the relaxation of the stresses by creep.

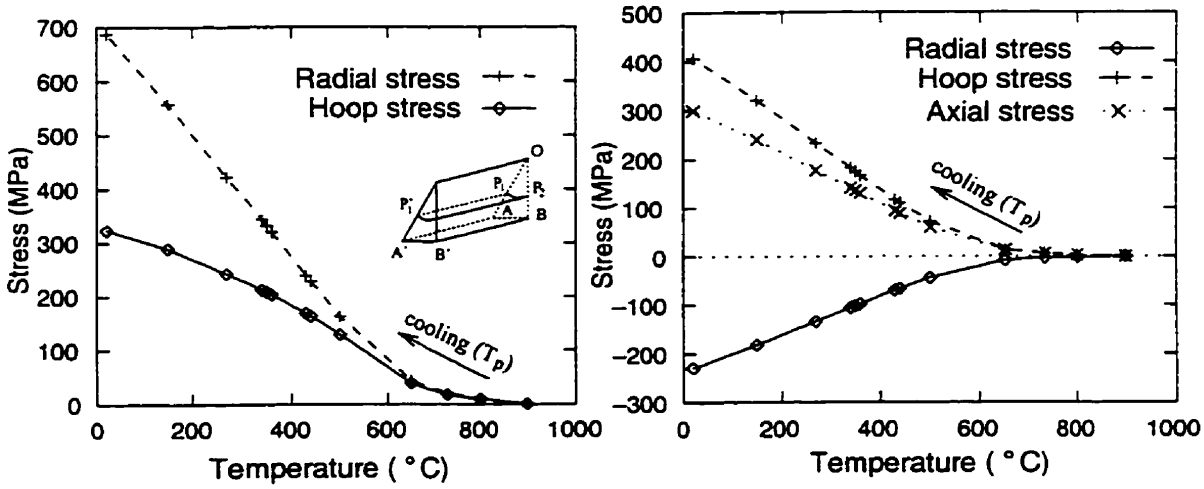

a) Stress components at P'_1 b) Stress components at P_2

Fig. 8.4: Stress components in the end zone (P'_1) and in the inner zone (P_2) during cooling from processing temperature (T_p).

Creep also affects the displacements. The variation of matrix displacement at locations A' and B' on the free surface with temperature is shown in Fig. 8.6. The maximum longitudinal displacement (U_z) of the composite decreased relative to the elasto-plastic case considered earlier (compare Figs. 7.11 and 8.6). The higher creep strain of the matrix relative to the plastic strain discussed in Chapter 7 reduces the axial

thermal contraction of the matrix. Also, as Fig. 8.6 shows, the displacement U_z for line AA' is slightly higher than for line BB' due to the higher distance of the nodes on the line AA' to the fiber. In conclusion, with creep in effect, the residual stresses in the MMC matrix (stresses at room temperature) are much lower than the stresses when only elasto-plastic deformation is considered. Also, due to the low displacements the dimensional stability of the composite increases.

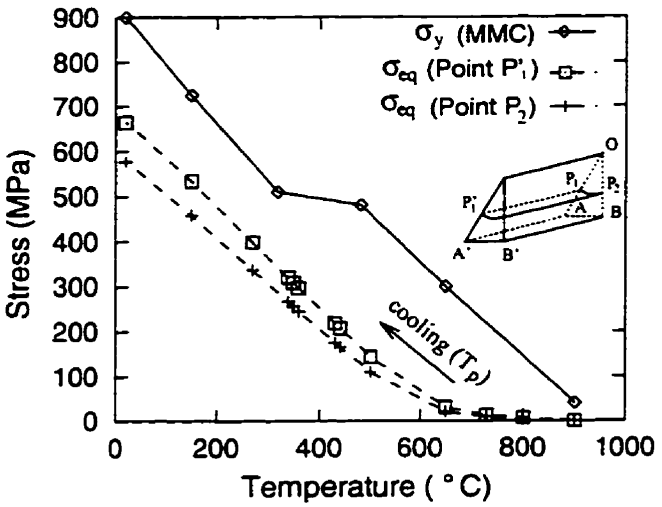

Fig. 8.5: Equivalent stress in the end zone (P'_1) and in the inner zone (P_2) during cooling from processing temperature (T_p).

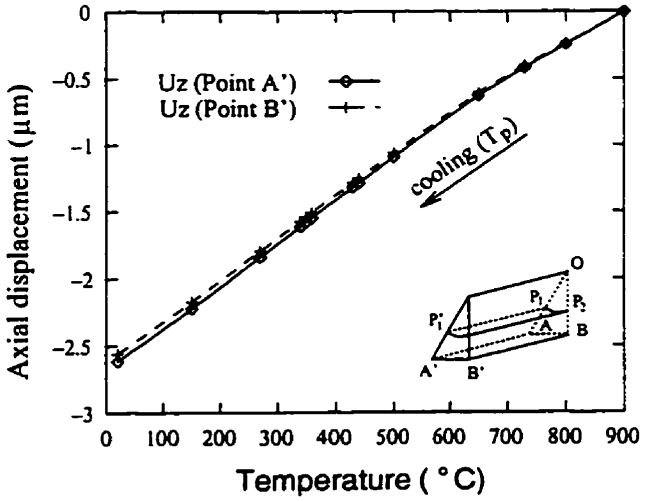

Fig. 8.6: Axial displacement at location A' and B' during processing temperature (T_p).

8.3 Effect of Temperature Cycling

It is assumed that the composite undergoes the temperature cycle depicted in Fig. 8.7. After cooling to room temperature, the composite is reheated to 600°C and then cooled again to room temperature. The maximum temperature in this cycle is slightly higher than the temperature at which matrix creeping was effectively stopped (T = 500°C) during cooling from the processing temperature.

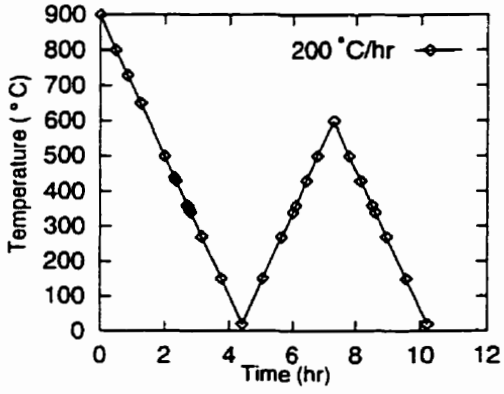

Fig. 8.7: Profile of the temperature cycle with slow cooling rate (200°C/hr).

Here, the discussion is focused on the results of the temperature cycling. The creep strains for the whole cycle for the inner zone (at location P_2) and the end zone (at location P'_1) are shown in Fig. 8.8. Also, shown in the figure is the plastic strain at P'_1. In the heating phase of the cycle, practically no more creep strains are produced for temperatures lower than T = 500°C. The strains increase from T = 500°C up to the maximum temperature of the cycle (T = 600°C). Since residual stresses decrease with increasing temperature, creep in this case is triggered mainly by temperature. The material continues to creep until the temperature of the composite is reduced to T = 500°C. Below this temperature level, no more creep occurs in the remaining part of the cooling phase to room temperature. Interestingly, the new creep strain during the temperature cycle appears in both the inner and end zones. This additional creep strain in the matrix affects the stress and displacement states of the composite. The variation of stress components and σ_{eq} in both the end and inner zones at locations P'_1 and P_2 with temperature for cooling from T_p

and also during the temperature cycle are shown in Figs. 8.9(a) and (b). Due to relaxation effect the stress components, and, consequently σ_{eq} for both zones decrease.

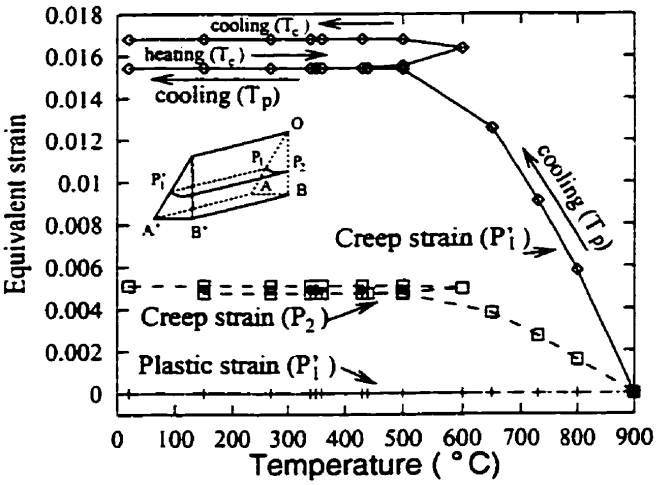

Fig. 8. 8: Creep strain in the end zone (P'_1) and in the inner zone (P_2) during temperature cycling (T_c).

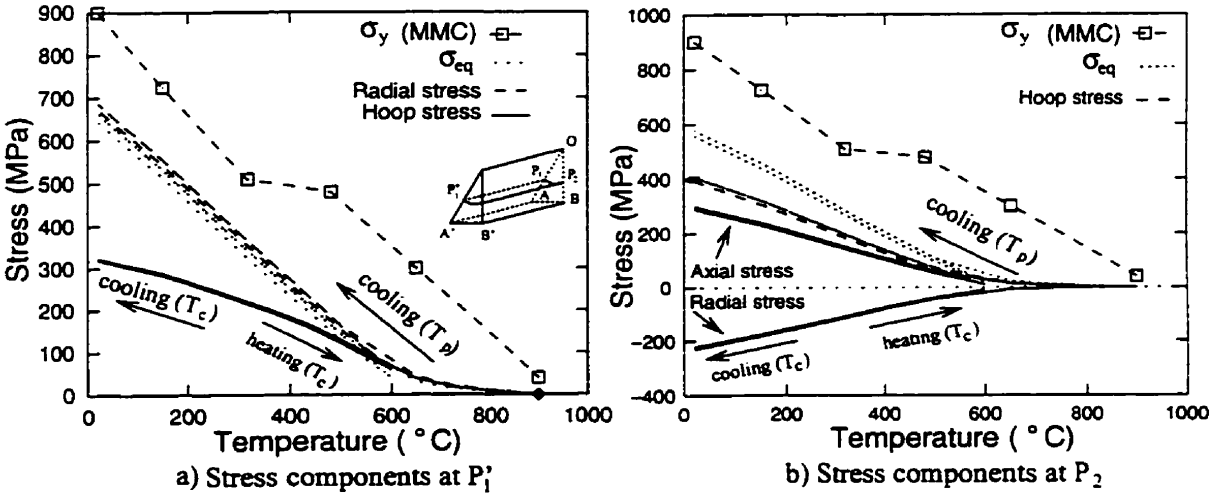

Fig. 8.9: Stress components in the end zone (P'_1) and in the inner zone (P_2) during temperature cycling (T_c).

Fig. 8.10 shows the variation of the axial deformation at locations A' and B' with time. The axial displacement at room temperature after cooling from T_p, U_z = -2.61473 μm while after completion of the temperature cycle, U_z = -2.60183 μm. Thus, the absolute value of the matrix displacement decreases after the additional temperature cycle. The tensile creep strain reduces the axial thermal displacement of the matrix. Therefore,

temperature cycling of this composite reduces the residual stresses and increases the dimensional stability of the composite.

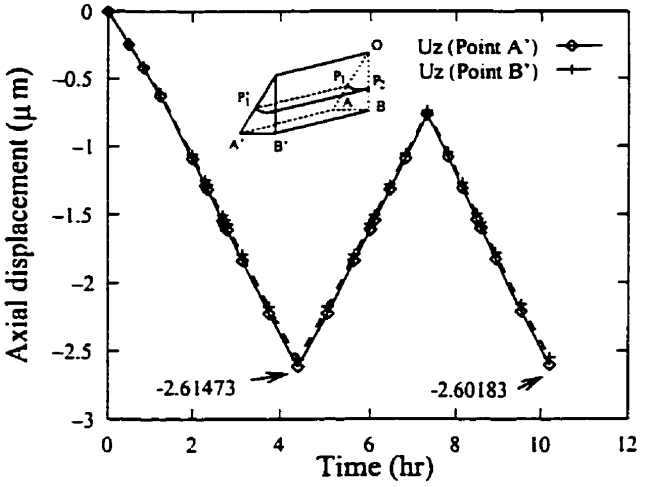

Fig. 8.10: Axial displacement at locations A' and B' during temperature cycling (T_c).

8.4 Long Period Creep at Room Temperature

The creep behavior of the matrix at room temperature over a long period of time after being cooled from the processing temperature is analyzed by keeping the composite at room temperature for 1000 hours. The only force causing creep is the residual stress present. The time-temperature profile of the test is shown in Fig. 8.11.

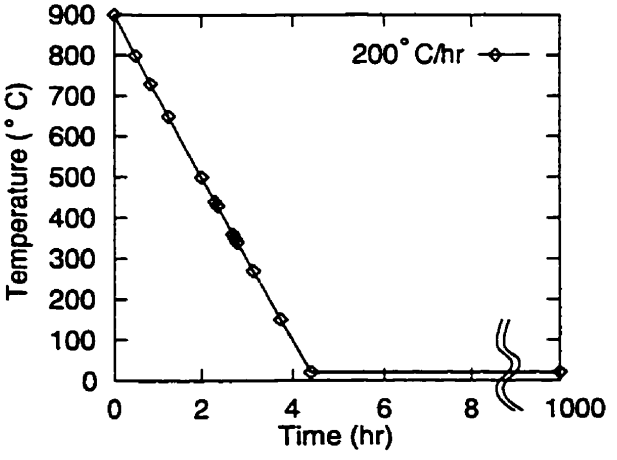

Fig. 8.11: Room temperature storage for 1000hr after cooling with slow rate (200°C/hr).

It is expected that most of the residual stresses resulting from the manufacturing stage relax after a long period of storing the composite at room temperature. The creep strains at the inner zone (at location P_2) and at the end zone (at location P'_1) after 1000hr of storing are shown in Fig. 8.12. Since creep in the MMC matrix occurs rapidly with decreasing temperature, practically no more creep strain occurs in the matrix after 1000hr of storage time (see Fig. 8.12). This implies that the residual stresses remain the same after 1000hr. The stress components and the equivalent stresses for both the inner and end zones are illustrated in Figs. 8.13(a) and (b), respectively.

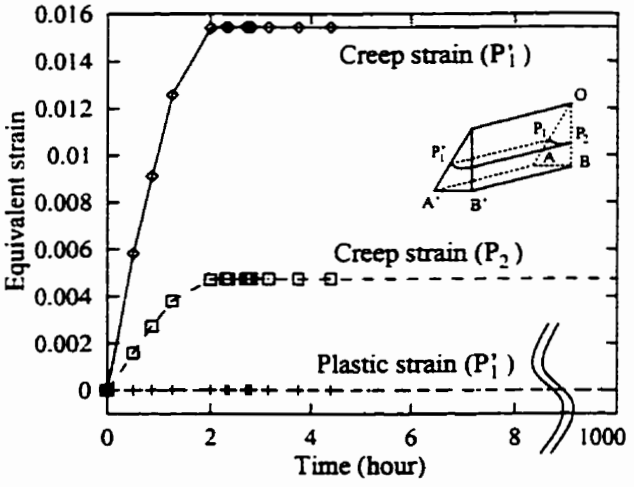

Fig. 8.12: Creep strain in the end zone (P'_1) and in the inner zone (P_2) during the storage time.

The axial displacements at locations A' and B' over the 1000hr period are shown in Fig. 8.14. The displacements also seem to remain constant with time. This dimensional stability over time could be a very positive point for the composite during service temperatures lower than T = 500°C.

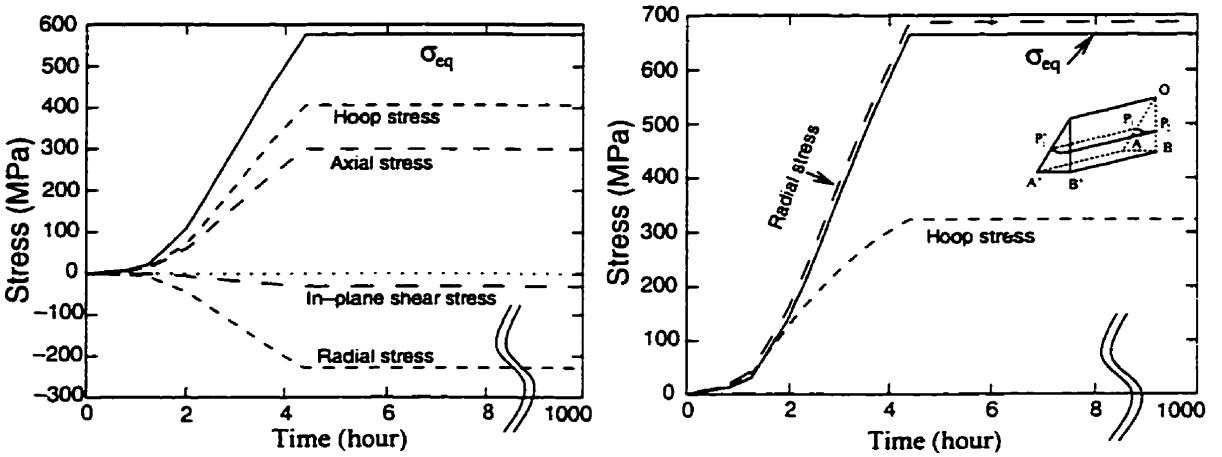

a) Stress components at P_2

b) Stress components at P_1'

Fig. 8.13: Stress components in the inner zone (P_2) and in the end zone (P'_1) during the storage time.

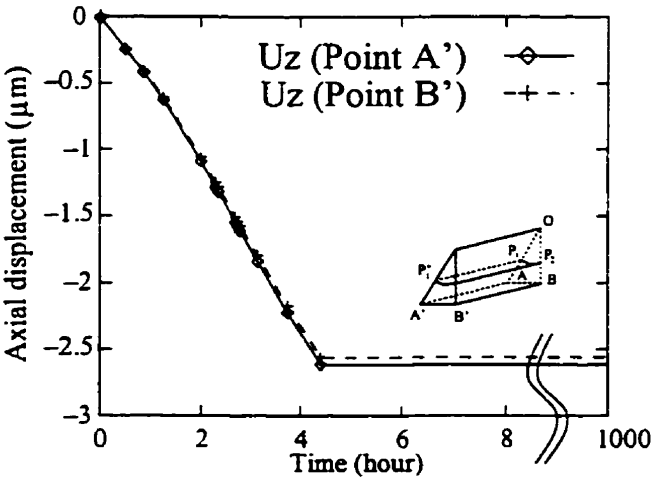

Fig. 8.14: Axial displacement at locations A' and B' during the storage time.

8.5 Creep Under High Cooling Rates

The effects of fast cooling rates (1000°C/hr and 10000°C/hr) on the stress and displacement states are presented in this section. For the first cooling scheme for which the rate is 1000°C/hr, the composite is cooled from 900°C (assumed to be the processing temperature) to room temperature in less than one hour. For the second scheme, the

cooling process is completed in 5.4 minutes. The time-temperature profiles of both schemes are shown in Fig 8.15.

The amount of creep strains in both the inner and end zones change with the cooling rate as illustrated in Fig. 8.16. The plots show that the creep strain decreases with increasing cooling rate. It is interesting to note that for all the cooling schemes considered, creep in the matrix stops at T=500°C.

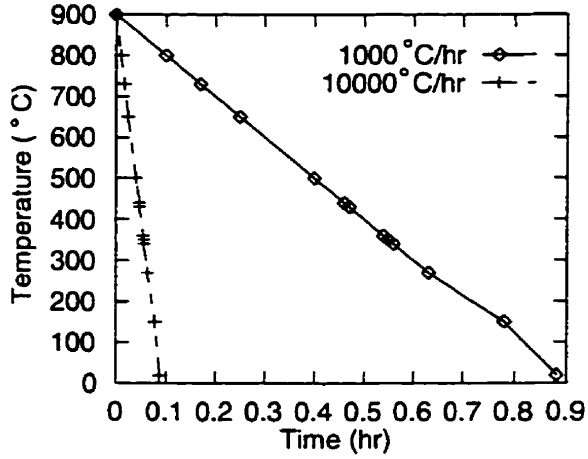

Fig. 8.15: Profiles of temperature for 1000°C/hr and 10000°C/hr cooling rates.

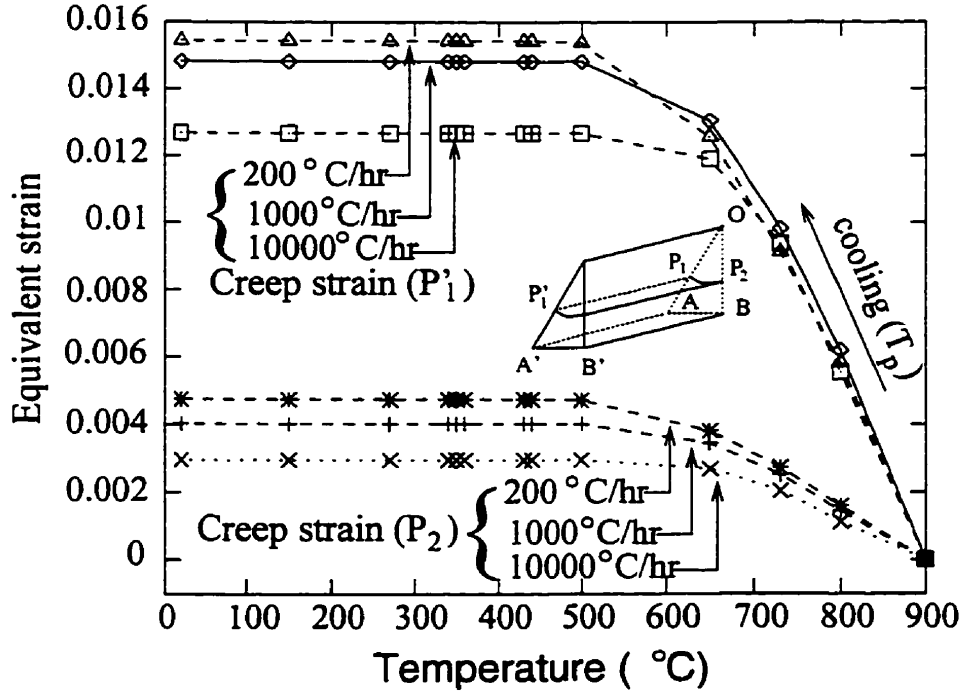

Fig. 8.16: Equivalent plastic strain in the end zone (P'_1) and in the inner zone (P_2) for three cooling rates.

The decrease in creep strains is accompanied by an increase in residual stresses. A comparison of the stress components in both zones for the 1000°C/hr cooling rate (Figs. 8.17(a) and (b)) with the similar stress components for the 200°C/hr cooling rate (Fig. 8.4) shows that the stresses are higher for the former. For very fast cooling rates (quenching in water or oil), the von Mises equivalent stress may eventually reach the yield stress of the matrix and create some plastic deformation as well as creep strains. However, this does not happen for the three different cooling rates discussed here. As Figs. 8.18(a) and (b) show, the von Mises equivalent stress increases with increasing cooling rate. However, no plastic deformation occurs even with the 10000°C/hr cooling rate since all the three von Mises curves fall under the yield strength of the material during the entire cooling processes.

As explained earlier, due to reduction of plastic strain with increase in cooling rate, the axial displacement of the matrix is expected to increase. Fig. 8.19 presents the axial deformation of the matrix at location A' (where the maximum U_z occurs) with respect to different cooling rates. As the plots show, the maximum absolute value of U_z occurs during the 10000°C/hr cooling rate.

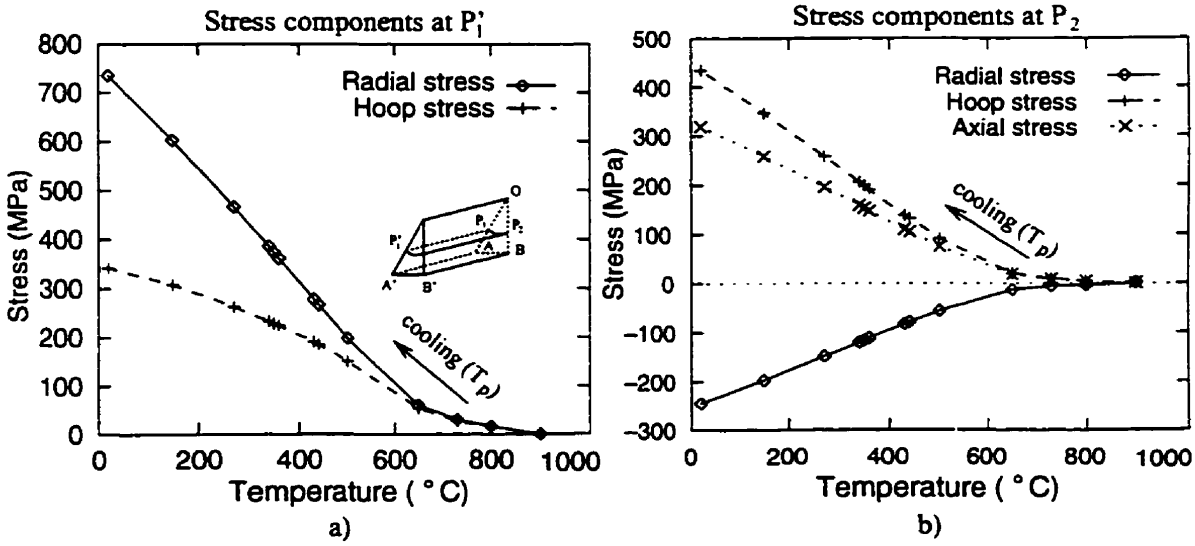

Fig. 8.17: Stress components in: (a) the end zone (P'_1) and (b) the inner zone (P_2) for 1000°C/hr cooling rate.

Comparing the elasto-plastic results presented in Chapter 7 with those obtained in this Chapter, the following conclusions can be made. For creep-prone materials, it is necessary to include the transient behavior of the material. Creep deformation changes the stress-strain and deformation states of the composite in both the inner and end zones substantially. Finally, in presence of creep strains, modeling the strain hardening phenomenon of the material with either isotropic or kinematic hardening does not affect the results. Note that if the composite is quenched in water, the time for cooling is sharply reduced and this will not allow the composite to creep. Usually, the cooling process for the MMC composite takes less than a few seconds (Chandra et al., 1994). Therefore, the transient behavior of the constituents, which requires a considerable amount of computational time, may be ignored.

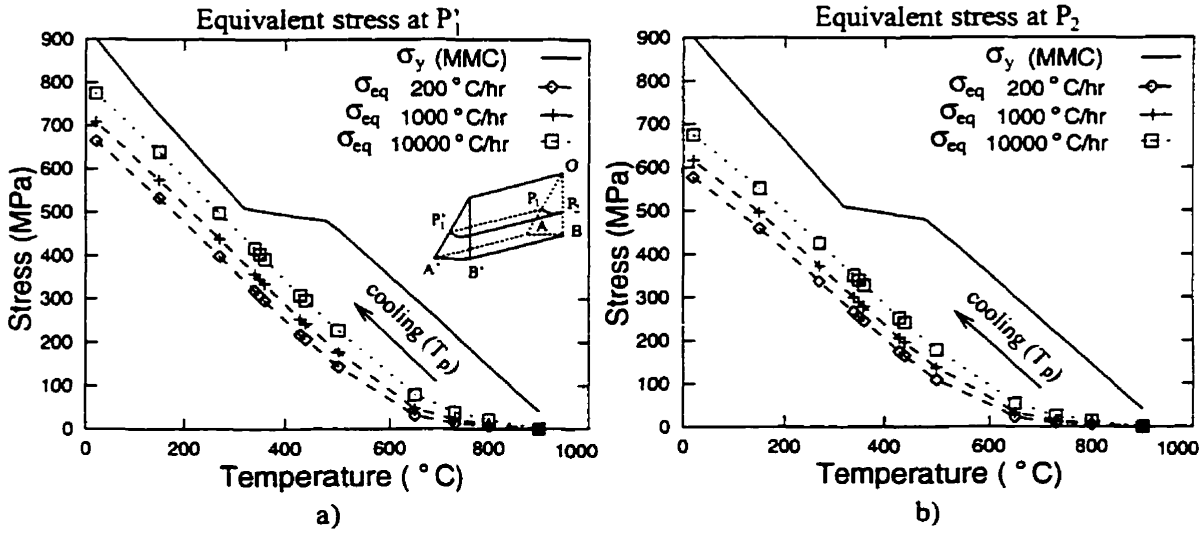

Fig. 8.18: Equivalent stress in: (a) the end zone (P'_1) and (b) the inner zone (P_2) for three cooling rates.

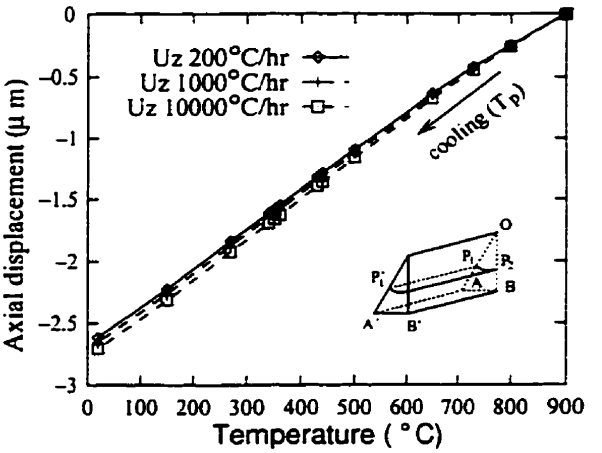

Fig. 8.19: Axial displacement at location A' for three cooling rates.

9. Effects of Surface Geometry of Composites on Thermal Stress Distribution

9.1 Introduction

In this chapter, the role of the free surface geometry on the stress field at the fiber end is analyzed. A practical solution to the cracking problem is presented as the conclusion of the analysis. It is shown that by covering the free surface of composites by a thin layer of matrix-like material the very high radial and hoop stress components at the fiber end are sharply reduced. In Chapter 5, these stresses were identified to be the major factor in initiating the matrix cracking and fiber/matrix debonding at the fiber end. With reduction of the stresses, it is expected that the matrix cracking and debonding are reduced or even eliminated. Various practical manufacturing processes are simulated and discussed. Covering the free surface of composites can be performed in several ways, two of which are considered here. In the one-stage covering process, the covering layer could be applied to the free surface of the composite during manufacturing of the composite. The two-stage covering method refers to the process of covering the free surface of a composite following manufacturing. In this method, the composite is first cooled from the processing temperature and then (in the second stage) the cover is applied. Typically, very high residual stresses may exist at the fiber end before the cover is applied. Different curing cycles can be considered before applying the cover to reduce the residual stresses. The two-stage covering can be conducted in two different ways, applying the cover either in the presence or absence of the pre-formed residual stresses.

All of the above manufacturing methods and curing schemes are discussed in detail in this chapter. First, the elastic analysis of one-stage covering under 1°C temperature change using axisymmetric models is examined. The elasto-plastic analysis of the

one-stage covering under the full processing temperature range using both the 3-D prism and axisymmetric models are also discussed. The elastic analysis of the two-stage covering under 1°C temperature change is also discussed followed by the elasto-plastic study of the process under the full temperature range. The two-stage processing is conducted using the axisymmetric model only.

9.2 The Elastic Analysis

The elastic analysis results presented here are obtained for +1°C uniform temperature change under which the variation of mechanical properties of both constituents due to temperature, presented in Table 5.1, is neglected. All the stresses presented in graphs and contour plots are in MPa and the models dimensions are all in μm.

9.2.1 Materials and Modeling

In this chapter, unidirectional composites with 7.62μm diameter graphite (AS) fibers embedded in epoxy matrix (this matrix has also been referred to in Chapters 5 and 6) with 35% fiber volume fraction (V_f) are simulated using axisymmetric FEM models. Since the thermal stresses in composites increase with reduction in the fiber volume fraction, such a low V_f is used to enhance the stress effects. The analysis in Chapter 5, using the 3-D prism model for the hexagonal fiber pattern, shows that the stresses along the fiber circumference change very little. The average values of the stress components from the 3-D model are approximately equal to the stresses calculated from the axisymmetric model. The effects caused by reconfiguring the free surface (the fiber protrusion or fibers end covered by the matrix) are much higher than the difference between the axisymmetric and the prism models. Therefore, in order to focus on these effects it has been decided to use the axisymmetric model, which substantially reduces the computation time and the efforts required for the mesh refinement.

The model along with the boundary conditions is shown in Fig. 9.1(a). The model was meshed with 8-noded axisymmetric elements with quadratic shape functions of the ANSYS software. A very fine mesh was considered at the fiber matrix interface (FMI) in

the vicinity of the free surface as shown in Fig. 9.1(b). Since (for the elastic case) the stress field is singular and the size of elements could affect the results (Abedian and Szyszkowski, 1997), for comparison, the size and orientation of elements at the FMI for all models considered are identical. In the vicinity of A, the element size is 1/64000 of the fiber radius.

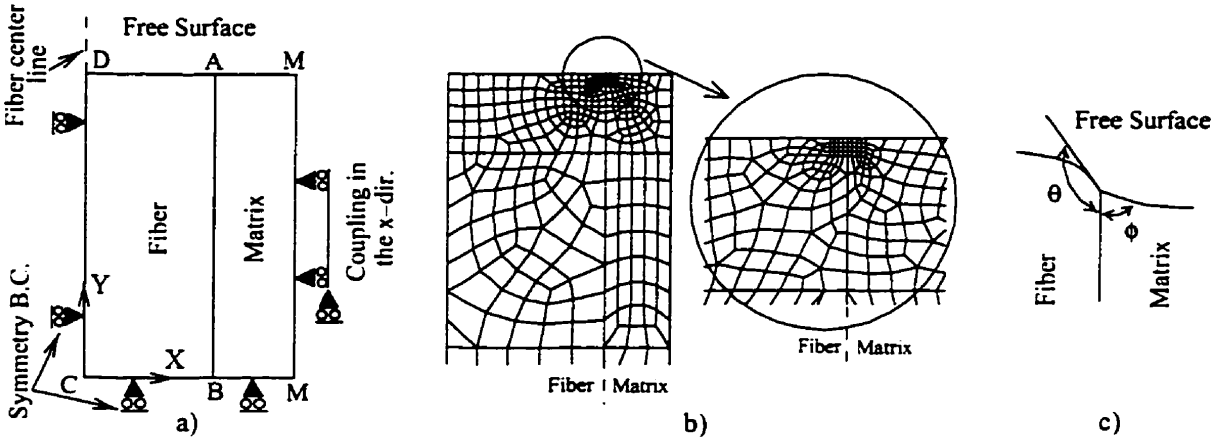

Fig. 9.1: Axisymmetric model of the composite.

In general, the free surface is not flat and may have a slope discontinuity as indicated in Fig. 9.1(c). The present study is focused on the effects of fiber/matrix contact angles, denoted as θ and ϕ in Fig. 9.1(c), on the stress distribution at the FMI in the vicinity of the free surface. More specifically, the models shown in Fig. 9.2(a)-9.2(h) will be considered in detail. In Figs. 9.2(a)-9.2(d), it is assumed that the fiber is extending out of the matrix such that $\theta = 180°$ and the matrix contact angle is varying from $\phi = 90°$ to $\phi = 11°$.

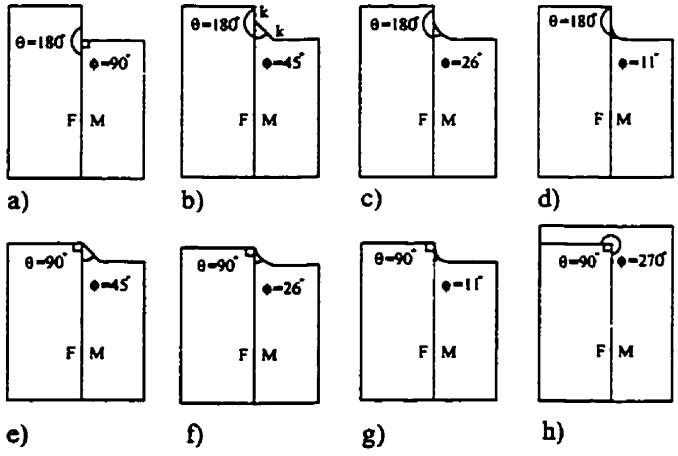

Fig. 9.2: Models with different fiber/matrix contact angles, i.e. (θ,ϕ).

Figs. 9.2(e)-9.2(g) show the cases with $\theta = 90°$ and with matrix contact angles of $\phi = 45°$, $\phi = 26°$, and $\phi = 11°$. In the case shown in Fig. 9.2(h), the free surface or the fiber and matrix cut surfaces are simply covered with a layer of matrix.

9.2.2 Effects of Different Fiber/Matrix Contact Angles on Free Surface Stresses

A brief review of the stresses at the FMI near the free surface for the flat free surface model ($\theta = \phi = 90°$) is presented in this section. Such a model has been discussed extensively in (Abedian and Szyszkowski, 1997). Then, the results for the models shown in Fig. 9.2 will be examined in detail sequentially.

9.2.2.1 Case 1: $\theta = 90°$, $\phi = 90°$

For comparison, contour plots of the radial, hoop, and longitudinal shear stress components at the FMI and in the vicinity of the free surface under a uniform unit temperature change (+1°C) for the basic model are presented in Fig. 9.3. Very high compressive radial and hoop stress regions as well as a relatively high interfacial shear stress are presented in this area. The details of the overlapping hypothesis, which was used to explain the stress state, were presented in Chapter 5.

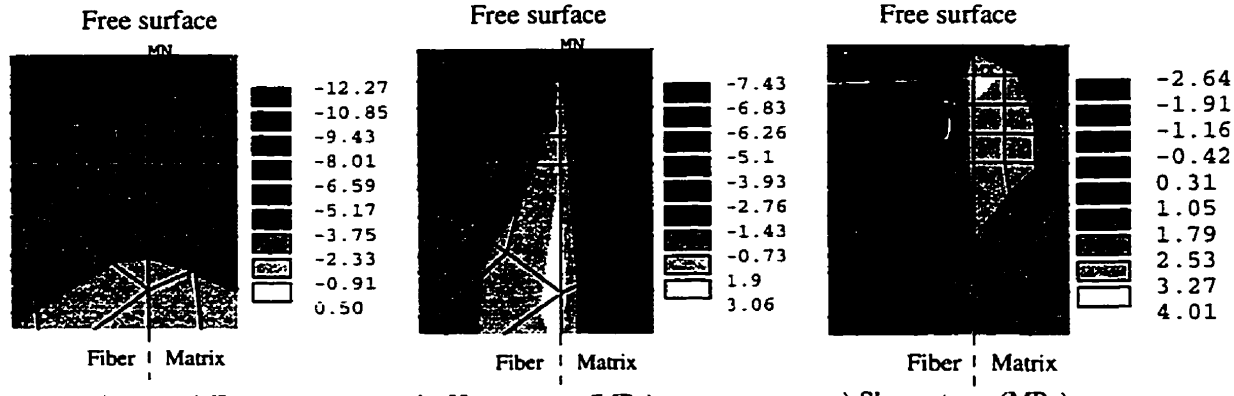

Fig. 9.3: Stress distributions for the flat surface model.

9.2.2.2 Case 2: $\theta = 180°$, $\phi = 90°$

When cutting composites, a very small portion of the fibers can be pulled out of the matrix. The magnified 3-D picture of such a cut surface along with its axisymmetric

meshed model is presented in Fig. 9.4. Here, the portion of the fiber that extends out of the matrix is assumed to be 5% of the fiber diameter. As Fig. 9.5 shows, the stress components change significantly under a small variation in the composite temperature (+1°C) relative to the stresses shown for case 1, i.e. composite cut surface with a perfect surface finish (see Fig. 9.3). For comparison, graphs of radial and hoop stress components along the FMI (line AB in Figs. 9.1 and 9.4) in the vicinity of the free surface for both cases are shown in Fig. 9.6. It appears that the stresses for case 2 are almost twice as high as in case 1 at the free surface, while away from the free surface the stresses are almost identical. One of the reasons for such a drastic change in the stress magnitude may be explained by the difference in the deformation of the fibers. The fiber under compressive radial load, which tends to eliminate overlapping (see Fig. 5.9), may deform radially more easily for case 1 than in case 2 (in which the fibers extend out of the matrix). Lower fiber deformations in case 2 cause higher compressive radial stresses in both the fiber and the matrix. Upon cooling, these stresses become tensile and can be very damaging to the fiber/matrix bonding. This indicates the importance of the surface finish when cutting composites. The analysis performed for a longer portion of the fiber extending out of the matrix, i.e. longer than 25% of the fiber diameter, shows a further small increase in radial and hoop stresses, thereby supporting the explanation based on the difference in the fiber compliance in the radial direction between cases 1 and 2.

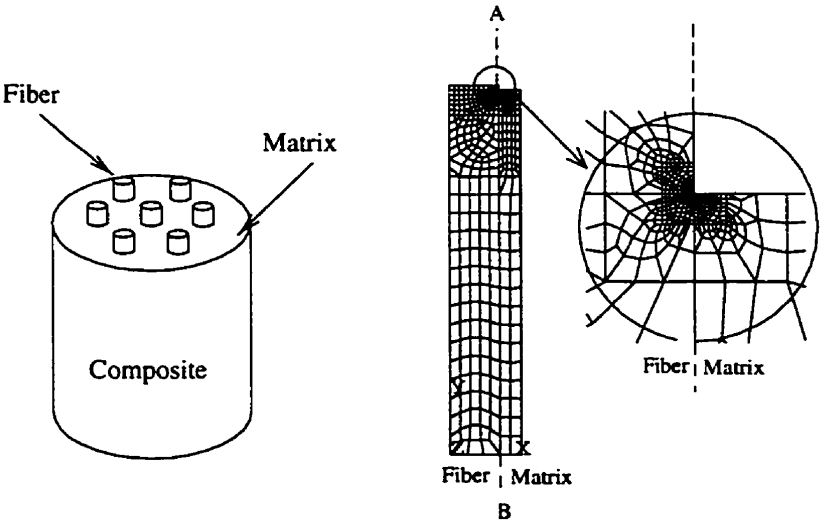

Fig. 9.4: Fiber extending out of the matrix.

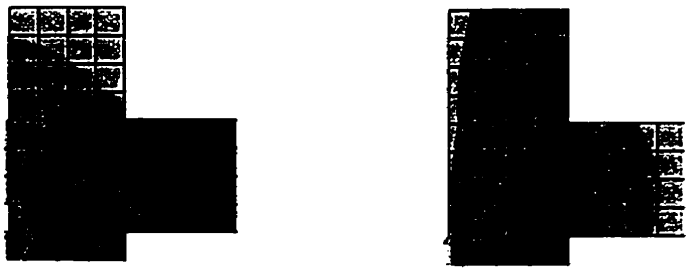

Fig. 9.5: Stress distributions for the model with the fiber extending out of the matrix.

Fig. 9.6: Radial and hoop stress components on the fiber/matrix interface in the vicinity of free surface.

9.2.2.3 Case 3: $\theta = 180°$, $\phi = 45°$

Filling the sharp free corner of the FMI and the free surface with the matrix material (the angle ϕ becomes smaller than 90°) will change the stress regimes substantially. In the current discussion, it is assumed that the corner is filled with the matrix material such that the contact angle of the matrix with the fiber is $\phi = 45°$ (see Fig. 9.7). This case and almost all of the following cases to be discussed in this section may mostly happen at the exposed end of composite parts during manufacturing or when a composite is cut. The dimensions of the ramp, i.e. $a = b = 0.02$ μm, are considered to be 0.0026 times the fiber diameter. The analysis was repeated with a similar density of mesh pattern at both sharp corners of the

ramp area. It appears that high stresses still occur at both corners, but it is clear that the stresses are substantially lower at the fiber-matrix contact corner when $\phi = 45°$ relative to $\phi = 90°$ (see Figs. 9.5 and 9.8). These changes, caused by the decrease in contact angle, may be explained by the hypothesis of overlapping as demonstrated in Fig. 5.9. Similarly as before, the difference in the fiber and matrix free thermal expansion causes radial and axial discontinuities. The load that is required for satisfying continuity in the axial direction again causes an overlap which, however, is smaller than in the previous cases. It is because, for $\phi = 45°$, the axial load is distributed on the 'a' dimension of the ramp (see Fig. 9.9) and the resultant load that is shown with the dashed arrow acts on the matrix hollow cylinder at some distance from its inner rim. This reduces the amount of overlapping and, as a result, lower radial stresses are required to eliminate the overlapping. As it turned out the other stress components decrease substantially as well.

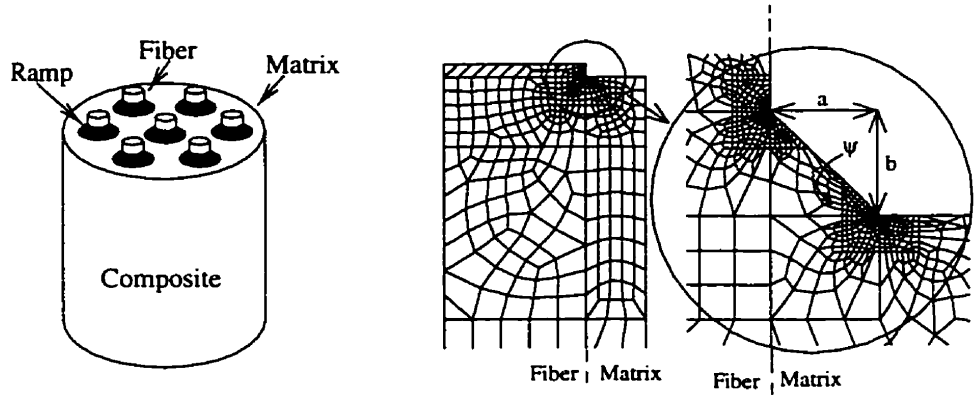

Fig. 9.7: The model with filled fiber-matrix corners.

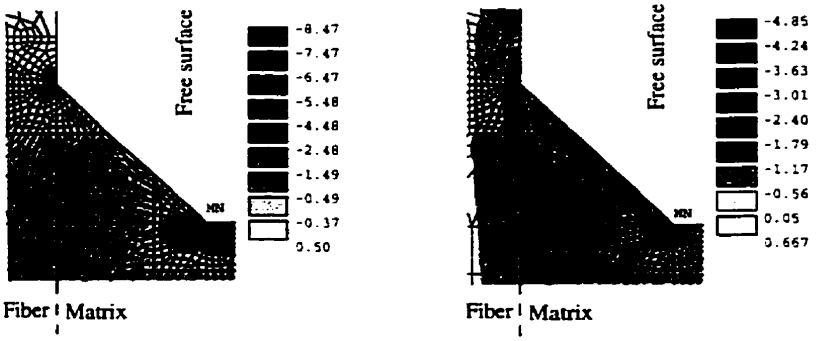

a) Radial stress (MPa) b) Hoop stress (MPa)

Fig. 9.8: Stress distribution for the model with filled fiber-matrix corner.

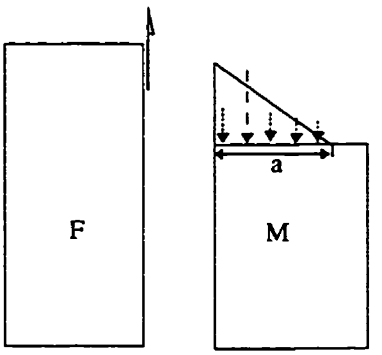

Fig. 9.9: Distribution of axial load in the ramp area.

The sharp corner of the ramp (ramp/matrix contact angle, $\tan\Psi = b/a$, Fig. 9.7) gives rise to stresses in the matrix. However, this stress concentration is related only to the geometrical discontinuity in the matrix material and should disappear if the discontinuity is removed. If this sharp corner in the matrix away from the fiber is still present, the corresponding stresses are high enough to damage the composite. This may be one of the reasons for cracks occurring in the matrix area away from the interface. This has also been found experimentally and will be discussed in Chapter 11.

It is worthy to see how the fiber and matrix contact angles affect the stresses. That is why two more cases were analyzed by replacing the straight line KK of the ramp area (see Fig. 9.2(b)) with curved lines having tangent angles $\phi = 26°$ and $\phi = 11°$ (see Figs. 9.2(c) and 9.2(d)). For comparison, the radial and hoop stress components along the fiber matrix interface for the last three cases are shown in Figs. 9.10(a) and 9.10(b). The graphs show

that the stress components are essentially the same away from the fiber end but, as the free surface is approached, the stresses show a large difference in magnitude. Note that for ϕ equal to 11° and 26°, the highest stress occurs away from the free surface. The lower matrix contact angles decrease the absolute values of the very high stresses at the free surface as shown in Fig. 9.11. For small ϕ, the stresses at the free surface drop to almost zero. In such cases, according to the results shown in Fig. 9.10, the maximum stresses will be located inside the matrix. For reference purposes, these stresses are also presented in Fig. 9.11.

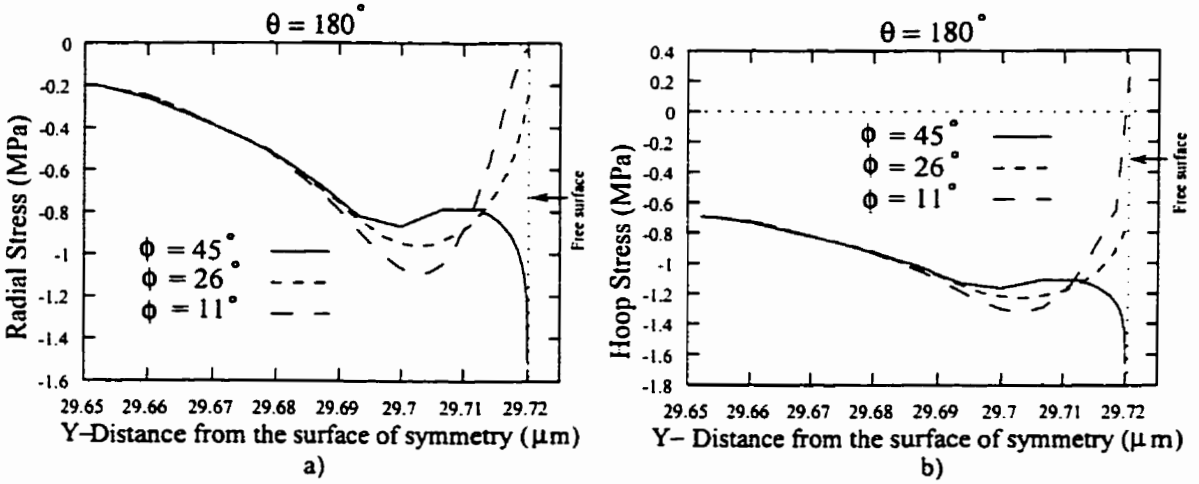

Fig. 9.10: Radial and hoop stress components along the fiber/matrix interface for case 2 (θ = 180°) with different matrix contact angles (φ).

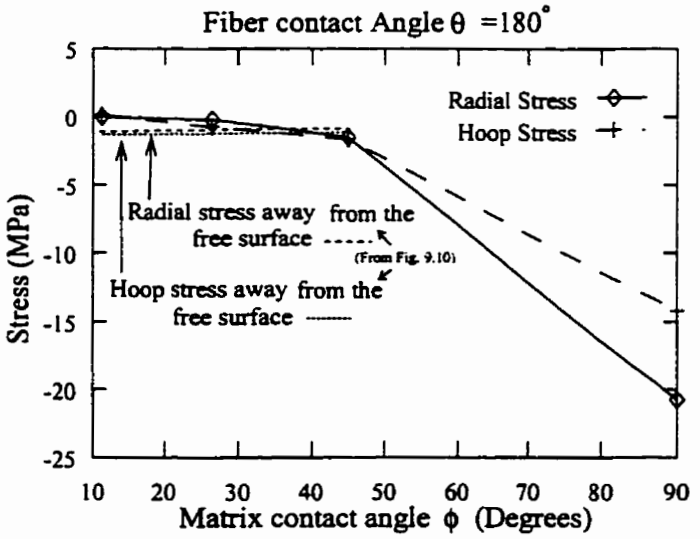

Fig. 9.11: Radial and hoop stress components at the interface on the free surface for case 2 (θ = 180°) with different matrix contact angles (φ).

Elimination of the sharp corners (i.e. reducing ramp/matrix contact angle, Ψ) by considering curved ramps generally reduces the stress concentration in the matrix as indicated in Fig. 9.12.

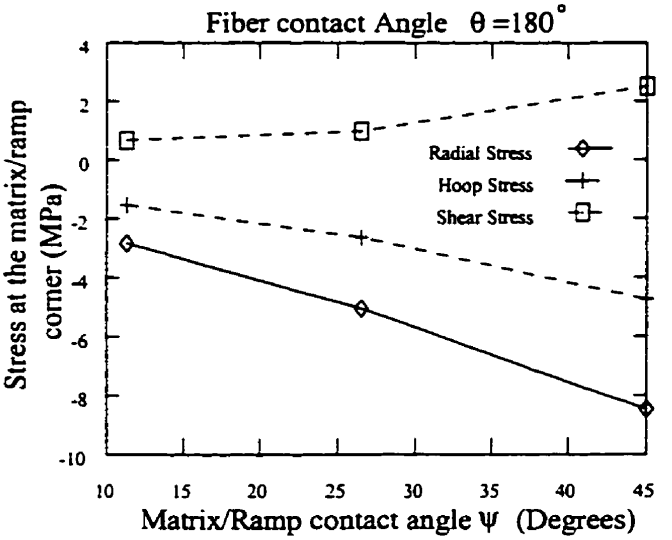

Fig. 9.12: Radial, hoop, and shear stress components at the free surface for case 2 (θ = 180°) with different matrix/ramp contact angle (ψ).

9.2.2.4 Case 4: θ = 90°, ϕ = 45°

The very high thermal residual stresses introduced during manufacturing (discussed in detail in Chapter 7) may be partially relaxed and/or cause some microscopic deformation on the cut surface of a composite. The creep phenomenon can also play a role in deforming the cut surface. Under these circumstances, the fiber and the matrix may end up at different heights on the cut surface as shown in Figs. 9.2(e)-2(g).

The mesh pattern for this case is presented in Fig. 9.13(a). The pattern of the mesh in both corners of the 45° ramp is exactly the same as the one considered in case 3 (θ = 180°, ϕ = 45°). For comparison, the stress components along the interface for the current case and also case 3 are presented in Fig. 9.13(b). The stresses seem to be higher for case 3 than for the present case. This may be attributed to the same reasons as those discussed for case 2 (θ = 180°, ϕ = 90°). That is, the fiber for the current case (θ = 90°) may deform more easily under the axial load which causes overlapping relative to case 3 where

$\theta = 180°$, reducing the absolute value of the radial component of the load. However, the stresses at the ramp/matrix contact corner (i.e. angle Ψ) are similar for both cases.

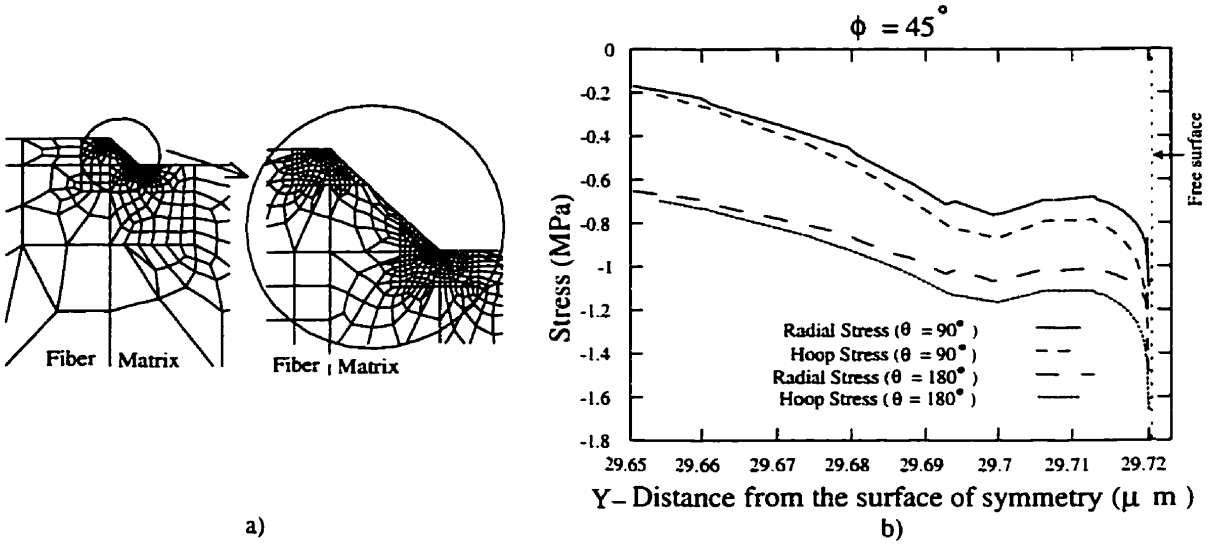

Fig. 9.13: Radial and hoop stress components along the fiber/matrix interface for matrix contact angle of ($\phi = 45°$).

The above numerical analysis was repeated for matrix contact angles of $\phi = 26°$ and $\phi = 11°$. Compared to the cases discussed previously, lower stresses were obtained for these angles as well. These results will be discussed in the next section.

9.2.2.5 Case 5: $\theta = 90°$, $\phi = 270°$ (Free Surface Covering)

Covering the free surface (cut edge) of the fiber and matrix with a thin layer of matrix-like material results in a contact angle of $\phi = 270°$ for the matrix at the interface (see Figs. 9.14(a) and 9.2(h)). The covering process can be performed either during manufacturing or as a repair process.

The FEM model with dense mesh pattern at the corner of the FMI is shown in Fig. 9.14(b). Upon covering the free surface, the stress regimes right at the corner are completely changed relative to the stresses presented for the composite model without the covering layer, see Figs. 9.3 and 9.15. Interestingly, the absolute values of the compressive radial and hoop stresses are substantially reduced. The reduction is so substantial that these stresses (which will become tensile on cooling and could potentially damage composites

by initiating circumferential and radial cracks in the matrix) should not be considered as causing damage to composites. Such changes to these stress components may also be explained again considering the free expansion of the composite constituents and the overlapping as presented previously. The block diagram of a single fiber embedded in matrix is shown in Fig. 9.16. Under axial load, which tends to satisfy the longitudinal continuity, the deformation of block-S is obstructed by the block-T. This greatly reduces the amount of overlapping and changes the deformation pattern. As a result, the absolute value of the very high compressive radial stress is reduced to a very small value. This radial stress can vary from a small compressive to a small tensile stress depending on the degree of overlapping allowed by the properties of the block-T and the value of the other stress components. The deformation of a hollow cylinder under a compressive axial load on its inner wall can be used to explain the small compressive hoop stress. A lower overlapping results in lower hoop stress as well. However, high stresses are still present in the elements adjacent to element E' (shown in Fig. 9.14(b)) due to a type of stress singularity which is inherent with sharp corners. Most notable are the very high tensile radial, hoop, and axial stresses for these elements, see Fig. 9.15. Upon cooling composites from the processing temperature, these stresses not only prevent cracking but also help to keep the fiber and matrix intact due to the sign change in the stresses. The only stress component, which may be detrimental at the fiber end (when covering the free surface), is the longitudinal shear stress at the interface.

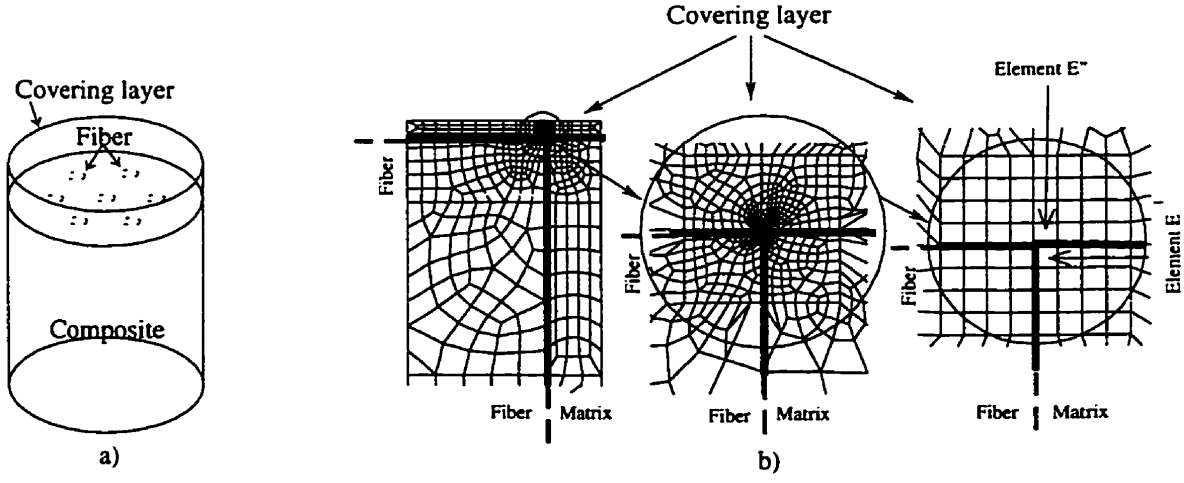

Fig. 9.14: Model of a composite with a covering layer on the cut surface.

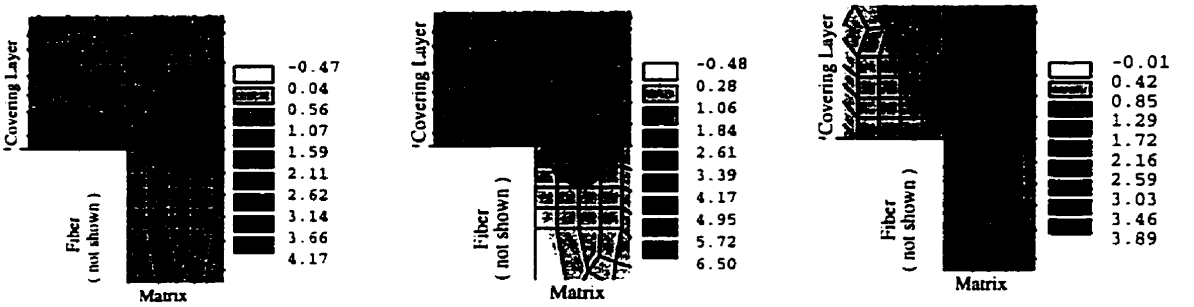

a) Radial stress (MPa) b) Hoop stress (MPa) c) Shear stress (MPa)

Fig. 9.15: Stress components for the model with a matrix-like covering layer.

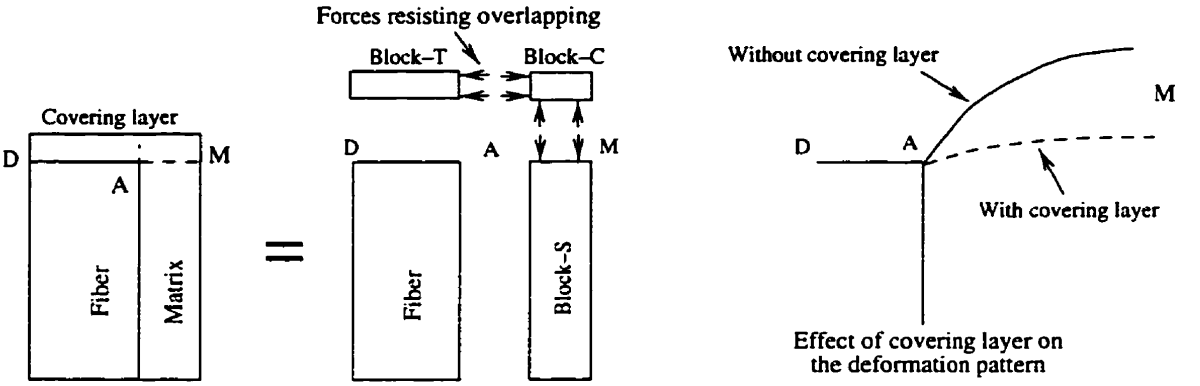

Fig. 9.16: Block diagram of a composite with a covering layer.

These shear stresses play a major role in increasing the tensile hoop stress in the elements adjacent to the element E' in the matrix area, see Fig. 9.15. Considering free expansion of the composite constituents and ignoring the overlapping effect, the blocks T and C will expand more than the fiber in the radial and hoop directions. To rejoin the block corners with the fiber end, a tensile radial stress along with a compressive hoop stress are required. Considering the overlapping effects of block-S, the stresses substantially change. In addition, there is another important factor that greatly influences the hoop stress. Under a shear stress, the corner elements (see Fig. 9.15) are pushed toward the fiber center, creating a high deformation as shown in Fig. 9.17. This deformation is balanced by a tensile hoop stress shown in the figure.

To determine the effects of the change in the fiber/matrix contact angles on the stresses, the stress components along the interface for this case and the cases discussed in

the previous section are plotted in Fig. 9.18. Large differences in stress values are seen in the area close to the corner tip. According to the corner tip values of the stress against the matrix contact angle of (ϕ) in Fig. 9.19, it seems that covering of the composite free surface is an effective and practical way for decreasing the damage due to thermal stresses at the fiber end in composites. This important finding has been verified experimentally and is discussed in Chapter 11.

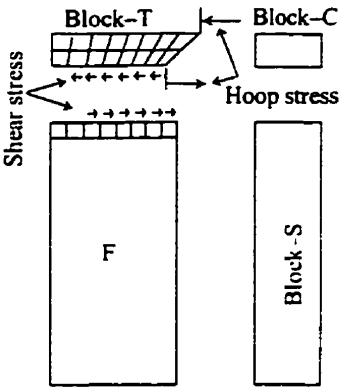

Fig. 9.17: Deformation of the block-T under shear stress.

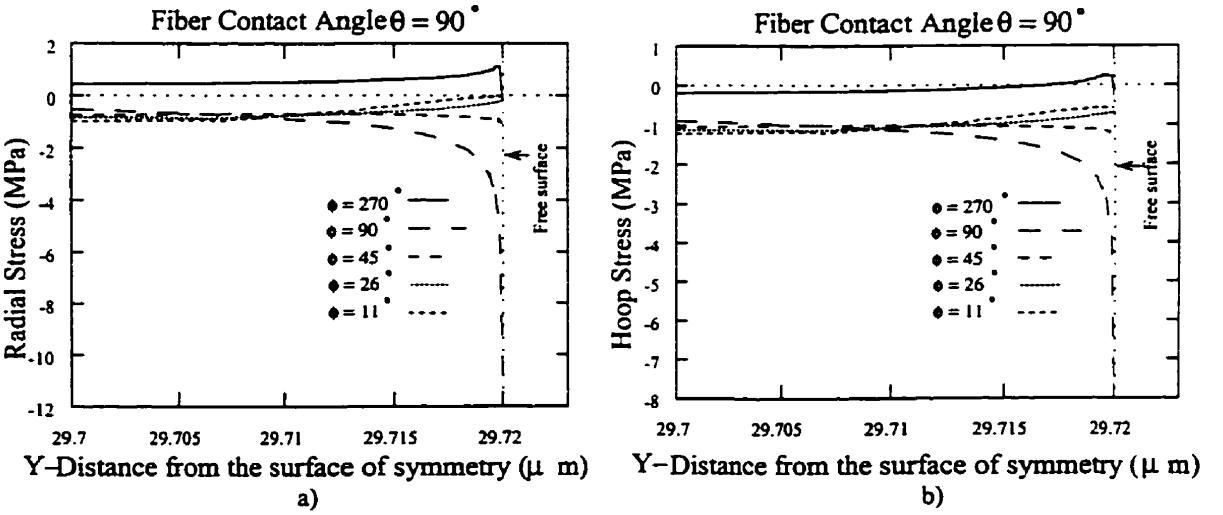

Fig. 9.18: Radial and hoop stress components along the interface for cases 4 and 5 (θ=90°) with different matrix contact angles (ϕ).

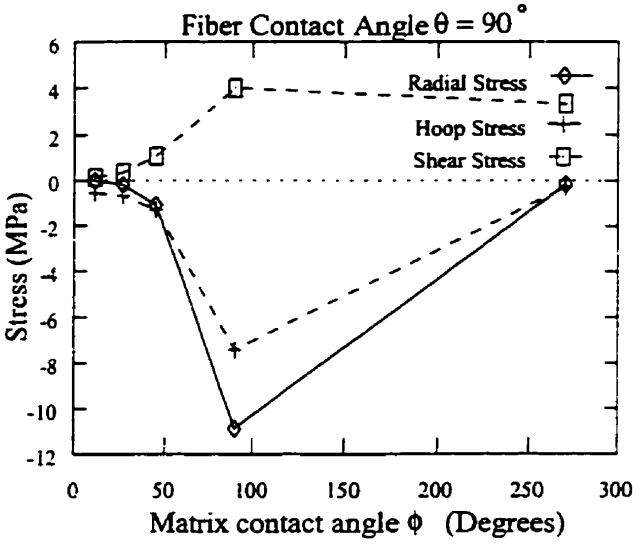

Fig. 9.19: Radial, hoop, and shear stress components at the interface on the free surface for cases 4 and 5 (θ =90°) with different matrix contact angles (ϕ).

9.2.2.6 Effects of Layer Thickness and its Material Properties

The radial, hoop, and shear stress components at the tip of the fiber/matrix contact corner are plotted against the thickness of the covering layer in Fig. 9.20. Significant changes in the radial and hoop stresses are observed if a cut is covered with a small layer of matrix material. The covering layer is most effective when its thickness is about 10% of the fiber diameter. Increasing the thickness further does not show a major effect on the stress components. However, a thicker covering layer causes a sign change in both the radial and hoop stress components which is desirable for the cooling phase of the manufacturing process. The higher thickness of the cover reduces the shear stress value by only a few percentage points. Therefore, the chance of fiber/matrix de-bonding is still high and it depends on the interface strength that is very critical in composites.

The effects of some of the properties of the covering layer on the stresses have also been studied. It may not be possible or practical to get the same properties for the covering layer as the ones for the matrix material. To investigate this, the modulus of the covering layer was assumed to vary from 0.1 to 10 times the matrix modulus. In addition, Poisson ratios of 50 to 75 percent of that of the matrix were considered. Also, some analysis was

performed on the effect of the thermal expansion coefficient of the covering layer on the stress concentration at the fiber-matrix contact corner.

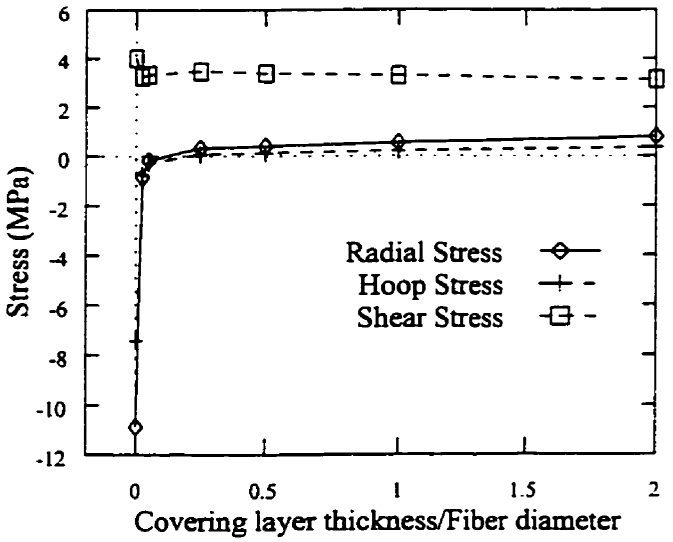

Fig. 9.20: Radial, hoop, and shear stress components at the fiber end vs. the ratio of the covering layer thickness to the fiber diameter.

As expected, the stiffness of the covering layer has a great effect on the nature of the stresses at the fiber-matrix contact corner. As explained earlier, block-T (see Fig. 9.16) plays a major role in preventing fiber/matrix overlapping under axial load. When block-T is of low modulus material, it deforms easily and despite the elimination of the free surface, very high compressive radial and hoop stress components appear at the corner tip. Also, the high deformability of the covering layer reduces the very high tensile radial and hoop stress components in the elements adjacent to the element E' in blocks T and C (see Fig. 9. 21). A plot of the radial, hoop, and shear stress components in the vicinity of the fiber-matrix corner tip against the ratio of the modulus of the covering layer to that of the matrix material is shown in Fig. 9.22. It appears that the radial and hoop stress components change from very high compressive to high tensile with increasing modulus of the covering layer. This change is desirable for preventing matrix cracking and de-bonding when cooling composites from their processing temperature. However, this may adversely affect the composite during the heating phase of working temperature cycles. The very high absolute values of the stresses for both the low and high modulus covering layers may damage the composite in either phase of the temperature cycle. The stress values are low

for $E_{(cover)} / E_m = 1$, therefore using a covering layer material identical to the matrix material is recommended. Choosing a high modulus material for the cover may eliminate the adverse effects of the radial and hoop stress components during cooling, but the high longitudinal shear stress will still be present.

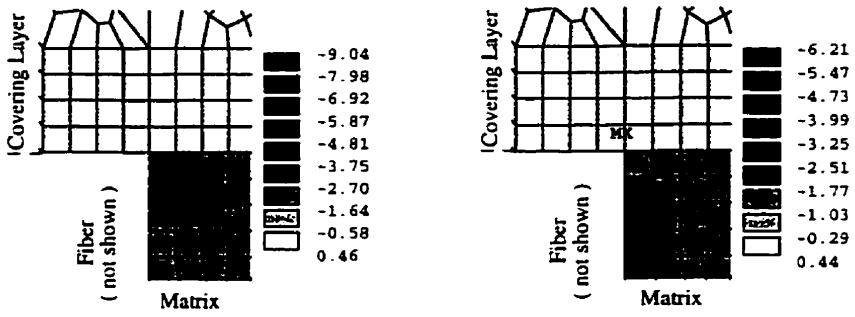

a) Radial stress (MPa)

b) Hoop stress (MPa)

Fig. 9.21: Stress components for the model with a low modulus-covering layer.

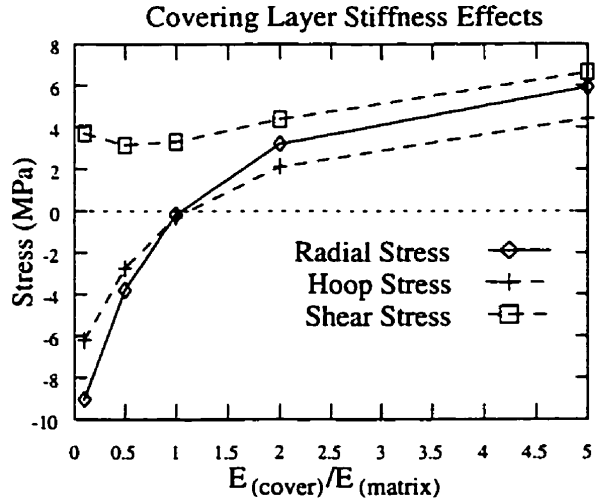

Fig. 9.22: Effects of the Young's modulus of the covering layer on the stress components at the fiber end.

The analysis of the changes in Poisson ratio of the covering layer reveals some interesting results. Fig. 9.23 indicates that the small compressive radial and hoop stress components at the tip of the contact corner of the fiber/matrix interface (see Fig. 9.15) are replaced with high tensile stresses when the layer Poisson ratio (ν_{cover}) is decreased relative to that of the matrix, ν_m. Such a change is desirable for cooling, but it may be harmful

during heating. This also introduces a positive change to the shear stress for the element E' in Fig. 9.14. A lower shear stress is detected at the tip of the fiber/matrix contact corner when Poisson's ratio is decreased. However, with a low ν_{cover}, a relatively high shear stress appears at the elements adjacent to element E' compared to that observed in case 5. In conclusion, a cover with a low Poisson's ratio might prevent cracking in composites during cooling even more effectively than using high modulus materials for the covering layer.

The changes in the radial and hoop stress components due to different Poisson ratios of the cover and matrix can be explained well with the differences in the amount of contraction of the matrix and the covering layer. When ν_{cover} is lower than that of the matrix, the covering layer tends to contract or expand less than the matrix in both the radial and hoop directions. Therefore, the cover not only prevents overlapping but also, to satisfy continuity, resists the matrix shrinkage in both radial and hoop directions generating high tensile radial and hoop stresses at the fiber matrix corner tip. Also, decreasing ν_{cover} results in an increase in the shear modulus of the cover ($G = E/2(1+\nu)$). The matrix with shear modulus lower than that of the covering layer tends to distort more than the covering layer. This decreases the shear stresses in the matrix while increasing them in the covering layer.

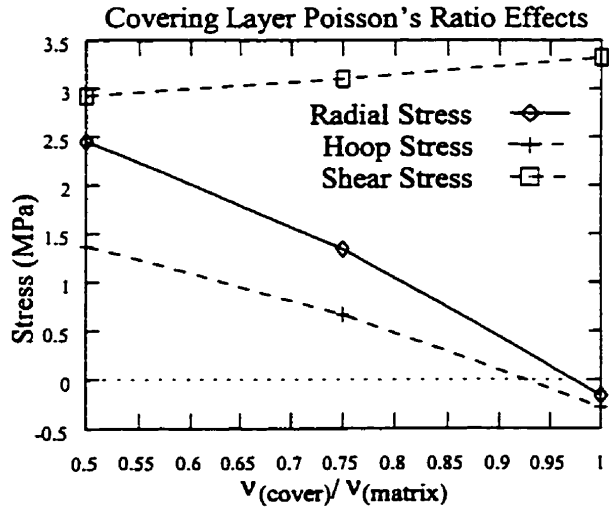

Fig. 9.23: Effects of the Poisson's ratio of the covering layer on the stress components at the fiber end.

Finally, the influence of different thermal expansion coefficients (CTE) for the matrix and the covering layer was investigated for the range $0.5CTE_m \leq CTE_{cover} \leq 1.5CTE_m$. The results indicate that though the CTE mismatch for the composite constituents is responsible for the thermal stress generation, it has little effect on the matrix stresses at the fiber/matrix contact corner. A plot of the radial, hoop, and shear stress components for the element E' against CTE_{cover} / CTE_m is shown in Fig. 9.24. The differences are negligible. The reason could be that other geometrical deformations due to overlapping at the fiber end, rather than the CTE mismatch (which imposes thermal stresses), affect the stress distribution. The differences in ν and E of the covering layer affect the geometrical deformations at the fiber end, while the difference in CTE affects the thermal stresses only. The changes due to the CTE mismatch of the cover and the matrix are pronounced more in the covering layer than in the matrix. This is due to the absence of geometrical deformations like those at the fiber end. The difference in CTE imposes different expansions on the matrix and the covering layer under a unit temperature change. For $CTE_{cover} \leq CTE_m$, the matrix comes under compressive radial and hoop stresses to maintain the same expansion as the covering layer and to satisfy continuity. Meanwhile, it puts the covering layer under tensile stresses in both directions. That is why higher compressive stresses are detected in both directions in the matrix relative to the values obtained when $CTE_{cover} = CTE_m$. It is noted that this phenomenon also increases the tensile stresses in both directions in the covering layer. The shear stress remains almost unchanged in both the matrix and the covering layer, since the mismatch in CTE does not affect the shear properties of the composite constituents.

In summary, with the 3 major material properties of the covering layer discussed so far, it is concluded that it is important to cover the composite cut edges or free surfaces with the same material as the matrix. In all cases, using similar materials for the matrix and the covering layer results in very small radial and hoop stress components that are very desirable. A covering layer with high modulus or with $\upsilon_{cover} < \upsilon_{matrix}$ can be helpful during cooling only.

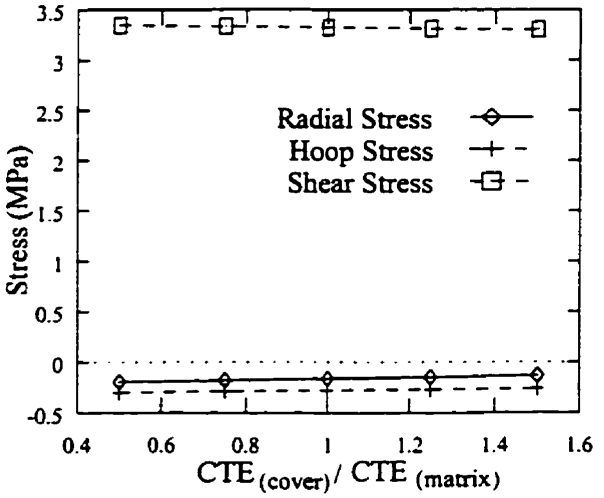

Fig. 9.24: Effects of the thermal expansion coefficient of the covering layer on the stress components at the fiber end.

9.2.3 Fibers Close to the Composite Side Edge (Edge-Fibers)

The study presented so far was conducted on fibers well away from the composite side edge (internal fiber). In this section, the effects of the composite side edge on the stress distribution around the fiber end are discussed. The analysis performed in case 1 (see Fig. 9.3) was repeated with the coupling boundary condition removed from the nodes along the matrix side edge, i.e. line M-M in Fig. 9.1(a). Coupling the nodes along line M-M in the radial direction results in the nodes being restrained against the relative movement in this direction, thus keeping the line straight at all times. The coupling assumption simulates the effects of an adjacent fiber on the line M-M. For the fibers at the composite side edge, the nodes on line M-M are not restrained by this boundary condition. Therefore, with a temperature change of +1°C, the matrix can deform down and inward more easily under the axial load that tends to satisfy continuity in this direction. This creates a higher degree of matrix overlapping at the fiber end than when line M-M is restrained. The differences between the deformation of the edge-fiber and the internal fiber are presented in Fig. 9.25. Much higher stresses appear along the interface in the vicinity of the free surface for the edge-fiber than the internal fiber. A comparison between the stresses shown in Fig. 9.26 and Fig. 9.3 indicates that, for edge fibers, about 50% increase

in stress occurs at the interface in the vicinity of the free surface. Considering this fact, it can be concluded that the edge fibers may be more prone to cracking than the internal fibers. Also, for edge-fibers with covered free surface (depending on the properties of the matrix and the covering layer and the interface strength) the possibility of matrix cracking is higher than for those of the internal fibers.

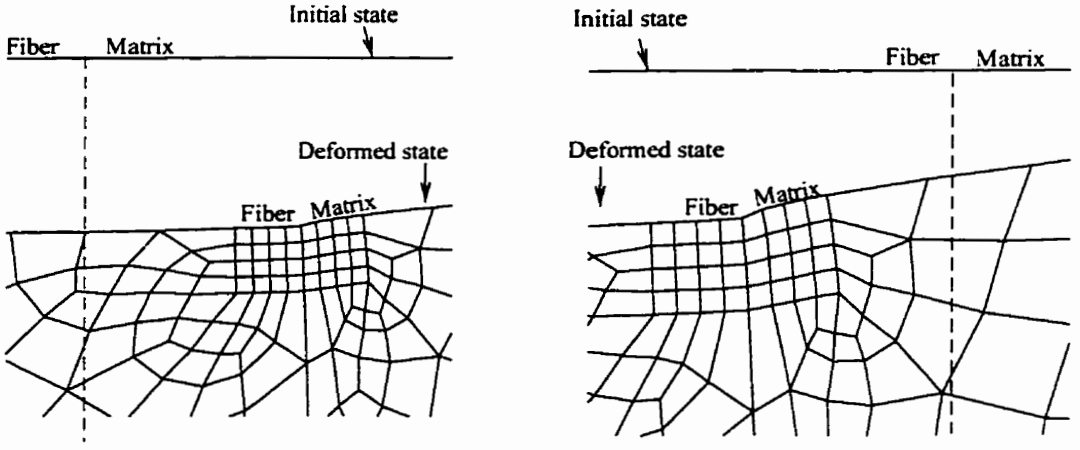

a) Internal fiber b) Edge fiber

Fig. 9.25: Effects of fiber location on the deformation pattern of the free surface.

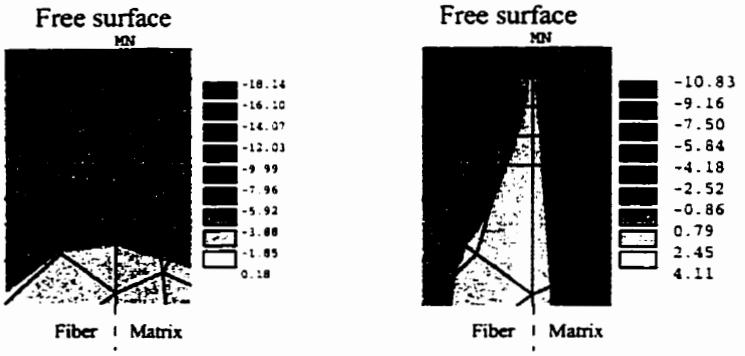

a) Radial stress (MPa) b) Hoop stress (MPa)

Fig. 9.26: Stress components at the side edge of a composite.

9.3 Inelastic Analysis of Composites with a Covering Layer

The elastic analysis has indicted that covering the free surface of composites with a thin layer of matrix-like material is the most effective way of eliminating the very high and damaging radial and hoop stress components at the fiber end. In this section, to examine these effects further, the inelastic behavior of the composite similar to that presented in Chapter 7 is performed. The transient effects are neglected for fast cooling processes (i.e. quenching in water). It is assumed that the free surface of the 3-D model is covered with a thin layer of matrix material (see Fig. 9.27). The thickness of the cover is considered to be one tenth of the fiber diameter. This study is conducted on titanium based matrices (Ti-6Al-4V or Ti-24Al-11Nb) reinforced with SCS-6 fibers.

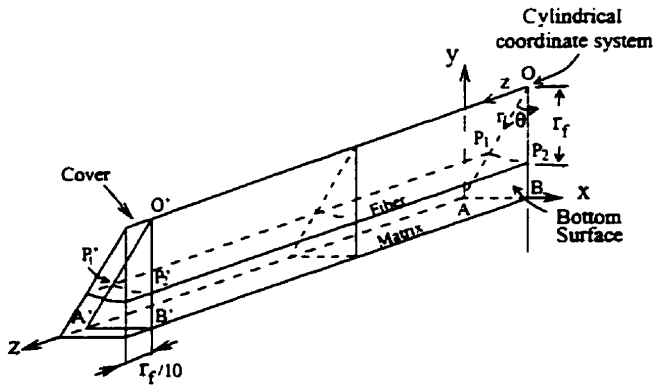

Fig. 9.27: 3-D model with a covering layer.

9.3.1 Residual Stresses in SCS-6/Ti-6Al-4V Composite

The 3-D prism model which simulates the SCS-6/Ti-6Al-4V composite with a matrix-like covering layer on its free surface is cooled to room temperature from the composite processing temperature (T_p = 900°C). Note that, as in Chapter 7, the Ti-6Al-4V matrix is referred to as MMC hereafter.

The thermal residual radial, hoop, and equivalent stress contours of the model at room temperature are shown in Fig. 9.28. To make the matrix interface stresses visible, the fiber stresses are not shown. Like the elastic case discussed previously in this chapter, the results of the inelastic analysis show that the radial and hoop stresses in the vicinity of the

interface at the fiber end are distinctly different from the stresses in composites without cover discussed in Chapter 7 (compare Figs. 9.28 and 7.2 for example). After cooling from T_p, the maximum value of the stress components, which were tensile and appeared at the interface on the free surface for the model without cover, become compressive and show lower absolute values at the interface. In fact, the extreme values of the stresses occur away from the interface when the free surface of the composite is covered. The compressive stresses, which are relatively small, appear at the interface in the vicinity of the fiber end.

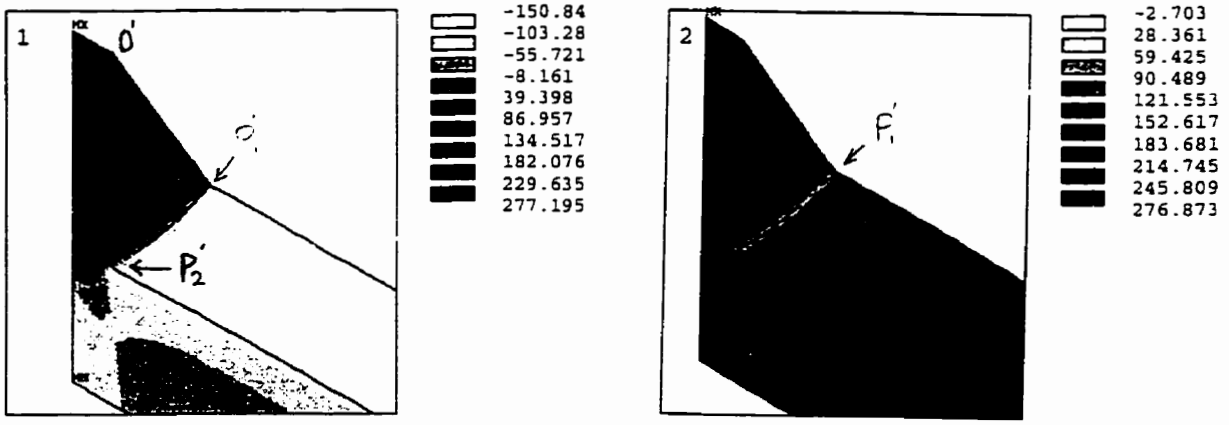

Radial stress (MPa)

Hoop stress (MPa)

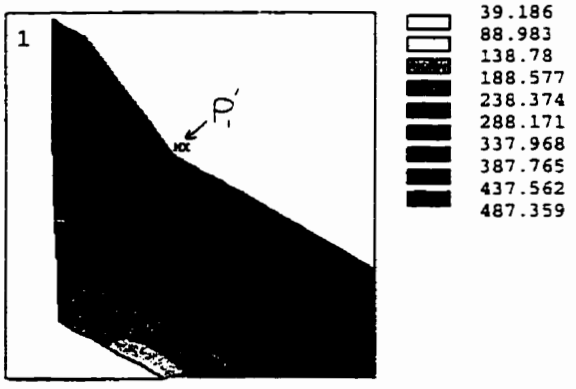

Equivalent stress (MPa)

Fig. 9.28: Effect of covering on the radial, hoop, and equivalent stresses of the Ti-6Al-4V matrix composite generated during cooling from T_p.

Despite the changes in radial and hoop stress components at the fiber end, the maximum value of the equivalent stress appears in this region at the interface at location P'_1. The equivalent von Mises stresses (σ_{eq}) in locations P'_1 and P_2 and the yield strength of the matrix (σ_y) during cooling from T_p are shown in Fig. 9.29. The curve for the inner zone will be discussed later. In the end zone, the figure shows that plastic deformation starts sooner than for the model without cover (compare Figs. 9.29 and 7.1). For the former, plasticity starts at T=650°C, while for the latter it starts at T=360°C. One reason for this difference could be the very high magnitudes of the axial and longitudinal shear stresses in the matrix at the fiber end. These stresses are generated due to the formation of a sharp corner in this location after covering the free surface. A 3-D contour plot of the axial and longitudinal shear stress components at room temperature is shown in Fig. 9.30. As the figure shows, very high axial and longitudinal shear stresses occur at the interface at the fiber end. The maximum of the compressive stresses appears at location P'_1. The origin of these stresses and their effects will be discussed in more detail in section 9.3.3.

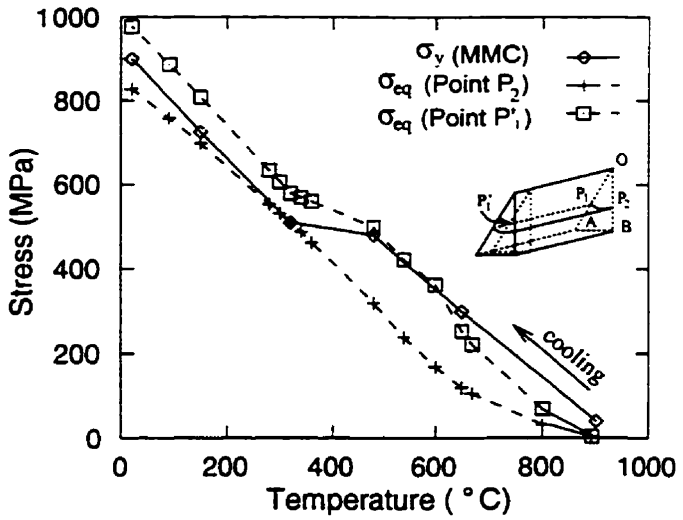

Fig. 9.29: Effect of covering on the stress history of Ti-6Al-4V matrix in the end zone (P'_1) and the inner zone (P_2).

For the composite without cover, these stress components are also present in the vicinity of the fiber end but they cause a lower equivalent stress. The reason is that (for the model without cover) all the stress components near location P'_1 are high and tensile but the differences between them are small, thereby resulting in small σ_{eq}. For the model with cover, the difference between the stress components is large due to smaller radial and hoop

stresses and this results in higher equivalent stresses. This high equivalent stress causes plastic strains in the early stage of cooling of the covered composite unlike in the composite without cover. Fig. 9.31(a) presents the equivalent plastic strain (ε_{eq}^{pl}) in the matrix at T=360°C. The strain values are much different from those of Fig. 7.3(a) for the model without cover. There are several other differences between the composites with and without cover. For example, comparing the curves for σ_{eq} at location P'_1 presented in Figs. 9.29 and 7.1, it is clear that higher equivalent stresses appear at room temperature in the end zone if the free surface of the composite is covered at the melting temperature.

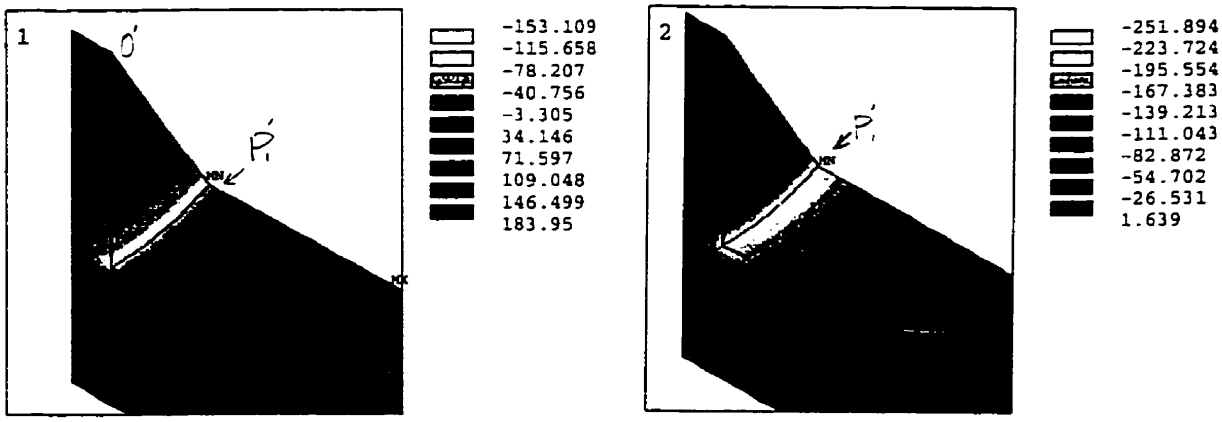

Axial stress (MPa)

Longitudinal shear stress (MPa)

Fig. 9.30: Effect of covering on the axial and longitudinal shear stress components of the Ti-6Al-4V matrix composite generated during cooling from T_p.

Comparing σ_{eq} at location P_2 in Figs. 9.29 and 7.1 shows that the plastic strain in the inner zone starts at the same temperature as that for the composite without cover (T=320°C). This indicates that covering does not influence the stresses in the inner zone. However, ε_{eq}^{pl} in the inner zone of the covered model at room temperature (see Fig. 9.31(b)) is slightly lower than ε_{eq}^{pl} at room temperature for the model without cover (see Fig. 7.3(b)) for the model without cover. One reason could be the high plastic strains in the end zone of the covered model which cause a large amount of stress relaxation in the rest of the composite, hence reducing the total amount of plastic strain in the inner zone. As Fig. 9.29 shows, like the composite without cover, the equivalent stress in the inner zone of the covered composite drops below the yield strength of the material at T=320°C.

As a result, for temperatures lower than T=320°C no more plastic deformation occurs in the inner zone. The stress components in the inner zone of the composite with cover (which are not shown here) are very close to the stresses for the composite without cover as shown in Fig. 7.5.

Again, the most important effect of covering the free surface of composites is the change in sign of the radial and hoop stress components at the end of the fiber during cooling from T_p. The compressive stresses prevent crack opening or interface debonding. For composites with free surfaces, the tensile radial and hoop stress components may damage the composite integrity by cracking the matrix or debonding the fiber/matrix interface.

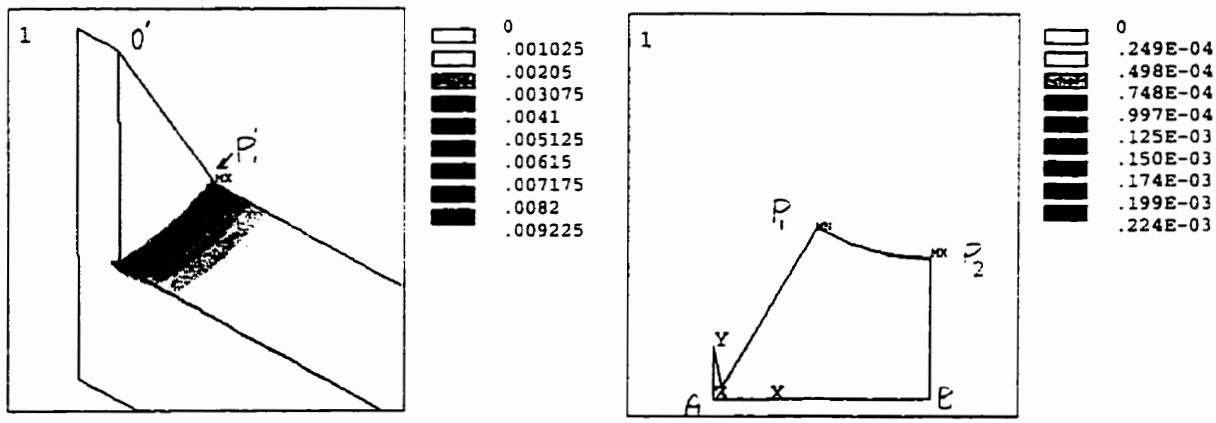

Equivalent plastic strain (full model) Equivalent plastic strain (inner zone)

Fig. 9.31: Effect of covering on the equivalent plastic strain in the end zone and the inner zone of Ti-6Al-4V matrix composite (at T = 360°C).

9.3.2 Residual Stresses in SCS-6/Ti-24Al-11Nb Composite

The effects of low strength matrices on the covering the free surface of composites is studied by repeating the elasto-plastic analysis of the SCS-6/Ti-24Al-11Nb composite (which was discussed in Chapter 7). Here, the composite is cooled from the processing temperature (T_p). As in the case of the composite without cover, the maximum values of σ_{eq} in the end zone and the inner zone occur at locations P'_1 and P_2, respectively. A graph

of σ_{eq} (in these locations) versus temperature is shown in Fig. 9.32(a). The figure also shows σ_y and σ_y^h (the yield strength of the strain hardened matrix) at both locations versus temperature. The corresponding equivalent plastic strain in the same locations is plotted against temperature in Fig. 9.32(b). The figure shows that covering the free surface of this composite also accelerates the plastic deformation of the matrix in the end zone. Changes in the status of the radial and hoop stress components in the end zone due to the covering layer affect the equivalent stress in this region. Upon cooling, an increase in σ_{eq} of the end zone quickens the onset of plasticity, a feature not seen in the composite without cover (compare Figs. 7.13(a) and 9.32). Therefore, more plastic strain is accumulated when the composite is covered with a thin layer of matrix-like material. The yield strength of the material is increased by the plastic strain accumulation due to the strain hardening characteristic of the matrix. The figures show that the increase in yield strength (σ_y^h) at point P'_1 is much higher than that obtained for the model without cover due to the higher plastic strain for the covered composite. As Fig. 9.32(a) shows, σ_y^h of the matrix in the end zone is well above σ_y. However, depending on the stress-strain characteristic of the material at a certain temperature level, the high plastic strain may strengthen the material such that σ_{eq} falls below σ_y^h. Such a stress state occurs at T=200°C as shown in Fig. 9.32(a). Therefore, as Fig. 9.32(b) shows, the plastic strain in the end zone at location P'_1 remains constant at temperatures lower than T=200°C. Since σ_y^h is history dependent, it increases until room temperature is reached.

Unlike the end zone, plastic deformation in the inner zone continues until room temperature is reached. Again, it appears that covering the composite free surface does not affect the start of the plastic deformation in the inner zone. However, at room temperature, the plastic strain of the material is slightly different when compared to the results obtained for the composite without cover (see Fig. 7.18(a)). The plastic strain of the composite with cover is lower than that for the model without cover (maximum ε_{eq}^{pl} = 0.2902e-2 and 0.2914e-2 for models with and without cover in the inner zone, respectively). As explained earlier, it could be due to the higher plastic strain in the end zone in presence of the cover.

The stress relaxation associated with the plastic deformation reduces the plastic strain in the inner zone. The changes in the yield strength and the inner zone stresses of the composite with cover appears to be negligible due to the small difference in the amount of inner zone plastic strains of the models with and without cover.

In general, as explained previously, the main effect of the covering is its ability to reduce the high magnitude of radial and hoop stress components at the fiber end.

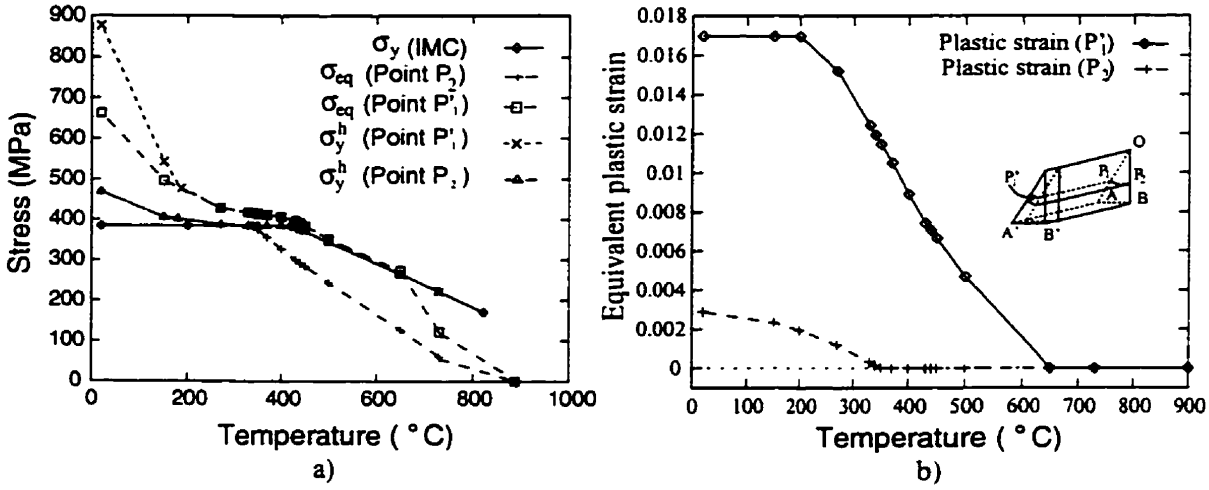

Fig. 9.32: Effect of covering on the equivalent stress and plastic strain generated in the end zone (P'_1) and in the inner zone (P_2) of the Ti-24Al-11Nb matrix composite during cooling from T_p.

9.3.3 Axisymmetric Analysis of Composites with Covered Free Surface

In the last two sections, the analysis of the covered 3-D model showed that σ_{eq} and ε_{eq}^{pl} in the end zone (at location P'_1) increase in comparison to their values for the composite without cover. To check how reliable these results are and whether the 3-D prism model can be utilized in analyzing the composite with cover, the study is repeated by employing the axisymmetric model. The same model used in Chapter 7 is considered with a thin layer of matrix-like material on its free surface. The details of the discretization of the model with its covered free surface in the vicinity of the singular point are similar to that shown in Fig. 9.14.

The yield strength of the matrix (σ_y), σ_{eq}, and σ_y^h at locations A, J, and B during cooling from T_p are presented in Fig. 9.33(a). As usual, A is located at the fiber end at the fiber/matrix interface, J is 0.01μm away from A at the interface, and B is located in the inner zone. The variation of equivalent plastic strain (ε_{eq}^{pl}) for the same locations with temperature are shown in Fig. 9.33(b). Comparing these plots with the plots of equivalent stresses and strains at the same locations for the model without cover (presented in Fig. 7.19) shows high changes in stress and strain magnitudes. The very high σ_{eq} and ε_{eq}^{pl} in the end zone (at location A) are sharply reduced when covering is employed. This is contrary to the results of the 3-D model mentioned above and will be explained in the next paragraph. The reduction in stress and plastic strain is due to changes in stress components at the fiber end in the presence of the cover. The radial, axial, and hoop stress components become compressive and, due to the relatively close values, the magnitude of the equivalent stress is reduced. These stresses and σ_{eq} during cooling from T_p for location A are shown in Fig. 9.34. Therefore, the plastic deformations for the model with covered free surface are lower than those for the model without cover. The compressive nature of the stress components at location A (Fig. 9.34) is substantially different than for the composite with no cover. This may be explained as follows: Upon cooling, the extra covering layer of the matrix on the fiber end will apply a compressive axial stress on the rest of composite due to the CTE mismatch (Fig. 9.35). The compressive axial stress causes the matrix to overlap the fiber end and is capable of changing the overall deformation and stress states at the fiber end. The overlapping generates compressive radial and hoop stresses at the fiber end (Abedian and Szyszkowski, 1997) (see Fig. 9.34). Note again that the stresses are tensile when cooling the composite without cover.

The contradiction between the results of the 3-D and axisymmetric models in predicting σ_{eq} and ε_{eq}^{pl} at the fiber end for the covered composite (as compared to the composite without cover) may be explained as follows. One reason may be the difference between the stress components calculated by the two models for the fiber end. Since the 3-D model is meshed with coarser elements, the magnitudes of the compressive radial and

hoop stress components are smaller than those obtained with the axisymmetric model. This will increase the equivalent stress and, as a result, the plastic strain shows some increase. Note that σ_{eq} is related to the difference between the stress components.

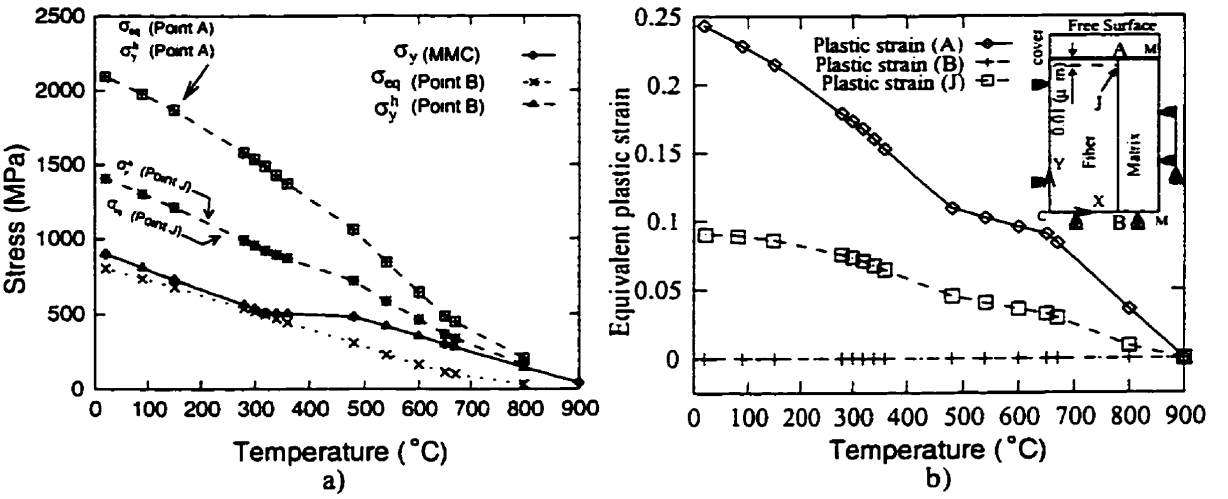

Fig. 9.33: Axisymmetric modeling of the covering process; (a) equivalent stress (b) equivalent plastic strain at locations A, J, and B.

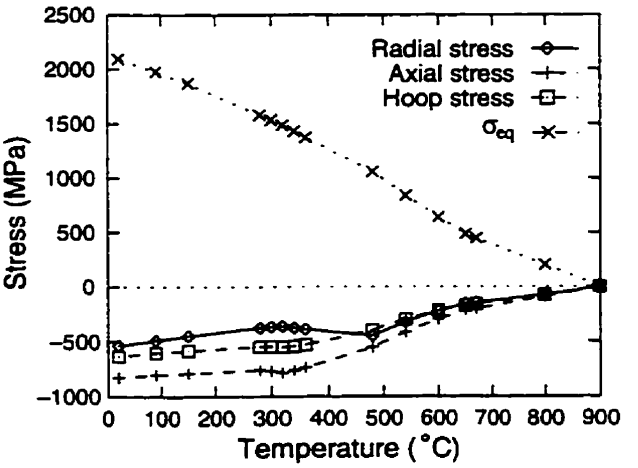

Fig. 9.34: Effect of covering on the stress components at the fiber end at location A.

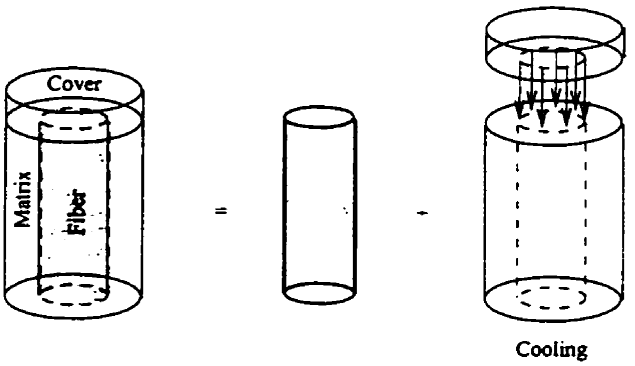

Fig. 9.35: Effect of thermal contraction of the cover on composite deformations.

The plastic strain distribution along the interface of the axisymmetric model at room temperature is shown in Fig. 9.36(a). A larger scale graph of the curve around location A in Fig. 9.36(a) is shown in Fig. 9.36(b). Like the composite without cover, the high plastic strain at location A is shown to be a very localized phenomenon. The plastic strain drops from about 0.25 at location A to less than 0.05 at about 0.06μm away from the fiber end. However, comparing the distribution of ε_{eq}^{pl} in Fig. 9.36(b) with that of the composite without cover presented in Fig. 7.20, the plastic strain along the interface in the vicinity of the fiber end (i.e. location J) is slightly higher for the model with cover. Comparing σ_{eq} and ε_{eq}^{pl} at location J in Figs. 9.33 and 7.19 shows some increment in their values when the free surface of the composite is covered. This may be due to the decrease in plastic strain at location A in presence of the cover. A low plastic strain at this point results in a low stress relaxation. Therefore, compared to the composite without cover, higher stresses and, consequently, higher plastic strain can be expected at some point away from location A, i.e. point J.

Comparing Figs. 7.19 and 9.33, the equivalent stress and plastic strain at point B seem to be also affected by the presence of a covering layer. Compared to the composite without cover, a higher plastic strain along the interface away from location A (i.e. at point J) affects the stresses in the inner zone i.e. at point B. This is due to the relaxation effect of the plastic strains, i.e. the lower stresses at point B result in lower plastic strains in the inner zone. Due to the scale of the graphs, these differences are not clearly shown.

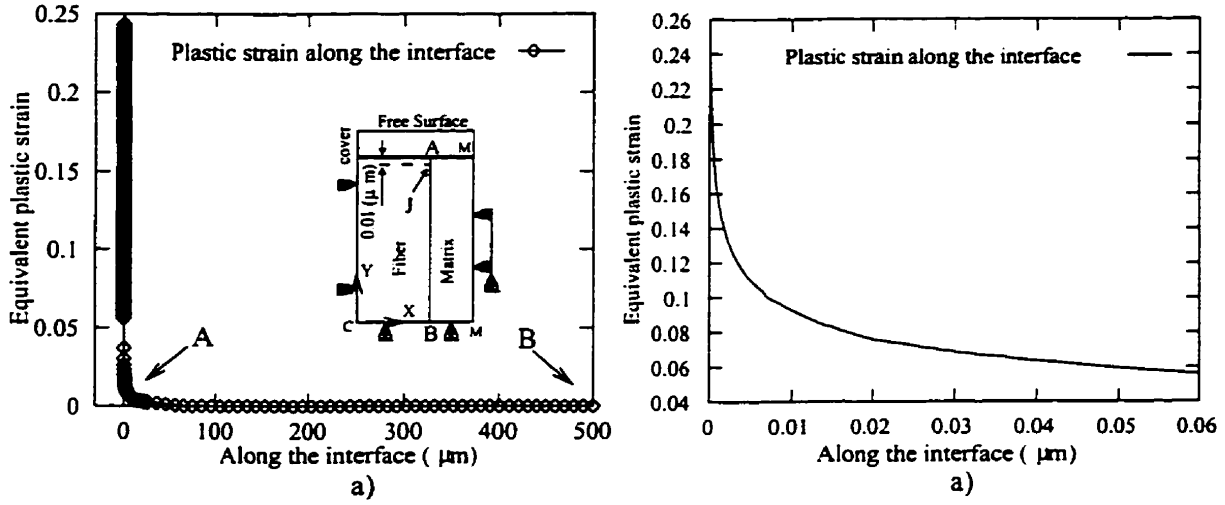

Fig. 9.36: (a) Plastic strain distribution along the interface, (b) magnification of the plastic strain in the vicinity of the fiber end

In general, the results obtained from the axisymmetric model are in a good agreement with those of the 3-D prism model. Of course, the 3-D model analysis (due to the coarse mesh) is less accurate in the neighborhood of the singular point than the axisymmetric analysis. However, the solution at a short distance from the singular point is very close. This similarity becomes more apparent when one compares the equivalent stress and plastic strain obtained by the 3-D model with the results at points J and B of the axisymmetric model. With covering, they show some increase at a short distance to the singular point relative to the composite without cover. However, they decrease in the inner zone.

9.4 Two Stage Process of Covering of Composites Free Surface

In the analysis of composites presented so far, it was assumed that the composite and the covering layer on the free surface were manufactured in one single processing stage. It was also assumed that the composite and the covering layer are cooled to room temperature at the same time. However, from the manufacturing point of view, different scenarios are possible. For example, for composite structures that are made from pre-manufactured composite panels or rods, any required cutting would generate new free surfaces. Also, drilling holes in composites makes fresh cut surfaces. Any fresh cut surface may then be covered with a layer of a new material or matrix-like material.

Simulation of such a covering process is analyzed in two successive stages. In the first stage, the stress and displacements on the free surface of a composite cooled from the processing temperature are analyzed. Very high residual stresses and plastic deformation are already present at the fiber end. The analysis of the covering process is performed in the second stage. Here, three schemes of the two-stage covering process that are different from the manufacturing point of view are studied.

In the first scheme, a thin layer of the molten matrix material is applied on the free surface of the composite which is at room temperature. In this scheme, the residual stresses are sufficiently high so that applying the hot cover material can disturb the residual stresses and plastic strains by partially relieving them. Note that for this scheme, the exact temperature distribution in the material is difficult to obtain.

In the second scheme, the cooled composite is re-heated to slightly below its processing temperature T_p, and then the cover is cast on the free surface. The difference between the two schemes is in the different magnitudes of the residual stress and plastic deformations in the composite before applying the cover. For this scheme, the analysis of the temperature distribution is easier. Also, re-heating of the composite close to its processing temperature can relieve most of the residual stresses present.

For the third scheme, the residual stresses and plastic strains at the fiber end are eliminated by physically cutting the end of the composite before applying the covering layer. These analyses will be presented in sequence. To highlight the differences between the one-stage and two-stage covering processes, an elastic study of the two-stage scheme is discussed first.

9.4.1 Elastic Analysis of the Two-Stage Covering Process

A simplified elastic analysis of the two-stage covering process is discussed in brief. The materials, which were considered in the elastic analysis of the one-stage scheme of the covering process, are considered here again. Since in ANSYS all the elements must be generated before the solution phase, the element birth-death capability is used. To model

any material addition or removal occurring in the two-stage covering process, the respective elements are deactivated or killed (material removal) or the previously killed elements are reactivated (material addition).

The full model consisting of the composite and the covering layer (see Fig. 9.14) is created first. To analyze the residual stresses before the cover is applied, the elements of the covering layer are deactivated. When killing elements, the modulus of the affected elements is reduced to a negligible value. In the second stage, to analyze the effect of the covering layer on the already stressed composite, the elements of the covering layer are reactivated (i.e. the elastic modulus of the elements is restored). Unlike the elastic analysis of the one-stage covering process, the analysis is performed for 1°C temperature reduction. In the second stage, after reactivating the elements of the cover, the temperature of the composite is increased by 1°C to see how the covering layer affects the stress state. It is expected that despite the assumed elastic nature of the process, the covering layer should prevent relaxation to occur after this temperature cycle. In the last phase of the analysis, the temperature of the system (i.e. composite plus the covering layer) is decreased by 1°C again to compare the stress state with the stresses of the first stage (i.e. the stresses of the cooled composite without the covering layer).

During the first cooling stage of the composite without the covering layer, very high tensile radial and hoop stress components are expected to occur at the singular point. A contour plot of the stress components for the composite cooled by 1°C is shown in Fig. 9.37. At this stage, the elements of the cover are reactivated. The absolute values of the stresses are the same as the results presented in Fig. 9.3 where a similar model was heated for 1°C. The stress components, in the presence of the cover and after 1°C heating, are shown in Fig. 9.38. After the temperature reversal, as the figure shows, the stresses change but there are still high tensile stresses present near the singular point in the composite. One reason for the stresses remaining high could be due to the resistance of the covering layer in relieving the previous deformations. The covering layer does not let the fiber and the matrix deform freely back to their original shape. For example, the axial

displacement of the composite during the three-stage temperature change is shown in Fig. 9.39. As Fig. 9.39(b) shows, the matrix contraction due to the first cooling stage (see Fig. 9.39(a)) does not disappear fully after heating the composite and the cover to the original temperature.

The above effects could also be explained by the overlapping hypothesis. Previously, (sections 9.2.2.5 and 9.3.3) it was shown that upon heating, the covering layer could change the sign and magnitude of radial and hoop stress components at the fiber end by reducing the overlapping. As Fig. 9.15 depicted, the stress values are sharply reduced at the singular point. Therefore, when heating the composite with the cover in the two-stage covering process, no more overlapping occurs. It results in very small changes in the residual stresses. Hence, the stresses generated in the composite without cover during cooling from the processing stage remain the same.

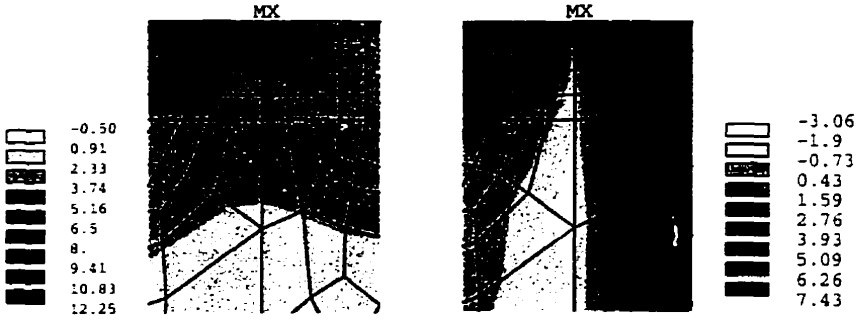

Fig. 9.37: Radial and hoop stress components generated by 1°C cooling of the graphite/epoxy composite without cover.

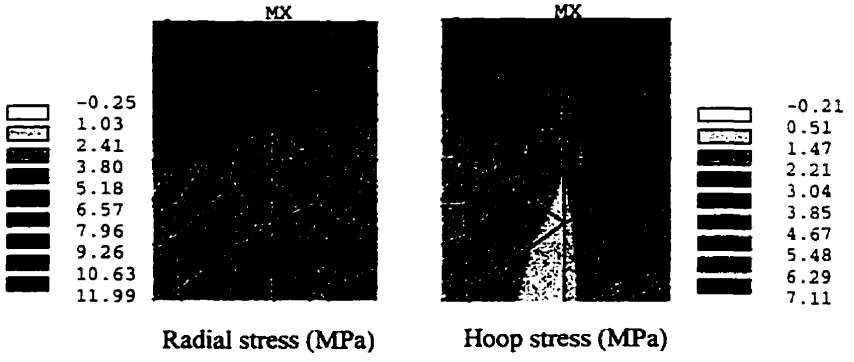

Fig. 9.38: Radial and hoop stress components generated during reheating the graphite/epoxy composite by 1°C in presence of the cover.

Cooling the composite with cover again by 1°C shows that the stresses at the singular point remain relatively constant. The radial and hoop stress contours for this stage are shown in Fig. 9.40. The cover influences the stresses very little. The free surface deformation is depicted in Fig. 9.39(c). The absolute value of the axial deformation of the matrix shows a small increase.

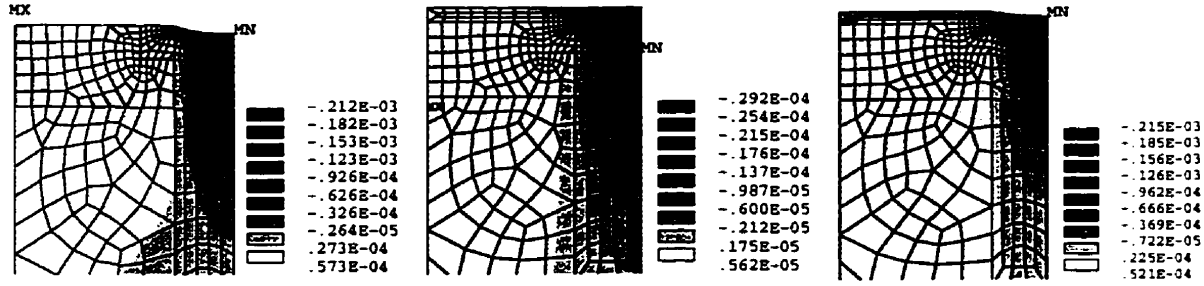

a) Without cover (1° C cooling) b) With cover (1° C heating) c) With cover (1° C cooling)

Fig. 9.39: Effect of covering on axial deformation of the composite during cooling and heating.

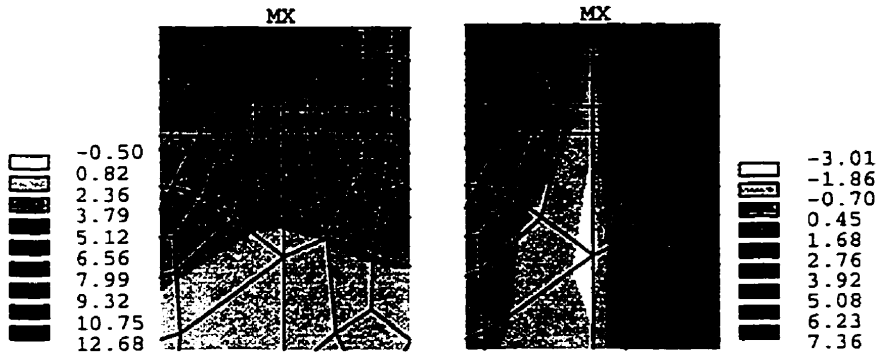

Radial stress (MPa) Hoop stress (MPa)

Fig. 9.40: Radial and hoop stress components at the fiber end in presence of the cover for 1°C cooling.

9.4.2 Nonlinear Elasto-Plastic Analysis of the Two-Stage Covering Process

Since pouring the hot covering material on the free surface of a composite sample disturbs the temperatures of the fiber and the matrix to a distance from the free surface, a coupled nonlinear thermal-stress study of the two-stage covering process was performed. The temperature disturbance may influence the thermal residual stress distributions in the

vicinity of the free surface. All three schemes discussed previously are considered. The analyses are conducted using the axisymmetric model with the dimensions and mesh pattern as used in section 9.3.3. The SCS-6/Ti-6Al-4V composite is again considered.

9.4.2.1 Thermal Analysis of the Two-Stage Covering Process (Scheme 1)

In the first manufacturing scheme, it is assumed that the composite is cooled down from the processing temperature (T_p) and then a hot covering material is poured on the free surface of the composite. The elements of the cover are "killed" first to obtain the temperature profile of the fiber and the matrix with time. The calculated temperature distributions are used to find the residual stresses at the fiber end on the free surface due to cooling of the composite from T_p.

The second stage of the thermal analysis simulates pouring the hot covering material on the free surface. A short extra thermal load step was added to the thermal analysis procedure such that after reactivating the "killed" elements in the first load step, these elements were heated to the composite processing temperature (T=900°C). To ensure that this heating stage of the elements of the cover is not affecting the temperature of the composite, the thermal conductivity of the elements of the fiber and the matrix were reduced to nearly zero, while their thermal capacities were assumed to retain their magnitudes. In this way, due to the negligible thermal conductivity of the fiber and the matrix, a very limited amount of heat could go through either one during heating the elements of the cover. The unchanged thermal capacity of the fiber and the matrix helps in retaining their temperature profiles (i.e. at room temperature). Finally, in the third stage, with the restoration of the thermal properties of the fiber and matrix to their original values, the heated cover and the composite were cooled together to room temperature. The calculated nodal transient temperatures (varying with time) are subsequently used in the stress analysis.

The temperature profiles at point A (which is located at the free surface at the singular point) and point M' (located in the matrix in the inner zone) during the 3 stage

thermal analysis are shown in Fig. 9.41. The cooling stage from T_p (the part marked with I on the graph) is similar to what was explained in Chapter 4. An almost uniform temperature occurs in the whole composite during this stage due to high thermal conductivity of the fiber and the matrix. However, the differences appear after the hot covering layer is poured on the free surface of the cooled composite. As Fig. 9.41 shows, upon pouring the hot covering material, the temperature of the nodes on the free surface sharply increases (thermal shock). But, due to the low temperature of the composite, the temperature of these nodes do not increase to the temperature of the cover. This is because of the very high conductivity of the composite constituents and low thickness of the covering layer. The thin covering layer stores a very low amount of heat that is not sufficient to increase the temperature of the whole composite. Also, the high conductivity of the composite constituents causes the composite to transfer heat from the covering layer to other parts of the composite in a very short time. As the temperature profile of point A shows, the temperature at this location increases to about 400°C. Point A is located on a node which is shared with four elements (see Fig. 9.42). Two of the elements are on the covering layer (which has a temperature of 900°C) and the other two elements are located on the fiber and the matrix regions that are at room temperature. Therefore, considering these elements temperature, an average temperature of more than 460°C is expected for the node at location A. However, the lower temperature of A (i.e. 400°C shown in Fig. 9.41) is due to the transfer of heat from the cover to the neighboring nodes in the fiber and matrix that takes place in a very short period of time.

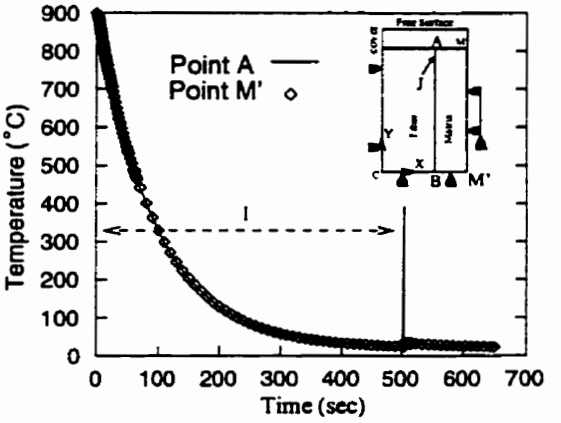

Fig. 9.41: Time-temperature profiles at locations A and M' during covering process.

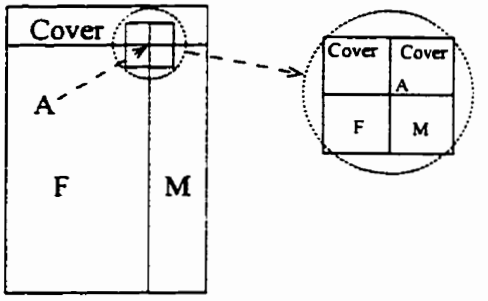

Fig. 9.42: The meshed pattern at the fiber end.

The mechanism of the heat transfer, which causes a very rapid drop in the temperature of the cover and the composite, is explained by the variation of temperature distribution in the covered composite with time (Fig. 9.43). The high temperature gradient between the cover and the composite and also between the cover and air cause the heat to flow out of the cover into the composite and also into the air. This causes the temperature of the cover to drop very fast. The conductivity of the fiber is higher than that of the matrix. This causes the temperature of the cover on top of the fiber to drop faster than that in the part that covers the matrix free surface (see Fig. 9.43(b)). In a very short time (t = 0.024 sec), the temperature becomes relatively uniform across the model with a very low gradient along the fiber length (Fig. 9.43(c)). The time is very short because of the very small amount of heat that the cover has (its thickness and volume are small). In about one second, the temperature of the system (fiber, matrix and cover) becomes uniform. The temperature value in Fig. 9.43(d) shows that the heat stored in the covering layer is just enough to increase the temperature of the whole composite by slightly over 10°C.

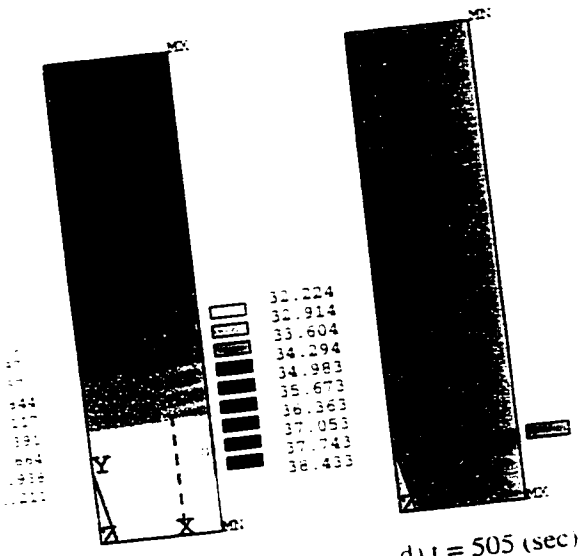

c) t = 504.024 (sec) d) t = 505 (sec)

ıtion in the first second of cooling of a hot
m temperature composite sample.

-Stage Covering Process (Scheme 1)

ling to the temperature distribution in the
section. The first stage of the process, whi
: from $T_p = 900°C$, is similar to what was
lanation on the small differences is present
ing) imposes a temperature cycle on the a
vas shown before, the inner zone tempe
10°C. The corresponding stress analys
ed in sequence.

· stresses for the stage where the composite
e cover are deactivated. Fig. 9.44(a) illustr
the variation of σ_y (of the matrix) with t
ne same locations is also shown in Fig.
comparing these results with the results
. 7.19). This could be the result of numeric

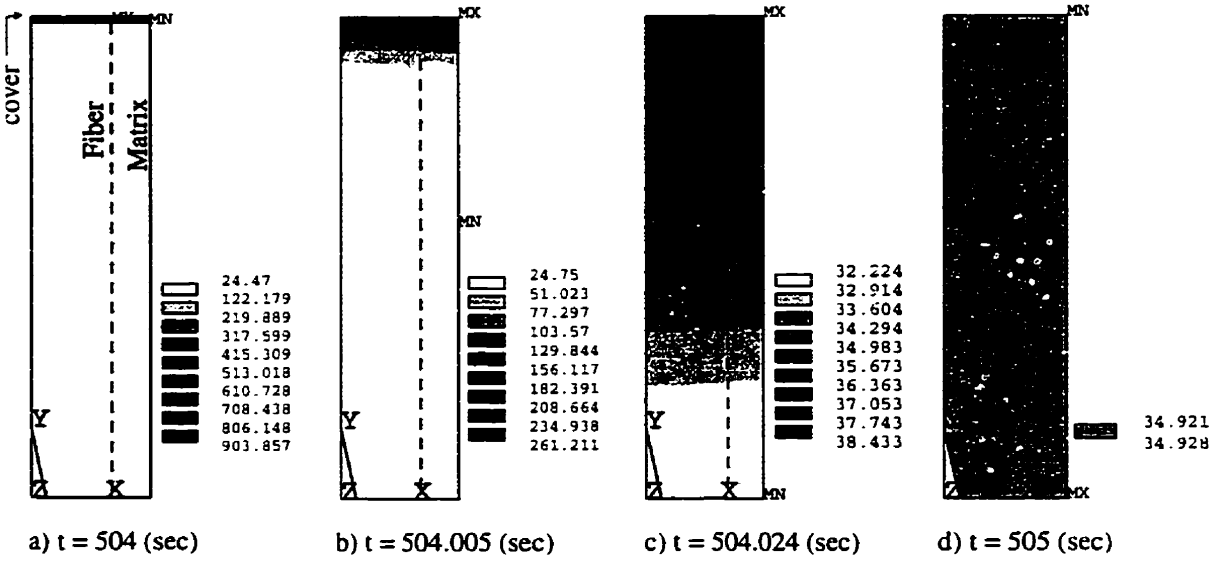

Fig. 9.43: Temperature distribution in the first second of cooling of a hot cover poured on a room temperature composite sample.

9.4.2.2 Stress Analysis of the Two-Stage Covering Process (Scheme 1)

The stress analyses corresponding to the temperature distribution in the composite (see Fig. 9.41) are discussed in this section. The first stage of the process, which involves cooling the composite without cover from $T_p = 900°C$, is similar to what was discussed in Chapter 7, section 7.6. A brief explanation on the small differences is presented here. The second stage of the process (covering) imposes a temperature cycle on the areas close to the free surface. However, as was shown before, the inner zone temperature of the composite is changed only by 10°C. The corresponding stress analysis under the temperature cycle will be discussed in sequence.

To model the free surface stresses for the stage where the composite is cooled from T_p, the elements representing the cover are deactivated. Fig. 9.44(a) illustrates σ_{eq} and σ_y^h at locations A, J, and B and the variation of σ_y (of the matrix) with temperature. The equivalent plastic strain at the same locations is also shown in Fig. 9.44(b). A small difference was found when comparing these results with the results obtained for the composite without cover (Fig. 7.19). This could be the result of numerical errors generated

by the element birth-death procedure. The deactivation process does not eliminate the effects of the elements completely. Although the elastic modulus of the elements is reduced, the elements still exist and this may affect the results by a small percentage. As Fig. 9.44 shows, this stage of the analysis results in high equivalent stress and plastic strain that are localized at the singular point as was discussed in Chapter 7.

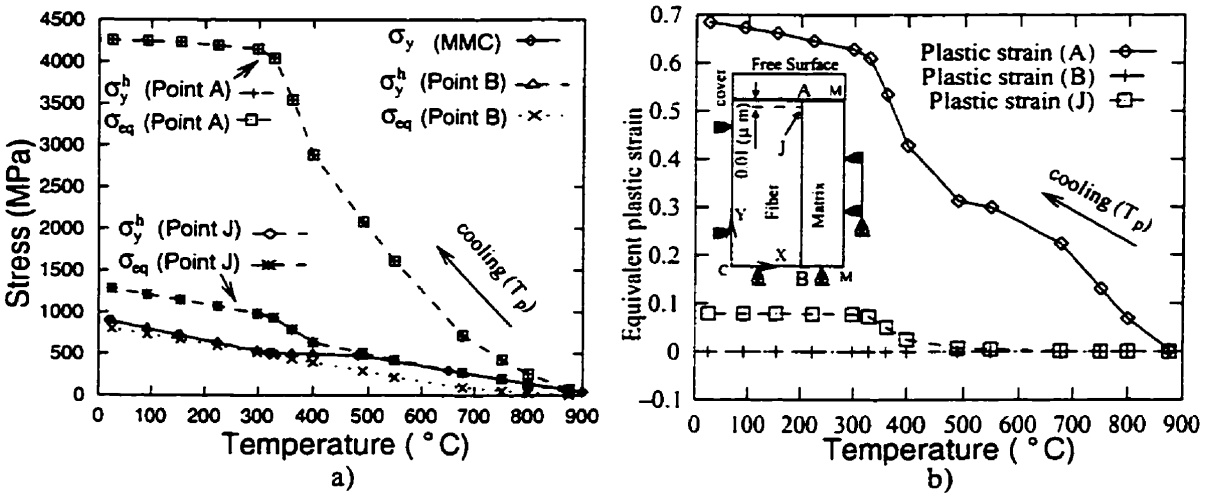

Fig. 9.44: Effect of two-stage covering on the equivalent stress and plastic strain at locations A, J, and B.

The process of pouring the covering layer on the free surface of the composite induces a temperature cycle in the composite. The temperature in the region close to the free surface goes up to about 400°C while the inner zone of the composite sees a temperature increase of no more than 10°C. The effects of this temperature cycle upon the residual stress and plastic strain states of the composite are explained here.

In addition to σ_{eq} and σ_y^h, the radial and hoop stress components at location A corresponding to the temperature profile of Fig. 9.41 are presented in Fig. 9.45. The thermal shock reduces the residual stresses at this location and consequently σ_{eq} is reduced. However, due to the strain hardening characteristic of the material and its dependence on the plastic strain history, the material yield strength increases with thermal shock. Comparing σ_{eq} and σ_y^h for the period of thermal shock shows that no more plastic strain occurs during the cycle at point A. Despite the presence of the cover during the

temperature cycle, the results obtained for σ_{eq} and σ_y^h are very similar to those of the composite without cover discussed in Chapter 7 (see Fig. 7.21(a)). The radial and hoop stress components are also similar to those of the model without cover (see Fig. 7.21(b)). Comparing the results of the one-stage covering process with the results of the two-stage process, some differences are noticed. The main difference appears in the sign of the stress components. Fig. 9.45 shows that the radial and hoop stress components for the two-stage covering are tensile, while the stresses are compressive for the one-stage covering (see Fig. 9.34). For the two-stage covering, despite the presence of the cover during the thermal shock, the high residual stresses left over during cooling from T_p govern the composite response to thermal shock. Therefore, upon cooling, these tensile stresses may provoke fiber/matrix debonding or matrix cracking while the compressive stresses prevent these kinds of damages for the one-stage covering process.

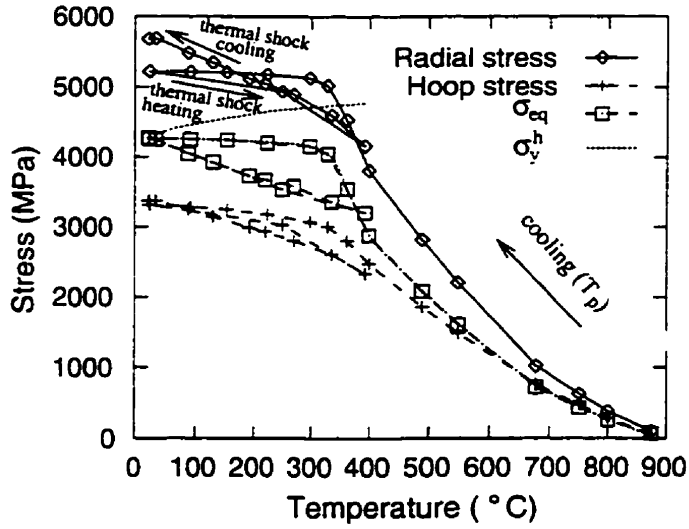

Fig. 9.45: Stress components at location A during cooling of the composite from processing and during temperature cycling.

A plot of σ_{eq} and σ_y^h for locations J and B for the temperature profile shown in Fig. 9.41 is presented in Fig. 9.46(a). The equivalent plastic strain values for points A, J, and B for the same temperature profile are also presented in Fig. 9.46(b). As the stress and plastic strain curves for point J show, the effects of thermal shock can be felt at some distance from the singular point. Like the axisymmetric analysis of the composite without cover in Chapter 7, the stresses at J show some increase and cause some more plastic strain

under the thermal shock situation. The increase in σ_{eq} and the formation of plastic strain under thermal shock are shown in Figs. 9.46(a) and (b).

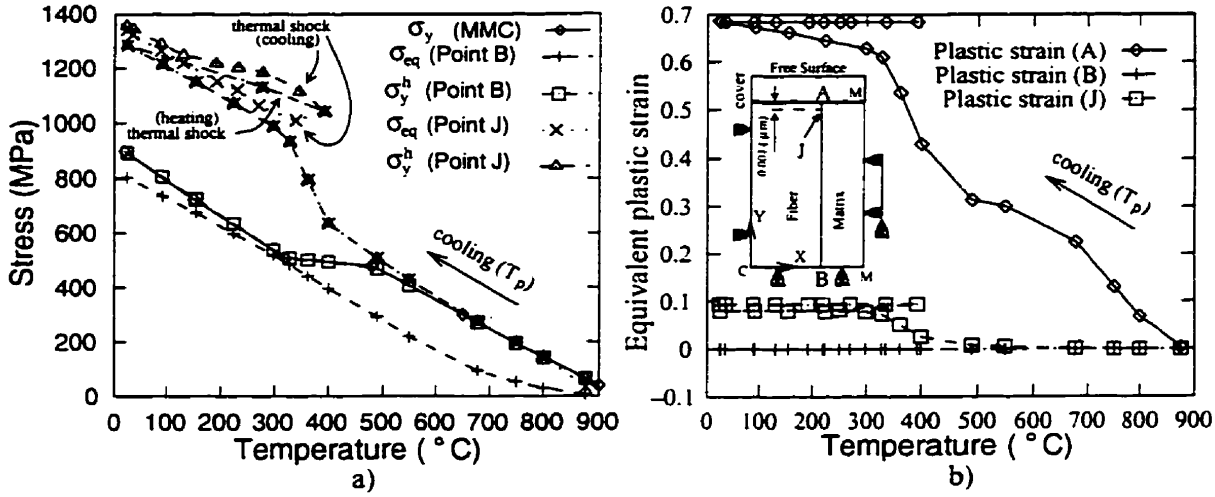

Fig. 9.46: Variation of the equivalent stress and plastic strain at locations A, J, and B during temperature cycle imposed by pouring hot cover on the room temperature composite.

Fig. 9.47 presents σ_{eq} and the stress components at location B in the inner zone for the temperature profile of Fig. 9.41. It seems that thermal shock has no effect on the stress and deformation of the inner zone. As Figs. 9.46(a) and 9.47 show, the equivalent stress and the stress components remain constant before and after the thermal shock. (The stress values for the thermal shock are located on top of the room temperature values of the graph.) This is because the temperature in the inner zone increases by only 10°C during the thermal shock that is negligible.

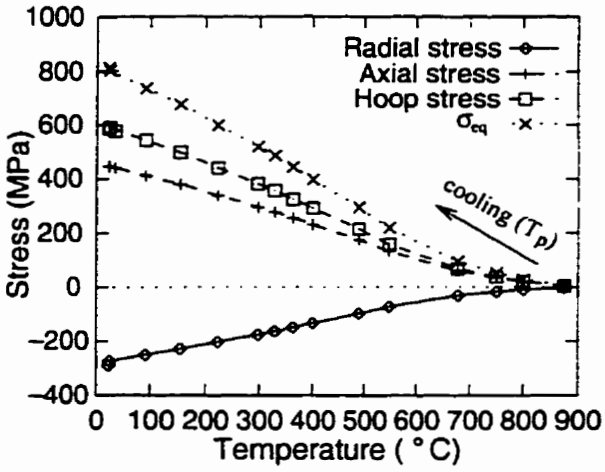

Fig. 9.47: Stress components at location B during two-stage covering process.

9.4.2.3 Thermal-Stress Analysis of the Two-Stage Covering Process (Scheme 2)

A simulation of pouring a hot covering material on the cold free surface of a pre-manufactured composite showed that the very high residual stresses at the fiber/matrix interface on the free surface will partially relax. However, after cooling the composite and the cover to room temperature, the residual stresses regained their previous values. This would make a composite very vulnerable to damage in service temperatures and/or under mechanical loads. The covering process may be more effective if the residual stresses induced due to the manufacturing of the composite are removed or partially relaxed. It would be ideal to provide the conditions of the one-stage covering process where the covering is performed with no residual stresses present at the fiber end. One way may be re-heating the composite, prior to casting the cover, to a high temperature close to the temperature of the hot covering material or to the solidification temperature of the composite. With re-heating the composite, most of the residual stresses left during the manufacturing process or due to service temperature will be relieved. Cooling the composite and the cover together to room temperature may change the residual stress state in the composite end zone and also in the interior (inner zone).

The thermal treatment of the composite is simulated as follows. The same FEM model used in scheme 1 is employed here. The cover elements are deactivated and the composite is cooled down from the 900°C processing temperature. The difference between this scheme and the previous one is that before the cover is cast on the free surface, the composite is reheated to 900°C. In the third step, the elements of the cover are reactivated with T=900°C To set the temperature of the elements of the cover to this value, the extra short thermal step explained before is also applied here. This step continues with the cooling of the composite and the cover to room temperature. Since uniform temperature is expected in the composite due to the high thermal conductivity of the constituents, only the temperature profiles at locations A, J, and B of the composite are plotted in Fig. 9.48. The three steps of the thermal analysis are labeled I, II, and III in the graph. As the figure shows, the cooling profiles of the composite without and with the cover (steps I and III) are similar. As expected, the profiles show that the composite loses heat very quickly at high temperatures. Also, as the temperature profile for step II shows, the temperature gradient is high at the beginning of the heating phase.

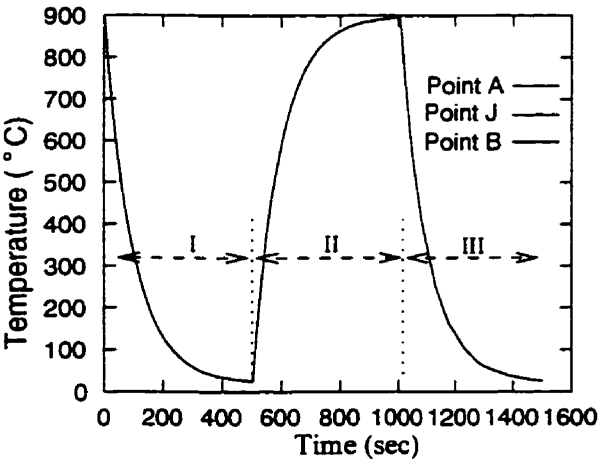

Fig. 9.48: The temperature profile at locations A, J, and B during the second scheme of the two-stage covering process.

The corresponding stress analysis follows the same procedure. The elements of the cover are "killed" to simulate the free surface stresses for the case when the composite is cooled from the processing temperature. After the stress analysis of the reheated composite

with the free surface, the elements of the cover are reactivated. The last step of the stress analysis is performed for the cooling of the composite and the cover to room temperature.

In addition to the matrix strength (σ_y), σ_{eq} and σ_y^h at locations A, J, and B for all three phases of the thermal treatment are presented in Figs. 9.49(a) and (b). The corresponding plastic strains are shown in Fig. 9.49(c). Comparing the values of σ_{eq} at room temperature (at the end of step I and step III) for locations A and J (see Figs. 9.49(a) and (b)) shows that the equivalent residual stress increases with the application of the cover. Also, Fig. 9.49(c) shows that more plastic strain occurs at locations A and J during the temperature cycle. The reason(s) for such a stress-strain behavior can be best explained when one looks at the stress components for these locations during the temperature cycle. The stress components vs. temperature for location A are plotted in Fig. 9.50(a). Here, radial, hoop, and axial stresses for steps I (i.e. cooling the composite without cover from T_p) and II (re-heating the composite without cover to 900°C) are presented. To show a clearer picture, the stresses for step III (cooling the composite and the cover to room temperature) are presented in Fig. 9.50(b) separately. Based on the overlapping hypothesis, as soon as the composite without cover begins to cool down from T_p, a tensile axial stress in the neighborhood of the singular point will be inserted by the fiber on the inner rim of the matrix hollow cylinder. The result of this tensile axial stress is very high tensile radial and hoop stress components (see Fig. 9.50(a)). During re-heating, this tensile axial load will be compressive and will result in compressive radial and hoop stresses at the singular point. These compressive stresses will reduce the previously tensile stresses generated during the cooling step I. However, from almost T = 400°C to T = 900°C the residual stresses are higher than the stress magnitudes at the same temperature levels of the cooling step I. This could be explained with the same reasoning detailed in Chapter 7. In brief, plastic deformation begins at the start of the cooling step I (see Fig. 9.49(c)). Therefore, the stresses are strictly controlled by the yield strength of the material. However, during the heating step II, the strain hardened matrix allows the stress components to increase. As a result, the stresses can increase to their real values without being relaxed by the plastic strain or controlled by the yield strength of the material. Due to this reason, all the stress

components at location A end up to be tensile at T = 900°C (see Fig. 9.50(a)). These stresses used to be compressive or almost zero for the end zone of the 3-D model for which the plastic process began half way through the cooling phase from T_p (see Fig. 7.8). The stress components at location J during the three step thermal procedure are shown in Fig. 9.51. According to Fig. 9.51(b), which presents the radial, hoop, and axial stress components at point J for steps II and III, the stresses for point J are similar to those of the 3-D prism model at T=900°C (i.e. the radial stress is compressive and the axial and hoop stresses are almost zero). This is because the plastic deformation at point J does not begin immediately with the start of cooling from T_p in step I (see Fig. 9.49(c)).

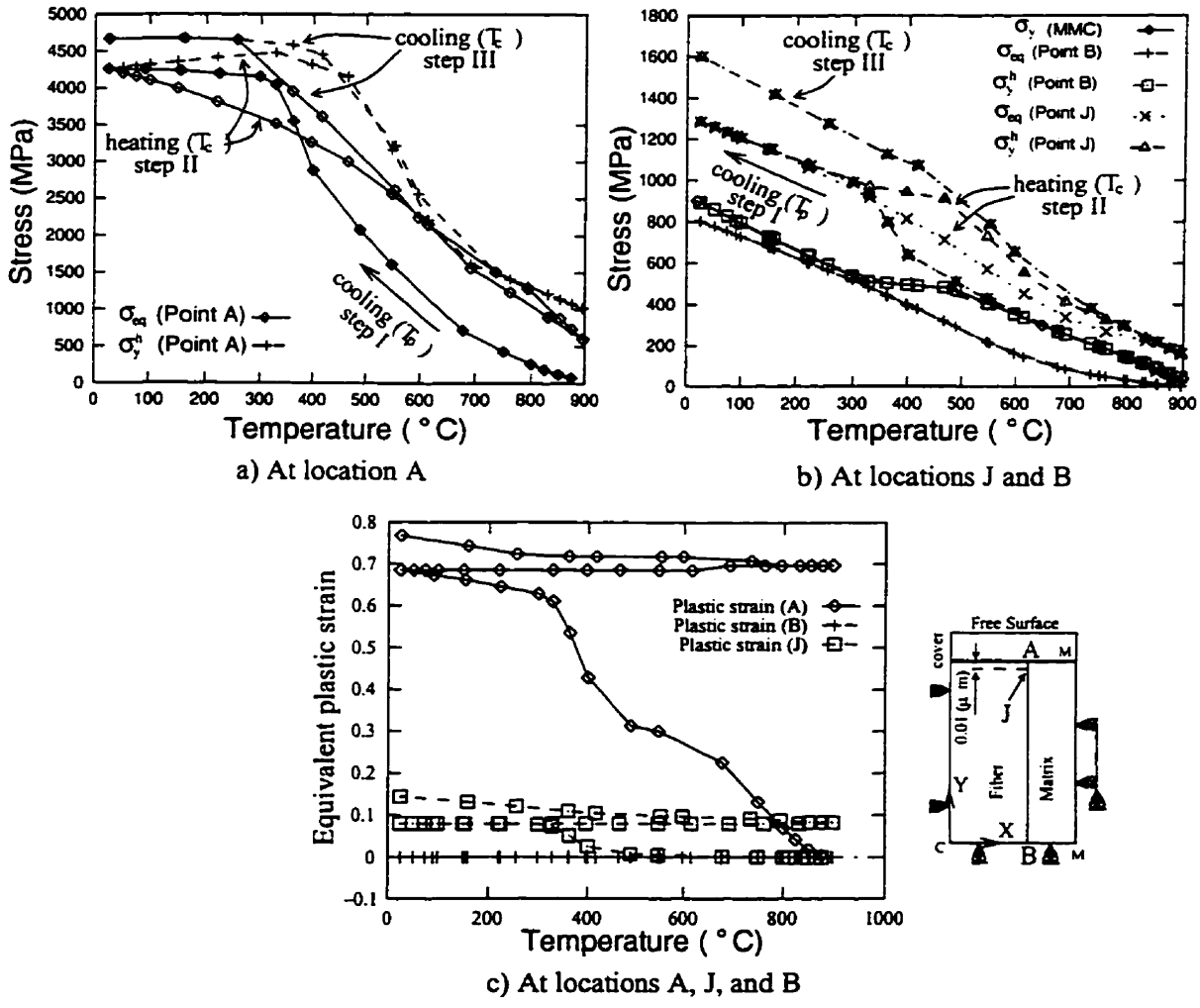

Fig. 9.49: Equivalent stress (a) at location A, (b) at locations J and B, and (c) equivalent plastic strain at A, J, and B during the two-stage covering process.

During the last step of the thermal treatment (step III), the cover is in place. Therefore, as explained in Fig. 9.35, upon cooling, a compressive axial load is expected to be exerted on the outer rim of the matrix hollow cylinder due to the CTE mismatch between the cover and the fiber. This compressive axial force gradually increases with the cooling of the composite. At about T = 450°C, this force overcomes the tensile axial stress left at location A after the heating step II (see Fig. 9.50(b)). During cooling from 900°C to 450°C, since the overall axial stress is tensile, the radial and hoop stresses will be tensile due to the overlapping hypothesis and will continue to increase down to 450°C. Below this temperature, the overall axial stress is compressive. So, the radial and hoop stress components generated by this force will also be compressive. Therefore, the resultant radial and hoop stresses begin to decrease down to room temperature. Consequently, the residual stress components after the three-phase thermal treatment appear to be much less than the corresponding residual stresses after cooling from T_p (end of step I). However, σ_{eq} is higher and more plastic strain occurs during step III of the thermal procedure (Fig. 9.49(c)). The change in σ_{eq} is due to increase in the difference between the stress components in the presence of the cover in step III. Comparing the differences in radial and hoop stresses with the axial stress at the end of steps I and III shows a high increase in these differences because the axial stress is compressive in step III at room temperature. In comparison to the one-stage covering process (see section 9.3.3), one similarity stands out between the stress components in these two cases at point A. The axial stress is compressive for both at the final step (compare Figs. 9.50(b) and 9.34).

The above rationale for the increase in σ_{eq} and ε_{eq}^{pl} at point A during the temperature cycle becomes clearer when one looks at the plots of radial, hoop, and axial stress components at location J against temperature for the last cooling step of the thermal procedure (step III). This is shown in Fig. 9.51(b). As the figure shows, these stresses are compressive for almost the entire temperature range of step III. This stress state is similar to that at location A for the one-stage covering process (see Fig. 9.34). Therefore, it can be concluded that the damage that may be inflicted by the tensile radial and hoop stresses at location A for the two-stage covering process (Fig. 9.50(b)) is very localized. The high σ_{eq}

will disappear at point J, which is located close to the free surface. However, according to Figs. 9.49(a) and (b), σ_{eq} and the plastic strain at J are increased after step III of the thermal treatment and this is not desirable.

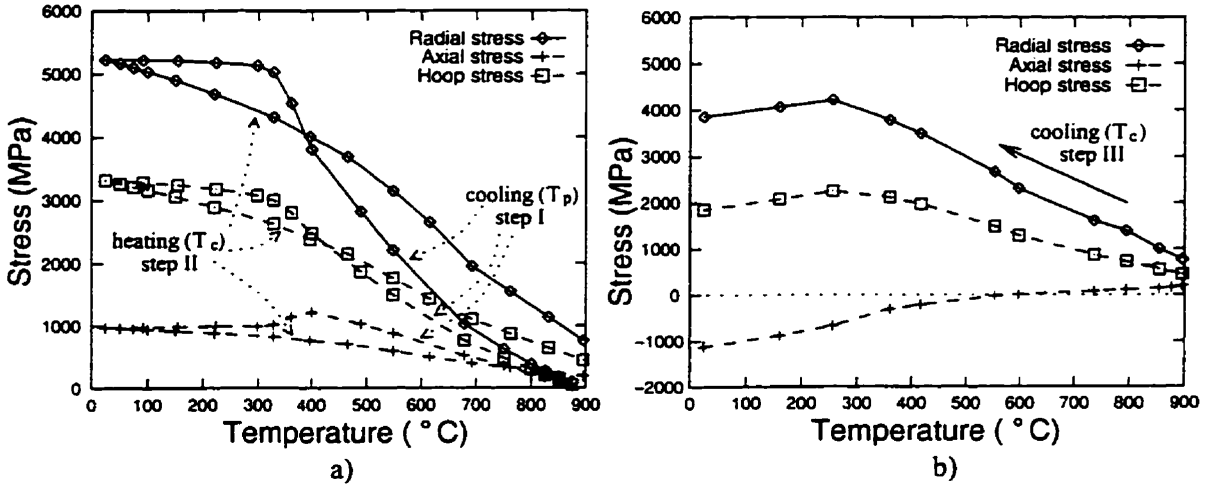

Fig. 9.50: Stress components at location A (a) during cooling from T_p and the heating phase of the covering process, (b) during cooling phase of the covering process.

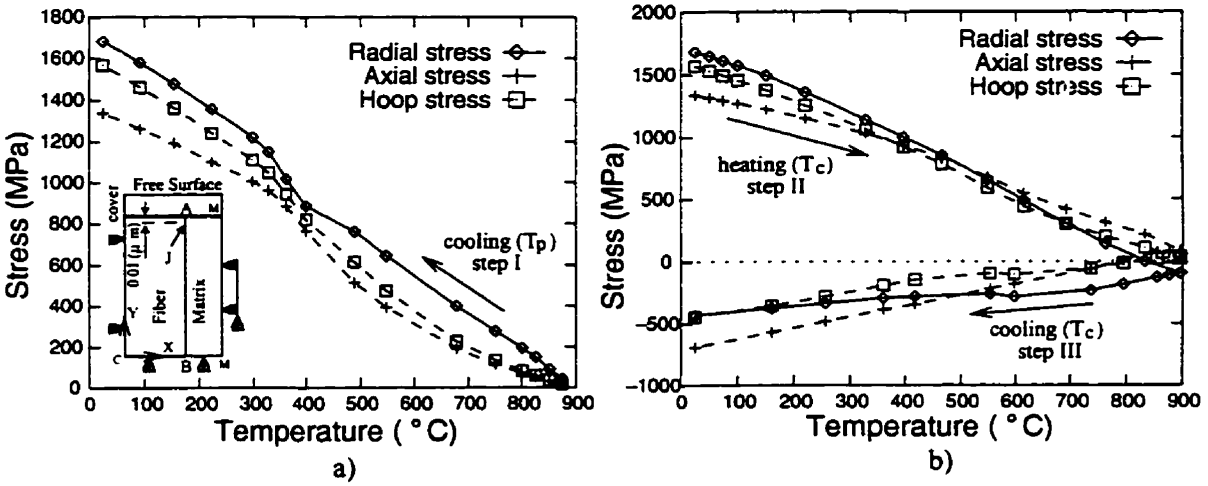

Fig. 9.51: Stress components at location J (a) during cooling from Tp, (b) during heating and cooling phases of the covering process.

The radial, hoop, and axial stress components and σ_{eq} at location B are shown in Fig. 9.52. As the figure shows, the stresses induced during cooling from T_p (step I) disappear when re-heating the composite to T = 900°C (step II). This is an important effect that is discussed further in the next section.

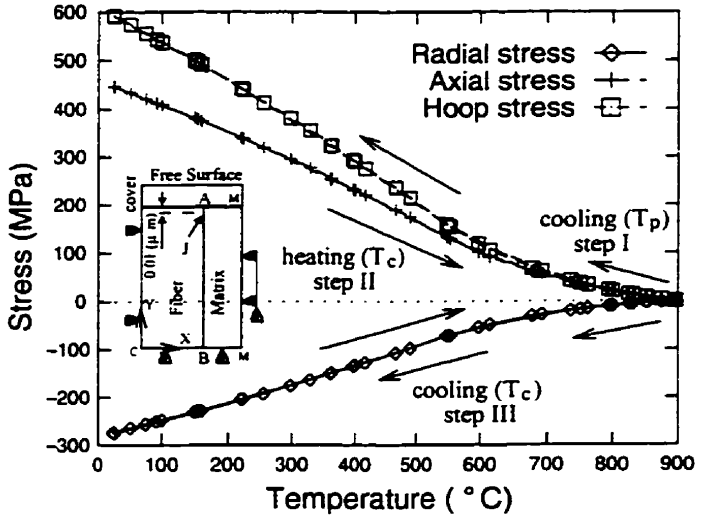

Fig. 9.52: Stress components at location B during cooling from T_p and during the heating/cooling phases of the covering process.

9.4.2.4 Thermal-Stress Analysis of the Two-Stage Covering Process (Scheme 3)

From the foregoing analyses, it can be concluded that the residual stresses at the end of the fiber left over from the processing of the composite cause a big difference in the stress and plastic strain states after covering. It was shown that this is the main difference between the one-stage and the two-stage covering processes. The thermal treatment of the composite before applying the cover (scheme 2) indicated that it has little effect on the final status of the residual stresses. Here, the stresses are considered to be eliminated by physically cutting the composite end. Then the cover is applied on the fresh cut surface. A long model was considered, the dimensions and the mesh configuration of which are shown in Fig. 9.53. The model consists of six areas. Areas 1, 3, and 5 model the fiber and areas 2, 4, and 6 represent the matrix. Areas 3 and 4 will serve as the cover after cutting the composite at the boundary of areas 1 and 2. The length of the model is assumed to be 1000μm, which is exactly twice that of the previous model. This provides the required

length for axisymmetric analysis after cutting the fiber end (i.e. cutting areas 3, 4, 5, and 6). As Fig. 9.53 shows, two regions of the model are densely meshed with very fine elements. One is the region close to the free surface. The other is the middle of the model where the composite is supposed to be cut and a new free surface formed. A dense mesh is required at the free surface in order to calculate more accurately the stress and plastic strain at the singular point and the relaxation effects of the plastic strain on the inner zone stress field.

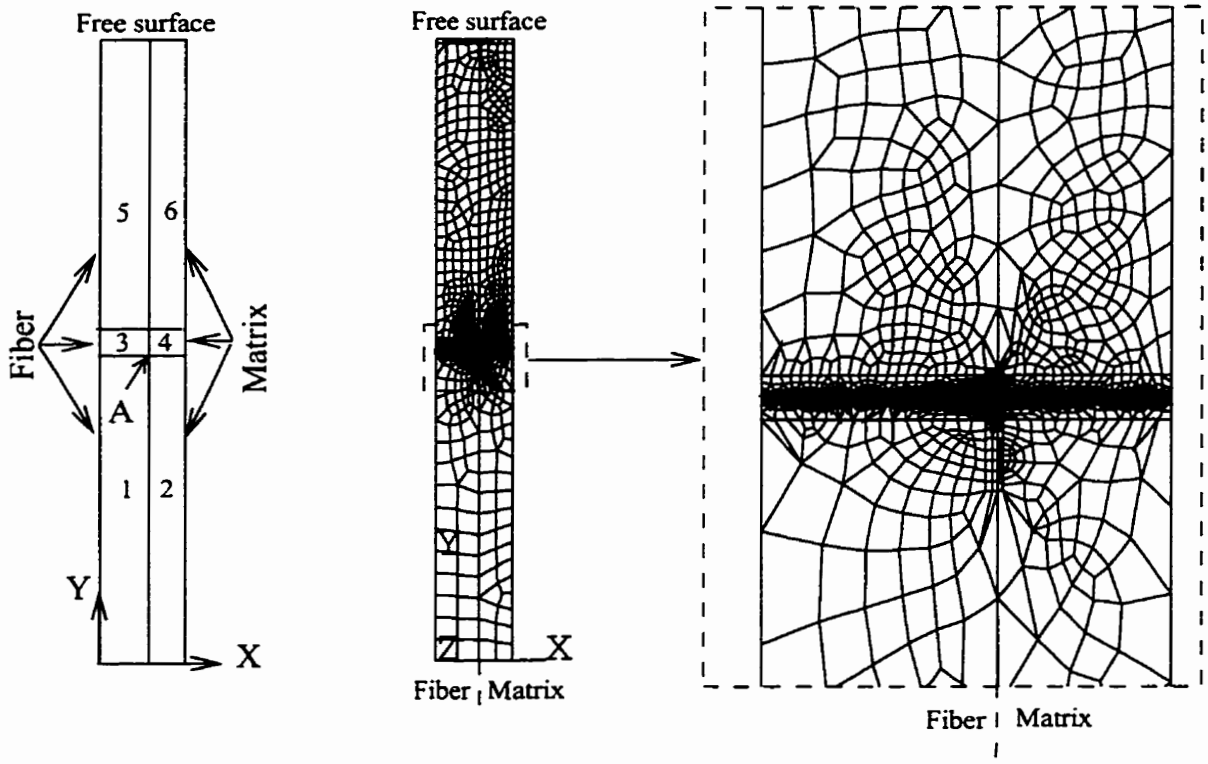

Fig. 9.53: Simulation of cutting the fiber end.

Different manufacturing procedures can be considered for this scheme. The composite can be cut and the covering material is poured while the composite is at room temperature or the composite can be reheated before the cover is applied. Another procedure could be re-heating the composite before the composite is cut and the cover is applied. Depending on the temperature level to which the composite is re-heated, the procedures may be modified and the results may be different. All the procedures must consist of cooling the composite (long model) from the processing temperature T_p to allow

for residual stresses to build up. Here, considering the discussion of the last two schemes, the analysis of three of the procedures will be presented in brief.

For the first procedure, the end of the pre-manufactured composite is to be cut at room temperature and the hot covering material poured on the new free surface of the cold composite. The temperature distribution in the composite will be similar to that of scheme 1 that was discussed in section 9.4.2.1 (see Fig. 9.41). Note that the time for cooling the large model from T_p is longer and the final resultant residual stresses are different than what was found for scheme 1. The reason is that the residual stresses on the free surface are different for the two schemes. For the first scheme, as the composite with no cover is cooled from T_p, the stresses on the surface (which is to be covered) are of the end zone type whereas in scheme 3, as the end effects are eliminated, the stresses on the cut surface are closer to the inner zone type. This difference in the free surface stresses of the two schemes may substantially change the final stress status at the fiber end. This is discussed in more detail later for the second procedure. Note that by cutting the fiber end, the axial residual stress on the new cut surface must vanish to satisfy the free surface boundary condition.

For the second thermal procedure, it is assumed that after cooling the composite from T_p, the end part of the model is cut at room temperature. However, to relax the residual stresses on the fresh free surface as much as possible before the cover is applied, the cut composite is re-heated to the temperature of the covering material. Thus, the heat from the cover does not disturb the composite temperature. This temperature (T=900°C) was chosen for re-heating the composite because this is the temperature at which the matrix has already solidified and shows some strength.

From the residual stress point of view, this procedure also has another advantage. The stresses on the new free surface are of the type of the inner zone stresses, therefore compressive radial and tensile hoop stresses exist at the fiber/matrix interface. The axial stress at the cut section due to the formation of the new free surface must become zero. According to the overlapping hypothesis, re-heating the cut composite to the temperature

of the cover should induce very high compressive radial and hoop stresses at the interface on the free surface. Therefore, superimposing these stresses on the stresses of the new free surface will increase the compressive radial stresses but will reduce the tensile hoop stresses. Both changes in the stress state are desirable from the design point of view. The compressive radial stress strengthens the fiber/matrix bond and the reduction of the tensile hoop stress lowers the risk of matrix cracking around the fiber.

In the last stage of the covering (i.e. when the fiber and matrix are cooled together to room temperature) compressive radial and hoop stresses are expected at the fiber end as before due to the presence of the cover. The reason for such a stress state was explained in Fig. 9.35. This procedure seems to be a very practical method. The final compressive radial residual stress should improve fiber/matrix bonding and compressive hoop stress should prevent the matrix from cracking at the fiber end.

In the third procedure, the long model is cooled from T_p and then reheated to T = 900°C before the fiber end effects are eliminated by physically cutting the composite end. The cutting is performed at T=900°C. In this step the hot cover is poured on the new fresh cut surface and then the composite and the cover are simultaneously cooled to room temperature. The temperature at location A is shown in Fig. 9.54. The time for steps I and II (cooling and re-heating the large model) will be longer than that of step III. This step involves cooling the cut composite and the cover to room temperature.

The stresses generated at location A during re-heating phase of the composite from room temperature to 900°C are different than those obtained for the previous procedure. The stress components at location A (which is located in the inner zone of the large model before the fiber end is cut) during cooling from T_p and the re-heating phase are shown in Fig. 9.55. The stresses for step III are also shown in this figure. Due to the negligible plastic strain in the inner zone, i.e. elastic stress state, the residual stresses at location A are completely released when the composite is re-heated. This is similar to the results of the inner zone presented in Fig. 9.52 for scheme 2. Cutting the composite at this step and applying the cover is the most effective method because there is no residual stress at the

cut surface to affect the covering process. Cooling the composite and the cover under this circumstance (i.e. no residual stresses at location A) is very similar to the one-stage covering process discussed in section 9.3.3. The stress components for location A during step III (Fig. 9.55) are very similar to the stresses obtained for the one-stage covering process shown in Fig. 9.34.

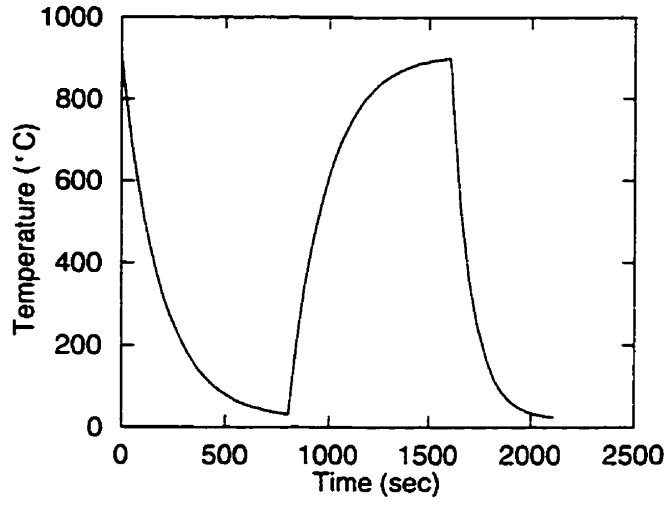

Fig. 9.54: The temperature profile at location A during scheme 3.

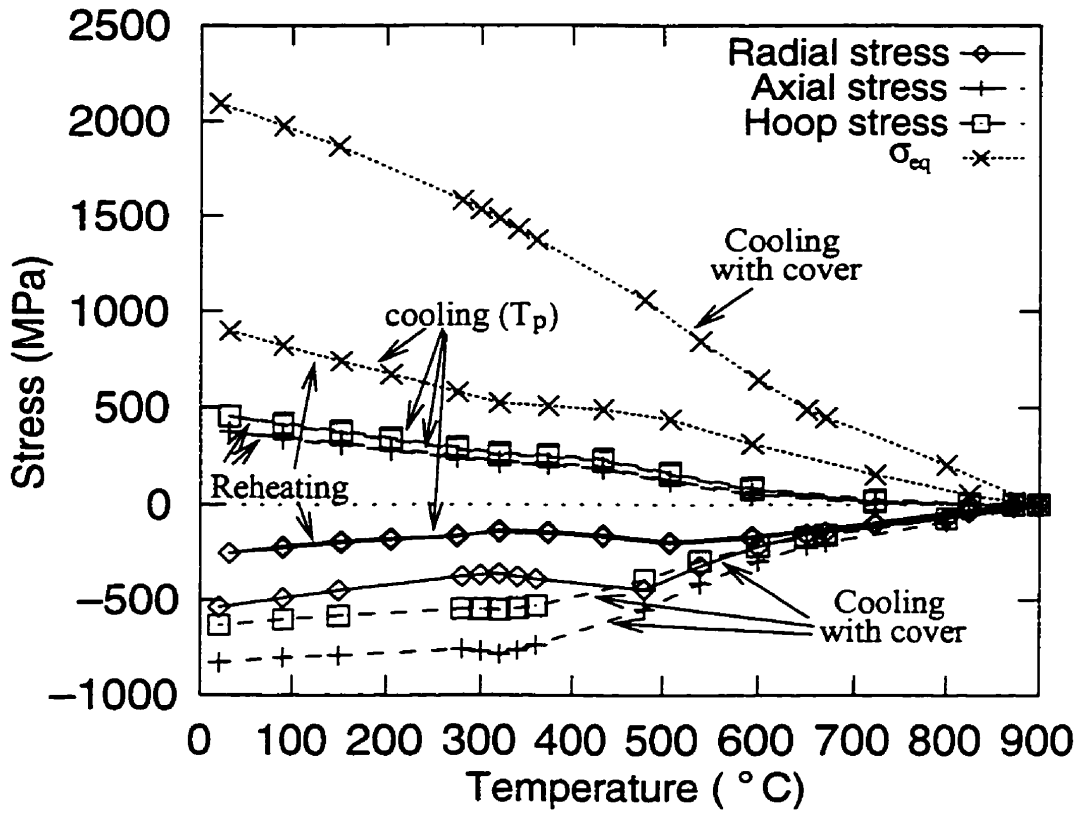

Fig. 9.55: Stress components at location A during the covering process of scheme 3.

10. Materials and Experimental Procedures

10.1 Introduction

The main objective of this part of the thesis is to experimentally study the effects of the free surface geometry of fiber composites on the initiation and progression of damage in the matrix and at the fiber/matrix interface with temperature cycling. In chapters 5-9, it was shown how the free surface geometry of fiber composites affects the stress and displacement states at the fiber end (end zone) and in the interior of the composite (inner zone). Particularly, the covering method that was investigated in chapter 9 was found very promising. As a result of covering the free surface with a thin layer of matrix-like material, the forces inflicting damage to the composite integrity were highly reduced.

These numerical results have been verified by a series of experiments on laboratory-made large-scale composite samples. Due to the small size of fibers in the commercially available composites, measurement and visualization of the damage introduced by temperature cycling is difficult. Therefore, large-scale composite samples were used. Similar large-scale samples were used by Biernacki (1996). Biernacki's experimental investigation was mainly focused on fiber protrusion, damage detection, and the progression of the damage with the number of temperature cycles in the same large-scale composites. The temperature-dependent properties of the matrix, the fiber/matrix bond strength, and the creep characteristics of the matrix were determined.

A new set of samples was made by modifying the molds and the molding procedure developed by Biernacki. In this chapter, the properties of the matrix, the temperature cycling apparatus and its calibration, and the molding procedure are discussed.

10.2 Material Properties

Polyester resin type 1811 with a glass transition temperature $T_g = 60°C$ was used as the matrix while 316L-type stainless steel rods were used as fibers. The variation of the mechanical properties of the resin with temperature are presented in Table 10.1. For the 316-L S.S. fiber, the coefficient of thermal conductivity (k) and the CTE were considered to be 75 ($W.m^{-1}.°K^{-1}$) and $8\times10^{-6}/°C$, respectively. More detailed information can be found in (Biernacki, 1996).

For $20°C < T < 60°C$, the creep characteristics of the resin are approximated by the following empirical equation (Biernacki, 1996)

$$\varepsilon_c = c\left(\frac{\sigma}{\sigma_0}\right)^{1.52}\left(\frac{T}{T_0}\right)^{2.53}\left(\frac{t}{t_0}\right)^{0.166} \qquad (10.1)$$

where $\sigma_0 = 1.375MPa$, $T_0 = 40°C$, $t_0 = 100min$. In the above equation, σ is the equivalent stress, T is the temperature in °C, and t is the elapsed time in minutes.

Table 10.1: Properties of the materials used in the experiments (Biernacki, 1996).

1811 polyester resin				
Temperature (°C)	E_e (MPa)	E_p (MPa)	CTE ($\times10^{-6}/°C$)	k ($W.m^{-1}.°K^{-1}$)
25	385.8	81.6	52	0.6
35	252	74. 7	53	-
45	140	55.7	66	-
55	70	32.4	76	-
62	30.8	15.9	83	-
70	-	-	88	-

10.3 Molding Procedure

A special pre-made mold made of high-density polyethylene was used to make the large-scale composite specimens. The mold consists of a rectangular bar with a cylindrical hole in its center and two endcaps (see Fig. 10.1). The stainless steel rods were arranged into hexagonal patterns by means of the caps. The hexagonal patterns were pre-drilled on the caps, which were used as holders for the reinforcements.

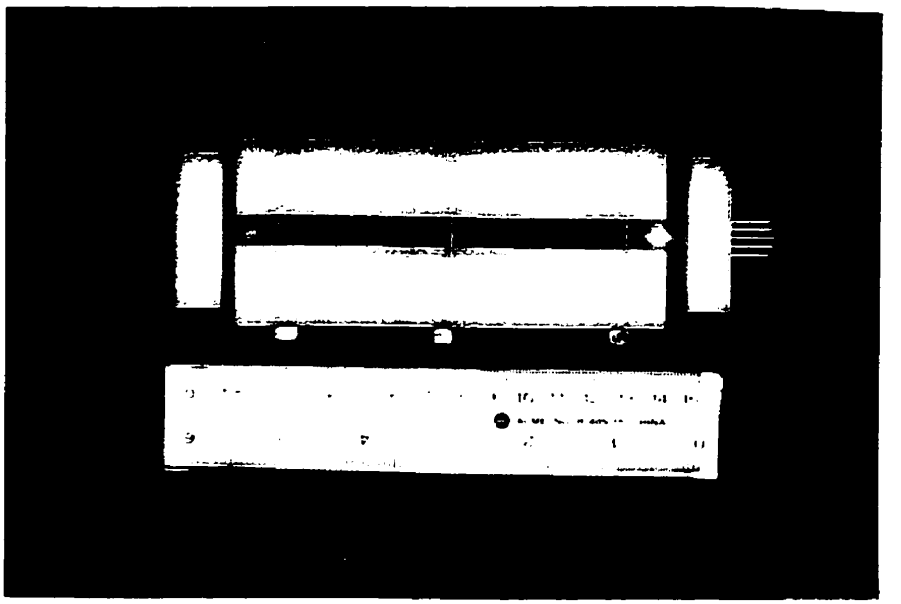

Fig. 10.1: Mold for large-scale composite samples.

After polishing the stainless steel rods with 120 grit emery paper and washing them with methanol, the rods were slid into the holes of the hexagonal patterns of the holders. The polishing may enhance the resin penetration into the rods, increasing the bond between the rods and the resin that is purely mechanical. After closing the mold, the liquid resin (with a composition of 1g of hardener for 100g of polyester) is poured into the mold. The solidification stage was performed in a ventilated booth. With 19 stainless steel rods

(each with a diameter of 1.6mm) and the 19mm diameter cylindrical hole of the mold, composite samples with 13.5% fiber volume fraction (V_f) were made. For making the required samples to fulfill the objectives of the study, the mold and the molding procedure used by Biernacki (1996) were slightly modified. These modifications are explained in what follows.

10.4 Temperature Cycling Apparatus

A temperature cycling apparatus was used to apply temperature cycles to the large-scale composite samples. The apparatus consists of a furnace (as a heat source) and a freezer (as a cooling chamber). The composite sample is moved between the furnace and the freezer by an air cylinder in a computer controlled temperature cycle.

A data acquisition system (lab-mate) was used to transfer the computer outputs into electrical signals. The signals were then used for controlling two 2-way and 4-way solenoid valves that supply air to the cylinder for transferring the samples from the furnace into the cooling chamber. A photograph and a schematic diagram of the apparatus are shown in Fig. 10.2.

10.5 Calibration of the Apparatus

The apparatus was calibrated for a temperature cycle of -21°C to +50°C. The minimum temperature was limited by the cooling capacity of the freezer, while the maximum temperature was kept below the T_g of the resin.

The calibration was performed for the free surface temperature of the sample only because cracking and debonding start at the interface on the free surface first. Also, the debonding continues along the interface deep into the composite where the interfacial temperature is very close to the free surface temperature due to the very high thermal conductivity of the steel rods. The temperature cycle used in the experiments is shown in Fig. 10.3. Close monitoring of the temperature of the free surface of the sample showed that a complete cooling phase takes 18.5 minutes while the heating phase takes 15 minutes.

Cooling from room temperature to -21°C takes 15 minutes. This is equal to the time for a complete heating phase (-21°C to +50°C). As mentioned by Biernacki, the difference in the free surface temperature and the matrix temperature well inside the large-scale sample is very small for such cycles.

a) Temperature cycling apparatus

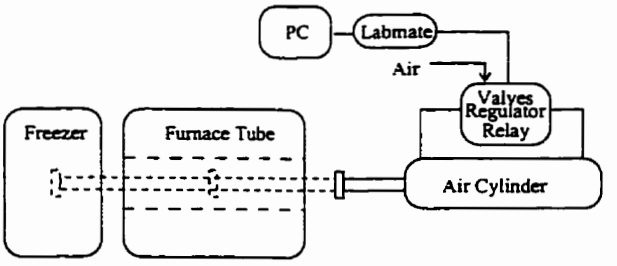

b) Schematic diagram of the apparatus

Fig. 10.2: Thermal cycling setup.

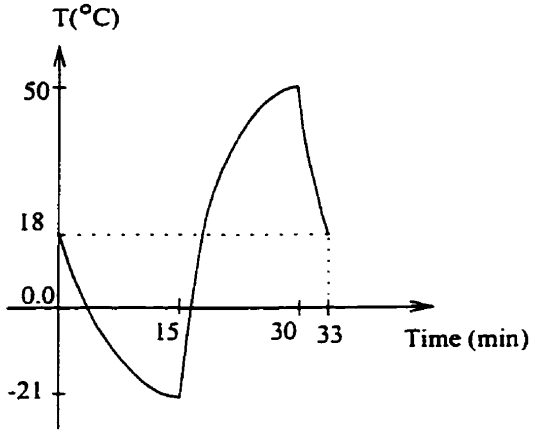

Fig. 10.3: Temperature cycle profile.

10.6 Experimental Procedure

In chapter 9, it was concluded that a rough cut surface of unidirectional composites increases the thermal residual stresses if the fiber ends protrude out of the matrix (see Fig. 10.4(a)). If the sharp contact angle of the fiber and matrix (shown as $\phi = 90°$ in Fig. 10.4(a)) is filled with some matrix-like material (ramp), the stresses change at the fiber/ramp interface depending on the angle ϕ. Note again that ϕ represents the angle between the fiber and the line tangent to the ramp where the ramp meets the fiber. The stresses decrease with decreasing ϕ. However, very high stresses still appear at the contact corner of the matrix with the ramp, causing matrix cracking. Similarly, stress concentrations occur in the matrix for the case where the fibers bulge out of the matrix (see Fig. 10.4(c)).

To experimentally verify these numerical results, the first type of samples was made such that the ends of the fibers extended out of the matrix for about half a fiber diameter. The samples were first made by partially embedding the stainless steel rods in the matrix and cutting the end of the extended rods out of the matrix to the required length. Due to vibrations of the unsupported fiber ends during cutting a lot of cracks were observed at the interface on the free surface after the sample was cut. To eliminate such cracking the mold shown in Fig. 10.5(a) was prepared to cut the sample with a slow speed diamond saw. The three segments of the mold shown in this figure were then

filled with the matrix material. After solidification of the matrix, the specimen was cut from the middle segment of the composite shown in Fig. 10.5(b) with two separate cuts through the high density Polyethylene holders (A and A' cut surfaces). The thin layers of the Polyethylene holders remaining on the specimen were then peeled off. The specimen, after being polished with 6μm and subsequently with 1μm diamond paste, is shown in Fig. 10.6(a).

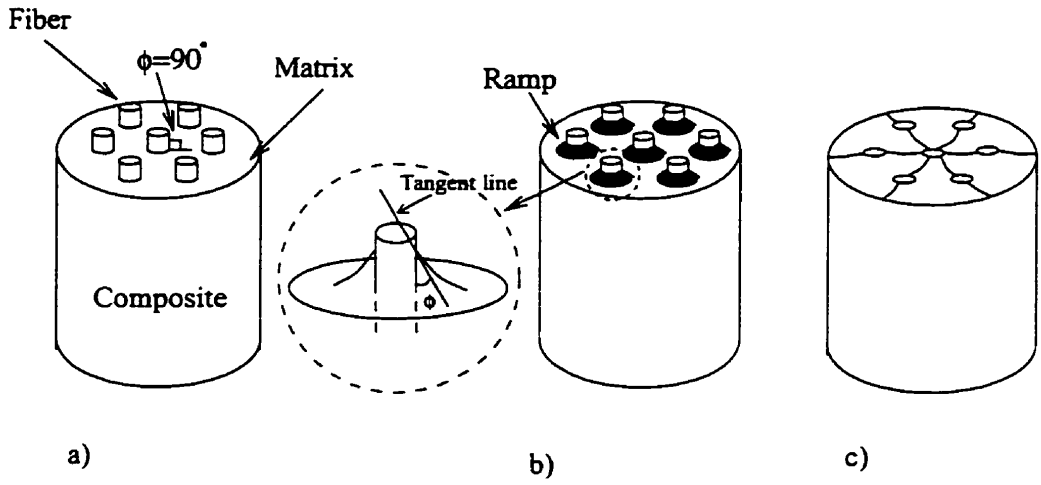

Fig. 10.4: Large-scale composite sample with fibers extending out of the matrix.

The second type of specimens has the fibers embedded in the matrix at one end and exposed at the other end. These specimens could also be cut from the pre-made composite shown in Fig. 10.5(a). Provided that the fibers are of the same length and the fiber cross sections are pre-polished and laid on a planar surface perpendicular to the fibers length, segments I and III of the composite could be used for making the second type of specimens. The finely polished specimen shown in Fig. 10.6(b) could be made by two cuts (B and D) in segment I or B' and D' in segment III (see Fig. 10.5(c)). The cut surface of D or D' of the specimen (the side with the end of fibers embedded in the matrix) was used to verify the numerical results for the covering of the fibers free end with a thin layer of matrix-like material. However, the B or B' end of the specimen was used to show the differences in the surface effects between the cut (exposed) and covered surfaces.

The third type of specimen, which has both ends covered with a thin layer of matrix-like material, was made by a different procedure (see Fig. 10.5(e)). Here, only one holder was used and the matrix material was poured in two separate stages. After solidification of the matrix that was poured in the first stage, the composite was removed from the holder, flipped over and then the second side of the specimen was made. The extra matrix from both sides was then removed using a diamond saw. A matrix layer with the thickness of one-tenth of the fiber diameter was left on the top end of the fibers. To keep the effects of the two-stage manufacturing process to a minimum on the fiber ends, the length of the specimen was considered to be twice that of the previous specimens. The finely polished sample is shown in Fig. 10.6(c).

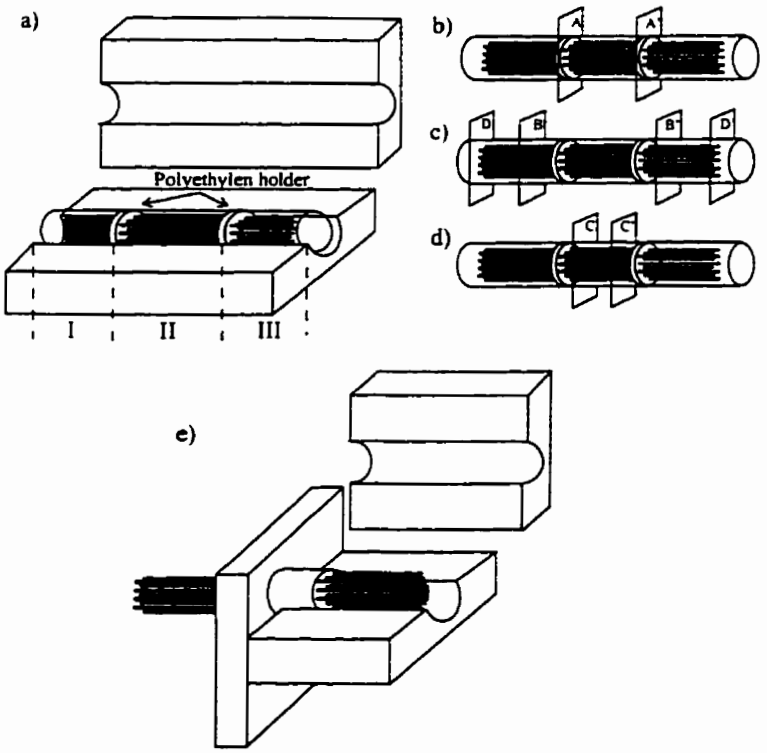

Fig. 10.5: Molding of large-scale composite samples.

The fourth type of specimens were made with two cuts going through the fibers (see the cut surfaces of C and C' in the middle segment of the composite shown in Fig. 10.5(d)). These specimens were used to analyze the effects of a covering layer that is applied in a separate stage (two-stage covering) on the cut surfaces of a fresh or a thermally cycled sample after being cut and exposed to free surface conditions.

To complete the curing process and to allow more relaxation of the residual stresses generated during the manufacturing process of the composite specimens, all the samples were stored in a desiccator for two weeks. Also, to prevent matrix deterioration due to ultraviolet rays, the specimens were kept in dark at all times. The specimens were then thermally cycled between -21°C and +50°C using the apparatus shown in Fig. 10.2. The free surface effects on matrix cracking on the exposed surface and fiber/matrix debonding along the fiber length are reported in the next chapter.

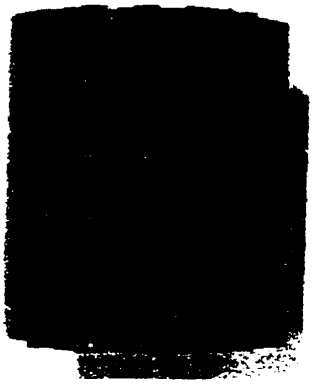

a) Fibers extending out of matrix.

b) One end free-one end covered.

c) Both ends covered.

Fig. 10.6: Uncycled large-scale laboratory-made samples.

11. Effects of Free Surface Geometry on Damage Initiation in Composites: An Experimental Investigation

11.1 Introduction

A series of experiments were designed and conducted on the samples described in Chapter 10 to verify the reduction of the thermally induced stresses and associated damages at the end zone of unidirectional fiber composites. In particular, the effects of a free surface, fibers extending out of the matrix, and covering the free surface by a thin layer of matrix on the stress and damage in composites were studied.

First, the damage induced by temperature change to the composite with no cover is investigated. The samples were carefully monitored before being cycled and the changes as cycling progressed were recorded. These observations are presented in the next section. The samples, which have the fiber ends extending out of the matrix, were also tested. Then tests were conducted on the samples with one or both of their cut surfaces covered. The results of these experiments revealed the effect of the covering layer in containing the damage. In particular, the effect of the two-stage covering process (discussed in Chapter 9) was also briefly studied by testing a sample that had its free surface covered in a separate stage. The results of the above tests are discussed sequentially in the following subsections.

11.2 Free Surface Effects on the Damage Induced in Composites

The assessment of initiation and propagation of damage in composite samples with exposed free surfaces is grouped and presented in two subsections. In the first subsection, the damage induced in the manufacturing stage and the ways to minimize it is discussed. Next, the damage due to temperature cycling is investigated. Also, the

influence of the damage initiated during the manufacturing process on matrix cracking and fiber/matrix debonding during exposure to the service temperature is discussed.

11.2.1 Damage in Composites Due to Manufacturing Process

The side and top views of a fresh specimen of the fourth type cut from the large-scale composite along with the schematic diagram of its cross section are shown in Figs. 11.1(a) and 11.1(b). The fibers in the hexagonal pattern, depending on their distance to the side-edge of the specimen, are designated A, B, C, and D; where A denotes the central fiber and D marks the fibers with the least distance to the side-edge of the composite.

a)

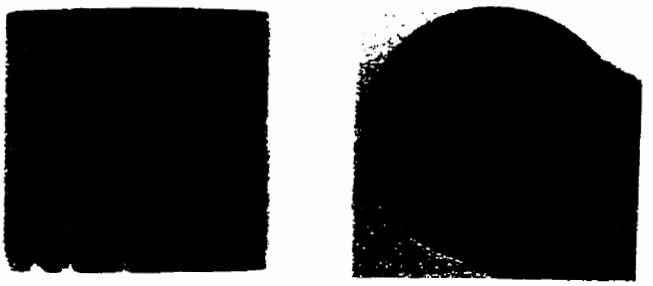

Side view. Top view.

b)

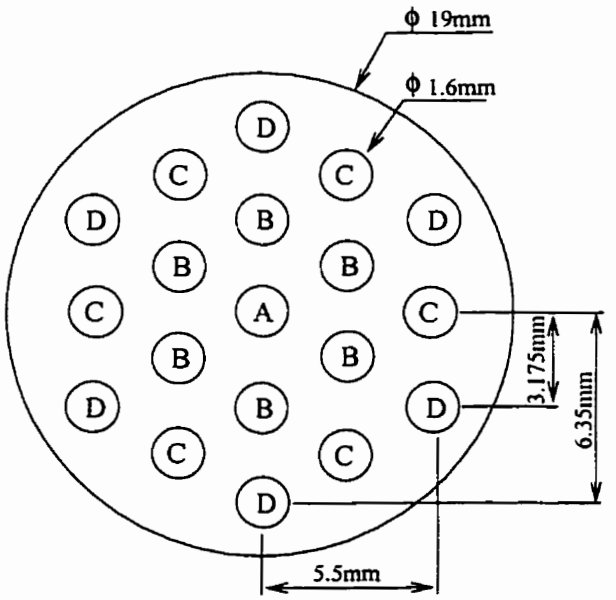

Fig. 11.1: (a) Top and side views of an uncycled sample with both ends free (b) Designating fibers with letters based on their distance to the center.

After cutting, for most of the D fibers and some of the C fibers, typically a very small portion of the fiber/matrix interface (which faces the side-edge of the sample) was debonded. The damage is shown on the side picture of the uncycled specimen. The debonded portions of the interfaces are shown as the white parts at the end of the fibers on Fig. 11.1(a). The length of the debonded interface is longer for the D than for the C fibers. However, much smaller or, in most cases, no debonding was observed for the fibers closer to the specimen center (A and B fibers). Soaking the sample in a colored liquid showed that the liquid does not penetrate into a very small portion of the white area. This indicates that the interface in this very small area is not completely debonded. Therefore, the white area around the C and D fibers may include some inelastic deformation of the matrix in the vicinity of the fiber. Interestingly, the pictures of the interface at the cut surface for all the D and C fibers (taken by a high-resolution optical microscope with a magnification of 800) show no sign of matrix cracking. However, it appears that the fiber and the matrix do not have the same heights at these areas.

The debonding phenomenon in the uncycled samples may have been caused by two different sources. The first source, which is normally unavoidable, could be the residual stresses that are present after manufacturing. When the fresh specimen is cut from the bulk composite, the residual stresses may exceed the fiber/matrix bond strength and/or the matrix yield strength causing debonding and/or matrix plastic deformation. The second source, which may be more controllable, would be related to the polishing, handling, and also storing conditions of the fresh sample. In fact, the debonding length for the fresh sample was greatly reduced by polishing the sample under a very low pressure, washing it with water at a controlled temperature of 20°C, and most importantly, avoiding direct contact of the specimens with fingers around fiber ends in all the processing and polishing steps explained above. It is very important to perform all the above steps at room temperature.

In the numerical studies in Chapter 9, it was shown that for edge-fibers (i.e. the C and D fibers), the stresses at the fiber/matrix interface in the vicinity of the fiber end are about 50% higher than those of the internal fibers (i.e. the A and B fibers). Thus, the

presence of free side-edge is responsible for the increase in the interfacial stresses. That is why the fiber/matrix debonding along the D and C fibers are higher than along the B and A fibers. The debonding of the D and C fibers normally starts at the sides that face the free side-edge of the specimen. The other side of the D and C fibers shows much less debonding because they are surrounded by other fibers. This reduces the magnitude of the radial stress that causes the debonding.

11.2.2 Damage Induced in Composites During Temperature Cycling

The specimen shown in Fig 11.1(a) was exposed to the temperature cycle shown in Fig. 10.2. The damage induced (i.e. fiber/matrix debonding, free surface deformation, and matrix cracking) was recorded after 1, 2, 5, 10, 20, 50, 100, 500, and 1000 thermal cycles. In this subsection, the increase in debonding length of the interface with the number of thermal cycles is discussed first. Fiber protrusion that was extensively discussed by Biernacki (1996) is briefly explained. Also, initiation and propagation of cracks in the matrix on the free surface around different fibers are commented upon.

It has been observed that debonding occurs around all the fibers and its extent increases as cycling progresses. The rate of debonding decreases as the number of cycles increases and is finally halted. The debonding stops to increase when the debonded length reaches some critical value that will be discussed later. Figs. 11.2(a)-11.2(f) show the progression of debonding after 1, 5, 10, 100, 500, and 1000 cycles. A plot of the average debonded length of the interface for the D and C fibers versus the number of cycles is shown in Fig. 11.3(a). The values represent the mean values of the debonded length of the interface of all the D and C fibers of the specimen. The debonded length of the interface for the D fiber reaches its final value faster (i.e. after a lower number of cycles) compared to the C fiber due to the higher stresses around the D fiber than the C fiber in the end zone. However, the final debonded length of the interface for all the other fibers eventually converges to a relatively similar value as that for the D fibers (see Fig. 11.3(b)). Fig. 11.3(b) shows the top view of the sample after 500 cycles where the debonding length for other fibers is visible. The side view of the sample is shown in

Fig. 11.2(e). The progression in the debonded length of the fiber/matrix interface stops due to a decrease in the radial stress values in the presence of a crack (King (1994) and Biernacki et al. (1998)). As explained earlier in Chapter 5, a very high tensile radial stress at the end of the fiber is responsible for the fiber/matrix separation (Abedian and Szyszkowski, 1997). The decrease in the radial stress was said to be due to the fact that the cracked layer of the matrix reduces the deformation gradient near the tip of the crack in comparison to the deformation gradient in the matrix at the free surface without any crack. Therefore, with more progression in the debonding length, lower tensile radial stresses are expected in the cooling phase of the subsequent cycles. The separation is continued until the tensile radial stress at the tip of the crack decreases to a value which is not high enough to further tear apart the fiber from the matrix. Therefore, no measurable increase in the debonding length is observed with further cycling. It is also interesting to note that the final debonding length as shown in Figs. 11.2(f) and 11.3(a) varies from three to four fiber diameters. This is in full agreement with the results discussed in Chapter 5 and by Abedian and Szyszkowski (1997) and Ostrowski et al. (1984) where it was shown that the fiber end effects vanish at about 3 fiber diameters from the fiber end.

The variation of the difference in height of the fiber and matrix at the free surface (protrusion) with the number of cycles was discussed by Biernacki et al. (1998). It was shown that protrusion is highest for the D fibers, decreases for the C fibers and is least for the A fiber. The higher protrusion for the D fibers compared to others was attributed to the small difference in temperature on the surface and at the interior of the specimen during temperature cycling. Although the temperature gradient may play a role in altering the fiber protrusion, the difference in debonded length of the D and the C fibers during manufacturing may influence the protrusion as well. When debonding occurs, the debonded portion of the matrix can contract more easily than the other parts because of the absence of the restraining effect of the fiber. Hence, upon cooling, the debonded portion of the matrix shows a high contraction thereby increasing the protrusion. As the largest debonding during manufacturing occurs around the D fibers, the largest matrix

contraction or the maximum fiber protrusion is expected to occur during cycling for these fibers. The protrusion is smaller for the C fibers than the D fibers because of the lower amount of debonding for the former than the latter. Protrusion is least for the A fiber due to the minimum debonding for this fiber.

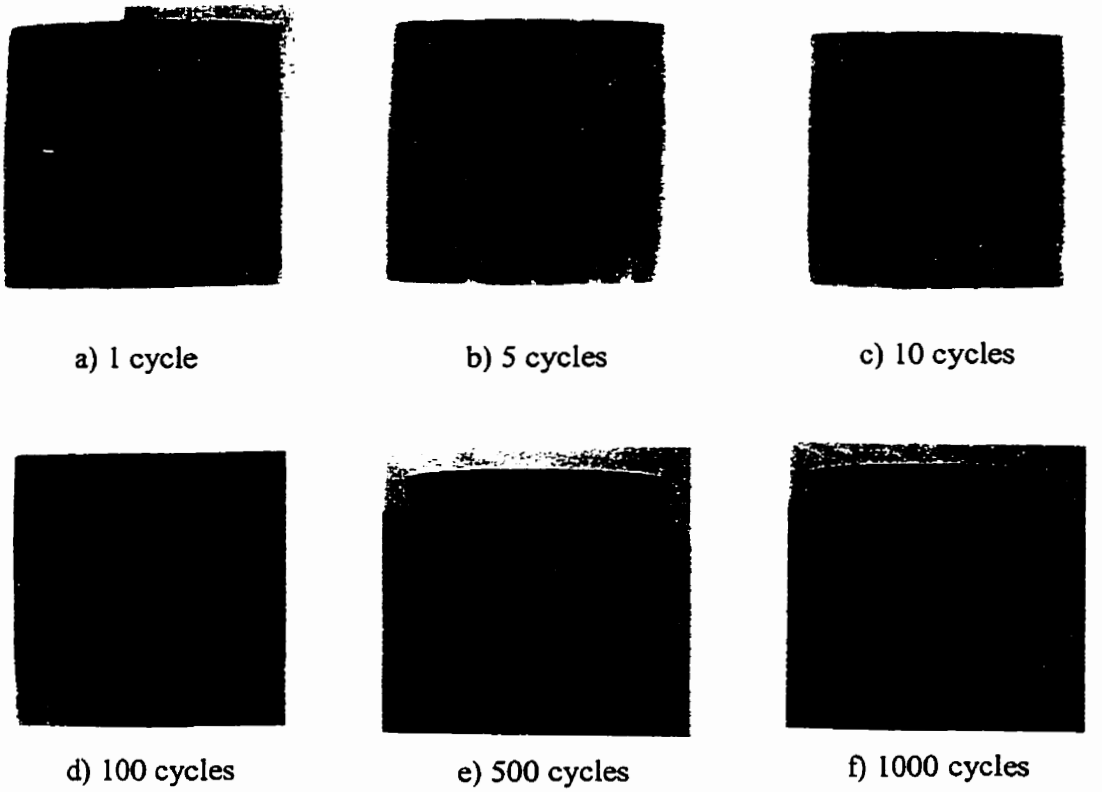

a) 1 cycle b) 5 cycles c) 10 cycles

d) 100 cycles e) 500 cycles f) 1000 cycles

Fig. 11.2: Effects of a free surface on the length of fiber/matrix debonding with the number of cycles.

a)

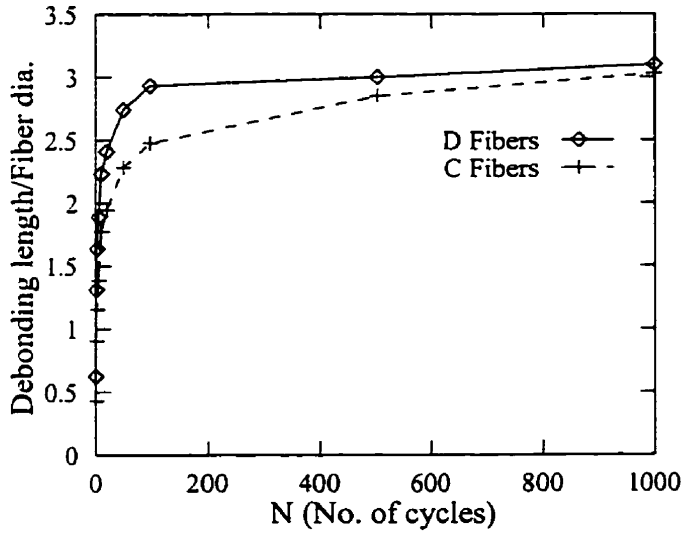

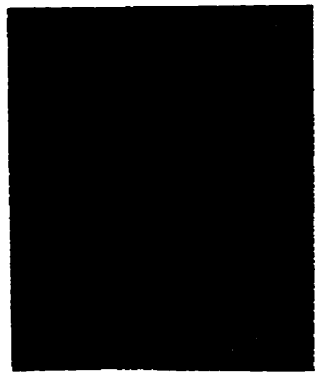

b) Top view after 500 cycles.

Fig. 11.3: Progression in the fiber/matrix debonding with number of cycles.

During the first cycle, the change in temperature of the specimen generates very high tensile radial as well as hoop stress components around the fiber end. These stresses are high enough to cause fiber/matrix debonding and matrix cracking. Fig. 11.4 presents the fiber/matrix interface region for the C and D fibers at two different locations on the free surface after one temperature cycle. The sides of the C and D fibers that face the side-edge of the specimen show a very limited number of cracks or, in most cases, no cracking at all. However, the sides facing the neighboring fibers show some cracks even after one temperature cycle. The reason could be that in the areas where the interface has already been debonded (the part of the interface that faces the side-edge of the composite and shows debonding during manufacturing) the stresses are more relaxed than the side where the fiber and matrix still have a strong bond. As a result, no cracking or a very limited number of cracks is observed in the debonded areas. With increasing number of cycles, the cracks that were initiated on the side of the D or C fiber propagate to the neighboring regions and this leads to a high degree of cracking in the matrix. However, in the area facing the composite side-edge some kinks occur in the matrix. Fig. 11.5 depicts the side of the D fiber that faces the side-edge of the sample after 2, 5, and 10 cycles. The number of kinks in the matrix increases with the number of cycles and, finally, they form shallow cracks in the matrix. The change in the cracking pattern in the matrix on the free surface around all the fibers after 1 and 5 cycles, based on scanning electron microscope observations, are sketched in Fig. 11.6. The circular lines around the fibers represent very small cracks while the zigzag lines indicate the kinks in the matrix. As the figure shows, the number of kinks around the C fibers is less than that of the D fibers for a higher number of cycles. This is most probably due to the difference in stress levels around these fibers. The stresses are more relaxed around the D fibers due to a higher degree of debonding along the D fibers than along the C fibers. Therefore, the kinks around the C fibers turn to low-depth cracks sooner than those surrounding the D fibers.

The crack pattern around the fibers further away from the side-edge of a composite was studied on the example of the A fiber since the C and D fibers exert an influence on

the B fibers. After the first cycle, a few cracks were observed around the A fiber using an optical microscope (see Fig. 11.7). However, by means of the scanning electron microscope it has been found (Biernacki, 1996) that very tiny cracks occur everywhere around the fiber even after the first cycle. The cracks are mostly initiated at the interface at the sites where the A fiber is at larger distances to the neighboring fibers. This kind of cracking pattern was also observed by other researchers (Morris et al. ($1989_{a,b}$) and Biernacki et al. (1998)). This can be explained by the fact that the local fiber volume fraction is smaller along the line which connects the center of the A and C fibers than along the line which connects the centers of the A and B fibers. This has been explained in detail in Chapter 5 and also by Abedian and Szyszkowski (1997). The propagation of the cracks to other sites with increasing the number of cycles is indicated in Fig. 11.6.

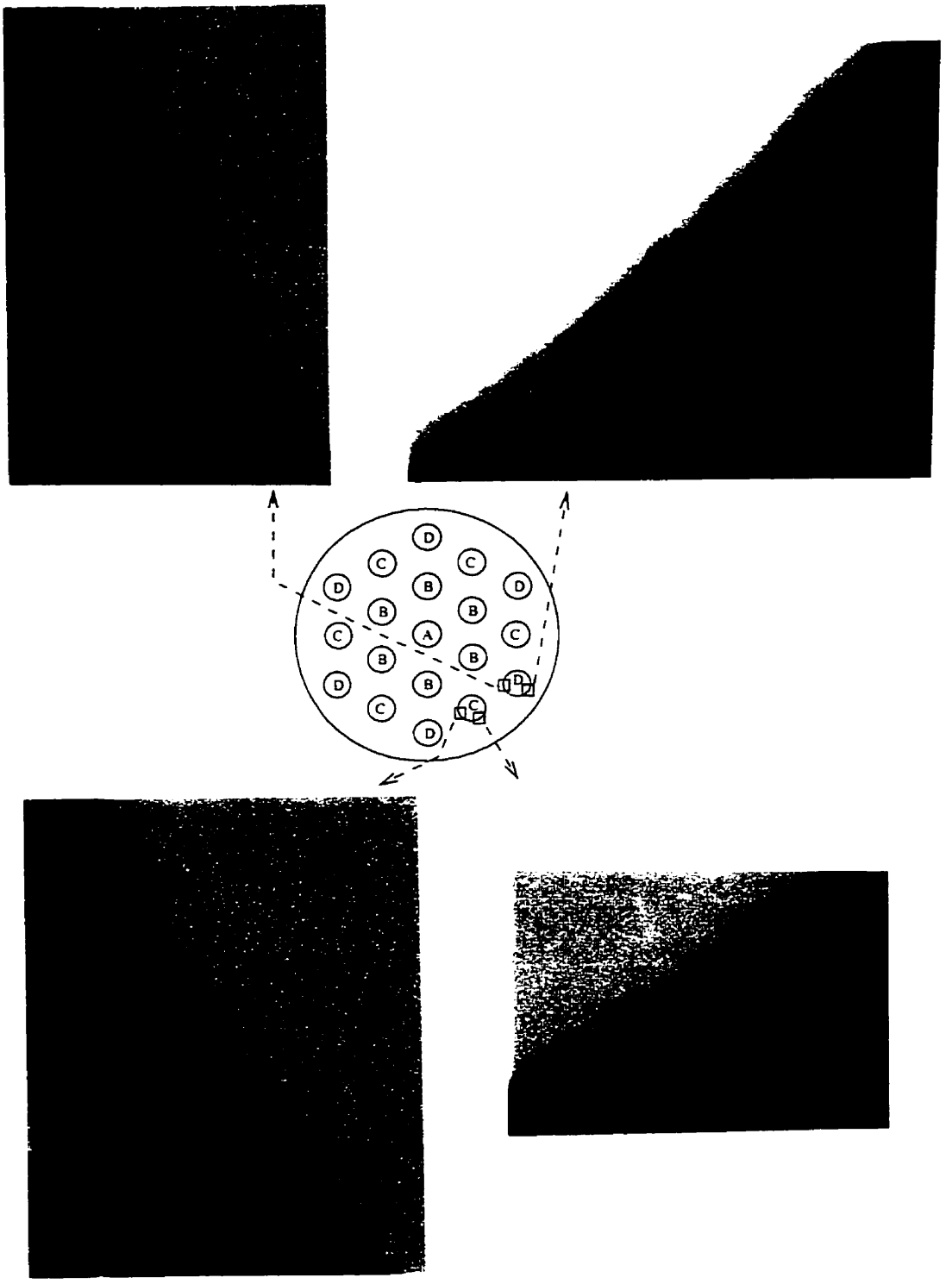

Fig. 11.4: Cracking pattern around the C and D fibers after the first cycle.

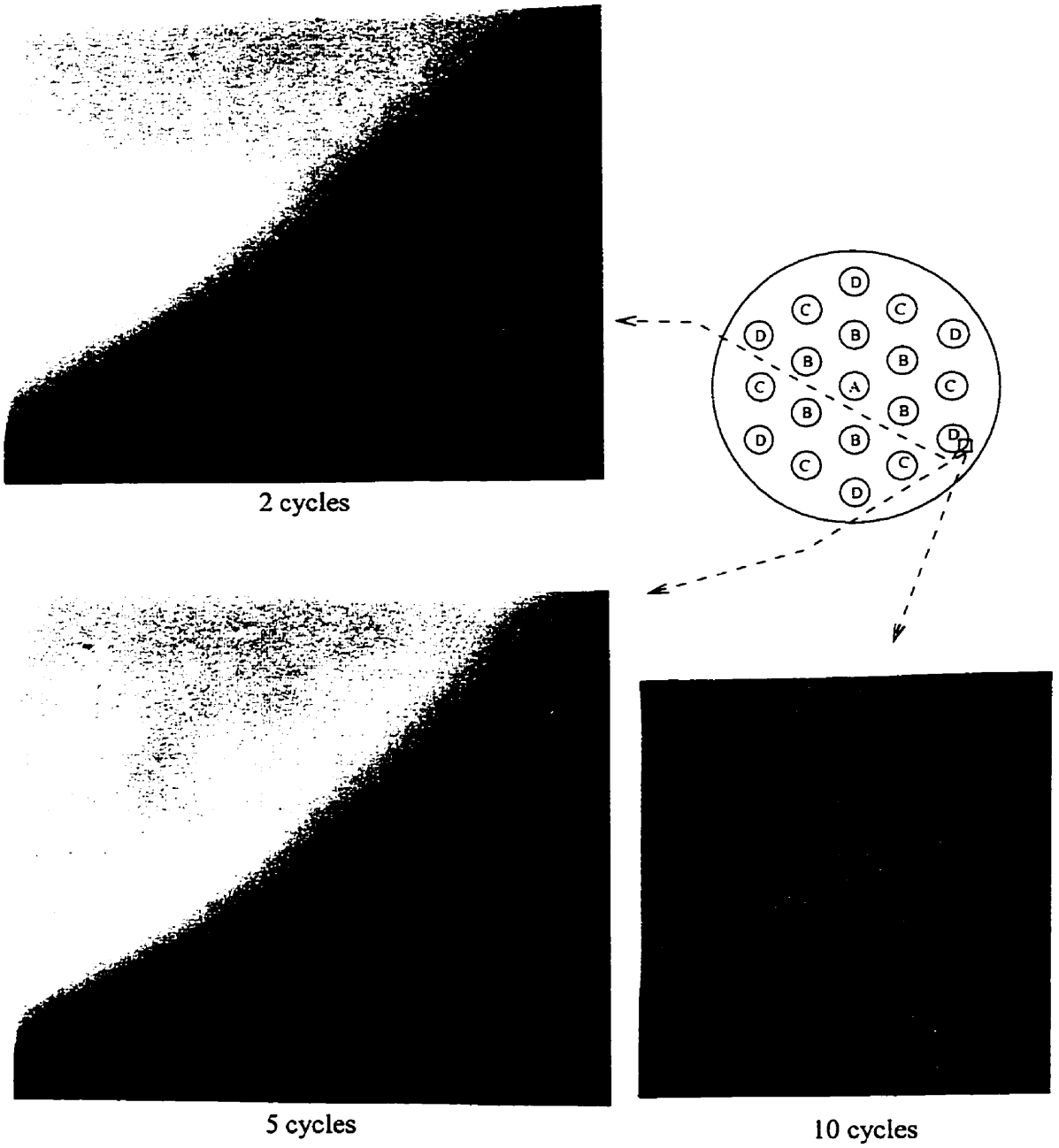

Fig. 11.5: Progression in matrix kinking around the C and D fibers with number of cycles.

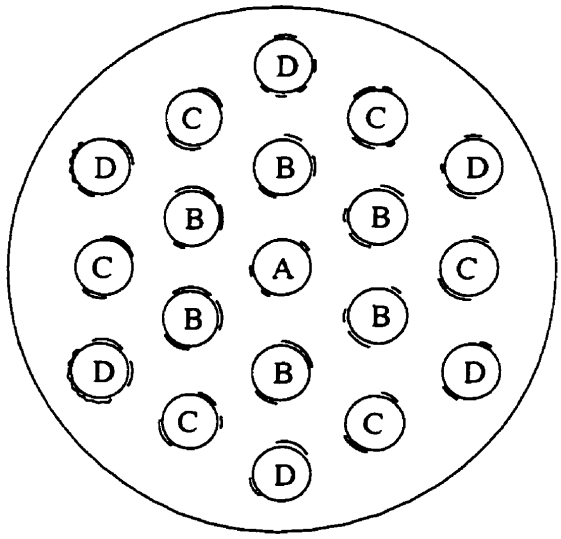

Cracking pattern after the first cycle.

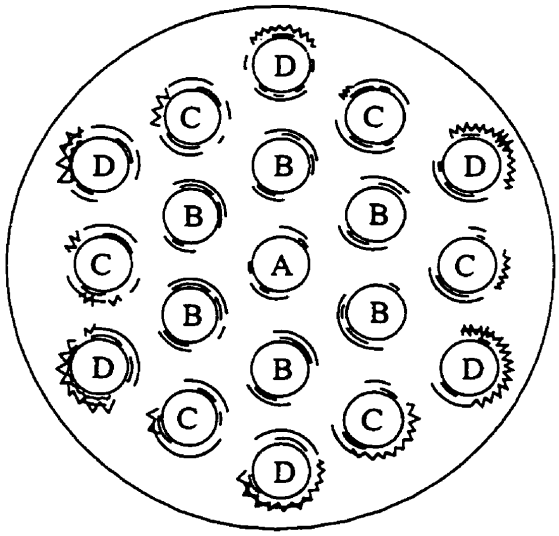

Cracking pattern after the fifth cycle.

Fig. 11.6: Crack propagation on the free surface of the large-scale composite specimens with number of cycles.

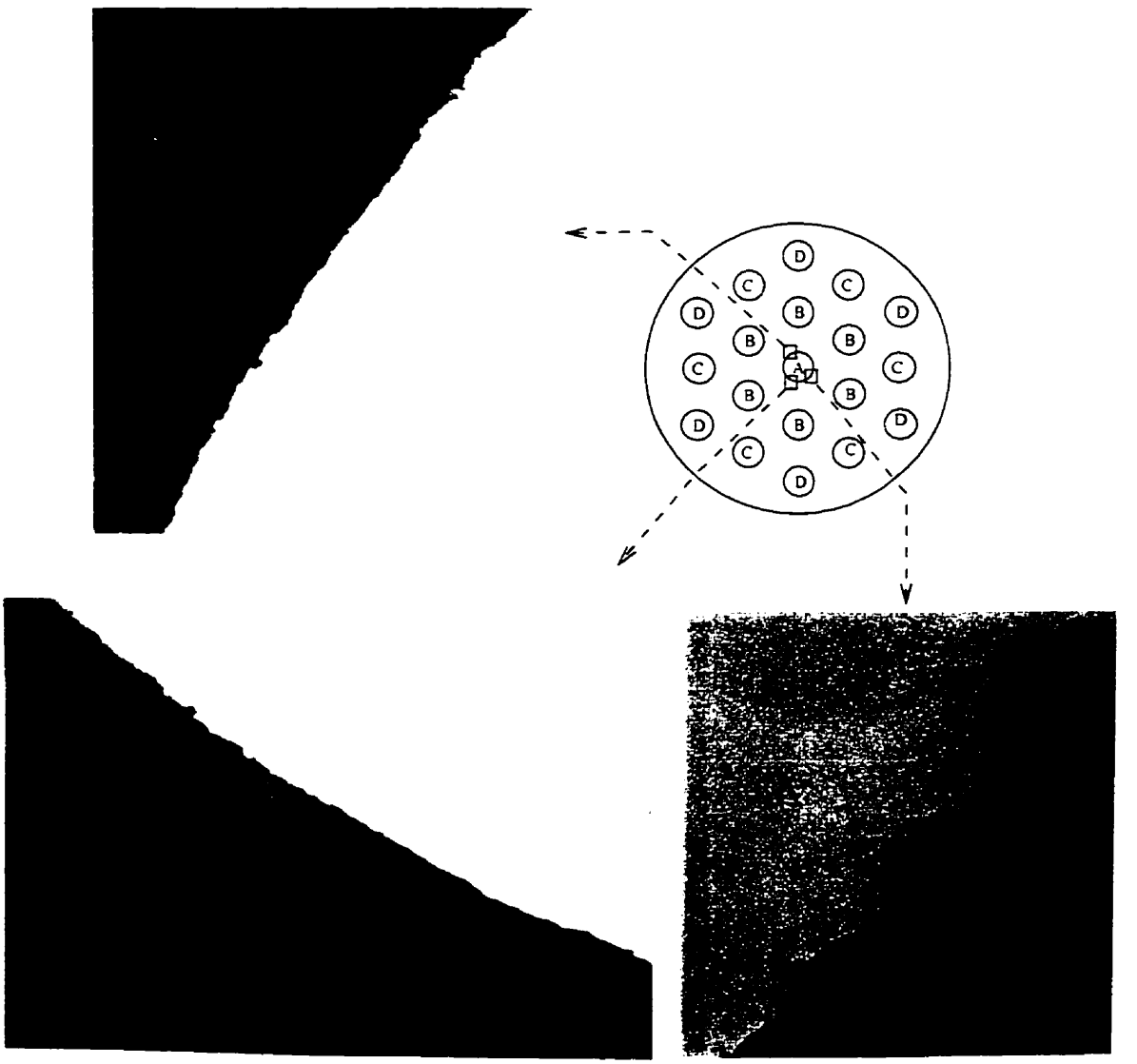

Fig. 11.7: Cracking pattern around the A fiber after the first cycle.

11.3 Effects of Fiber Protrusion on the Composite Deformation

As discussed in Chapter 9, the cut surface of a fiber composite may have three different configurations that greatly influence the stress state at the fiber end. These configurations are as follows. A small portion of the fiber end may extend out of the matrix (see Fig. 10.4(a)), the sharp corner of the fiber and the matrix on the cut surface may be filled with a ramp matrix-like material (Fig. 10.4(b)), and the fiber and matrix may not have the same heights on the free surface (the fiber bulge out) as shown in Fig. 10.4(c)).

The stresses for the first case (Fig. 10.4(a)) were shown to be higher than the stresses for the flat cut surface presented in Fig. 9.1(a) (see Chapter 9). For the second case (Fig. 10.4(b)), the high stresses may shift from the fiber/matrix interface to the region away from the interface where the ramp meets the matrix. Depending on the matrix strength and the fiber/matrix interface strength, cracks may develop either at the interface or in the matrix. These results were experimentally examined by exposing the first type of specimens (see Fig. 10.6(a)) to a single thermal cycle.

A sample with a small ramp of matrix around most of its fibers on the free surface was manufactured for this purpose. However, the angle ϕ (see Fig. 10.4(b)) is not easily controllable when manufacturing the specimen and is not the same for all the fibers. Therefore, depending on the magnitude of this angle, different stress levels appear at the contact corner of the ramp and the fibers on the free surface (Abedian et al., 1998) which result in different debonding lengths along different fibers. Small ϕ's reduce the stresses and result in short debonding lengths. For some fibers no debonding was observed at all. In some cases, where there was no measurable ramp around the fiber (see Fig. 10.4(a)), longer debonding appeared along the fiber. In this case, the stresses were much higher than in the case when the fiber and the matrix have ideally the same heights on the free surface (flat cut surface, Fig. 9.1(a)).

After exposing the specimen to a full temperature cycle, many deep cracks in the matrix area away from the interface were observed (see Fig. 11.8(a)). Deep cracks also appeared around the A fiber as shown in Fig. 11.8(b). The deep circumferential cracks in the matrix away from the interface confirmed the occurrence of the maximum radial stress away from the interface. This is caused by the sharp contact angle of the ramp and the matrix as predicted by the numerical analysis (see Fig. 9.10(a) and (Abedian et al., 1998)). These circumferential cracks in the matrix have also been observed by Biernacki (1996). Some cracks were also observed at the fiber/matrix interface that might be due to the weak interface strength or a high stress caused by the fiber/matrix sharp corner (see Fig. 11.8(c)). The high number of cracks and long fiber/matrix debonding show the adverse effects of a fiber extending out of the matrix on a composite cut surface.

11.4 Effects of the Covering Layer on The Composite Deformation

Based on the fiber-matrix overlapping hypothesis explained in Chapter 5, the high radial stress at the fiber end rather than the longitudinal shear stress was suggested to be responsible for the damage on the free surface of composites. It was numerically shown in Chapter 9 that upon cooling, the very high tensile radial and hoop stresses at the fiber end of a composite without cover are either eliminated or become compressive when the free surface is covered with a layer of matrix-like material (resin). Upon cooling, this extra layer of resin on the cut surface promotes overlapping thereby reducing the radial and hoop stress components, substantially. However, high longitudinal shear stress components still exist at the fiber end due to the fiber/matrix sharp corner. Therefore, if the radial stress causes cracking, the cracking should be eliminated or reduced by covering the fiber end. A specific test was designed to check the above numerical results. The test required specimens that have the end of their fibers embedded in the matrix. The specimens were made with two different processing schemes. The first scheme, in which the sample was made in one single processing stage, was presented in Chapter 10 (see Figs. 10.5(c) and (e)).

a) Large crack in the matrix away from the interface around the B fiber.

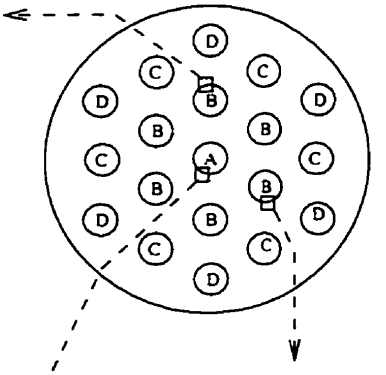

b) Large crack in the matrix away from the interface around the A fiber.

c) Fiber/matrix debonding.

Fig. 11.8: Cracking pattern on the free surface of the sample with fibers extending out of the matrix.

Two different samples were made using the first scheme. The fibers of the first sample were embedded in the matrix at one end and the other end was free. The second sample had the fibers embedded in the matrix at both ends. The samples were exposed to thermal cycling and analyzed after 1, 2, 5, 10, 20, 50, 100, 500, and 1000 cycles. Fig. 11.9 shows the photographs of the samples after 10, 50, 100, 500, and 1000 cycles. A comparison of both ends of the sample reveals a noticeable difference. The free surface end shows a similar behavior to that previously observed for the sample having both of its ends free (see Fig. 11.2). A similar progression in the debonding length and crack pattern around the fibers on the free surface as that of the previous sample (Fig. 11.3) were observed as cycling progressed.

For the covered end shown in Fig. 11.9, no sign of debonding or cracking was found. Even the matrix around the D and C fibers (which are vulnerable to small temperature change and show debonding even before being exposed to the actual working temperature cycles) show no sign of cracking or debonding. As expected, the thin matrix-like covering layer eliminates the very high radial tensile stress at the fiber end that is generated in the cooling phase of the thermal cycle. As the numerical study by Abedian et al. (1998) suggests, the normal axial and longitudinal interfacial shear stresses (generated by the sharp contact corner of the fiber end with the cover) are not high enough to cause fiber/matrix debonding. Also, at the contact surfaces between the fiber cross section and the covering layer, no sign of any damage was observed. In fact, upon cooling, the cover on the cross section of the fibers presses the fibers in the axial direction, thus preventing fiber/cover debonding. In fact, this compressive axial load causes overlapping which results in a compressive radial stress at the fiber end during the cooling phase of the temperature cycle. Comparing the deformations at both ends of the sample shows that one end of the sample is independent of the other or, simply, the sample is sufficiently long that the stresses at each end do not interfere with each other.

The experiments were repeated for the second sample with both ends covered. The thermal cycling results of these samples are shown in Fig. 11.10. Again, no sign of

cracking or debonding is present at either end of the fiber. These results show the effectiveness of the one-stage covering method.

The samples that were covered in a separate stage, behaved slightly differently. They did not show any cracking or debonding for about 20 cycles. However, after 50 cycles, fiber/matrix debonding was observed along the fiber length and also at the interface between the fibers and the cover as shown in Fig. 11.11. This indicates that the samples prepared by the two-stage covering scheme are affected by the residual stresses from the processing stage.

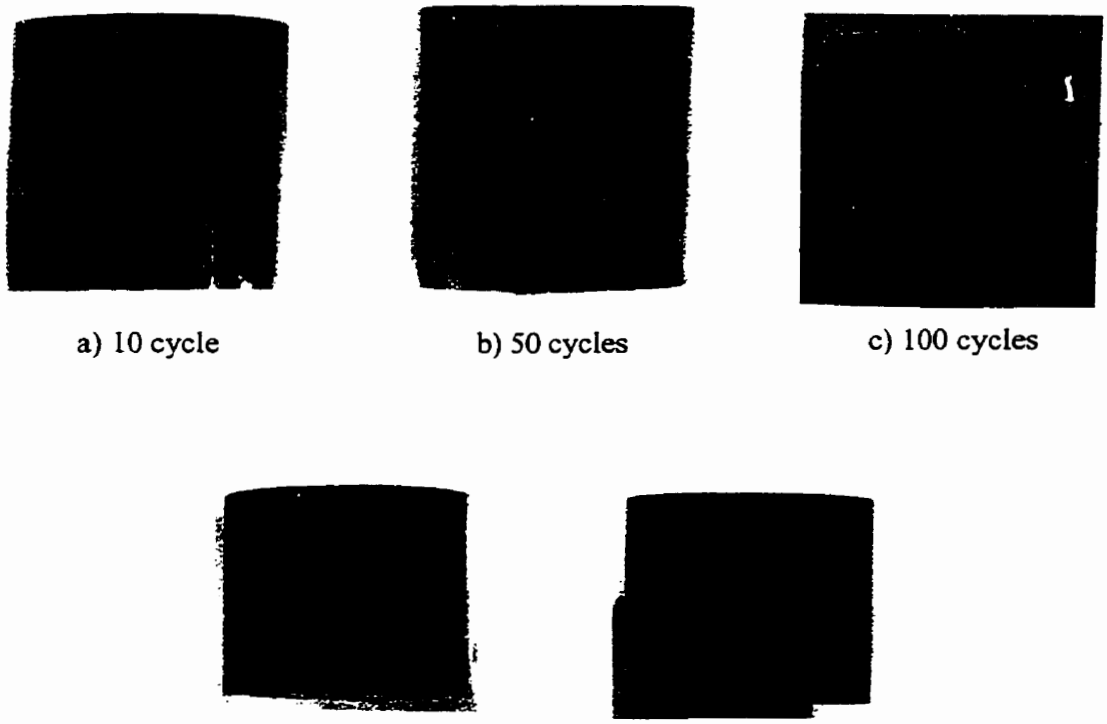

a) 10 cycle b) 50 cycles c) 100 cycles

d) 500 cycles e) 1000 cycles

Fig. 11.9: Effect of a covering layer on the damage at the fiber end with number of cycles for a specimen with one end covered and one end free.

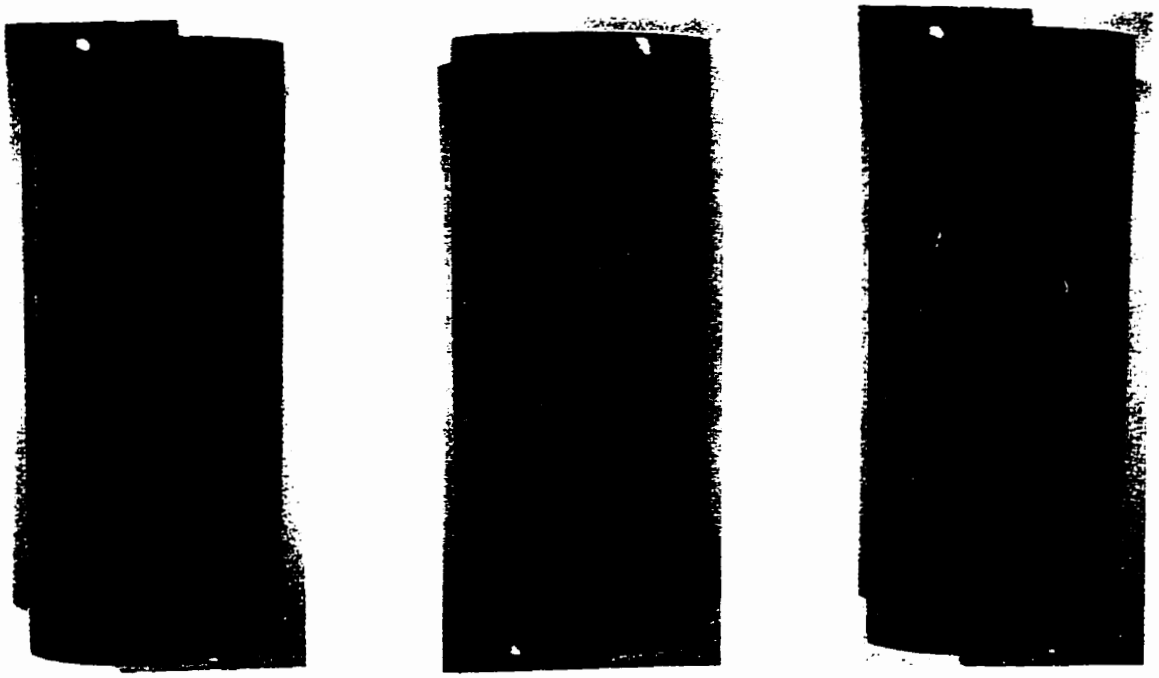

a) 1 cycle b) 100 cycles c) 500 cycles

Fig. 11.10: Effect of a covering layer on the damage at the fiber end with number of cycles for a specimen with both ends covered.

Fig. 11.11: Effect of the covering layer on the damage at the fiber end for a specimen covered by a two-stage manufacturing scheme (after 50 cycles).

12. Conclusions and Recommendations

12.1 Conclusions

Several conclusions regarding modeling and technical handling of fiber composites can be drawn from the study presented. These conclusions are divided into recommendations to facilitate preparation of the simulation model, and recommendations to help reduce the undesirable effects of temperature fluctuations.

12.1.1 Modeling

To model the variation in the stress and deformation states along the fiber length, in the interior and specifically at the fiber end near a free surface, three-dimensional models must be considered. The length of the model must be at least three times the fiber diameters or longer. Due to the large stress gradient expected at the fiber/matrix interface (which is generated by the mismatch in the modulus of elasticity or thermal expansion coefficient of the constituents) very small, in comparison to the fiber diameter, FEM elements and preferably of a higher order should be used in this area. The mesh could be coarser in the fiber away from the interface due to the more uniform distribution of the stress and deformation in the fiber. However, for thermal analyses, the elements can be larger due to the relatively smaller mismatch in thermal capacitance or thermal conductivity of the constituents.

Solving 3-D models requires a very large computational time and space. However, assuming axisymmetric states of stress and deformation may reduce the cost of calculations. This was shown to have little effect on the results achieved throughout this investigation. From elastic, elasto-plastic, and elasto-visco-plastic analyses conducted employing both types of models, the following observations were made:

- The elastic analysis indicated that, the stress field is singular at the fiber end. This area must be meshed with elements at least 1/10000 of the fiber radius to determine the order of singularity.

- Analysis of the singularity may be conducted using both the prism and axisymmetric models. Due to lower number of degrees of freedom, the axisymmetric model allows for the singular area to be meshed with a large number of fine elements. Using the 3-D model requires the use of a sub-modeling approach.

- The elasto-plastic analysis indicated that, the stress relaxation due to the plastic deformation along the fiber length influences the stress state in the interior of fiber composites. Therefore, for inelastic study of composites, using 2-D generalized plane strain assumption is not sufficient.

- For creep analysis, since the material is rate dependent, very small time steps are required. This increases the computational time considerably. However, the creep phenomenon may be ignored for very high cooling rates i.e. a few seconds (quenching in oil or water).

- Modeling the covering process needs careful use of element birth-death option. Also, the analysis of covering does not need a very fine mesh at the fiber end.

- The temperature dependent properties have a considerable impact on the state of stress and deformation during manufacturing and service temperatures.

- The inelastic behavior of materials plays a major role in relaxing and redistributing the residual stresses in the manufacturing process.

12.1.2 Technical Observations

Traditionally, the shear-lag theory has been dominating the stress analysis at the fiber/matrix interface. This theory ignores the radial and hoop stresses along the fiber length and concentrates only on the longitudinal shear stress. This stress component is next related to possible fiber/matrix debonding at the fiber end. However, the present study

indicated that the radial and hoop stresses are important especially at the fiber end. The overlapping hypothesis proposed in this study explains how these stresses are generated. In comparison to the longitudinal shear stress, the radial and hoop stress components at the fiber end are much larger which may influence the composite integrity to a higher extent.

The radial and hoop stresses at the fiber end are singular in nature if the analysis is elastic. The regular FEM elements are capable of calculating the order of singularity to a satisfactory degree. It was shown that the singular stresses are of the type $r^{-\alpha}$. The order of singularity (α) is sensitive to the material properties and is close to 1/3. This makes it difficult to assess the initiation and propagation of cracks at the fiber end using classical fracture mechanics that deals with singularities of the orders of 0.5.

The strength of the matrix is influencing significantly the integrity of composites and should be carefully chosen. High strength matrices prevent residual stress relaxation, increasing the chance of cracking during service temperatures. Low strength matrices are preferable since the residual stresses are much smaller, however, the deformation of the whole composite would be greater necessitating larger design tolerances. The creep phenomenon reduces the residual stresses. Thus, creep sensitive matrices may be advantageous. However, excessive creep strains threaten the dimensional stability of the composite. To reduce the creep effects, cooling from the processing temperature should be conducted with a very high rate (i.e. quenching in oil or water).

One of the contributions of the study is to suggest ways of reducing the thermal stresses in composites. This was accomplished by the analysis of the covering process and the effects of the free surface geometry. In particular, the study suggests that:

- The stress state at the free surface becomes more damaging if a fiber end extends out of the matrix. Therefore, any fiber end extending out of the matrix should be removed.
- On the other hand, polishing the free surface of composites in order to produce a smooth surface (removing fiber bulge-out) should also be avoided.

- Covering the free surface of composites with a thin layer of matrix like material can change the magnitude and sign of the lateral stresses at the fiber end upon cooling. The thickness of the cover should be about 1/10 of the fiber diameter. For best results, the covering should be performed during manufacturing of the composite. This is because there would exist no residual stresses at the fiber end prior to casting the cover to influence the process. However, if it is not technically possible to perform the simultaneous covering during the manufacturing process, two different covering schemes are considered. In both schemes, prior to casting the cover, the fiber end effects are to be removed by physically cutting the end of the composite part. Therefore, the lateral stresses at the fiber end on the newly generated free surface would be of the inner zone type which are small and relatively less damaging. In the first scheme, prior to casting the hot covering material, the composite is to be reheated to a temperature close to the temperature of the cover. In the second scheme, the covering is to be performed while the composite is at room temperature.

12.2 Future Work

Modeling the influence of the free surface and the covering process on the stress and deformation states of fiber composites presented here is in its preliminary stage only. The information presented in this thesis, is a portion of a more involved study that should be conducted using the proposed models and approaches. Several studies should be carried out in the future to complement the results presented in this thesis.

- The inelastic analysis of the covering process was performed without considering the creep deformations. It was assumed that the rate of cooling is fast enough to prevent creep strains from occurring. However, it would be interesting to know how creep affects the whole process.

- The present study provided information on thermal loads only. It would be useful to know how the free surface and covering process influence the composite performance under combined thermo-mechanical loads. The research group plans to repeat some of the work conducted in this study under various temperature and mechanical load

regimes. The effect of various rates of mechanical loading/unloading and heating/cooling, in-phase and out-of-phase, will be considered.

- A perfect interface was assumed in the present study. It is known that some intermediate layer between the fiber and the matrix may exist and influence the composite behavior. The effects of such layer on the stress state near the free surface or after covering should be examined.

- Further experimental work concerning the two-stage covering of laboratory-made large-scale composite samples should be performed to verify the numerical results obtained in this study.

- The experimental study of the covering process should be extended to examine its effectiveness in preventing thermal cycling induced damage in commercially available unidirectional reinforced composites.

References

Abedian, A. and Szyszkowski, W. 'Numerical study of thermal stress concentration on the free surface of unidirectional composites' *Proceedings of the Third Annual ISME Conference, Edited by Safar-Aval, M.*, p.633, (**1995**).

Abedian, A., and Szyszkowski, W. 'Influence of the free surface on the thermal stresses in unidirectional composites' *Composites, Part A: Applied science and manufacturing,* 28A(6), p. 573, (**1997**).

Abedian, A., Szyszkowski, W., and Yannacopoulos, S. 'Numerical analysis of process-induced thermal residual stresses in metallic matrix composites' *Thermal Stresses '97, The Second International Symposium on Thermal Stresses and Related Topics R.I.F., Rochester, New York,* p. 107, (**1997**).

Abedian, A., Szyszkowski, W., and Yannacopoulos, S. 'Residual thermal stresses in metallic and intermetallic matrix composites after cooling from processing temperature' Accepted in *J. of Composites Technology and Research,* (**1998**).

Abedian, A. and Szyszkowski, W., and Yannacopoulos, S. 'Effects of surface geometry of composites on thermal stress distribution; A numerical study' Accepted in *Composites Science and Technology,* (**1998**).

Adams, D. F. and Doner, D. R. 'Transverse Normal loading of a unidirectional composite' *J. of Composite Materials,* 1, p. 152, (**1967**).

Adams, D. F. and Tsai, S. W. 'The influence of random filament packing on the transverse stiffness of unidirectional composites' *J. of Composite Materials,* 3, p. 368, (**1969**).

Akin, J. E. 'The generation of elements with singularities' *Int. J. Num. Meth. Engng,* 10, p. 55, (**1976**).

Amirbayat, J. and Hearle, W. S. 'Properties of unit composites as determined by the properties of the interface. Part I: Mechanism of matrix-fiber load transfer' *Fiber Sci. Technol.*, 2, p. 123, (**1969**).

Ananth, C. R., Chandra, N., Murali, K., and Garmestani, H. 'Effect of inelastic material behavior on residual stresses in metal matrix composites' *Advanced Composites*

'93, Int. Conference on Advanced Composite Materials, Edited by Chandra, T., and Dhingra, A. K., The Minerals, Metals & Materials Society, p. 1317, **(1993)**.

ANSYS 'Engineering Analysis System,User's Manual' *Swanson Analysis Systems Inc.*, **(1996)**.

Arnold, S. M., Arya, V. K., Melis, M. E. 'Reduction of thermal residual stresses in advanced metallic composites based upon a compensating/compliant layer concept' *J. of Composite Materials*, 26(9), p. 1287, **(1992)**.

Biernacki, K. 'Micromechanics of composites under temperature cycling' *M.Sc. Thesis, Univ. of Saskatchewan, Saskatoon, SK, Canada,* **(1996)**.

Biernacki, K., Szyszkowski, W., and Yannacopoulos, S. 'A study of large-scale-model composite materials under thermal fatigue' *Accepted in principle in Composites*, **(1998)**.

Bigelow, C. A., Bahei-El-Din, Y. A., and Mirdamadi, M. 'Time-dependent deformation of titanium matrix composites' *ASTM STP 1253, W. S. Johnson, J. M. Larsen, and B. N. Cox, Eds., American Society for Testing Materials,* p. 278, **(1996)**.

Bigelow, C. A., Johnson, W. S., and Naik, R. A. 'A comparison of various micromechanics models for metal matrix composites' *Mechanics of Composite Materials and Structures, Reddy, J. N. and Teply, J. L. ASME, New York,* p. 21, **(1989)**.

Bogy, D. B. 'Edge-bonded dissimilar orthogonal elastic wedges under normal and shear loading' *ASME Trans. J. Appl. Mech.*, 35, p. 460, **(1968)**.

Broutman, L. J. and Agarwal, B. D. 'A theoretical study of the effect of an interfacial layer on the properties of composites' *Polymer Eng. Sci.*, 14, p. 581, **(1974)**.

Brown, K. M., Hendricks, R. W., and Brewer, W. D. 'X-ray diffraction measurements of residual stresses in SiC/Ti composites' *TMS Fall Meeting, Indianapolis, IN,* 1-5 October, p. 55, **(1989)**.

Carddock, J. N. 'Using finite element analysis to verify micromechanical models' *Advanced Composites '93, Int. Conference on Advanced Composite Materials, Edited by Chandra, T., and Dhingra, A. K., The Minerals, Metals & Materials Society,* p. 275, **(1993)**.

Carrara, A. S. and McGarry, F. J. 'Matrix and interface stresses in a discontinuous fiber composite model' *J. Composite Materials,* 2, p. 222, **(1968)**.

Chandra, N., Ananth, C. R., and Garmestani, H. 'Micromechanical modeling of process-induced residual stresses in Ti-24Al-11Nb/SCS-6 composite' *J. of Composites Technology & Research,* 16(1), p. 37, **(1994)**.

Chandra, N., Xie, Z.-Y. 'Application of superposition method to the thermal stress problem in composites' *Advanced Composites '93, Int. Conference on Advanced Composite Materials, Edited by Chandra, T., and Dhingra, A. K., The Minerals, Metals & Materials Society*, p. 323, (**1993**).

Chang, D. J. and Muki, R. 'Stress distribution in a lap joint under tension-shear' *Int. J. Solids Structures*, 10, p. 503, (1974).

Chawla, K. K. 'Composite materials science and engineering, Materials Research and Engineering (MRE) ' *Edited by Ilschner, B. and Grant N. J., Springer-Verlag New York*, (**1987**).

Chen Y.-C., Daehn, G. S., Wagoner, R. H. 'The potential for forming metal matrix components via thermal cycling' *Scripta Metallurgica et Materialia*, 24, p. 2157, (**1990**).

Chen, D. and Nisitani, H. 'Singular stress field in jointed materials due to thermal residual stress' *Nihon Kikaigakkai Rombunshu. A-Hen. Trans. of the Japan Society of Mech,. Eng. Series A.*, 59, p. 1937, (**1993**).

[a]**Cheng, C. and Aravas, N.** 'Creep of metal-matrix composites with elastic fibers-Part I: Continuous aligned fibers' *Int. J. Solids Structures*, 34(31-32), p. 4147, (**1997**).

[b]**Cheng, C. and Aravas, N.** 'Creep of metal-matrix composites with elastic fibers-Part II: A damage model' *Int. J. Solids Structures*, 34(31-32), p. 4171, (**1997**).

Cheong Y. M. and Marcus, H. L. 'In-situ thermal cycling in SEM of a graphite-aluminum composite' *Scripta Metallurgica*, 21, p. 1529, (**1987**).

Coker, D., Ashbaugh, N. E., and Nicholas, T. 'Analysis of thermomechanical cyclic behavior of unidirectional metal matrix composites' *Thermomechanical fatigue behavior of materials' ASTM STP 1186, H. Sehitoglu, ED., American Society for Testing and Materials, Philadelphia*, p. 50, (**1993**).

Cox, H. L. 'The elasticity and strength of paper and other fibrous materials' *Br. J. Appl. Phys.*, 3, p. 73, (**1952**).

Daehn, G. S. 'Plastic deformation of continuous-fiber reinforced composites subjected to changing temperature' *Scripta Metallurgica*, 23, p. 247, (**1989**).

Daniel, I. S. and Ishai, O. 'Engineering mechanics of composite materials' *Oxford University Press*, (**1994**).

Davy, P. J. and Guild, F. J. 'The distribution of interparticle distance and its application in finite-element modelling of composite materials' *Proc. Roy. Soc. London, Ser. A*, 418, p. 95, (**1988**).

De Kok, J. M. M., van Klinken, E. J., and Peijs, A. A. J. M. 'Influence of fiber surface treatment on the transverse properties of carbon fiber reinforced composites' *Advanced Composites '93, Int. Conference on Advanced Composite Materials, Edited by Chandra, T., and Dhingra, A. K., The Minerals, Metals & Materials Society,* p. 427, **(1993)**.

Dundurs, J. and Lee, M.-S. 'Stress concentration at a sharp edge in contact problems' *J. of Elasticity*, 2, p. 109, **(1972)**.

Durodola, J. F. and Ruiz, C. Thermal residual stresses in Ti-6-4/SiC_f metal matrix composite' *Advanced Composites '93, Int. Conference on Advanced Composite Materials, Edited by Chandra, T., and Dhingra, A. K., The Minerals, Metals & Materials Society,* p. 1133, **(1993)**.

[a]Fletcher, A. J., Oakeshott, J. L. 'Thermal residual microstress generation during the processing of unidirectional carbon fiber/epoxy resin composites: regular fiber arrays' *Composites*, 25(8), p. 797, **(1994)**.

[b]Fletcher, A. J., Oakeshott, J. L. 'Thermal residual microstress generation during the processing of unidirectional carbon fiber/epoxy resin composites: random fiber arrays' *Composites*, 25(8), p. 806, **(1994)**.

Folias, E. S. and Hohn, M. 'On the prediction of crack initiation in composite material systems due to a thermal expansion mismatch' *Twelfth U.S. National Congress of Applied Mechanics, Univ. of Washington, Seattle, Washington, USA*, p. 144, **(1994)**.

Folias, E. S. 'On the stress singularities at the intersection of a cylindrical inclusion with the free surface of a plate' *Int. J. of Fracture*, 39, p. 25, **(1989)**.

Foye, R. L. 'An evaluation of various engineering estimates of the transverse properties of unidirectional composites' *Proceedings of the Tenth National SAMPE Symposium-Advanced Fibrous Reinforced Composites*, p.155, **(1966)**.

Furness J. A. G. and Clyne, T. W. The application of Scanning laser extensometry to explore thermal cycling creep of metal matrix composites' *Materials Science and Engineering*, A141, p. 199, **(1991)**.

Gallagher, R. H. 'A review of finite element techniques in fracture mechanics' *Numerical Methods in Fracture Mechanics, Edited by Luxmore and Owen, Swansea*, p. 255, **(1978)**.

Gdoutos, E. E. & Theocaris, P. S. 'Stress concentrations at the apex of a plane indenter acting on an elastic half plane' *ASME Trans. J. Appl. Mech.*, 42, p. 688, **(1975)**.

Gdoutos, E. E., Karalekas, D., and Daniel, I. M. Thermal stress analysis of silicon carbide/aluminum composite' *Experimental Mechanics*, 45, p. 202, **(1991)**.

Goodier, J. N. 'Concentration of stress around spherical and cylindrical inclusions and flaws' *ASME Trans. J. Appl. Mech.*, 55, p. 39, (**1933**).

Goree, J. G. 'In-plane loading in an elastic matrix containing two cylindrical inclusions' *J. Composite Materials*, 1, p. 404, (**1967**).

Grayson, M. 'Encyclopedia of Composite Materials and Components' *John Wiley & Sons*, (**1983**).

Haener, J. and Ashbaugh, N. 'Three dimensional stress distribution in a unidirectional composite' *J. of Composite Materials*, 1, p.54, (**1967**).

Hahn, T. A. Thermal stress relaxation due to plastic flow in the fiber coating of a continuous fiber reinforced composite' *J. of Composite Materials*, 27(16), p. 1545, (**1993**).

Haritos, K. G. and Keer, L. M. 'Stress analysis for an elastic half space containing an embedded rigid block' *Int. J. Solids Structures*, 16, p. 19, (**1980**).

Hein, V. L. and Erdogan, F. 'Stress singularities in a two-material wedge' *Int. J. of Fracture Mech.*, 7, p. 317, (**1971**).

Hildebrandt J. R. 'The effects of thermal fatigue on fiber reinforced composites' *M. Sc. Eng. Thesis, University of Saskatchewan*, (**1990**).

Hughes, T. J. R. and Akin, J. E. 'Techniques for developing special finite element shape functions with particular reference to singularities' *Int. J. Num. Meth. Engng*, 15, p. 355, (**1980**).

Inoue, T., Koguchi, H. and Yada, T. 'Basic characteristic on distribution of thermal stresses near apex in dissimilar materials' *Nihon Kikaigakkai Rombunshu. A-Hen. Trans. of the Japan Society of Mech,. Eng. Series A.*, 61, p. 65, (**1995**).

Ioka S., Kubo, S., and Ohji, K. 'Free-edge stress singularity and its disappearance in bonded dissimilar materials under thermal stress loading' *Thermal Stresses '95, Proceedings of the First International Symposium on Thermal Stresses and Related Topics*, p. 19, (**1995**).

Ioka S., Kubo, S., and Ohji, K. 'Free-edge stress singularity and its disappearance in bonded dissimilar materials' *Computational Mechanics '95, Proceedings of the International Conference on Computational Engineering Science*, p. 2389, (**1995**).

Ioka, S., Kubo, S., Ohji, K., Kishimoto, J. 'Thermal residual stresses in bonded dissimilar materials and their singularities' *Trans. of the Japan Society of Mech,. Eng. JSME International Journal, Series A.*, 39(2), p. 1049, (**1996**).

James, M. R. 'Behavior of residual stresses during fatigue of metal matrix composites' *presented at the International Conference on Residual Stresses, ICRS-2, 23-26 July, Tokushima, Japan*, p. 105, (**1991**).

Jeng, S. M. and Yang, J.–M. 'Creep behavior and damage mechanisms of SiC-fiber-reinforced titanium matrix composite' *Materials Science and Engineering*, A171, p. 65, (**1993**).

Keer, L. M., Dundurs, J. and Kiattikomol, K. 'Separation of a smooth circular inclusion from a matrix' *Int. J. Engng Sci*, 11, p.1221, (**1973**).

Kelly, A. and Tyson, W. R. 'Fiber-strengthened materials' *J. Mech. Phys. Solids*, 10, p. 199, (**1963**).

Kelly, J. L. and Wilhoit, L. C. 'The stresses produced by uniform radial and lateral displacements of of two circular holes in an infinite plate' *Proceedings of the Fourth U. S. Natinal Congress of Applied Mechanics*, 1, p. 735, (**1962**).

King, J. A. 'A numerical study of thermal stress in composite materials' *M. Sc. Thesis, Univ. of Saskatchewan, Saskatoon, SK., Canada*, (**1994**).

Koufopoulos, T. and Theocaris, P. S. 'Shrinkage stresses in two-phase materials' *J. of Composite Materials*, 3, p. 308, (**1969**).

Kroupa, J. L. 'Elastic-plastic FEM analysis of MMC subjected to thermomechanical fatigue' *In Proceedings from Titanium Aluminide Composite Workshop, Smith, P. R., Balsone, S. J., and Nicholas, T., Eds., WL-TR-91-4020, Materials Behavior Branch, Wright Laboratory, WPAFP*, (**1991**).

Kupperman, D. S., Majumdar, S., Singh, P. J., and Sigal, A. 'Application of neutron diffraction time-of-flight measurement to the study of strain in composites, in measurement of residual and applied stress using neutron diffraction' *Kluwer Academic Publisher*, p. 439, (**1992**).

Kyriakopoulos, M. K., Kostopoulos, V. and Paipetis, S. A. 'Residual thermal stresses in unidirectional composites and their effect on the longitudinal e-modulus' *Advance Composites in Emerging Technologies, Paipetis, S. A. and Philippidis, T. P. AMATEC Publications*, p. 269, (**1991**).

Li, C. C. and Folias, E. S. 'Edge effect of a carbon fiber meeting a surface' *J. of Mechanics of Materials*, 12, p. 267, (**1991**).

Luk, V. K. and Keer, L. M. 'Stress analysis for an elastic half plane space containing an axially-loaded rigid cylindrical rod' *Int. J. Solids Structures*, 15, p. 805, (**1979**).

Macherle, J. and Fredriksson, B. 'Fracture mechanics' *Structural Mechanics Software Series III, Edited by Pilkey and Purman, Univ. of Virginia Press,* **(1980)**.

Majumdar, S., Singh, J. P., Kupperman, S. D., and Krawitz, A. 'Application of neutron diffraction to measure residual strains in various engineering composites composite materials' *Trans. ASME, J. Eng. Mater Technol,* 113(1), p. 51, **(1991)**.

Maksimovich G. G., Filipovskii, A. V., Mikheev, V. I., Gordienko, A. I., and Tarasenko, I. V. 'Effect of thermal cycling on the processes of deformation and failure of composite materials based on magnesium and reinforced with high-strength fibers' *G. V. Kharpenko Physicomechanical Institute, academy of Sciences of the Ukrainian SSR, Lvov, Translated from Fiziko-khimicheskaya Mekhanika Materialov,* 4, p. 47, **(1988)**.

Mall, S. and Ermer, P. G. 'Thermal fatigue behavior of a unidirectional SCS6/Ti-15-3 metal matrix composite' *J. of Composite Materials,* 25, p. 1668, **(1991)**.

Marloff, R. H. and Daniel, I. M. 'Three dimensional photo-elastic analysis of a fiber reinforced composite material' *Experimental Mechanics,* 9, p. 156, **(1969)**.

Mikata, Y. and Taya, M. 'Stress field in a coated continuous fiber composite subjected to thermo-mechanical loadings' *J. of Composite Materials,* 19, p.554, **(1985)**.

Mikata, Y. and Taya, M. 'Thermal stress in a coated short fiber composite' *J. of Applied Mechanics,* 53, p. 681, **(1986)**.

Misra, A. K. 'Effect of thermal cycling on interface bonding requirements in Al2O3 fiber reinforced superalloy composites' *Scripta Metallurgica et Materialia,* 28, p. 1189, **(1993)**.

[a]Morris, W. L., Inman, R. V. and Cox, B. N. 'Microscopic deformation in a heated unidirectional graphite - epoxy composite' *J. of Materials Science,* 24, p. 199, **(1989)**.

[b]Morris W. L., James, M. R., and Inman, R. V. 'Accelerated aging of the thermal expansion of unidirectional graphite/epoxy composites by thermal fatigue' *J. of Engineering Materials and Technology, Transactions of the ASME,* 111, p. 331, **(1989)**.

Murakawa, H. and Ueda, Y. 'Effect of singularity in stress field on optimum shape of ceramics/metal joint' *Trans. JWRI 20(1),* p. 109, **(1991)**.

Murakawa, H. and Ueda, Y. 'Shape optimization for reducing stress at ceramics/metal joints' *Trans. JWRI 18(2),* p. 133, **(1989)**.

Nairn, J. A. 'A variational mechanics analysis of the stresses around breaks in embedded fibers' *Mechanics of Materials,* 13, p. 131, **(1992)**.

Nairn, J. A. 'Thermoelastic analysis of residual stresses in unidirectional high performance composites' *Polymer Composites,* 6, p. 299, **(1985)**.

Nedele, M. R. and Wisnom M. R. 'Micromechanical modeling of a unidirectional carbon fiber-epoxy subjected to mechanical and thermal loading' *Proceedings of the 7th Technical Conference of the American Society for Composites, Publ. by Technomic Publ. Co. Inc.*, p. 328, (**1992**).

Nimmer, R. P. 'Fiber-matrix interface effects in the presence of thermally induced residual stresses' *J. of Composites Technology & Research*, 12(2), p. 65, (**1990**).

Nimmer, R. P., Bankert, R. J., Rusell, E. S., Smith G. A., and Wright, P. K. 'Micromechanical modeling of fiber/matrix interface effects in transversely loaded SiC/Ti-6-4 metal matrix composites' *J. of Composites Technology & Research*, 13(1), p. 3, (**1991**).

Ostrowski, J., Will, G. T. and Piggott, M. R. 'Poisson's stresses in fiber composites. I: Analysis', *J. of Strain Analysis*, 19(1), p. 43, (**1984**).

Penado, F. E. and Folias, E. S. 'The three-dimensional stress field around a cylindrical inclusion in a plate of arbitrary thickness' *Int. J. of Fracture*, 39, p. 129, (**1989**).

Pickard, S. M. and Derby, B. 'The behavior of metal matrix composites during temperature cycling' *Mterials Science and Engineering*, A135, p. 213, (**1991**).

Rangaswamy, P. and Jayaraman, N. 'Residual stresses in SCS-6/Ti-24Al-11Nb composite: part II-finite element modeling' *J. of Composites Technology & Research*, 16(1), p. 54, (**1994**).

Rangaswamy, P., Revelos, W. C., and Jayaraman, N. 'Residual stresses in SCS-6/Ti-24Al-11Nb composite: Part I-Experimental' *J. of Composites Technology & Research*, 16(1), p. 47, (**1994**).

Rosen, B. W. 'Mechanics of composite strengthening, in: Fiber Composite Materials' *American Society of Metals, Metals Park, Ohio*, p. 37, (**1964**).

Schiermeier, J. E. & Szabo, B. A. 'Numerical analysis of stress singularities in composite materials' *Eng. Fracture Mechanics*, 32, p. 979, (**1989**).

Sherwood, J. A., Quimby, H. M. 'Micromechanical modeling of damage growth in titanium based metal-matrix composites' *Computers & Structures*, 56(2/3), p. 505, (**1995**).

Soh, A. K. 'Development of a simulation procedure for the analysis of three-dimensional fiber-reinforced composites' *Composites*, 10, p. 925, (**1994**).

Sottos, N. R., McCullough, R. L. and Guceri, S. I. 'Thermal stresses due to property gradients at fiber/matrix interface' *Mechanics of Composite Materials and Structures, Reddy, J. N. and Teply, J. L. ASME, New York*, p. 11, (**1989**).

Staab, G. H. 'Estimating Singularity powers with finite elements' *Computers & Structures*, 17(1), p. 73, (**1983**).

Stern, M. 'Families of consistent conforming elements with singular derivative fields' *Int. J. Num. Meth. Engng*, 14, p.205, (**1979**).

Szyszkowski, W. and King, J. A. 'Stress concentration due to thermal loads in composite materials', *J. of Computer and Structures*, 56(2/3), p. 345, (**1995**).

Tirosh, J., Katz, E., Lifschuetz, G., and Tetelman, A. S. 'The role of fibrous reinforcements well bonded or partially debonded on the transverse strength of composite materials' *Engineering Fracture Mechanics*, 12, p. 267, (**1979**).

Tracey, D. M. and Cook, T. S. 'Analysis of power type singularities using finite elements' *Int. J. Num. Meth. Engng*, 11, p. 15, (**1977**).

Weeton, J. W., Peters, D. M. and Thomas, K. L. 'Engineer's guide to composite materials' *American Society for Metals*, (**1987**).

Wen Y. F., Gibson, R. F., Sullivan, J. L. 'Prediction of momentary transverse creep behavior of thermoplastic polymer matrix composites using micromechanical models' *J. of Composite Materials*, 31(21), p. 2124, (**1997**).

Westmann, R. A. 'Geometrical effects in adhesive joints' *Int. J. Engng Sci*, 13, p. 369, (**1975**).

Wetherhold R. C. and Westfall, L. J. 'Thermal cycling of tungsten-fiber-reinforced superalloy composites' *J. of Materials Science*, 23, p. 713, (**1988**).

White, S. R. and Hahn, h. T. 'Cure cycle optimization for the reduction of processing-induced residual stresses in composite materials' *J. of composite Materials*, 27(14), p. 1352, (**1993**).

[a]White, S. R. and Hahn, H. T. 'Process modeling of composite materials: residual stress development during cure. Part I. Model formulation' *J. of Composite Materials*, 26(16), p. 2402, (**1992**).

[b]White, S. R. and Hahn, H. T. 'Process modeling of composite materials: residual stress development during cure. Part II. Experimental Validation' *J. of Composite Materials*, 26(16), p. 2423, (**1992**).

Whitney, J. M. and Drzal, L. T. 'Axisymmetric stress distribution around an isolated fiber fragment' *Toughened composites, ASTM STP*, 937, p. 179, (**1987**).

Yamada, Y., Ezawa, Y., Nishigachi, I. and Okabe, M. 'Reconsiderations on singularity or crack tip elements' *Int. J. Num. Meth. Engng*, 14, p. 35, (**1979**).

Yeh, N.-M. and Krempl, E. The influence of cool-down temperature histories on the residual stresses in fibrous metal-matrix composites' *J. of composite Materials*, 27(10), p. 973, (**1993**).

Yu, I.-W. and Sendeckyj G. P. 'Multiple circular inclusion problems in plane elastostatic' *J. of Applied Mechanics, Trans. of the ASME*, p. 215, (**1974**).

Appendix A. Derivation of the Governing Equations of Unidirectional Composites

In general, the matrix and the fiber satisfy the usual equations of continuum mechanics that is the equilibrium equations

$$\sigma_{ij,j} = 0. \qquad i, j = x, y, z \tag{A.1}$$

The constitutive law

$$\sigma_{ij} = D_{ijkl}\,\varepsilon_{ij} \tag{A.2}$$

and the relations

$$\varepsilon_{kl} = \frac{1}{2}\left(u_{k,l} + u_{l,k} + u_{i,k}\,u_{i,l}\right) + \delta_{kl}\,\alpha_{kk}\,\Delta T \tag{A.3}$$

where all the material properties for the matrix are different than for the fiber. The proper continuity conditions must be satisfied at the fiber/matrix interface. Due to this complexity only unusual solutions are possible. Typically fibers are cylindrical. Therefore, cylindrical coordinate systems are used especially in analytical solutions (Figs. A.1(a) and A.1(b)).

The general 3-D equilibrium equations in cylindrical coordinates for an arbitrary element (as shown in Fig. A.1(c)) of the fiber or matrix have the following form

$$\begin{cases} \sum F_r = 0 \\ \sum F_\theta = 0 \Rightarrow \\ \sum F_z = 0 \end{cases} \qquad \begin{cases} \dfrac{\partial \sigma_r}{\partial r} + \dfrac{1}{r}(\sigma_r - \sigma_\theta) + \dfrac{\partial \tau_{rz}}{\partial z} + \dfrac{1}{r}\dfrac{\partial \tau_{r\theta}}{\partial \theta} = 0 \\ \dfrac{1}{r}\dfrac{\partial \sigma_\theta}{\partial \theta} + \left(\dfrac{\partial \tau_{r\theta}}{\partial r} + \dfrac{\partial \tau_{\theta z}}{\partial z}\right) + \dfrac{1}{r}\tau_{r\theta} = 0 \\ \dfrac{\partial \sigma_z}{\partial z} + \dfrac{1}{r}\left(\dfrac{\partial \tau_{\theta z}}{\partial \theta} + \tau_{rz}\right) + \dfrac{\partial \tau_{rz}}{\partial r} = 0 \end{cases} \tag{A.4}$$

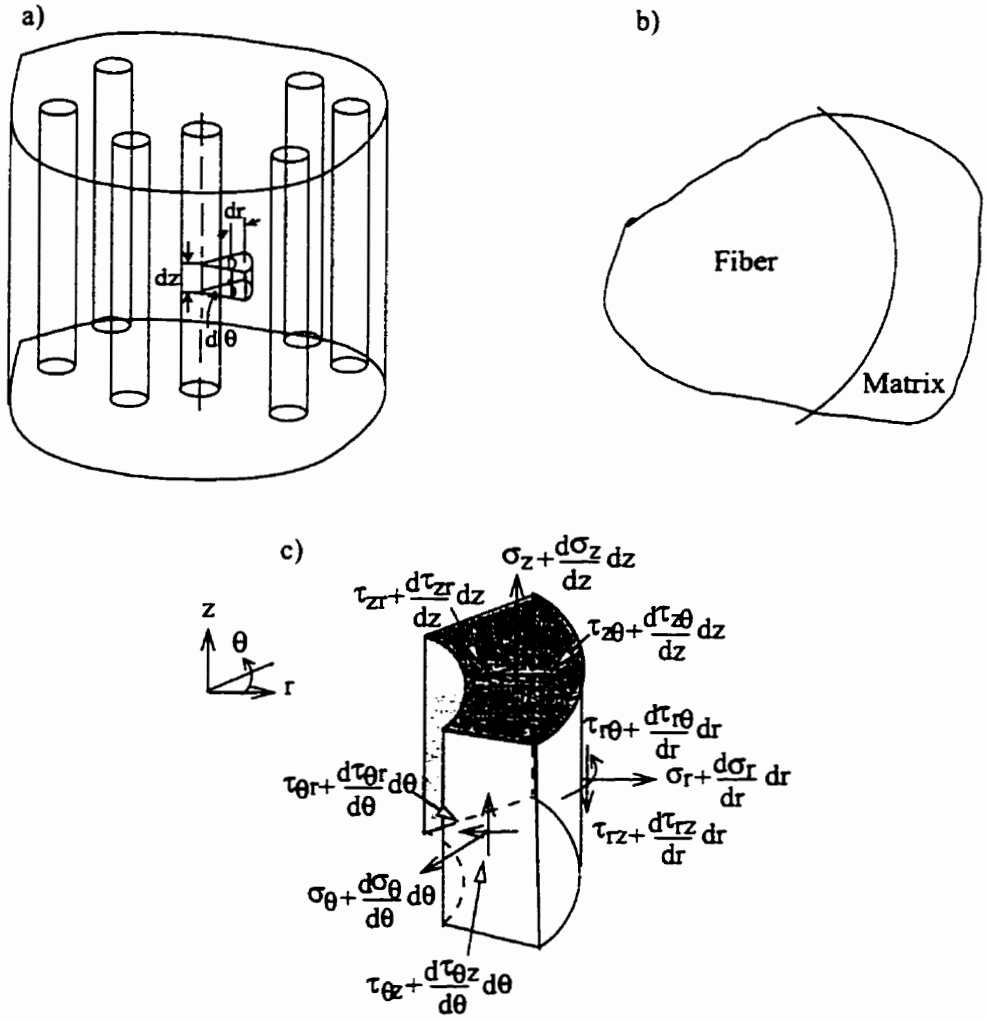

Fig. A.1: An arbitrary element representing the fiber or matrix in cylindrical coordinates.

For elastic behavior, using the generalized Hook's law for orthotropic materials and the linear form of strain tensor for cylindrical coordinates, the equilibrium equations may be written in terms of the displacements as follows

$$\begin{cases} A_1\left(\frac{\partial^2 u_r}{\partial r^2}+\frac{1}{r}\frac{\partial u_r}{\partial r}-\frac{u_r}{r^2}\right)+\frac{A_2}{r^2}\frac{\partial^2 u_r}{\partial \theta^2}+A_3\frac{\partial^2 u_r}{\partial z^2}+\frac{A_4}{r^2}\frac{\partial u_\theta}{\partial \theta}+\frac{A_5}{r}\frac{\partial^2 u_\theta}{\partial \theta\,\partial r}+A_6\frac{\partial^2 u_z}{\partial z\partial r}=A_7\frac{\partial T}{\partial r} \\ \frac{B_1}{r^2}\frac{\partial^2 u_\theta}{\partial \theta^2}+B_2\frac{\partial^2 u_\theta}{\partial r^2}+B_3\frac{\partial^2 u_\theta}{\partial z^2}+\frac{B_4}{r}\frac{\partial^2 u_r}{\partial \theta\,\partial r}+B_5\frac{\partial u_r}{\partial \theta}+\frac{B_6}{r}\frac{\partial^2 u_z}{\partial \theta\,\partial z}=B_7\frac{\partial T}{\partial \theta} \\ C_1\frac{\partial^2 u_z}{\partial r^2}+\frac{C_2}{r^2}\frac{\partial^2 u_z}{\partial \theta^2}+\frac{C_3}{r}\frac{\partial u_z}{\partial r}+C_4\frac{\partial^2 u_z}{\partial z^2}+\frac{C_5}{r}\frac{\partial^2 u_\theta}{\partial \theta\,\partial z}+C_6\frac{\partial^2 u_r}{\partial z\,\partial r}+\frac{C_7}{r}\frac{\partial u_r}{\partial \theta}+\frac{C_8}{r}\frac{\partial u_r}{\partial z}=C_9\frac{\partial T}{\partial z} \end{cases}$$

(A.5)

where A_1-A_7, B_1-B_7, and C_1-C_9 are material constants. These constants are different for the fiber and matrix. For isotropic materials the constants are presented bellow.

$$
\begin{aligned}
&A_1 = B_1 = B_5 = -C_4 = \frac{1-\upsilon}{(2\upsilon^2+\upsilon-1)}E \\
&A_2 = A_3 = B_2 = B_3 = C_1 = C_2 = C_3 = C_8 = G \\
&A_4 = \frac{1-\upsilon}{(2\upsilon^2+\upsilon-1)}E - G \\
&A_5 = A_6 = B_4 = B_6 = C_5 = C_6 = \frac{-\upsilon}{(2\upsilon^2+\upsilon-1)}E + G \\
&A_7 = B_7 = \frac{-(1+\upsilon)}{(2\upsilon^2+\upsilon-1)}E\omega \\
&C_7 = \frac{-\upsilon}{(2\upsilon^2+\upsilon-1)}E \\
&C_9 = \frac{-1}{(2\upsilon^2+\upsilon-1)}E\omega
\end{aligned}
\qquad \text{(A.6)}
$$

where E, υ, and G are the material constants either for the matrix or for the fiber. Here, ω represents the CTE of the composite constituents. One of the most popular models is the general 3-D model shown in Fig. A.2. The boundary conditions and continuity assumptions are as follows

Boundary conditions:

$$
\begin{aligned}
&\text{at } z = 0 \Rightarrow \tau_{rz} = \tau_{\theta z} = 0 \\
&\text{at } z = L/2 \Rightarrow \sigma_z = \tau_{rz} = 0 \\
&\text{at } r = r_f \Rightarrow \sigma_r^f = \sigma_r^m \\
&\text{at } \theta = 0^\circ \Rightarrow u_\theta^m = u_\theta^f = 0 \\
&\text{at } \theta = 30^\circ \Rightarrow u_\theta^m = u_\theta^f = \text{constant} \\
&\text{at } x = 0 \Rightarrow u_y^m = \text{constant} \\
&\text{at } z=0 \Rightarrow u_z^m = u_z^f = 0
\end{aligned}
\qquad \text{(A.7)}
$$

Continuity:

$$\text{at } r = r_f \Rightarrow u_r^m = u_r^f ;\ u_\theta^m = u_\theta^f ;\ u_z^m = u_z^f$$

To solve the above set of partial differential equations (PDE), all the boundary conditions as well as the continuity requirements should be satisfied.

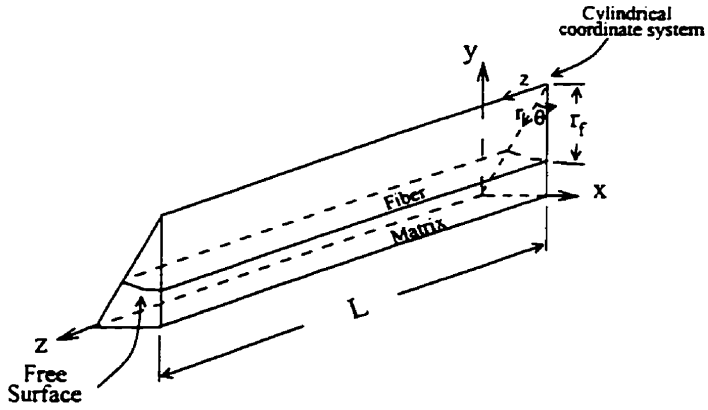

Fig. A.2: The general 3-D model.

The next level of assumptions is based on the assumption of axisymmetric displacement field. Equations (A.5) simplify to

$$\begin{cases} A_1\left(\frac{\partial^2 u_r}{\partial r^2}+\frac{1}{r}\frac{\partial u_r}{\partial r}-\frac{u_r}{r^2}\right)+A_3\frac{\partial^2 u_r}{\partial z^2}+A_6\frac{\partial^2 u_z}{\partial z\partial r}=A_7\frac{\partial T}{\partial r} \\ B_2\frac{\partial^2 u_\theta}{\partial r^2}+B_3\frac{\partial^2 u_\theta}{\partial z^2}=0 \\ C_1\frac{\partial^2 u_z}{\partial r^2}+\frac{C_3}{r}\frac{\partial u_z}{\partial r}+C_4\frac{\partial^2 u_z}{\partial z^2}+C_6\frac{\partial^2 u_r}{\partial z\,\partial r}+\frac{C_8}{r}\frac{\partial u_r}{\partial z}=C_9\frac{\partial T}{\partial z} \end{cases} \tag{A.8}$$

All the derivatives with respect to z-direction are significant only in the vicinity of the free surface. Since any changes in the θ-direction are neglected, the concentric cylindrical model shown in Fig. A.3 can be considered. The boundary conditions and continuity assumptions for the axisymmetric case are as follows

Boundary conditions:

$$\text{at } z=0 \Rightarrow \tau_{rz}=\tau_{\theta z}=0$$

$$\text{at } z=L/2 \Rightarrow \sigma_z=\tau_{rz}=0$$

$$\text{at } r=r_f \Rightarrow \sigma_r^f=\sigma_r^m \tag{A.9}$$

$$\text{at } r=r_m \;\&\; -L/2\le z\le L/2 \Rightarrow u_r^m=\text{constant}$$

Continuity:

$$\text{at } r=r_f \Rightarrow u_r^m=u_r^f;\; u_\theta^m=u_\theta^f;\; u_z^m=u_z^f$$

Finally, if in the axisymmetric model the end effects are neglected, Eq. (A.8) can be further simplified to the so-called Lame-problem. For this problem the equilibrium equation (A.4) reduces to

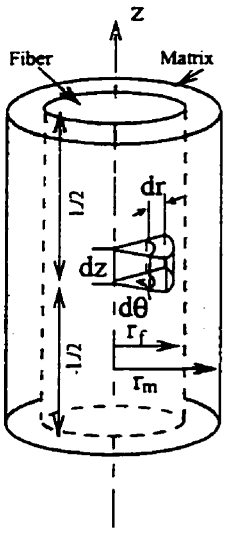

Fig. A.3: Concenteric cylinder model.

$$\begin{cases} \dfrac{d\sigma_r}{dr} + \dfrac{1}{r}(\sigma_r - \sigma_\theta) = 0 \\ \sigma_z = \text{constant} \end{cases} \tag{A.10}$$

The strain tensor will have only the following terms

$$\begin{cases} \varepsilon_r = \dfrac{du_r}{dr} \\ \varepsilon_\theta = \dfrac{u_r}{r} \\ \varepsilon_z = \text{constant} \end{cases} \tag{A.11}$$

It is assumed that the change in stresses and displacements along the fiber length are constant. Therefore, Eq. (A.8) reduces to

$$\begin{cases} A_1\left(\dfrac{d^2u_r}{dr^2} + \dfrac{1}{r}\dfrac{du_r}{dr} - \dfrac{u_r}{r^2}\right) = A_1\dfrac{d}{dr}\left[\dfrac{1}{r}\left(\dfrac{d(ur)}{dr}\right)\right] = A_7\dfrac{dT}{dr} \\ B_2\dfrac{d^2u_\theta}{dr^2} = 0 \end{cases} \tag{A.12}$$

This set is usually referred to as the Lame equations. Note that the stress and displacement components are in term of the radius r only. These solutions are used to analyze the plane stress (if σ_z=0), the plane strain (if ε_z=0), or in the generalized plane strain (if ε_z= constant)

states. A solution of the Lame equation is presented here and a comparison of the results with the FEM solution obtained using ANSYS, a commercial software, is discussed.

If the temperature gradient is negligible, Eq. (A.12) reduces to

$$u = C_1 r + \frac{C_2}{r} \tag{A.13}$$

A small temperature change creates a contact pressure at the interface (P_c). Substituting Eq. (A.11) into Eq. (A.2) and subsequently substituting the resultant equation into Eq. (A.13) yields

$$\sigma_r = \frac{E}{(1+\upsilon)(1-2\upsilon)}\left[C_1 - (1-2\upsilon)\frac{C_2}{r^2} + \upsilon\varepsilon_z\right] - K \tag{A.14}$$

where

$$K = \frac{E}{(1-2\upsilon)}\omega\Delta T \tag{A.15}$$

Considering the boundary conditions for the fiber, i.e.

$$\text{At } r = 0, \text{ since } \sigma_r \text{ must have finite value, } \Rightarrow C_2 = 0$$

$$\text{At } r = r_f \Rightarrow \sigma_r^f = P_c \Rightarrow C_1 = \frac{(P_c + K^f)(1+\upsilon_f)(1-2\upsilon_f)}{E_f} - \upsilon_f \varepsilon_z^f$$

Substituting C_1 and C_2 into Eq. (A.13) yields

$$u^f(r) = \left[\frac{(P_c + K^f)(1+\upsilon_f)(1-2\upsilon_f)}{E_f} - \upsilon_f \varepsilon_z^f\right] r \tag{A.16}$$

Similarly, the boundary conditions for the matrix are

$$\text{At } r = r_f \Rightarrow \sigma_r^m = P_c \tag{A.17}$$

$$\text{At } r = r_m \Rightarrow \sigma_r^m = 0$$

Substituting Eqs. (A.17) into Eqs. (A.14) and (A.15) yields

$$u^m(r) = \left[\frac{(1+\upsilon_m)(1-2\upsilon_m)}{E_m}\left(K^m + \frac{P_c r_f^2}{r_f^2 - r_m^2}\right) - \upsilon_m \varepsilon_z^m\right] r + \left[\frac{P_c (1+\upsilon_m) r_m^2 r_f^2}{E_m (r_f^2 - r_m^2)}\right]\frac{1}{r} \tag{A.18}$$

At $r = r_f \Rightarrow u^m(r) = u^f(r)$, hence

$$\varepsilon^z = \frac{(1+\upsilon_m)(1-2\upsilon_m)}{E_m(\upsilon_m - \upsilon_f)}\left(K^m + \frac{P_c r_f^2}{r_f^2 - r_m^2}\right) + \frac{(1+\upsilon_m) P_c r_m^2}{E_m(\upsilon_m - \upsilon_f)(r_f^2 - r_m^2)} - \left[\frac{(P_c + K^f)(1+\upsilon_f)(1-2\upsilon_f)}{E_f(\upsilon_m - \upsilon_f)}\right] \tag{A.19}$$

Since ε_z and P_c both are unknown, one more equation is required to solve for the unknowns.

Rewriting the strain components in terms of the stresses from Eq. (A.2)

$$\varepsilon_z = \frac{1}{E}[\sigma_z - \upsilon(\sigma_r + \sigma_\theta)] + \alpha_z \Delta T \tag{A.20}$$

To compute the axial strain (ε_z), both sides of the above equation are multiplied by (Er) and then integrated over the composite cross section (see Fig. A.3).

$$\varepsilon_z \int_0^{r_m} Er\,dr = \int_0^{r_m} \sigma_z r\,dr - \int_0^{r_m} \upsilon(\sigma_r + \sigma_\theta) r\,dr + \int_0^{r_m} \omega_z E \Delta T r\,dr \tag{A.21}$$

For Lame solution ε_z is constant. Thus;

$$\varepsilon_z \int_0^{r_m} Er\,dr = \frac{1}{2}\varepsilon_z \left[E_f r_f^2 + E_m\left(r_m^2 - r_f^2\right)\right] \tag{A.22}$$

The first term of the right hand side of Eq. (A.20) is zero. From the equilibrium equation in the axial direction;

$$\sum F_z = 0 \Rightarrow \frac{d\sigma_z}{dz} = \frac{dP_z}{dz} \quad \text{or} \quad \sigma_z = P_z \tag{A.23}$$

Since no external stress is considered, thus ($P_z = \sigma_z = 0$).

Eq. (A.10) may be used to calculate the second term of the right hand side of Eq. (A.21).

$$\int_0^{r_m} \upsilon(\sigma_r + \sigma_\theta) r\,dr = \int_0^{r_m} \upsilon \frac{d}{dr}\left(r^2 \sigma_r\right) dr = (\upsilon_f - \upsilon_m) r_f^2 P_c \tag{A.24}$$

And the third term is calculated as follows

$$\int_0^{r_m} \alpha_z E \Delta T r\,dr = \left[\frac{\omega_f E_f r_f^2 + \omega_m E_m\left(r_m^2 - r_f^2\right)}{2}\right] T \tag{A.25}$$

Substituting Eqs. (A.22)-(A-25) back into Eq. (A.21) yields

$$\varepsilon_z = \frac{1}{E_c}[-2(\upsilon_f - \upsilon_m) V_f P_c + \omega_c E_c T] \tag{A.26}$$

where

$$V_f = \frac{r_f^2}{r_m^2} \quad ; \quad V_m = \frac{r_m^2 - r_f^2}{r_m^2}$$
$$E_c = E_f V_f + E_m V_m \tag{A.27}$$
$$\alpha_c = \frac{\omega_f E_f V_f + \omega_m E_m V_m}{E_c}$$

Eqs. (A.19) and (A.27) are solved for ε_z and P_c.

To test the accuracy of the solution, an example was solved using the above analytical formulation and ANSYS, a FEM software. Assuming the following data

$\omega_f = -0.99e-6 \ \mu m/\mu m/^\circ C$ $\omega_m = 102.6e-6 \ \mu m/\mu m/^\circ C$

$E_f = 213.73 \ GPa$ $E_f = 3.44 \ GPa$

$\upsilon_f = 0.2$ $\upsilon_f = 0.41$

$V_f = 0.4935$ $V_m = 0.5065$

$r_f = 3.81 \ \mu m$ $r_m = 5.4235 \ \mu m$

$\Delta T = 100^\circ C$

The axial stresses in the fiber and matrix at the interface calculated by the analytical method using Eqs. (A.19) and (A.26) are as follows

$$\text{At} \quad r = r_f \Rightarrow \sigma_z^f = 49.472 \quad MPa$$
$$\text{At} \quad r = r_f \Rightarrow \sigma_z^m = -49.0174 \quad MPa$$

Similar stresses were calculated by ANSYS for the same problem.

$$\text{At} \quad r = r_f \Rightarrow \sigma_z^f = 49.205607 \quad MPa$$
$$\text{At} \quad r = r_f \Rightarrow \sigma_z^m = -48.00609 \quad MPa$$

The error is less than 2%.

Appendix B. The Shear-Lag Theory

Normally, it is assumed that, transfer of the applied load to the fiber occurs by means of the shear stress at the interface. The matrix behavior can influence the load transfer. Here, the effects of two options, i.e. elastic and elasto-plastic response of the matrix material are discussed.

B.1 Elastic Matrix

Assume the displacement of point K that is sufficiently away from the fiber end (see Fig. 2.7) to be u in the presence and v in the absence of the fiber, respectively. Therefore, the load transfer from the matrix to the fiber can be written as

$$\frac{dP_f}{dx} = B(u - v) \tag{B.1}$$

Where B (the shear interaction parameter) is a constant that depends on the geometrical packing of the fibers and the matrix properties. Differentiating this equation and substituting for the strain in the fiber ($\frac{du}{dx} = \frac{P_f}{E_f A_f}$) and for the strain in the matrix away from the fiber ($\frac{dv}{dx} = e$, the imposed strain) yields

$$\frac{d^2 P_f}{dx^2} = B(\frac{P_f}{E_f A_f} - e) \tag{B.2}$$

The solution to this partial differential equation (PDE) has the form

$$P_f = E_f A_f e + S\sinh\beta x + T\cosh\beta x \tag{B.3}$$

where

$$\beta = (\frac{B}{A_f E_f})^{1/2} \tag{B.4}$$

Using the boundary conditions of $P_f = 0$ at $x = 0$ and $x = L$ the following is obtained

$$\sigma_f = \frac{P_f}{A_f} = E_f e\left[1 - \frac{\cosh\beta(L/2 - x)}{\cosh\beta L/2}\right] \quad \text{for } 0 < x < L/2 \tag{B.5}$$

The maximum possible strain in the fiber is the imposed strain e, which creates a maximum stress of $\sigma_{fu} = eE_f$. A plot of σ_f for a sufficiently long fiber is shown in Fig. 2.7. The stress in the fiber will increase from both ends (where it is zero) to its maximum i.e. $\sigma_{fu} = eE_f$. The variation of the shear stress along the fiber length can also be found by balancing the forces over an element of the fiber

$$\frac{d\sigma_f}{dx} = \frac{2\tau}{r_f} \tag{B.6}$$

Substituting the differential of σ_f from Eq. (B.5) into Eq. (B.6) yields

$$\tau = \frac{E_f r_f e}{2}\beta\frac{\sinh\beta(L/2 - x)}{\cosh(\beta L/2)} \tag{B.7}$$

Variation of τ along the fiber length is also presented in Fig. 2.7. It has been shown that the geometric parameters (B or β) has the following form

$$B = \frac{2\pi G_m}{\ln\frac{R}{r_f}} \quad \text{or} \quad \beta = \left[\frac{2\pi G_m}{E_f A_f \ln\frac{R}{r_f}}\right]^{1/2} \tag{B.8}$$

where G_m is the shear modulus of the matrix. For example, for hexagonal fiber packing $\ln\frac{R}{r_f} = \frac{1}{2}\ln\left(\frac{2\pi}{\sqrt{3}V_f}\right)$ and $\ln\frac{R}{r_f} = \frac{1}{2}\ln\left(\frac{2\pi}{V_f}\right)$ for square packing. Defining ϕ_{max} as the maximum packing factor and substituting $\ln\frac{R}{r_f} = \frac{1}{2}\ln\frac{\phi_{max}}{V_f}$ in Eq. (B.8) yields

$$\beta = \left[\frac{4\pi G_m}{E_f A_f \ln\frac{\phi_{max}}{V_f}}\right]^{1/2} \tag{B.9}$$

Considering Eqs. (B.5) and (B.9), the variation in the fiber stress greatly depends on the ratio of G_m/E_f. The greater is this ratio, the more rapid is the increase in value of the stress in fiber from the either ends.

B.2 Elasto-Plastic Matrix

Loading high strength fibers to their breaking stress in ductile matrices may be accompanied by plastic flow of the matrix. Of course, the fiber/matrix interface will fail if it is weaker than the matrix itself. Ignoring the matrix strain hardening, the shear yield strength of the matrix (τ_y) or the interface strength in shear (τ_i) can be considered as the upper limit for the shear stress at the fiber surface (τ_{rf}). The equilibrium of forces then gives;

$$\sigma_f \frac{\pi d^2}{4} = \tau_y \pi d \frac{L}{2} \tag{B.10}$$

$$\frac{L}{d} = \frac{\sigma_f}{2\tau_y} \tag{B.11}$$

The fiber length plays a major role in loading the fiber to its breaking strength (σ_{fu}) through the load transfer by the flowing matrix around it. If the critical length for a fiber with constant diameter is called (L_c) then

$$\frac{L_c}{d} = \frac{\sigma_{fu}}{2\tau_y} \tag{2.12}$$

Over length (L_c) the stress builds up on the fiber from both ends. Beyond L_c, the fiber and matrix displacements are the same and the fiber carries most of the load while the matrix role in carrying the load is minor. For $L < L_c$, the fiber is loaded to only

$$\sigma_f = \frac{2\tau_y L}{d} < \sigma_{fu} \tag{2.13}$$

The L/d ratio is called the fiber aspect ratio and $(L/d)_c$ the critical aspect ratio. The load in the fiber as a function of its aspect ratio is shown in Fig. B.1.

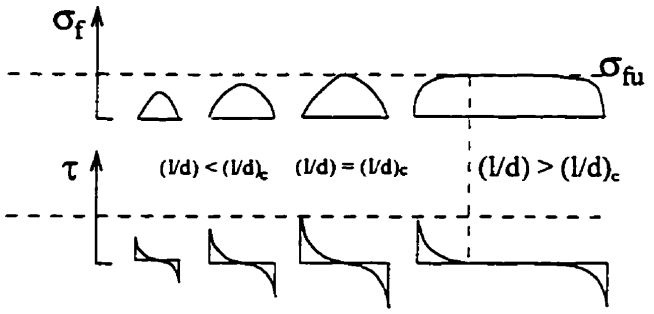

Fig. B.1: Effect of fiber length on the stress distribution.

IMAGE EVALUATION
TEST TARGET (QA-3)

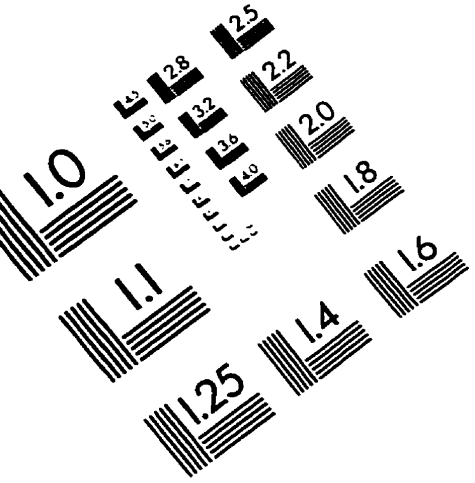

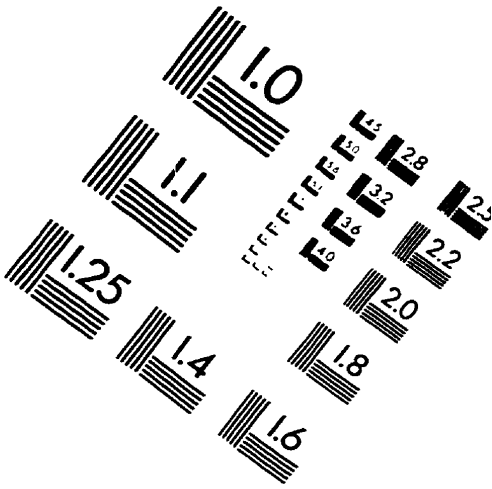

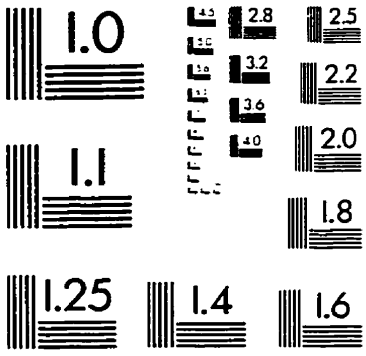

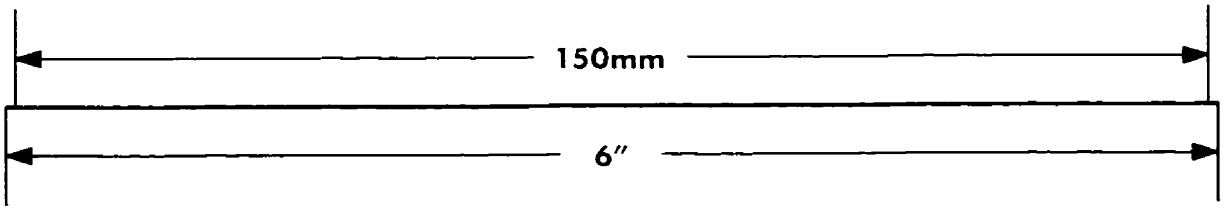

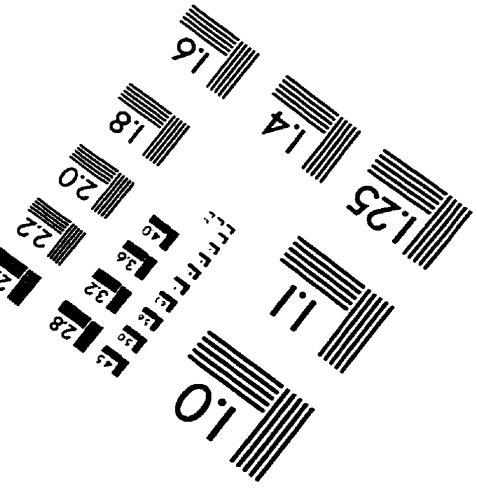

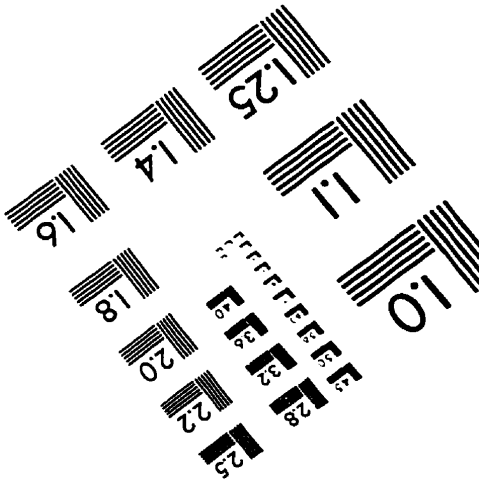

APPLIED IMAGE . Inc
1653 East Main Street
Rochester, NY 14609 USA
Phone: 716/482-0300
Fax: 716/288-5989